

Valence Shell Photoionization of Soot Precursors with Synchrotron Radiation

Dissertation zur Erlangung des
naturwissenschaftlichen Doktorgrades
an der
Julius-Maximilians-Universität Würzburg

vorgelegt von

Melanie Lang

aus Erlau

Würzburg 2015

Eingereicht am

an der Fakultät für Chemie und Pharmazie

1. Gutachter:

2. Gutachter:

der Dissertation

1. Prüfer:

2. Prüfer:

3. Prüfer:

des öffentlichen Promotionskolloquiums

Tag des öffentlichen Promotionskolloquiums:

Doktorurkunde ausgehändigt am

Contents

List of abbreviations	iv
List of publications	vii
1 Introduction and motivation	1
2 Basic principles	7
2.1 Principles of gas phase experiments	7
2.1.1 Skimmed molecular beam expansion	7
2.1.2 Generation of reactive intermediates	10
2.2 Synchrotron Radiation	14
2.2.1 Generation of SR	15
2.2.2 Properties and Quantification	16
2.2.3 Light source and front-end at the <i>Swiss Light Source</i>	17
2.3 Photoionization	19
2.3.1 Dissociative photoionization	21
2.3.2 Photoelectron spectroscopy	23
2.4 Theoretical concepts	32
2.4.1 Electronic and vibrational structure of molecules	32
2.4.2 DFT and <i>ab initio</i> computations with Gaussian 09	33
2.4.3 The program FCFit	36
2.4.4 The RRKM statistical theory of unimolecular rates	37
2.4.5 The program MinimalPEPICO	39
3 Experiment	47
3.1 The VUV beamline at the SLS	47
3.1.1 Apparatus	47
3.1.2 Molecular sources and sample containers	48
3.2 General procedures in experimental analysis	51
4 Photoionization of hydrocarbon radicals	53

4.1	Butynyl radicals C_4H_5	53
4.2	Methylallyl radicals C_4H_7	66
4.3	Fluorenyl radical $C_{13}H_9$	92
4.4	Benzhydryl $C_{13}H_{11}$ and diphenylmethylene $C_{13}H_{10}$	101
5	Photoionization of $C_{14}H_{10}$, $C_{18}H_{12}$ and $C_{22}H_{16}$	109
5.1	TPES of 1,2-Dihydropyrycene	110
5.2	TPES of 1-(Phenylethynyl)naphthalene	112
5.3	1,2,7,8-Tetrahydrocyclopenta[fg,op]-tetracene	113
6	Diazomeldrum's acid and its pyrolysis products	117
6.1	Photoionization and dissociative photoionization of DMA	119
6.2	Thermal decomposition upon pyrolysis	127
7	Summary	139
8	Zusammenfassung	141
	Appendix	145
	Bibliography	159
	Danksagung	173

List of abbreviations

AE	appearance energy
B3LYP	Becke (3 Parameter) Lee, Yang, Parr
CBS-QB3	complete basis set-quadratic Becke 3 (parameter)
CGF	contracted Gaussian functions
DPI	dissoziative photoionization
dpc	diphenylmethylene (diphenylmethyl carbene)
dpr	diphenylmethyl (radical)
DHP	1,2-dihydropyrazylene
DIB	diffuse interstellar bands
DLD	delay line detector
DNQ	diazo-naphthoquinone
DMA	diazomeldrum's acid
(TD)-DFT	(time-dependent) density functional theory
fc	false coincidences
FC	Franck-Condon
fs	femto-second
FWHM	full width at half maximum
G4	Gaussian4
GGA	Generalized Gradient Approximation
GTO	Gaussian-type orbitals
HACA	Hydrogen-abstraction-C ₂ H ₂ -addition
HF	Hartree-Fock
HOMO	highest occupied molecular orbital
IE _{ad}	adiabatic ionization energy
MCP	micro channel plate
MO	molecular orbital
MP2	Møller -Plesset perturbation theory
ms	mass-selected
MS	mass spectrum
NMR	nuclear magnetic resonance
PAH	polycyclic aromatic hydrocarbon

1-PEN	1-phenyl(ethynyl)naphthalene
PES	photoelectron spectrum/spectroscopy
PIY	photoion yield
SE	Schrödinger equation
SLS	Swiss Light Source
S/N	signal to noise ratio
SOMO	single occupied molecular orbital
STO	Slater-type orbitals
THCT	1,2,7,8-Tetrahydrocyclopenta[fg,op]-tetracene
TOF	time-of-flight
TPE	threshold photoelectron
(T)PEPICO	threshold photoelectron photoion coincidence
(T)PES	threshold photoelectron spectrum
TS	transition state
UIB	unidentified interstellar (IR) bands
VMI	velocity map imaging
VB	Valence Bond (model)
VUV	vacuum ultraviolet
WR	Wolff rearrangement

List of publications

Parts of this thesis have already been published in the following manuscripts:

Reference:^[1] M. Lang, F. Holzmeier, P. Hemberger, I. Fischer, Threshold Photoelectron Spectra of Combustion Relevant C₄H₅ and C₄H₇ Isomers. *J. Phys. Chem. A* **2015**, *119*, 3995.

Reference:^[2] M. Lang, F. Holzmeier, P. Hemberger, I. Fischer, Threshold Photoionization of Fluorenyl, Benzhydryl, Diphenylmethylene, and Their Dimers. *J. Phys. Chem. A* **2013**, *117*, 5260.

Reference:^[3] P. Constantinidis, M. Lang, J. Herterich, I. Fischer, J. Auerswald, A. Krüger, Electronic spectroscopy of 1-(phenylethynyl)naphthalene. *J. Phys. Chem. A* **2014**, *118*, 2915.

Reference:^[4] M. Lang, F. Holzmeier, P. Hemberger, I. Fischer, Decomposition of Diazomeldrum's Acid: A Threshold Photoelectron Spectroscopy Study. *J. Phys. Chem. A* **2014**, *118*, 11235.

Further publications that are not content of the present work:

(5) F. Holzmeier, M. Lang, I. Fischer, X. Tang, B. Cunha de Miranda, C. Romanzin, C. Alcaraz, P. Hemberger, Threshold photoelectron spectroscopy of unstable N-containing compounds: Resolution of ΔK subbands in HNC⁺ and vibrational resolution in NCO⁺. *J. Chem. Phys.* **2015**, *142*, 184306.

(6) F. Holzmeier, M. Lang, P. Hemberger, I. Fischer. Improved Ionization Energies for the Two Isomers of Phenylpropargyl Radical. *ChemPhysChem* **2014**, *15*, 3489.

(7) F. Holzmeier, M. Lang, P. Hemberger, A. Bodi, M. Schäfer, R. D. Dewhurst, H. Braunschweig, I. Fischer. Photoionization and Pyrolysis of a 1,4-Azaborinine: Retro-Hydroboration in the Cation and Identification of Novel Organoboron Ring Systems. *Chem. Eur. J.* **2014**, *20*, 9683.

(8) F. Holzmeier, M. Lang, K. Hader, P. Hemberger, I. Fischer. H₂CN⁺ and H₂CNH⁺: new insight into the structure and dynamics from mass-selected threshold photoelectron spectra. *J. Chem. Phys.* **2013**, *138*, 214310.

(9) J. Auerswald, B. Engels, I. Fischer, T. Gerbich, J. Herterich, A. Krueger, M. Lang, H.-C. Schmitt, C. Schon, C. Walter. The electronic structure of pyracene: a spectroscopic and computational study. *Phys. Chem. Chem. Phys.* **2013**, *15*, 8151.

- (10) P. Hemberger, M. Lang, B. Noller, I. Fischer, C. Alcaraz, B. K. Cunha de Miranda, G. A. Garcia, H. Soldi-Lose. Photoionization of Propargyl and Bromopropargyl Radicals: A Threshold Photoelectron Spectroscopic Study. *J. Phys. Chem. A* **2011**, *115*, 2225.
- (11) M. Steinbauer, M. Lang, I. Fischer, B. K. Cunha de Miranda, C. Romanzin C. Alcaraz. The photoionisation of propargylene and diazopropyne. *Phys. Chem. Chem. Phys.* **2011**, *13*, 17956.
- (12) H. Braunschweig, M. Fuß, K. Kraft, T. Kupfer, M. Lang, K. Radacki, M. Tamm. Synthesis and Reactivity of Boron, Silicon, and Tin-Bridged ansa-Cyclopentadienyl-Cycloheptatrienyl Titanium Complexes (Troticenophanes). *Chem. Eur. J.* **2010**, *16*, 11732.

1 Introduction and motivation

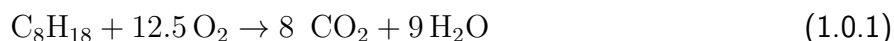
Organic radicals and carbenes are very interesting species with regards to their comparably high reactivity. One of the most significant discoveries in chemistry was the preparation and identification of the stable triphenylmethyl radical by Gomberg in 1900.^[5,6] By the early beginning in the investigation of radicals, the belief in the existence of open shell species was seeded with doubt,^[7] so Gomberg's achievement was never honored by a Nobel prize. Radicals possess an unpaired electron, whereas carbenes have a free pair of electrons. This means, caused by the high reactivity, low reaction barriers will lead to fast reactions if collisions with other particles occur. However, in isolated environments, many radicals and carbenes are thermodynamically stable.^[8]

But, where do organic radicals and carbenes in particular play an important role? Radicals contribute to biochemical processes,^[9-11] where for example nitric oxide, NO^\bullet , is a unique intracellular messenger that modulates blood flow, thrombosis, and neural activity.^[12] In our earth's atmosphere and stratosphere the species involved in radical chemistry comprise especially O^\bullet , HO^\bullet , HOO^\bullet and the biradical O_2 as the most prominent radicals.^[13] The atmosphere of Titan, a moon of Saturn, is dominated by methane, CH_4 , argon and N_2 . Titan's atmosphere is very similar to that of the early earth's one concerning the layer and temperature divisions. Since Titan has a reducing atmosphere, several hydrocarbon radicals and ionic species have been explored there.^[14,15]

The wide field of synthetic organic chemistry, which is assembled by numerous reactions of stable but also highly reactive radicals should also be mentioned. Only a few examples, like radical initiations with benzoylperoxide^[16] or the photo-induced C-O cleavage in aromatic ethers or esters,^[17] are mentioned here. The occurrence of radicals in combustion processes, in plasmas and in the interstellar space provide examples, in which predominantly small and highly reactive species can be observed in the gas phase.^[18] In this work, the focus is set on small hydrocarbon radicals and carbenes, relevant in combustion. Understanding the complex gas phase chemistry in combustion processes is the main aim in combustion research. Thus, accurate information on the identity and the quantity of the involved species is required.

But, how are hydrocarbon radicals involved in combustion processes? Hydrocarbon fuels are dominated by long aliphatic hydrocarbon chains, e.g. C_8H_{18} in gasoline. Since complete combustion of hydrocarbons, given for C_8H_{18} according to eq. 1.0.1, is never achieved, several high temperature

processes lead to the cleavage of C-C and C-H bonds of the initial compound.



In those reactions hydrocarbon radicals are formed, which further undergo a cascade of diverse processes, like, for example, reactions with oxygen to oxy- and peroxyradicals or radical-radical recombination. A group of interesting and very important reactions, in which small hydrocarbon radicals and also carbenes serve as the initiators in complex cascades, lead to the formation of polycyclic aromatic hydrocarbons (PAH).^[19,20] Polycyclic aromatic hydrocarbons are unsaturated hydrogenated cyclic (planar) carbon systems which are assumed to be soot particle precursors (among further relevance *vide infra*). Since soot is not only harmful to humans, but has further negative effects like lowering the efficiency of engines and finally causing their damage, its reduction or even prevention is worthwhile. So far, the formation of the first hydrocarbon ring is better understood than further reactions which lead via polycyclic aromatic hydrocarbons to soot.^[21] Several mechanisms, forming the first benzene derivatives have been suggested over the last 20 years. One of those is the bimolecular recombination of two propargyl radicals, C_3H_3 , which, in a sequence of rearrangements, form benzene, C_6H_6 .^[22] Further growth is predicted by addition of acetylene, C_2H_2 , that is added to an aromatic ring after an H-atom is abstracted in a radical reaction (*H*-Abstraction- C_2H_2 -Addition: HACA), which is supposed to be a repetitive reaction building polycyclic aromatic hydrocarbons (fig. 1.0.1).^[23]

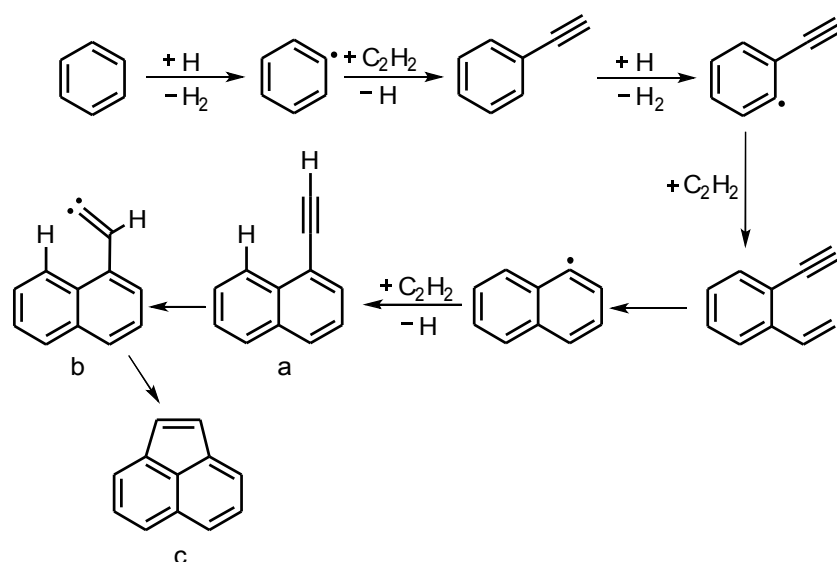


Figure 1.0.1: Scheme of the suggested HACA mechanism and further ring growth of 1-ethynyl naphthalene **a** by 1,2-H-migration of the ethynyl H-atom yields the 2-(1-naphthyl)ethyldiene carbene **b**. The latter can insert the carbene center into the *peri* C-H of the naphthyl ring to form acenaphthalene **c**.

Increasing ring formation is suggested to proceed via vinylidenes, $R_2C=C\bullet$ (R: phenyl, naphthyl), as the reactive intermediates in soot formation mechanisms. The latter insert their carbenic center into the *peri* C-H bond of the attached aromatic moiety to form another condensed ring system (see scheme 1.0.1).^[19,21]

However, the ubiquity of the hydrogen-abstraction- C_2H_2 -addition mechanism is still critically discussed. The large mass of high-order polycyclic aromatics which are formed by only adding the small C_2H_2 unit in each single step raised doubts on the ability of the hydrogen-abstraction- C_2H_2 -addition mechanism to form such large molecules with the experimentally observed rates.^[24,25] Recent experiments suggest an alternative mechanism for ring growth by phenyl addition cyclization (PAC) and methyl addition cyclization (MAC). Especially via the proposed phenyl addition cyclization large-mass polycyclic molecules are formed with rates that are more reliable.^[26] However, the presence of hydrocarbon radicals in the proposed ring growth mechanisms seems to be widely accepted.

But, how can radicals be identified in such processes? The main challenge when evolving combustion reactions is to monitor the wide range of reactive intermediates that are formed at the same time and with a short lifetime. Thus, not many analytical techniques can be applied. Moreover, because the concentrations of the reactive intermediates are very low, very sensitive methods are required.^[27-30] A powerful approach represents the spectroscopic analysis in burning fuel-air mixtures and the observation of intermediates in flames on-line. Such experiments are for example conducted by employing Raman scattering.^[31] State-of-the-art detection is performed by VUV-photoionization with subsequent analysis of intermediates by (molecular beam) Time-of-Flight mass spectrometry (PI-MBMS).^[29,30,32-34] From the latter, the formed combustion fragments can be observed by particular mass signals. The increase or decrease of the mass signals is viewed with increasing photon energy. If the individual total ionization cross sections of the observed species are known, the absolute concentrations of each detected species in the flame will be derived from photoionization mass-spectrometry experiments. With the knowledge of the absolute concentrations kinetic models to predict chemical processes can be performed.

But, why is it important to perform kinetic models of the reactions observed in combustion? Such complex processes depend on various factors, e.g. temperature, pressure or concentrations as relevant reaction parameters. Kinetic modeling is therefore necessary to reconstruct a process in a combustion engine. This enables to understand the chemical reactions and the combustion process itself. From photoionization mass spectra, at a given mass, isomer-specific ionization thresholds can be obtained by comparison to databases or spectra of the pure compounds.^[35] The obtained mass-selected ion signal does in most cases not contain unique molecular information. In addition, due to several reactive intermediates with the same mass (isomers) produced at the same time, there is sometimes the problem of overlapping signals in a distinct energy range. Since identification of combustion intermediates is not always achieved by probing them with photoionization

mass-spectrometry, there is a need to provide unique data on reactive intermediates. Threshold photoelectron photoion coincidence (TPEPICO) spectroscopy extracts both ions and electrons of the same ionization event and correlates them in time. This method is also combined with a molecular beam, which produces low particle densities and prevents reactive intermediates from further aggregations. Mass-selected threshold photoelectron spectra of isolated radicals yield therefore the spectroscopic fingerprint of a reactive intermediate that is necessary for its identification in reactive environments.

Going further, identification and characterization of polycyclic aromatic hydrocarbon is also a general need to draw reaction pathways for soot formation. As already implied, the scientific interest on these species is manifold. Beside their occurrence in combustion processes, they are of further importance in extraterrestrial regions and in the atmospheres of other planetaries. At the beginning of the 20th century it was discovered that the absorption spectra of several stars showed the same spectral features.^[36] These absorption features were, compared to the known absorption lines of atoms, covering broader line widths and showing diffuse edges.^[37, 38] The diffuse bands were observed to be ubiquitous in the interstellar medium and were therefore referred to as diffuse interstellar bands (DIB). To this day, a few hundred of diffuse interstellar bands are known, but none of them is convincingly identified to originate from specific elements or molecules.^[39] Recent studies suggest that the diffuse interstellar bands are caused by absorptions of polyatomic carbon-containing molecules.^[40, 41] The spectrum of these absorption lines exhibits the range from the visible to the near infrared light. Carriers of diffuse interstellar bands were early supposed to be dust and metal crystals, but were revised again after some highly resolved DIB spectra did not reproduce the lines expected from solid state species.^[42] By now, it is generally believed that diffuse interstellar band carriers are free molecules in the gas phase. Beside further suggested reasonable carriers of diffuse interstellar bands, polycyclic aromatic hydrocarbons became the leading candidates as carriers because of their suggested role in interstellar IR emission features.^[43] The latter are referred to as unidentified infrared emission bands (UIBs) and reveal in low density circumstellar clouds a specific series of distinct emission bands at 3.3 μm , 6.2 μm , 7.7 μm , 8.6 μm and 11.3 μm .^[44] All of the detected emission features can be explained by vibrational activity in polycyclic aromatic hydrocarbons.^[45, 46] As stated before, planetary atmospheres like that of Titan is rich on methane and nitrogen. Photoinduced reactions are proposed to be the reason for complex organic materials that were found in Titan's atmosphere by the Cassini mission.^[15, 47] However, although much evidence exists which suggests the presence of polycyclic aromatic hydrocarbons in extraterrestrial environments no particular polycyclic aromatic hydrocarbon has been identified in the interstellar medium, in circumstellar environments or in the planetary atmospheres.^[43] The main challenges in their identification are that the IR active modes of their vibrational frequencies are predominantly similar for a range of these molecules, not permitting to use these vibrational features as fingerprints of a particular species. Moreover, the small dipole moments of PAH leads to weak rotational transitions, which impedes

their detection by millimeter-wave spectroscopy. Thus, electronic spectroscopy of these system is essential to get closer to definite identification of particular molecules. To perform electronic spectroscopy, for example by resonance enhanced multiphoton ionization presumes the knowledge of the exact ionization energy of the investigated system. Since low cost computational values for such comparably large molecules are not always accurate, determining experimental ionization energies is of great importance. In addition, polycyclic aromatic hydrocarbons are also expected to be present in the interstellar medium as ions. The electronic transitions in the cations are more likely to correspond to the low-lying diffuse interstellar bands, since they are observed in the IR- or visible region for some examined molecules like naphthalene or phenanthrene, thus, significantly lower than in the neutral molecules.^[48,49] Therefore, the investigation and characterization of polycyclic aromatic hydrocarbon cations reveals a promising and important part not only in concerns of combustion research, but also in the context of identifying constituents of our universe.

In the context of the previously stated facts, the aim of the present work is summarized as follows:

1. Several hydrocarbon radicals will be produced upon pyrolysis from suitable stable precursors. Ideally, they can be identified isomer-selectively from a threshold photoelectron spectrum and the adiabatic ionization energy (IE_{ad}) and vibrational activity in the cation can be assigned.
2. Polycyclic aromatic hydrocarbon will be characterized by threshold photoelectron spectroscopy and their ionization energies will be derived.
3. Diazomeldrum's acid is an interesting precursor of potentially reactive intermediates relevant for combustion and astrochemistry. It will therefore be investigated upon pyrolysis and the formed intermediates will be identified and characterized. In another context, diazomeldrum's is a model compound which undergoes a thermally and photochemically induced Wolff rearrangement. Since the dissociation dynamics in the neutral molecule gained very great interest, it seemed worthwhile to study the fragmentation in the cation, too.

2 Basic principles

2.1 Principles of gas phase experiments

An important requirement to investigate highly reactive intermediates is to keep them under inert conditions, i.e. low particle densities and low temperatures. Isolation and spectroscopic characterization of radicals was initially carried out in matrices, where experimental temperatures do not exceed 20 Kelvin. In matrix isolation that is conducted in a noble or inert gas, radicals are kinetically stabilized by the cage of matrix atoms or molecules around them. The reactive intermediates get additionally immobilized and diffusion is inhibited by the low temperatures. An explicit advantage of isolating radicals in matrices is the extreme slow-down of bimolecular and unimolecular reactions or the complete inhibition of the latter.^[50] On the other hand rotational activity cannot be observed. In addition, a further handicap when investigating radicals in matrices is that, if produced from photolysis, they may easily recombine. In addition to this, matrix isolation of molecules is only established in combination with IR-, Raman-, UV- and EPR spectroscopy and does in general not provide mass selectivity.^[51]

Another method to investigate kinetically non-stable species is to prepare them in Helium nanodroplets. In this approach molecules are cooled down to some milli-Kelvin and several electronic spectroscopic methods can be combined with He nanodroplets.^[52]

A different and versatile method to observe reactive species is to expand them in a molecular beam. Since this method has been applied in this works' experiments, it will be described in detail.

2.1.1 Skimmed molecular beam expansion

A further approach to investigate reactive molecules is to generate them in the gas phase and to expand the pure or diluted sample in a molecular beam in which collisions are reduced. Different types of molecular beams are basically the *supersonic jet* and the *effusive beam*. The expansion of a room temperature high pressure (p_0) sample from a container can be characterized by the relation of the nozzle's aperture d and the mean free path λ_0 of the molecules. When d is significantly smaller than λ_0 , an effusive beam will be formed. This is the case when ambient background pressure is applied. The temperature of the latter can be described by a Boltzmann distribution with a

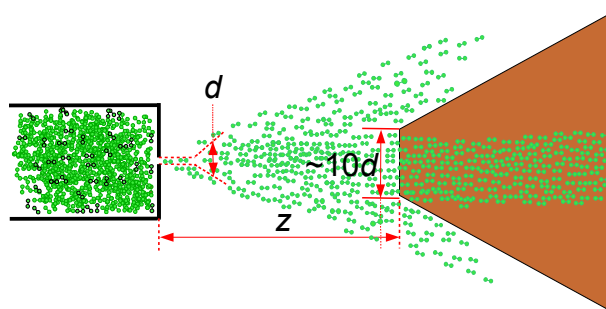


Figure 2.1.1: Scheme of a molecular beam expansion. The skimmer is ideally mounted 5-10 mm from the nozzle. The relation of the source diameter d , the opening diameter of the skimmer and the distance z from the source to the skimmer refer to real proportions.

temperature that is equivalent to that of the sample.^[53] When d is significantly greater than λ_0 , a molecular *jet* will form. The relation $d \gg \lambda_0$ can be achieved by increasing the initial pressure p_0 of the carrier gas and the sample, which is ultimately limited by the pumping speed.

In the experiments performed in this work an “in-between” of an effusive beam and free jet was applied. The molecular beam was employed in a continuous mode, accounted for the continuous operation mode of the light source. The absolute pressure prior expansion was chosen from 1.5 bar to 3.5 bar and the gaseous mixture of the carrier gas and sample was heated up to 1000 °C in the pyrolysis tube, which acts as the “final nozzle” (*vide infra*). Thus, the characteristics of the formed molecular beam are also found “in-between” a jet and an effusive beam.

From the warm beam the “coldest” part is filtered by the skimmer (see fig. 2.1.1), that the expanded gas will pass before interacting with the light source. The skimmer is a conical device (nickel or copper) mounted as the gate for the molecular beam to arrive at the experimental chamber of the vacuum apparatus (compare sec. 3.1.1). As the detection of charged particles is employed by multi-channel plates (MCP), only low particle densities corresponding to a pressure of about 10^{-6} mbar display reasonable experimental conditions. Therefore the detector is placed in a second differentially pumped chamber, separated by the skimmer with the intention to operate the two chambers at different working pressures. These pressure differentials can comprise about two orders of magnitude.^[54] The skimmer has an opening of about 1-2 mm, “shaping” the expanding molecular beam in that way that only the coldest and central part of it can reach the experimental chamber. It is important to find the perfect distance of the molecular source from the skimmer. If it is mounted too close to the skimmer, the “hot” outer parts of the beam will also reach the experimental chamber.^[55] If it is mounted too far away, the density of the beam will be too low in order to get a sufficient signal from ionization, as the beam’s density is estimated to drop with $(z/d)^2$.^[54]

Cooling of the internal degrees of freedom (translation, vibrations and rotations) in a continuous beam is observed to a lesser extent than in a pulsed beam, formed from a room temperature

high pressure sample. Taking into account the high temperatures (800-1200 °C) prior expansion, vibrational temperatures are typically found around a few hundred degrees Celsius. Recent pyrolysis experiments combined with a continuous molecular beam showed vibrational temperatures of 350 ± 70 K for the CF_3 radical at 50 W pyrolysis power^[56] and 550 K for the CH_3 radical at 40 W pyrolysis power.^[57] These pyrolysis power are estimated to correspond to 1200 °C at 50 W and 900 °C at 40 W, based on the temperatures measured in dependence of the applied pyrolysis power throughout this work. Vibrational cooling is initiated by collisions of molecules and atoms of the carrier gas, but is also effected by further issues. These are for example the total energy of the molecule and the vibrational energy spacing.^[58] The lower the frequencies of a molecule, the faster it relaxes and transfers vibrational energy to the diluent gas.^[59] The nature of the diluent gas also influences the cooling efficiency. Argon is for example more effective in cooling vibrational energy than Helium since Ar is heavier than He and allows a better match for momentum transfer with other (large sized) molecules. Nevertheless, the cooling of the internal degrees of freedom is more efficient, the lower the translational temperature, since vibrational and rotational energy may flow into translational energy.

A possibility to assess the vibrational temperature T_{vib} is given by the evaluation of *hot bands* that are transitions from a vibrationally excited electronic ground state to the vibrational ground state of the final state. The hot band intensity I is proportional to a Boltzmann distribution of states of the vibrations. The relation is given according to eq. 2.1.1,

$$I = |\langle \Psi' | \Psi'' \rangle|^2 \exp\left\{-\frac{E''}{kT_{vib}}\right\}, \quad (2.1.1)$$

where Ψ' and Ψ'' are the vibrational wavefunctions of the excited and the respective ground state. E'' is the energy of the initial vibrational state relative to the ground vibrational state. Beside this convenient approach to estimate vibrational temperatures^[54] another method to estimate the vibrational energy can be applied by determining the onset in breakdown diagrams of fast unimolecular dissociation reactions. The onset is predominantly appointed for the thermal energy distribution (vibrations and rotations) of the ground state molecule: the higher the temperature the greater the redshift of the dissociation onset^[60,61] (see sect. 2.3.1). In contrast to vibrational cooling, the efficiency of translational cooling can be more easily established by the width of TOF peaks in a TOF-mass spectrum.^[62]

2.1.2 Generation of reactive intermediates

In order to investigate reactive intermediates in a way that can easily be combined with the molecular beam expansion of a gas, they have to be produced *in situ* since they are kinetically labile under ambient conditions. Different approaches for radical generation have been established, comprising photolysis,^[63–70] electrical discharge,^[71–73] and pyrolysis (*vide infra*). All three methods can be combined with a molecular beam. Especially photolysis is so far the only method that provides access to the generation of peroxy radicals.^[74] With electrical discharges radical yields are often very good,^[75] but the non-selectivity and the high amounts of side-products generated from this method is disadvantageous. Nevertheless, with this approach thermochemically unfavorable radicals that cannot be produced using other methods can be formed. Since pulsed discharges constitute a low temperature plasma, especially reactive species relevant in plasma chemistry can be investigated.^[18] In addition, radicals can also be produced by chemical methods, for example abstraction of hydrogen atoms by atomic fluorine, chlorine or hydrogen in a chemical reactor.^[76] But, the approach only works well when the precursor molecule contains equivalent hydrogen atoms^[77,78] and becomes insufficient for a selective production of reactive intermediates. In addition, its application within a supersonic molecular beam expansion has not yet been achieved.^[79] The generation of radicals performed by pyrolysis constitutes a convenient method with a comparable high selectivity in radical production since the pyrolysis power is easy tunable. The pyrolysis method has been applied in this work and will therefore be highlighted in the following section.

Flash pyrolysis

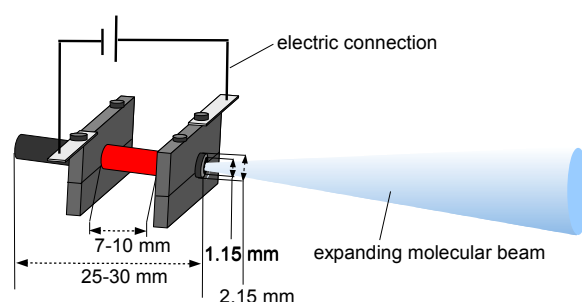


Figure 2.1.2: Scheme of the pyrolysis source used in this work.

The design of a *flash pyrolysis* source^[80] consists of a little tube that is mounted onto the nozzle ($\sim 70\text{-}150\ \mu\text{m}$) of the molecular beams' source (fig. 2.1.2). The pyrolysis tube is of semiconducting silicium carbide (SiC) and is electrically heated.^[18] The geometric parameters of the SiC tube (Saint Gobain Ceramic, Hexeloy SE, SiC tube) used in this work are as follows. The inner diameter is 1.15 mm, the outer diameter is 2.15 mm and the length should be chosen to be about 25-30 mm,

as can be seen in fig. 2.1.2. In SiC tubes temperatures up to 1500 °C can be achieved. However, the lifetime of a SiC tube operated in the upper range of the temperature region is very short.

In the hottest zone the radicals are produced by thermal bond cleavage from the precursor molecules. The heating electrodes are positioned as close as possible to keep the hot part of the tube as short as possible, to prevent the formed reactive intermediates from further gain of thermal energy and therefore from secondary reactions. A short residence time (in the range of 25-150 μs) in the active contact zone of the tube will not only be affected by the length of the heated zone, but also by the flow of the gaseous mixture of precursor and carrier gas passing the tube. Therefore the initial pressure of the rare gas is a crucial parameter to influence the residence times.^[81] In general, a dilution of the precursor molecule in the order of 0.2-1 % is preferable. This is achieved by seeding a precursor with a vapor pressure of 20 mbar in 3 bar of the rare gas, which was argon in all presented experiments. Normally a constant volumetric flow is set (by a mass flow controller or a precisely adjustable needle valve) and therefore, in the course of heating the pyrolysis tube, the pressure drops across the tube. Since the pressure is directly proportional to the velocity in the tube, the latter will also decrease while heating. Due to the velocity distribution in the tube, a distribution of different residence times results along the radial axis of the tube.^[81]

Reactions with the wall depend on the relation of the residence time τ_{res} of the flow and the radial diffusion τ_{res} which give the Péclet number P_e . So P_e can be expressed by the product of the tube's length L and the average velocity of the flow u related to the diffusion coefficient D (eq. 2.1.2).

$$P_e = \frac{\tau_{res}}{\tau_{diff}} = \frac{Lu}{D} \quad (2.1.2)$$

For small Péclet numbers the residence time is too short for radial diffusion. Therefore wall reactions will not be dominating. In contrast, for large Péclet numbers diffusion dominates and wall reactions might contribute to a larger extent.^[81] Radical recombination reactions are of particular interest, since they are intended to be suppressed in experiments on the isolated molecule. They occur extremely rapid, since nearly no reaction barriers exist. As these are second-order reactions, the destruction rate for the radicals is quadratic in the radical concentration, $[R]$.^[81] Thus the pressure and the temperature should be varied to achieve effective residence times in the tens of μs . This means, if the radical concentration is low enough, secondary reactions of radicals and recombination reactions will be effectively minimized.^[82] Note however, in some of the studies the radical-radical recombination was deliberately used to investigate dimers of the radicals.

Choice of precursor molecules

As stated before, pyrolysis constitutes a comparably selective tool for radical formation when the pyrolysis power and the precursor molecule are chosen appropriately. Therefore the molecular system applied as a precursor in a pyrolysis experiment should fulfill some requirements that ideally are the following:

- The radical should be produced from the precursor molecule in a clean way. Although side products can be distinguished in a coincidence-experiment, they nevertheless compromise the signal of the intended radical.
- The precursor should be completely converted to the radical, ideally upon mild pyrolysis conditions.
- The *IEs* of the precursor and the radical should differ as much as possible (3-4 eV). If the precursor is not completely converted (which is often the case for chlorides and bromides), the radical signal and the signal from DPI of the precursor to a fragment with the same m/z like the radical interfere if the ionization energies (*IE*) are too close.

Nevertheless, the ideal requirements are often not fulfilled. Therefore the choice of the precursor is usually dictated by practical criteria. Those are, for example, easy synthetic access and a sufficient vapor pressure to transfer the precursor molecule in the gas phase. Typical precursor molecules for the generation of hydrocarbon radicals in pyrolysis experiments are halogenides, nitrites and amines. Thus, the bond dissociation energies (*BDE*) should be significantly lower than the *BDE* of C-H bonds for clean conversion. The respective values are given for comparison in Table 2.1.

bond	BDE /kJ · mol ⁻¹ (eV)	bond	BDE /kJ · mol ⁻¹ (eV)	bond	BDE /kJ · mol ⁻¹ (eV)
<i>C</i> _{prim} -I	241 (2.50)	<i>C</i> _{allyl} -I	191 (1.98)	<i>C</i> _{benzyl} -I	214 (2.21)
<i>C</i> _{prim} -Br	302 (3.13)	<i>C</i> _{allyl} -Br	247 (2.57)	<i>C</i> _{benzyl} -Br	264 (2.73)
<i>C</i> _{prim} -Cl	350 (3.63)	<i>C</i> _{allyl} -Cl	-	<i>C</i> _{benzyl} -Cl	310 (3.21)
<i>C</i> _{prim} -NO ₂	255 (2.65)	<i>C</i> _{allyl} -NO ₂	-	<i>C</i> _{benzyl} -NO ₂	211 (2.19)
<i>C</i> _{prim} -NH ₂	357 (3.70)	<i>C</i> _{allyl} -NH ₂	-	<i>C</i> _{benzyl} -NH ₂	300 (3.11)
compared to C-H bonds					
<i>C</i> _{prim} -H	440 (4.56)	<i>C</i> _{allyl} -H	372 (3.85)	<i>C</i> _{benzyl} -H	377 (3.90)

Table 2.1: Bond dissociation energies of labile bonds in precursor molecules used for radical generation.^[83]

2.2 Synchrotron Radiation

Synchrotron radiation is easily tunable, has a quasi-continuous structure with a sufficient photon flux, is available over a broad energy range and is therefore an appropriate light source to record (threshold) photoelectron spectra. The basic principle for the generation of synchrotron radiation (SR) follows the observation that charged particles emit light when they are accelerated.^[84] In a synchrotron, electrons are ejected from an electron gun by thermionic emission from a hot filament into the linear accelerator (*linac*). There they are accelerated up to 100 MeV. As electrons happen to collide with residual gas particles and therefore get lost, they are regularly supplied from the electron source. From the *linac* they get ejected into the *booster* ring for further acceleration. When the desired ring current, that is 400 mA at the *Swiss light Source* (SLS) at the Paul Scherrer Institute in Villigen, is reduced by less than 1% of the original beam current, the electrons are quasi-continuously injected into the storage ring. The storage ring is operated in the so called “top-up” mode of injection. In the storage ring the electrons are held at a constant energy, and are forced onto their path by the use of bending magnets. Quadrupol magnets focus the electron beam and the chromatic aberrations caused by the quadrupol magnets are corrected by sextupole magnets. While circling the electrons gain energies of 2.4 GeV, corresponding to a speed nearly as high as the velocity of light. Thus, their physics has to be evaluated from a relativistic point of view. The mass m of the electrons is then given as a function of their velocity v :

$$m(v) = m_0 \frac{1}{\sqrt{1 - \frac{v^2}{c^2}}}, \quad (2.2.1)$$

where m_0 is the rest mass of the electron and c the speed of light. The power of the emitted radiation P depends on the angle between the propagation of the electrons movement and the direction of the electrons' acceleration. For an electron, accelerated on an orbit with the radius R , the radiated power is given according:

$$P(E, R) = \frac{e^2 c}{6\pi\epsilon_0} \frac{E^4}{(m_0 c^2)^4 R^2} = \frac{e^2 c \gamma^4}{6\pi\epsilon_0 R^2} \quad (2.2.2)$$

ϵ_0 is the permittivity of the vacuum, e the elementary electric charge and γ displays the relation of the total energy to the rest mass energy. The energy ΔE that is irradiated during every full orbit is related to eq. II:

$$\Delta E = \int P dt = \frac{P \cdot 2\pi R}{c} = \frac{e^2 \gamma^4}{3\epsilon_0 R}. \quad (2.2.3)$$

Due to the emission of photons, energy is lost from the electrons, which therefore has to be replenished by radio frequency (RF) sources. As implied in fig. 2.2.1 the arrangement of the storage ring

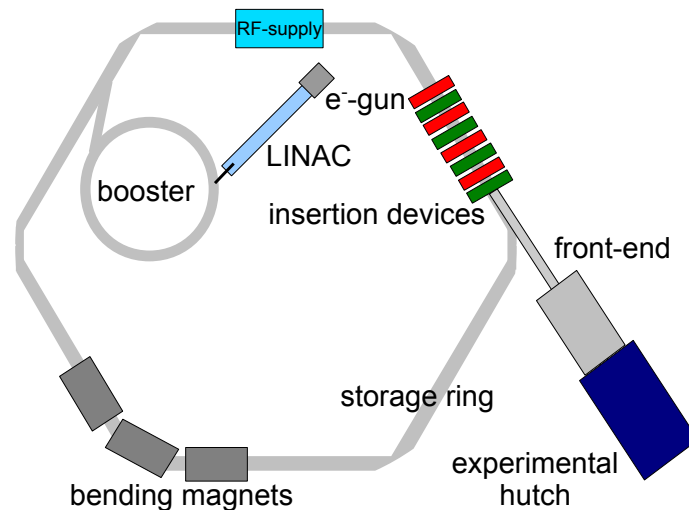


Figure 2.2.1: Schematic view from the top onto a synchrotron. (according^[85])

contains curved sections in that the bending magnets are placed, followed by straight sections with *insertion devices* (fig. 2.2.2) that themselves produce synchrotron radiation (SR). The beamlines are placed along the axes of the insertion devices and tangentially to the bending magnets.^[85]

2.2.1 Generation of SR

Electrons accelerated to relativistic velocities emit radiation in a narrow cone of light that is propagating in the same direction as the electron. The properties of the SR depend on the angular frequency and the energy of the electrons in the storage ring. Radiation is emitted at the bending magnets and the insertion devices and the lost kinetic energy is replenished by every full orbit around the ring, when the electrons pass the radio frequency cavity. Due to the fact that this process is a self-correcting process and the electrons can either enter the RF cavity in the right phase of the RF voltage cycle or not, the ones that do not gain the correct energy boost, are lost. As a result, the electrons circle in small packets, so called bunches. The time structure of a synchrotron is therefore determined by the amount of bunches produced by the RF. In the SLS storage ring 500 bunches separated by 60 cm, corresponding to 2 ns, are produced. A typical bunch length is 10 ps. The storage ring can be operated only with a single bunch (single bunch mode) to perform time-resolved experiments or, as it is used for normal operation, in the multi-bunch mode. The bending magnets hold the circulation of the electron on a closed path. The bending magnet radiation is produced as a flat cone with a large fan angle that allows for positioning of more than one beamline at one bending magnet. The power emitted is defined in terms of the storage-ring energy and the magnetic field strength. Obviously, the emitted light from a bending magnet has a higher horizontal divergence, which causes the apertures to the beamlines to cut off high amounts of photons. Much higher flux and brilliance is supplied by the radiation of insertion devices. These devices placed

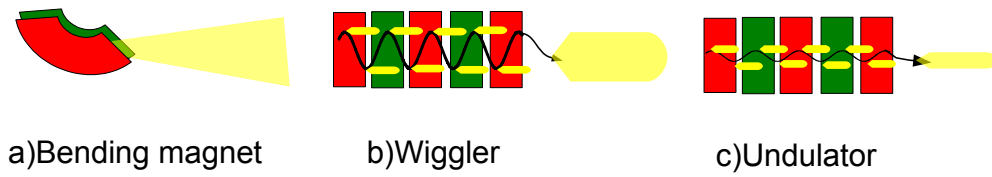


Figure 2.2.2: Schematic representation of a bending magnet (a) and the insertion devices wiggler (b) and undulator (c).

in the straight sections of the ring between the bending-magnet segments are built of a range of magnets producing alternating magnetic fields pointing up and down. Therefore the electron beam oscillates. Its pathway deviates from the straight pathway to a lesser extent with an *undulator* and deviates to a greater extent in a *wiggler*. Therefore wigglers emit a continuum range of light whereas undulator-SR shows a narrow spectrum due to interference.

2.2.2 Properties and Quantification

The quality of a synchrotron beamline facility is characterized by the flux and the brilliance of the photon beam. The higher both quantities, the better! With a repetition rate in the upper MHz range, synchrotron light displays a quasi-continuous light source. The flux gives the number of photons per second per unit bandwidth passing through a defined area. The flux is proportional to the square of the electron's centripetal acceleration, which is proportional to the square of the Lorentz factor γ^2 . According to eq. 2.2.2 the flux is proportional to γ^4 . The brilliance B is defined as the flux $\Delta N/t$ per unit source area A and unit angle $\Delta\Omega$ and states how the flux is distributed in space and in angular range (eq. 2.2.4).^[85] High-energy synchrotron rings supply therefore radiation with high flux and high brilliances.

$$B = \frac{\Delta N}{t \cdot A \cdot \Delta\Omega \cdot \frac{\Delta\lambda}{\lambda}} \quad (2.2.4)$$

The emittance is the product of the linear source size and the beam divergence in the same plane. It is imposed to be kept as small as possible since it is inversely proportional to the brilliance. The SR is linearly polarized in the plane of the storage ring, but left-circularly polarized for the observer above the plane and right-circularly polarized below the plane of the storage ring.^[85]

2.2.3 Light source and front-end at the *Swiss Light Source*

Before the SR beam enters the apparatus in the experimental hutch (fig. 2.2.1) it passes the front-end. Here the separation of wavelengths takes place. The radiation is supplied by the bending magnet and spreads over an horizontal angle of 8 mrad. The spectrum is not influenced by the horizontal angle whereas the vertical distribution is determined by the photon energy. High energetic radiation as X-rays are mainly emitted in the plane of the storage ring whereas softer radiation like VUV, visible or infrared light has a considerably wider radiation cone above and below the storage ring.^[86] The ring shield and the Pb shield are further devices to prevent high energetic reflections from entering the beamline.

The power of the beam is regulated in first instance by a set of horizontal and vertical slits that are placed before the first mirror. Before the light is collimated onto the copper mirror with a platinum reflective coating, most of the high energetic light ($h\nu > 150$ eV) is absorbed by the X-ray blocking shield (fig. 2.2.3).

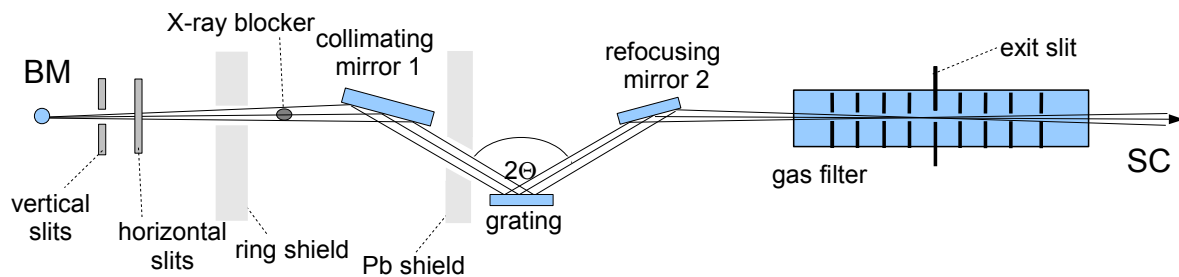


Figure 2.2.3: Side view of the front-end of the VUV X04DB beamline. (adapted from^[86])

VUV light is monochromatized by a diffraction grating because it is the only applicable dispersive element. Prism material is not able to reflect or transmit VUV photons. The radiation is therefore spread from the collimating mirror onto the monochromator plane grating and to the refocusing mirror. These three elements form the constant deviation angle monochromator, which is equipped with three different gratings with line densities of 1200, 600 and 150 lines mm^{-1} . The 600 mm^{-1} grating has a resolving power of 10^4 at 10 eV and delivers a photon flux of about 10^{11} s^{-1} at 10 eV. It has a tuning range comprising VUV/XUV radiation from 5 eV (248 nm) to 15 eV (83 nm). The grating moves according to eq. 2.2.5, and is thereby the only moving optical element during an energy scan, since $2\Theta = \text{const.}$ ^[86]

$$m\lambda = 2d\cos\Theta\sin\phi. \quad (2.2.5)$$

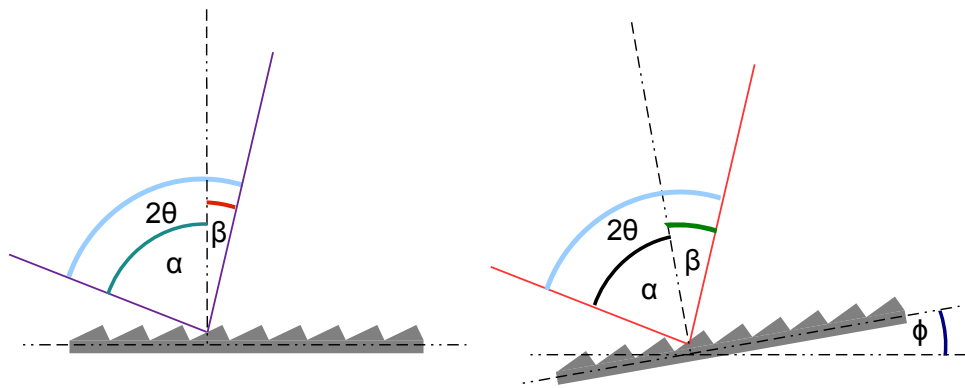


Figure 2.2.4: Monochromator blaze grating with the light entering the grating under the incident angle α and leaving the grating under the diffracted angle β . On the left the scan angle ϕ is 0° while on the right $\phi > 0^\circ$. The constant deviation angle Θ is given by the difference of $\alpha - \beta$.

Here m is the diffraction order, λ the wavelength, ϕ is the scan angle, d the line spacing and Θ the constant deviation angle with $2\Theta = \alpha - \beta = 130.9^\circ$. α is the incident angle and β the diffracted angle. From eq. 2.2.5 can be concluded that the diffracted wavelength only depends on the scan angle ϕ , which is visualized in fig. 2.2.4.

The flux decreases with higher line density N_d while the resolution $\lambda/\Delta\lambda$ increases, as can be deduced from eq. 2.2.6:

$$\frac{\lambda}{\Delta\lambda} = mN_d(\sin\alpha + \sin\beta). \quad (2.2.6)$$

By passing the monochromator the beam is refocused into the gas filter onto a vertical exit slit which can be adjusted from $110 \mu\text{m}$ to $1000 \mu\text{m}$. From the exit slit in the gas filter the diverging light beam enters the experimental chamber of the vacuum apparatus.^[86]

2.3 Photoionization

When an electron is removed from a particle, an ion is generated.^[87] The respective ionization energy IE_m corresponds to that energy which is needed to remove the electron. Knowing IE is crucial to retrieve thermochemical data, like bond dissociation energies (BDE) or heats of formation (ΔH_f^0).^[88] Moreover, ions are short lived species, which are formed as reactive intermediates in chemical reactions. For example Ion-Molecule reactions form large molecules in the interstellar space. Thus, ions are interesting species to be characterized.^[89] Methods for ionization comprise electroionization, Penning ionization, charge exchange ionization, field ionization and photoionization.^[90,91] Photoionization can be performed by different techniques. In multiphoton ionization (MPI) processes several (at least two) photons of either the same or different energies are used to ionize the molecule (fig. 2.3.1, a). In such a process the first photon(s) reaches an excited state in the neutral molecule and the last photon applied ends above the ionization threshold. Since a large photon density is necessary for MPI, tunable dye lasers are typically used as the photon source. Photoionization achieved by only one photon can be carried out with lower photon densities as available from discharge lamps or in synchrotron light. One-photon processes are typically applied in photoionization mass spectrometry (PIMS) and in photoelectron spectroscopy (PES). With PIMS the ion yield is observed as a function of the photon energy. Conventional PES observes the electron kinetic energy at a constant photon energy. PIMS and PES complement each other, since both methods lack the information that is provided from the other approach. Since PES has been applied in this work, it will be discussed in sec. 2.3.2 in more detail.

In general, direct and indirect photoionization processes are known. Direct ionization is observed as a transition from the neutral potential energy surface to a binding cationic potential surface. Indirect ionization is observed from a transition to a high lying neutral state (super-excited state) with significant Franck-Condon factors (FCF)^[92] which in a subsequent decay forms an ion.^[93] This often complicates the detection of direct ionization processes. Super-excited states represent highly excited electronic states, for example Rydberg states, which autoionize or predissociate. The photoionization process depicted in figure 2.3.1 (b), displays the transition from a neutral diatomic molecule to different states in the cation. Corresponding to the transitions, different ionization thresholds exist which are indicated by the respective steps of the idealized photo-ion yield (PIY) curves (c). Direct ionization of the diatomic molecule is achieved as follows. The cationic ground state $AB^+(X)$ is excited by the energy E_X and can be populated up to the fourth vibrational level with increasing photon energies. If energies from E_A to $E_1(A^+)$ are applied, the cation will be formed in the excited state $AB^+(A)$ with full vibrational energy. The highest electronic state that will be observed from direct ionization is $AB^+(B)$, which only can be populated in the vibrational ground state $\nu = 0$.

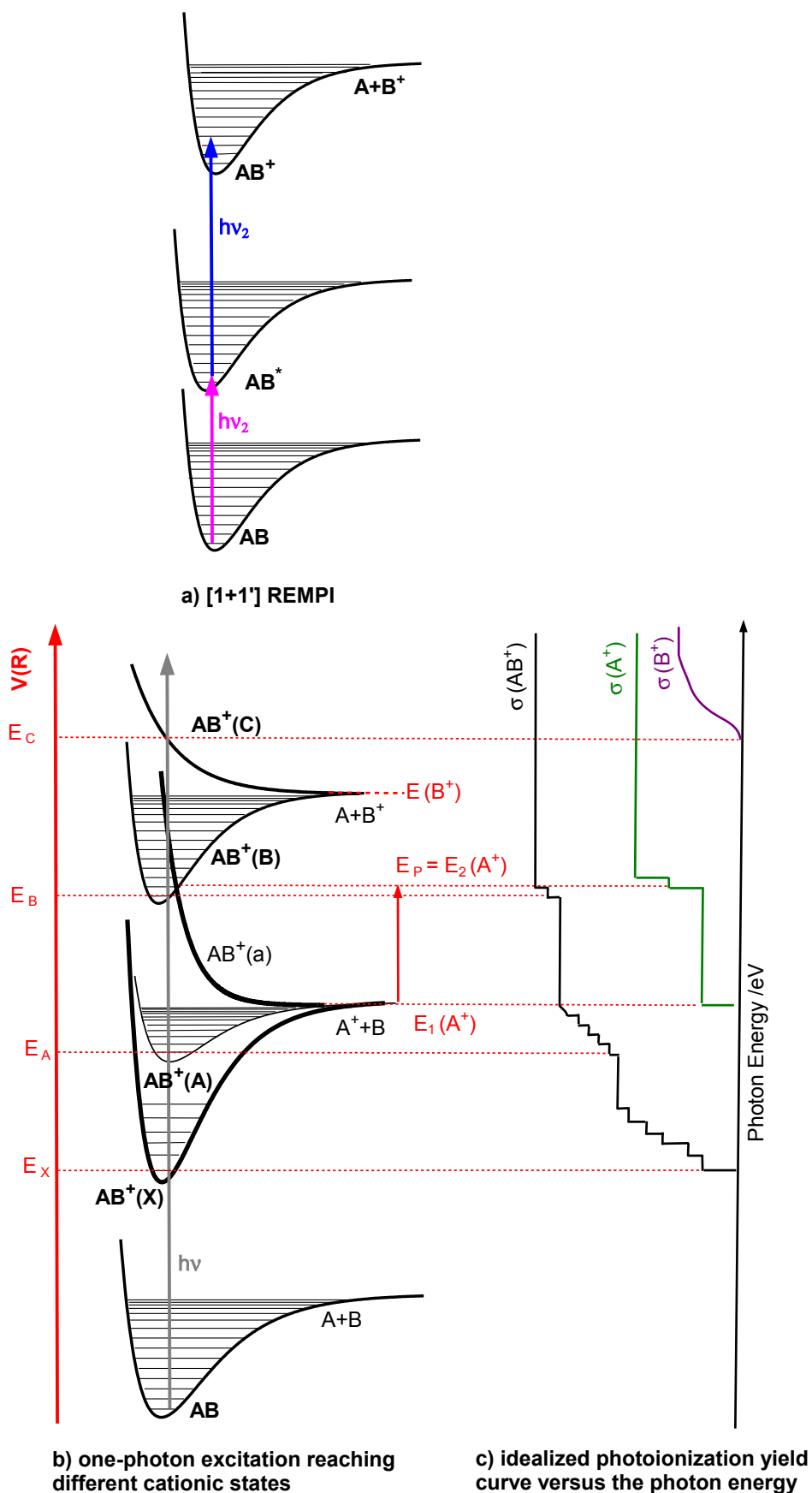


Figure 2.3.1: Schemes for different photoionization processes. a) [1+1']-REMPI process b) single photon ionization to several ion states and c) the idealized photo-ion yield curve for the transitions displayed by b) (A similar figure is given in reference^[91]).

The corresponding idealized PIY curve of AB^+ (fig. 2.3.1, c, black) shows a staircase rising for the bound electronic states $AB^+(X)$, $AB^+(A)$, $AB^+(B)$ and the vibrational excitation within these states.

For polyatomic molecules ionization yield curves show a gradual and continuous increase instead of a staircase structure. This typical behavior is due to the tight spacing of vibrational energy levels and the higher contributions of autoionization. Nevertheless, often the curve has a sharp onset which enables to deduce the adiabatic ionization energy. The appearance of a mass signal in the mass spectrum and the increase of the ion yield curve is not only characterized by the successive energy thresholds, but also by the time scale of their formation, whereupon direct ionization occurs within 10^{-16} s.^[91] The different cases of dissociative photoionization and the appearance of the respective fragment mass signals of a parent ion, shown in fig. 2.3.1, will be highlighted in sec. 2.3.1.

In addition, not only positive ions, but also negative ions play an important role in the research field of photoionization. When negative ions are investigated in photodetachment photoelectron spectroscopy, details on the structure of the neutral molecule and electron affinities can be obtained.^[90, 91]

2.3.1 Dissociative photoionization

A molecule will dissociatively ionize if the photon energy exceeds the dissociation limit of the generated cation,^[61, 94] Nevertheless, it can be possible that ionization of a molecule leads immediately to the fragmentation of the cation, since the shape of the molecule's cationic ground state potential energy surface is repulsive. This was, for example, observed for the nitrite precursors of the C_4H_7 radicals (4.2). As already implied in figure 2.3.1, DPI can occur from any cationic state, but gets restricted by transition selection rules (symmetry), non-crossing rules of excited states and Franck-Condon factors. If the dissociation proceeds fast on the time scale of the experiment, it can be seen as a direct dissociation along a repulsive state. Direct dissociation occurs on the timescale of a vibrational period around 10^{-13} - 10^{-14} s. This means for the simple case of a diatomic molecule (displayed in fig. 2.3.1, b), when applying photon energies in the range from $E_1(A^+)$ to E_B , direct dissociation from the repulsive cationic state $AB^+(a)$ to the fragments $A^+ + B$ will be observed. With energies equal or higher than E_P the second threshold $E_2(A^+)$ for the production of $A^+ + B$ is reached and so these fragments originate from indirect dissociation of the $AB^+(a)$ potential surface. The two dissociation thresholds to the fragment A^+ are visualized by the stairs in the photo-ion yield curve of A^+ (fig. 2.3.1, c, green). An indirect ion dissociation, that is a predissociation, will proceed in between 10^{-13} - 10^{-3} s, which indeed depends on the process that is responsible for indirect dissociation. Different cases of these slow dissociations and their origin will be discussed in sec. 2.4.5. With photon energies above $E(B^+)$, direct dissociation to the fragments $A + B^+$ via the cationic state $AB^+(C)$ will occur, which gives rise to the photo-ion yield curve of B^+ (fig. 2.3.1, c, purple). In the context of investigating reactive intermediates that are generated from a precursor

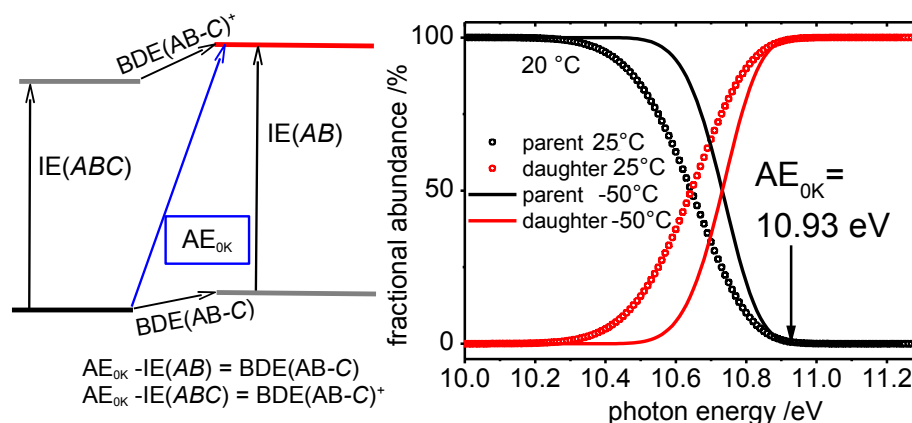


Figure 2.3.2: Thermochemical cycle to derive the BDE from DPI (left) and the corresponding breakdown diagram for the single fast dissociation of ABC to AB^+ at $T=100$ K (solid line) and $T=290$ K (open dots) (right). The appearance energy AE_{0K} is derived to 10.93 eV for both temperatures.

molecule, the dissociative photoionization of the precursor is crucial to know. Since the precursor can undergo DPI to the fragment with the same m/z as the reactive intermediate, the DPI represents a competing and potentially interfering process. If a precursor signal cannot be completely destroyed by pyrolysis, it will not be possible to prevent DPI. Therefore it is necessary to examine the precursor cation's fragmentation in detail. Within this analysis one has to determine the so called appearance energies AE_{0K} of the formed fragments. The AE_{0K} is defined as the energy at which every parent ion has fragmented.

Besides, the analysis of a molecule's DPI allows to retrieve thermochemical information, e. g. $BDEs$ and ΔH_f^0 values. The $\Delta BDE((AB-C)^+)$ of the cation ABC^+ can be obtained if the molecule ABC dissociates in a DPI channel that does not include a reverse barrier, a tunneling process or a rearrangement reaction (see 2.4.5) to the fragments AB^+ and C . In the case that the neutral fragment AB is in addition formed upon pyrolysis and its IE to AB^+ is retrieved, the $\Delta BDE(AB-C)$ in the neutral molecule ABC can also be derived by a thermochemical cycle, as shown in fig. 2.3.2.

The dissociative photoionization is experimentally evaluated by the fractional abundances of the mass-selected threshold photoelectron signals of the parent ABC^+ and the daughter fragment(s) A^+ that are plotted in a breakdown diagram (fig. 2.3.2, right). It can also be determined from the fractional abundances of the total ion yields, but with lower accuracy. In the case of a dissociation reaction $ABC^+ \rightarrow AB^+ + C$ the fractional abundances S_{ABC^+} and S_{AB^+} are evaluated according eq. 2.3.1,^[60,61]

$$S_{ABC^+} = \frac{ABC^+}{ABC^+ + AB^+} \text{ and } S_{AB^+} = \frac{AB^+}{ABC^+ + AB^+} \quad (2.3.1)$$

where ABC^+ and AB^+ are the mass selected threshold photoelectron signals of the species. From the breakdown curve the 0 K appearance energy can be determined. In this work this has been done with the program *mPEPICO*. Hence, the assumptions for the theoretical description, the modeling of breakdown data and retrieving AE_{0K} is described in subsection 2.4.5 in detail.

2.3.2 Photoelectron spectroscopy

Photoelectron spectroscopy is an excellent method to investigate molecular ions. When a molecule is ionized by one photon that has more energy than the minimum energy necessary for valence ionization, some excess energy will be left. Due to conservation of momentum the excess energy ε_{kin} will be partitioned between the ions internal energy E_i and (or) the kinetic energy ε_{kin} of the photoelectron (eq. 2.3.2).

$$\varepsilon_{kin} + E_i = h\nu - IE \quad (2.3.2)$$

The resulting electron is much lighter than the molecule cation so that the cation will approximately not carry away kinetic energy from the ionization process. Thus, the photoelectron will take away most of the kinetic excess energy and yields therefore information on the electronic structure of the ion. The first ionization energy IE , which equals the negative binding energy of the ejected electron, corresponds to the energy that is necessary to remove the electron from the molecule's highest occupied molecular orbital (HOMO). Since the valence molecular orbitals are the ones involved in chemical bond formation, the investigation of their energies is of special importance. Conventional PES is performed non-resonantly by applying a fixed wavelength, often $h\nu=21.22$ eV (from a He discharge lamp) for valence ionization. Figure 2.3.3 shows the non-resonant (Hel α) photoelectron spectrum of CO. It contains the transitions $X^{+2}\Sigma^+ \leftarrow X^1\Sigma^+$ from the neutral molecule's ground state $X^1\Sigma^+$ to the ground state cation $X^{+2}\Sigma^+$, the respective transition $A^{+2}\Pi \leftarrow X^1\Sigma^+$ to the first excited state cation $A^{+2}\Pi^+$ and $B^{+2}\Sigma^+ \leftarrow X^1\Sigma^+$ to the excited state $B^{+2}\Sigma^+$. In addition, the squares of the vibrational wavefunctions are drawn onto the vibrational levels, permitting to estimate the probability density at each vibrational level. For an electronic transition, which can be accompanied by vibrational excitation (see sec. 2.4.1), the intensity I of the transition is given by the Franck-Condon factors (FCF).

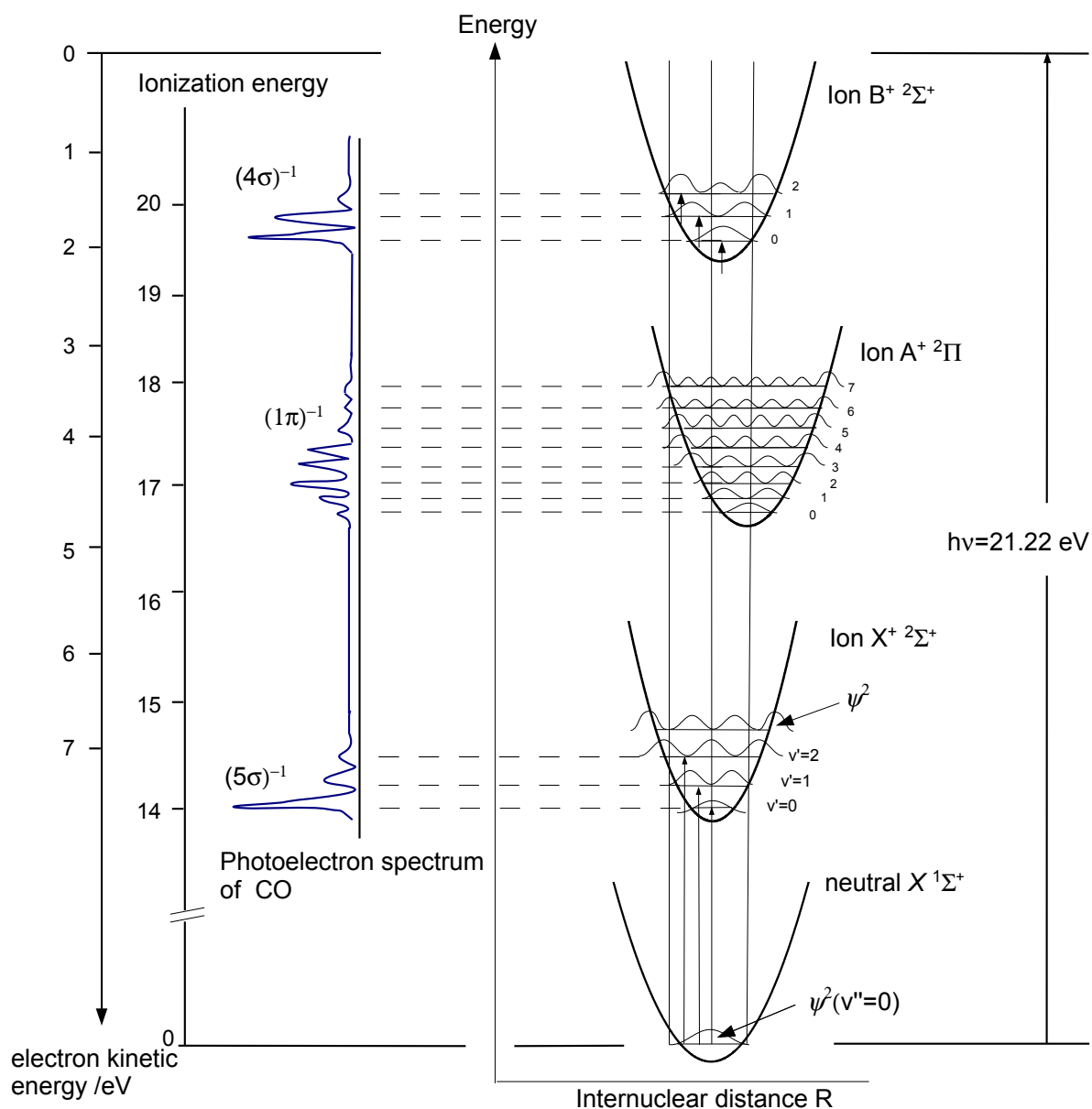


Figure 2.3.3: Photoionization transitions in CO with the corresponding photoelectron spectrum. (This scheme is based on a figure shown in reference.^[91])

Equation 2.3.3 reveals that the most intensive transitions are those with the greatest overlap integral of the respective vibrational wavefunctions Ψ_v . Therefore the FCF can be expressed by (for details on the calculation of FCF see subsect. 2.4.3):

$$I \propto FCF = \left| \langle \Psi_n | \Psi_n^+ \rangle \right|^2, \quad (2.3.3)$$

The most intense transition can be assigned to the vertical ionization energy IE_{vert} whereas the one with the lowest energy corresponds to the adiabatic IE_{ad} . In fig. 2.3.3, the adiabatic and the vertical

ionization energy to the ground state ion $X^{+2}\Sigma^+$ coincide, whereas the energies of the adiabatic and the vertical excitation energies to the cationic state $A^{+2}\Pi^+$ are different.

When a photoelectron spectrum of an organic molecule covers an energy range of ~ 8 eV up to ~ 12 eV above the ionization threshold, several ionization energies corresponding to the respective orbital energies can be obtained. This is also the case in fig. 2.3.3. Since in conventional PES no information on the mass of the ion is gathered, it cannot be evolved if the latter is still intact as the parent cation or if transitions to non-bound electronic states and therefore dissociation to fragment ions occur. This information can be retrieved from a mass selected PES and even more reliably from (T)PEPICO experiments (2.3.2). The ionization process is about 10^3 times faster than the fastest dissociation process. Thus, in a mass-selected PES or TPES, the fragments resulting from dissociating or predissociating states will show no distinct vibrational structure but rather a continuous shape ($AB^+(C)$ state in fig. 2.3.1).

Most PES experiments are set up in the gas phase and the analysis of the photoelectrons' kinetic energy distribution is achieved by an electron energy analyzer. The latter can either have a retarding field which is scanned, so that for each potential applied electrons with a kinetic energy higher than the retarding potential are transmitted.^[90] Another version of electron energy analyzers are deflecting devices that have widely been used in the form of a hemispherical analyzer.^[95] The kinetic energy spectrum is retrieved from the measured electron current as a function of the varied voltage of the hemispheres. The typical resolution of this experiment is 10-30 meV, i.e. rotations cannot be resolved.^[90,96] A second disadvantage of the conventional PES method is that no mass selectivity can be achieved. If a sample is contaminated by some other substances, the photoelectrons of different species will not be distinguishable. In the case of the investigation of reactive intermediates, like radicals that are generated *in situ* from precursor molecules, this experimental disadvantage becomes quite severe. Since from the non mass-selective experiment no information on the conversion efficiency or the selectivity of fragment formation can be gained, the analysis of photoelectrons will need more effort, when for example difference spectra have to be taken.

(T)PEPICO

Ionization of molecular systems cannot be completely described by PES since the energy of the incoming photon can be shared between the internal energy of the ion (rotations and vibrations), the translational energy of the ion and the kinetic energy of the photoelectron. While PES lacks mass selectivity and PIMS does not provide state selectivity (unless in favorable cases), the two methods are combined in the threshold photoelectron photoion coincidence (TPEPICO) technique. The intention to supply a coincidence detection of ions and electrons is to know the internal energy of both species at the same time. Furthermore, the technique permits to analyze their energy-dependent fragmentation (compare to sec. 2.3.1). When a tunable light source is used, at the

threshold of ionization photoelectrons with nearly no kinetic energy ($\varepsilon_{kin} \approx 0$), so-called threshold photoelectrons, are produced. If only the latter are selected, the ion internal energy E_i will be directly deduced at any photon energy according to eq. 2.3.2. The latter equation is then simplified to $E_i = h\nu - IE + E_{th}$, when the thermal energy E_{th} is considered, too.

TPEPICO permits to perform threshold photoelectron spectroscopy (TPES) on mass-selected parent ions. This is a great advantage when working in a molecular beam that contains several masses, for example when radicals are produced from a precursor molecule. Moreover, the selection of threshold photoelectrons (TPE) with a tunable light source provides a higher spectral resolution than for the photoelectrons with kinetic energy (*vide infra*).

A special approach to obtain electrons without kinetic energy is the pulsed field ionization method where zero kinetic energy electrons (PFI-ZEKE) are selected. The basic principle of the PFI-ZEKE method is that the applied photon matches the energy of a rovibronic transition from the neutral molecule (ground state) to a very highly excited Rydberg state ($n \geq 100$). Those Rydberg states have very long lifetimes compared to the timescale of the experiment and are close to the ionization threshold. This lifetime is utilized to ionize the excited neutral molecule by a delayed electric pulse. The approach permits to get very highly resolved transitions, which enables to determine accurate ionization energies and geometry parameters like bond lengths and rotational constants. The resolution of the spectra is practically only limited by the light source's bandwidth. The most common experimental realization of ZEKE is applied in the combination with REMPI.^[97,98] Mass selectivity cannot be achieved by PFI-ZEKE, but in a closely related approach called mass analyzed threshold ionization (MATI) spectroscopy.^[99] In contrast to ZEKE, where photoelectrons generated from pulsed-field ionization of Rydberg molecules are analyzed, with MATI the respective ions are detected. Since both PFI-ZEKE and MATI are typically operated with 10 Hz pulsed lasers, the produced particle densities per light pulse are too high to apply an efficient coincidence scheme (*vide infra*).^[100]

Detection: electron VMI and ion TOF-MS spectrometer iPEPICO

After ionization the charged particles (electrons and ions) spread in 3-dimensional (3D) particle "clouds", so called Newton-spheres. The extraction fields in the flight tubes are applied to force the ions to drift perpendicular to the propagation direction of the molecular beam down to the MCP of the Wiley-McLaren (WM)-TOF and the electrons to move upwards onto the electron detector (fig. 2.3.5). Electrostatic lenses are applied in the direction of the electron detector to focus the photoelectrons' trajectories. Thus, when the 3D sphere is mapped on the 2D detector a given initial momentum of the charged particle corresponds to a given arriving point on the detector.^[101,102] The TPE, which initially do not have any velocity, will be accelerated with a velocity in the direction of the extraction field. Therefore they will arrive in the center of the detector, thus in the center of the

2D-electron image. The kinetic photoelectrons will end in the outer range of the image, with radii proportional to their speed perpendicular to the extraction voltage. The kinetic energy range imaged on the detector depends on the focusing and the flight tube voltages and is preferably kept small to achieve a good kinetic energy resolution^[100] However, both ions and electrons are extracted in the same electric field and both mass and photoelectron resolution are of contradictory needs (*vide infra*). The higher the extraction field and with that the repeller voltage V_{rep} , the higher the kinetic energy of the electrons that will be mapped onto the detector. From eq. 2.3.4 follows, that the radius R in which electrons with a given kinetic energy ε_{kin} will arrive on the detector gets smaller with a higher repeller voltage V_{rep} .^[103]

$$R \propto \sqrt{\frac{\varepsilon_{kin}}{V_{rep}}} \quad (2.3.4)$$

As a consequence, the larger V_{rep} , the lower is the photoelectron kinetic energy resolution. The latter also depends on some further aspects, like the photon energy resolution and the limitations of the detector delay lines itself (*vide infra*). The collection efficiencies of threshold photoelectrons is high (nearly 100%), compared to those that have kinetic energy, since they are focused onto a very small area on the detector.^[60,100,103] The electrons are registered by a delay line detector (DLD) that is built as a lattice of an x- and a y-filament, providing a particle's time of arrival and from that its local position.^[104] This is possible as the differences in the elapsed time for the striking electron(s) is recorded for the two x_1, x_2 and the y_1, y_2 signal times (fig. 2.3.4).

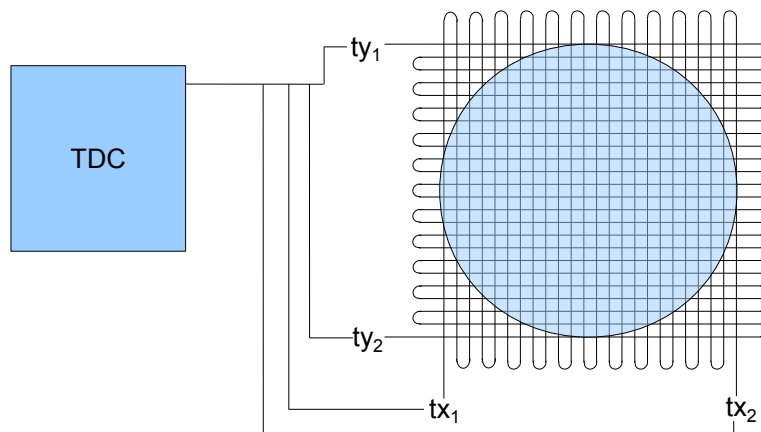


Figure 2.3.4: Delay line detector (DLD) connected to a time-to-digital converter (TDC).

The DLD is mounted at the back of dual multi-channel plates (not shown in fig. 2.3.4), on which the electron hits first. The electron signal will be amplified by the MCP and transmitted to the DLD at the same position where it hits the MCP. Multiple hits can be analyzed with a dead time of 10-15 ns per channel. If the difference of their relative arrival times is shorter, they may be registered if their relative distance in x and y position exceeds a certain value at the DLD.^[105] The arrival times are

then sent to a time to digital converter which encodes the time information to the information of the local appearance of the electron.^[104] Ions were mass-analyzed in conventional Wiley-McLaren time-of-flight mass spectrometry (WM-TOF-MS).^[106] The general principles of WM-TOF-MS are as follows. The electrons provide the start signals for taking the TOF of the ions.

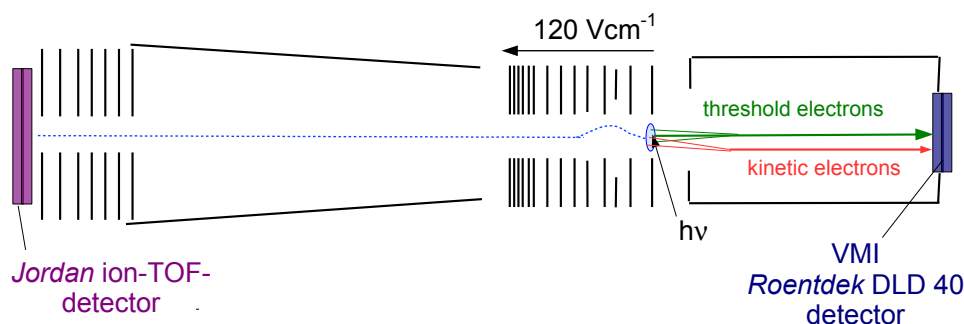


Figure 2.3.5: Setup of the spectrometer in the vacuum chamber at VUV X04DB beamline at the SLS.(according^[100]) On the left side the *Jordan* ion C-726 detector and on the right side the electron VMI detector is positioned, which is a *Roentdek* DLD 40 delayline detector.

The ions formed at time zero enter one or several constant electric fields in which they are accelerated towards the detector, after having passed a field free drift zone. The particle's time of flight is given by eq. 2.3.5:

$$t = \sqrt{\frac{m \cdot s^2}{z \cdot 2eU}} \quad (2.3.5)$$

when the energy of the electric field $E = z \cdot e \cdot U$ equals the kinetic energy $E_{kin} = \frac{1}{2} m \cdot (\frac{s}{t})^2$ of the ion. Here z is the ion's charge, U the voltage of the field and s is the length of the drift tube. In WM-TOF spectrometers several ion optics are employed to focus the ions. The resolution of a TOF spectrometer depends on the spread of flight times for ions of the same m/z , which itself depends on several aspects. It can be improved for example by space focusing and beam cooling. The best mass resolution in ion TOF is achieved by applying a high electric field, which unfortunately is detrimental for the electron analysis (*vide supra*). This relation shows that operating a TPEPICO experiment requires some compromises in the aimed overall resolutions of the experiments. An experimental enhancement of the iPEPICO setup to the i²PEPICO setup is possible: the ions can be mapped onto a PSD via VMI in delayed coincidence, too.^[107]

Data acquisition - coincidence principle

How can an ion and an electron be identified to originate from the same ionization event? In general, such problems are treated by statistical analysis, which always includes uncertainties in the nature of its process. Therefore, analysis of coincidence events will never achieve a 100% certainty. Different approaches have been developed to correlate oppositely charged particles generated in coincidence. As already stated, the electron signal is used to trigger the ions' TOF since the electron is much faster than the ion. Common TOF acquisition approaches are the single start/single stop (SS) technique, the single start/multiple stop (SM) and the multiple start/multiple stop (MM) schemes. With the high count rates in the continuous particle formation experiment it is superior to collect all starts and stops, which is not permitted within the SS and SM approaches, as the two approaches have periods of idle times. The problem can be circumvented by a Masterclock which gives timestamps to all registered incoming signals of the electron x_1, x_2, y_1, y_2 at the DLD and also to every registered signal at the MCPs of the ion detector. The electron signals are registered in order to get the position information with the time stamp of the electron. These information then are correlated with all ion signals.^[100] This statistically treated correlation has the challenge to minimize false coincidences (fc). Fc are correlated signals which do not originate from the same ionization event, whereas true coincidences do. When the MM scheme of data acquisition is applied, every event that is recorded from the MCPs is registered. This means that only the dead time in a single channel of the MCP limits the registration rate. The dead time of the MCPs is some 10 ns,^[100] relating to a maximum detection frequency of 1 MHz in continuous particle extraction. As a consequence, the total amount of ionization events per second should not be significantly higher than 10^5 . For 10^{11} initial photons/s and 10^5 absorbed photons/s results that only one out of 10^6 initial photons leads to an ionization event. With a repetition rate of 10^8 s^{-1} , the number of photons per pulse is 10^3 . From this follows, that the average count rate per pulse should converge to zero to retrieve the correlation of coinciding particles. For this reason the repetition rate is high in order to get sufficient signal intensities.

The data acquisition scheme employed in the software i^2 PEPICO at the VUV X04DB beamline follows the MM principle. Therefore the background of fc is uniform over the whole TOF range of the experiment.^[108] Thus the fc can be included in the data evaluation by taking the total photoelectron signal in a TOF mass range that shows no peak. The fc are considered by subtracting this signal from each signal belonging to a "real" TOF mass peak.

Selection of threshold photoelectrons

The selection of the threshold photoelectrons can be done easily, as nearly all of the produced TPE will be mapped on the center of the electron image (*vide supra*). Considering that the 3D Newton-

sphere is projected as an 2D image onto the detector plane, in the space volume, close to the center of the sphere, electrons with small kinetic energy (e.g. from autoionization) will be found. These so called *hot electrons* that have a velocity vector in the direction or in the opposite direction of the extraction field and will also be accelerated to the center of the electron image. To correct the center signal (fig. 2.3.6) from the hot electron contamination a ring around the circle signal is chosen, which is weighted by an empirical factor and then subtracted from the area of the circle.

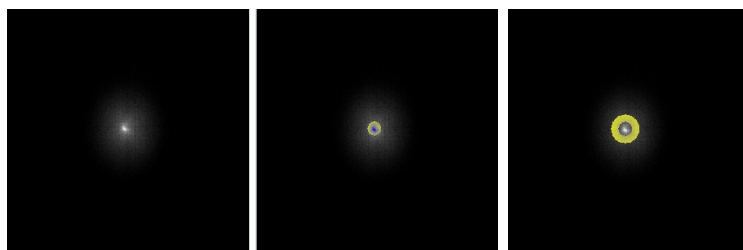


Figure 2.3.6: Electron images without a region of interest (left), circle (middle) and ring (right).

This factor f is chosen in that way that the area of the circle A_c and the ring A_r are equal. This approach has been approved for a variety of molecules.^[60] Nevertheless, in the few case in which $A_c = f \cdot A_r$ does not give a plausible result, f should be chosen so that the resulting threshold electron signal shows positive values at all energies. Circle and ring selection is done with the i²PEPICO software which is used for data collection and data evaluation.

Why Synchrotron radiation for (T)PEPICO experiments?

In addition to the SR, some other laboratory light sources are applicable that provide radiation in the VUV range. These are continuum and line discharge sources and also laser systems. Line and continuum discharge sources are mainly generated from noble gases like He, Ar or from H₂. The most common line source is the HeI α resonance line at 21.22 eV, which corresponds to the transition between He* ($1s2p,^1P$), the first excited state, and ground state Helium ($1s^2,^1S$). In addition, other gases are used, but for example Neon produces lines with lower energy and is therefore not as versatile as He for valence shell ionization. The typical flux of a line discharge lamp is 10^{10} – 10^{11} photons \cdot s⁻¹. H₂ is a typical continuum laboratory source, but also He and Ar emit continuous spectra. Due to the low brilliance of the quasi-continuous source the flux is low with 10^8 – 10^9 photons \cdot s⁻¹ and the resolution of $E/\Delta E=10^3$ is moderate.^[86] Tunable VUV radiation is produced as laser radiation by two photon resonantly enhanced four-wave mixing using rare gases as non-linear medium.^[109] Although pulsed low repetition rate UV or VUV lasers provide a very high resolution ($E/\Delta E=10^7$) and photon flux (10^{15} photons \cdot s⁻¹), the pulse peak powers are too high to generate sufficiently low amounts of electron-ion pairs per pulse. Thus, they lack the repetition rate required

for coincidence experiments.^[54] In addition, the tunability of laser systems in the VUV is limited, prohibiting to investigate an ion over a large energy range.

A main advantage of using SR is that users may be obliged to arrive at a VUV-beamline with not more than their sample. The wide, easily tunable photon energy range is an advantage over lasers and provides the ability to study molecular ions comprehensively. An advantage compared to discharge lamps provides the flux and the resolution. Appropriate to special needs of the user's experiment, the flux can be increased at the cost of the photon resolution.^[110]

The main demands in a coincidence experiment are high pulse repetition rates and low count rates that provide a good resolution. These properties are perfectly combined by VUV synchrotron radiation.

2.4 Theoretical concepts

2.4.1 Electronic and vibrational structure of molecules

The experimental investigation of ionization processes needs to be supported and evaluated with the help of quantum chemical computations. The required theoretical concepts will be highlighted in the following section. The description of a molecule's structure is based on the solution of the time-independent non-relativistic Schrödinger equation (SE) of a molecule with i electrons with the coordinates r_i and A nuclei R_A (eq.):

$$\hat{H}(r_i, R_A) |\Psi_{mol}(r_i, R_A)\rangle = E |\Psi_{mol}(r_i, R_A)\rangle \text{ with } \hat{H}(r_i, R_A) = \hat{T}_{el} + \hat{T}_n + \hat{V}_{el-el} + \hat{V}_{n-n} + \hat{V}_{el-n} \quad (2.4.1)$$

The SE comprises the molecular wavefunction $\Psi_{mol}(r_i, R_A)$, the energy eigenvalue E and the Hamiltonian $\hat{H}(r_i, R_A)$. The latter includes the kinetic energy of the electrons and the nuclei \hat{T}_{el} and \hat{T}_n and the potential energies of the electron-electron interaction \hat{V}_{el-el} , the nuclei-nuclei interaction \hat{V}_{n-n} and the electron-nuclei interaction \hat{V}_{el-n} .^[90] The electron movement and the movement of the nuclei can be viewed independently so that the electron transition is rapid with respect to the time of a molecular vibration. Because of this fact the molecular wavefunction $\Psi_{mol}(r_i, R_A)$ can be separated, which is known as the Born-Oppenheimer approximation:

$$|\Psi_{mol}(r_i, R_A)\rangle = |\Psi_{el}(r_i, R_A)\rangle |\Psi_n(R_A)\rangle. \quad (2.4.2)$$

The Schrödinger equation for the electron is represented in eq. 2.4.3, where the coordinates of the nuclei R_A are fixed and therefore only used as a parameter. The retrieved energy eigenvalue $E_{el}(R_A)$ represents the potential energy of the electrons for a fixed nuclei arrangement, also including nuclei-nuclei repulsion and can therefore be used as the operator for the potential energy \hat{V}_{el-n} to compute the nuclear Schrödinger equation (eq. 2.4.4) that describes the molecular vibrations and rotations. The energy eigenvalues E determine the shape of the potential energy surfaces.

$$(\hat{T}_{el} + \hat{V}_{el-el} + \hat{V}_{el-n}) |\Psi_{el}(r_i, R_A)\rangle = E(R_A) |\Psi_{el}(r_i, R_A)\rangle \quad (2.4.3)$$

$$[\hat{T}_n + E(R_A)] |\Psi_n(R_A)\rangle = E |\Psi_n(R_A)\rangle \quad (2.4.4)$$

In order to analyze electronic transitions, potential energy surfaces are simplified. When only one coordinate is selected the potential energy surface is reduced to that reaction coordinate that is of interest for the observed transition. This potential energy curve mainly illustrates a cut through the complete potential energy surface along the axis which represents the active coordinate and is most often expressed by a Morse potential (eq. 2.4.5, left) or the potential of the harmonic oscillator that

are both analytic solutions of the Schrödinger equation:

$$E(R_A) = D_e[1 - e^{-\alpha(R-R_0)}] \text{ and } V(R_A) = \frac{1}{2}k(R - R_A)^2 \quad (2.4.5)$$

Here D_e is the sum of the zero point vibrational energy (ZPE) and the dissociation energy. A vibronic transition induced by the interaction of a molecular system with a photon has the transition probability $|M_{if}|^2$ that is described by the transition dipole matrix element M_{if} :

$$M_{if} = \langle \Psi_n \Psi_{el} | \mu_n + \mu_{el} | \Psi_n^+ \Psi_{el}^+ \rangle, \quad (2.4.6)$$

where Ψ_n , Ψ_{el} and Ψ_n^+ , Ψ_{el}^+ are the vibrational and electronic wavefunctions of the initial and the final states and μ is the electric dipole moment operator. The latter depends on all charged particles Q_n of the system and their positions vectors x_n and it is split in the electronic part μ_{el} and the nuclei part μ_n . Simplification of eq. 2.4.6 leads to eq. :

$$M_{if} = \langle \Psi_n \Psi_{el} | \mu_{el} | \Psi_n^+ \Psi_{el}^+ \rangle + \underbrace{\langle \Psi_n \Psi_{el} | \mu_n | \Psi_n^+ \Psi_{el}^+ \rangle}_{=0} = \langle \Psi_{el} | \mu_{el} | \Psi_{el}^+ \rangle \langle \Psi_n | \Psi_n^+ \rangle. \quad (2.4.7)$$

The transition dipole matrix element consists of the electronic transition term, $|\langle \Psi_e | \mu_{el} | \Psi_e^+ \rangle|$, that can be determined by symmetry selection rules and the overlap integral $\langle \Psi_n | \Psi_n^+ \rangle$ which expresses the FCF in $|\langle \Psi_n | \Psi_n^+ \rangle|^2$.

Molecular vibrations are often well described within the harmonic approximation. Therefore the energy levels of molecular vibrations and the vibrational frequencies can be retrieved according eq. 2.4.4, including the harmonic oscillator potential (eq. 2.4.5).

2.4.2 DFT and *ab initio* computations with Gaussian 09

Quantum chemical computations have been applied in this work to maintain the interpretation of experimental results. All computations were performed with the Gaussian09^[111] suite of programs at the *Leibniz Rechenzentrum München*. The general issue has been to compute ionization energies IE and appearance energies AE_{0K} (eq. 2.4.8).

$$\begin{aligned} \text{a) } E_0(\text{ion}) - E_0(\text{neutral}) &= IE \\ \text{b) } E_0(TS^+) - E_0(P) &= AE_{0K} \end{aligned} \quad (2.4.8)$$

The total energy E_0 of a molecule is given by the sum of the electronic energy $E_{\text{electronic}}$ and the zero point vibrational energy E_{ZPE} . To obtain the total energy of the neutral and the cationic

molecule, geometry optimization to the minimum energy structure of the respective ground states were performed. In addition vibrational frequencies were computed to perform FC simulations (*vide infra*). The appearance energy AE_{0K} is computed by the difference of the total energy of the transition state $E_0(TS^+)$ and the neutral parent molecule $E_0(P)$. A TS is the highest point on the potential energy surface from the starting molecule to the products. If the dissociation does not proceed via a transition state, i. e. no reverse barrier is included on the pathway to the products, then instead of the $E_0(TS^+)$ the sum of all products of the DPI $E_0(D^+) + E_0(F)$ is used in eq. 2.4.8.

For the most part the computations were conducted using density functional theory (DFT). The DFT method^[112] combines low costs in computational time compared to other *ab initio* methods like MP2, while yielding similar accuracies. The fundamental idea of the DFT method is to improve the Hartree-Fock(HF)-method to provide a more accurate solution for a many-electron system.^[113] The HF-energy is given according to eq. 2.4.9 and incorporates the kinetic energy E_T , the potential energy of the electrons E_V , the Coulomb interactions E_J and the HF-exchange energy E_K .

$$E^{HF} = E_T + E_V + E_J + E_K \quad (2.4.9)$$

The three first parts of eq. 2.4.9 are the same in the DFT-energy, but E_K is substituted by the correlation and exchange term E_{XC} :

$$E^{DFT} = E_T[\rho] + E_V[\rho] + E_J[\rho] + E_{XC}[\rho]. \quad (2.4.10)$$

With the exception of E_T , every part of eq. 2.4.10 depends on the electron density $\rho(r)$. The density $\rho(r)$ gives the probability to find an electron in a region dr around r . It is the central assumption in the DFT approximation.

$$\rho(r) = \sum_i^M |\phi_i(r)|^2 \quad (2.4.11)$$

The orbitals ϕ_i , used to express the electron density are the Kohn-Sham (KS) orbitals. The latter and with them the electron density $\rho(r)$ are iteratively determined in a procedure similar to the SCF-approach applied within the HF-method. Beside the term E_{XC} , the energy E^{DFT} can be exactly determined. Thus, there is a need to introduce approximations for the unknown exchange correlation functional and the respective potential. Therefore, the more accurate the chosen functional is, the higher the quality of the DFT calculation will be. In practice today quantum chemists apply functionals that combine contributions of exchange and correlation derived from different approaches.

In this work, the most common functional used was the B3LYP functional. It combines the pure *Generalized Gradient Approximation* (GGA) functional B88 developed by Becke^[114] and the correlation functional LYP,^[115] also named by its inventors Lee, Yang and Parr. In addition, by mixing the

HF-exchange energy to some extent to the GGA-exchange, the three-parameter hybrid functional B3LYP^[116–118] is generated. In addition to the functional for the electron density, also the basis set, which describes the spin orbitals, has to be selected. In general two different types of orbitals exist: Gaussian-type orbitals (GTO) and Slater-type orbitals (STO). The latter incorporate exponential functions combined with spherical harmonics in order to approximate the exact eigenfunctions of the hydrogen atom, whereas the GTOs only consist of Gaussian functions. The latter are combined by a linear combination to a single contracted Gaussian function (CGF). The basis set chosen throughout this work is the 6-311G(d,p) basis-set.^[119] The understanding of this basis set is given from left to right:

- 6** One contracted Gaussian function that consists of 6 GTOs is used to represent every non-valence shell orbital .
- 311** The three numbers behind the hyphen imply a split-valence triple basis set. Each valence shell orbital consists of three CGFs, which is represented by the three numbers. The numbers 311 themselves indicate that the first CGF of an orbital consists of three GTOs, the second CGF of one GTO and the third CGF is also built from one primitive Gaussian function
- G** The G is the sign for the use of GTOs.
- (d,p)** The two letters give the kind of orbitals, which are additionally included as polarization functions to every atom. d-Orbitals are used for all atoms, except the H-atom and p-orbitals are used for the H-atom.

Supplementary to DFT computations, geometry optimizations of some molecules were also conducted with the Møller-Plesset perturbation theory (MP2).^[120] The latter is an *ab initio* method. In order to get more accurate results for ionization and appearance energies, the computations have also been performed with the CBS-QB3^[121] methods, whereupon the latter method implies very accurate results but owes higher costs of computation time. In addition time dependent DFT (TDDFT)^[122] computations were performed to locate excited cationic states.

A comparison of the ionization energies of 12 hydrocarbon radicals computed with the B3LYP functional and the 6-311++G(d,p) basis set showed a mean absolute deviation of 0.14 eV. Thereby the IEs are merely underestimated.^[43] The CBS-QB3 method in contrast supplies ionization energies which have a mean absolute deviation of 0.87 kcal/mol (0.038 eV) found for a test set of more than 125 experimental energies (dissociation, energies, ionization energies, electron affinities and proton affinities).^[123]

2.4.3 The program FCFit

The basic function of the program FCFit_2.8.2 is to calculate Franck-Condon factors of a vibronic transition.^[124] Therefore an experimental absorption or emission spectrum can either be simulated or fitted. In the context of this work, only simulations of FCF were performed. The FCF of a vibronic transition depends on the squared overlap integral of the respective vibrational wavefunctions and is generally expressed according to eq. 2.4.13:

$$FCF = N_{n''}^2 N_{n'}^2 \left\langle H_{n'}(Q') e^{-0.5(Q')^2} \middle| H_{n''}(Q'') e^{-0.5(Q'')^2} \right\rangle^2. \quad (2.4.12)$$

N_ν displays the normalization constant of the Hermite function and H_n a Hermite polynomial. Q' are the normal coordinates of the excited and Q'' of the ground state. The relation of the different coordinates is given by a displacement k with $Q' = Q'' + k$. In the N -dimensional case the respective N -dimensional wavefunction $\Psi(Q)$ is given as the product of the Hermite functions ν'_N . The FCF are computed according to eq. 2.4.13:

$$FCF = \langle \Psi'(Q') | \Psi''(Q'') \rangle^2 = \langle \nu' \dots \nu'_N | \nu'' \dots \nu''_N \rangle^2, \quad (2.4.13)$$

When the normal modes of the initial and the target electronic state are significantly different, they are non-parallel and so are the nuclear coordinates of the respective wavefunctions, too. As a consequence the normal coordinates Q' and Q'' of the neutral and the ion are related by a linear orthogonal transformation (eq. 2.4.14):

$$Q'' = S Q' + \vec{d}. \quad (2.4.14)$$

Eq. 2.4.14 shows a Duschinsky rotation,^[125] where S is the Duschinsky matrix, rotating the coordinate system of one state into that of the other state and \vec{d} is the displacement vector. S can be expressed by the matrices L , which themselves contain the eigenvectors from diagonalization of the force constant matrix and \vec{d} is expressed by the diagonal matrix M , containing the square roots of the atomic masses on the diagonal (eq. 2.4.15). \vec{R}_{eq} are the equilibrium geometry parameters of the respective states.

$$S = (L'')^T L' \text{ and } \vec{d} = (L'')^T M^{1/2} (\vec{R}_{eq}'' - \vec{R}_{eq}') \quad (2.4.15)$$

The necessary input parameters are the optimized geometry and the force constant matrix (mass weighted hessian) which can be retrieved from the output of a quantum chemical computation. From the context stated above, *FCFit* computes the FCF following a recursion formula.^[126,127] The program yields the intensity as a function of a transition's wavenumber, with respect to the 0-0

transition. The intensity of the 0-0 transition is arbitrarily set to 1. The active modes of the computed transition are represented in the output file. The latter contains a $(3N - 6)$ -digit number (eq. 2.4.16), as each computable molecule has $3N - 6$ vibrational normal modes. Linear molecules cannot be simulated with the program. The number for the n -th position in the numbers of the ket shows, how many quanta of the n -th mode are activated in the respective transition.

$$\langle 0000000000 | 0001002030 \rangle \quad (2.4.16)$$

The bra in eq. 2.4.16 of the string shows no excited vibrations, because this applied version of the program presumes a molecular beam experiment without vibrational excitation in the ground state. The ket shows a combination vibration in that the fourth mode is excited with one quantum, the seventh mode is excited by two quanta and the ninth mode is excited with its second overtone. The quanta-size and the total energy size to be activated in the simulation can be stated in the input-file of *FCFit*.

The retrieved Franck-Condon simulation displays a stick spectrum. To match the experimental and the simulated TPES, the 0-0 transition of the computed spectrum is shifted to the adiabatic ionization energy of the experiment. The stick-spectrum is further convoluted by a Gaussian function whose full width at half maximum is determined by the experimental peaks and bands.

As already stated, beside simulating transitions also a fit of a computed molecular structure to the experimental spectrum can be done. However, to do a reasonable fit, one of the computed geometries, either the ground state or the excited state geometry has to be known exactly. If this is the case, the second structure can be fitted, while the other one is retained. If none of the two geometries is exactly known, the fit has to be performed by choosing one of the two geometries to change. As this yields several possibilities to obtain a good fit, fitting a spectrum becomes ambiguous.

2.4.4 The RRKM statistical theory of unimolecular rates

In the approach of *Rice, Ramsberger, Kassel and Marcus* (RRKM) a unimolecular reaction,^[128,129] for example a fragmentation process is treated from the view of statistical mechanics. The general assumptions of the theory are as follows. A molecule dissociates on a bound potential energy surface and the dissociating molecular system is seen as a collection of s identical oscillators. The internal redistribution of vibrational energy is fast in comparison to the fastest dissociation process. The energy is distributed statistically among all the s oscillators of the molecule and excitation of one oscillator is equally probable to any other excitation. The energy deposited in only one certain, so called critical, oscillator will lead to dissociation. The reaction will proceed if this critical oscillator has an energy higher than the dissociation barrier E_0 , which corresponds to the energy of the

reaction's transition state. When the TS is passed, the reaction products will inevitably be formed. The reaction's rate constant is determined by the probability how fast energy flows into the critical mode. The rate constant for a dissociating ion can therefore be considered to be only dependent on its total energy E , while the energy dependent rate constant $k(E)$ has a minimum value $k(E_0) \neq 0$:

$$k(E) = \frac{\sigma N^\ddagger(E - E_0)}{h\rho(E)}. \quad (2.4.17)$$

The density of states $\rho(E)$ at an energy E represents the number of possibilities how the vibrational energy can be distributed in the ion. The respective possibilities for energy distribution, which may lead to the reaction is given by the number of states $N^\ddagger(E - E_0)$ of the transition state. $N^\ddagger(E - E_0)$ can be calculated in first approximation from the harmonic frequencies of the dissociating transition state in the energy interval from 0 to $E - E_0$ by a direct count algorithm developed by Stein and Rabinovitch.^[130] The harmonic frequencies and rotational constants are taken from DFT or *ab initio* computations. As the density and the sum of states of the reactant and the transition state are calculated without taking the respective symmetries into consideration, equation 2.4.17 is then multiplied by the reaction symmetry σ , which reveals the degeneracy of the reaction.^[54, 131]

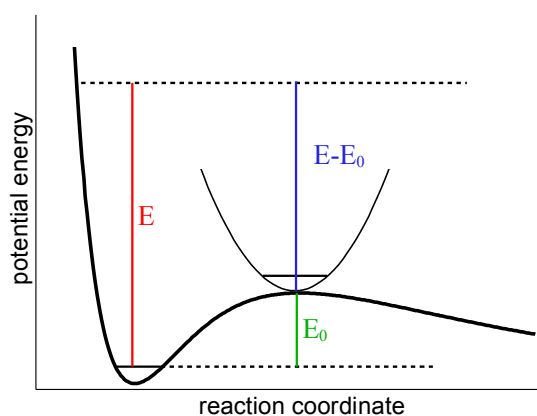


Figure 2.4.1: Potential curves along the reaction coordinate of the TS with the excess energy ($E - E_0$) which dictates the dissociation rate constant $k(E)$. (This figure is similar to a figure presented in reference.^[131])

The most important parameter of a dissociation process, the dissociation barrier E_0 is determined from a fit of the experimental data, which will be described in the following section 2.4.5.

2.4.5 The program MinimalPEPICO

The program *minimal(m)*PEPICO has been developed by Bálint Sztáray, András Bódi and Tomas Baer for the modelation of breakdown diagrams of unimolecular dissociation reactions to retrieve e. g. BDE and thermochemical information.^[132] In general, different approaches of the statistical treatment of unimolecular reaction rates can be applied with the program. In this work no consecutive processes have been modeled, so the cases of **fast, slow or/and parallel dissociations** and their fitting procedures are described in this section. The application of fitting a slow parallel DPI is given in sec. 6.1. The input-files of the dissociation processes described in 4.3 and 6.1 and the explanation of all keyword used is given in the appendix. The following description is given according to the literature.^[61, 132]

Generation of the thermal energy distribution of the molecular ion

The dissociation of a molecular ion is an internal energy dependent process and has to be analyzed in terms of the ion's internal energy distribution $P(E)$. To calculate $P(E)$, the density and number of states $\rho(E)$, according to the Boltzmann distribution of the neutral parent molecule has to be calculated with *m*PEPICO from the rotational and vibrational density of states functions. The latter are calculated from the computed values (*ab initio*) or experimentally determined values of the vibrational frequencies and the rotational constants. These values are needed as input data. With the density of states the internal energy distribution $P(E)$ of the neutral parent at the temperature of the experiment is computed according to eq. 2.4.18.

$$P(E) = \frac{\rho(E)e^{-E/k_B T}}{\int_0^\infty \rho(E)e^{-E/k_B T}} \quad (2.4.18)$$

It is generally assumed, that the neutral's internal energy distribution can be transposed to the ionic manifold (fig. 2.4.2). This originates from the transition probability, which is independent of the molecule's initial internal energy.^[133] With this precondition the ion's internal energy can easily be retrieved according to eq. 2.4.19.

$$E_{int}^{M^+} = E_{int}^M + h\nu - IE_{ad} \quad (2.4.19)$$

The parent ion's internal energy distribution $P(E)$ is computed according to eq. 2.4.19 by a convolution of the neutral parent's $P(E)$ with the photon energy resolution and the electron energy resolution. The latter two are included with the keywords RESO and FWHM. Reasonable values to be chosen for the two options are given in the appendix.

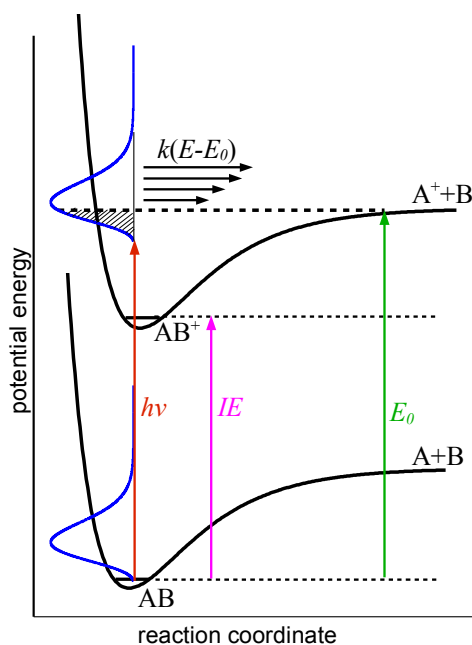


Figure 2.4.2: Direct dissociative photoionization (DPI) and its correlation to the internal energy distribution $P(E)$ of the parent. The photon energy $h\nu$ exceeds the ionization energy IE , but is lower than the dissociation limit E_0 . $k(E - E_0)$ gives the energy depending rates.

Calculation of the dissociation rates $k(E)$ in dependence of the ion internal energy

To obtain the fractional abundances in a **slow dissociation**, the internal energy dependent rates $k(E)$ (sec. 2.4.4, eq. 2.4.17) have to be modeled. The number of states of the TS $N^\ddagger(E - E_0)$ is calculated from the computed frequencies and the rotational constants of the transition states that lead to the dissociation. The frequencies and rotational constants of the TS are needed as input parameters. There are different unimolecular rate theories that can be applied. In the present work these were the rigid activated complex (RAC)-RRKM theory (see sec. 2.4.4) and the simplified statistic adiabatic channel (SSACM) model.^[54] The different rate theories use the usual transition state theory expression to obtain dissociation rates according eq. 2.4.17. The main difference between the two approaches is found how transitional modes are handled and therefore in calculating the sum of states $N^\ddagger(E - E_0)$.^[132,134] The assumption incorporated in the **SSACM** model is based on the phase space theory (PST).^[135] Actually, the transitional modes are treated as free rotations in the PST model. Product vibrational frequencies and moments of inertia are used to calculate $N^\ddagger(E - E_0)$. An adjustable function which is called the *rigidity factor* is added to the functional forms of the rotational density of states which prevents the rates from rising high too fast with increasing ion internal energy.

In the rigid activated complex **(RAC)-RRKM** approach the transitional modes are converted from vibrations to rotations or translations upon the dissociating TS. Thus, they are separated from the remaining vibrational modes. The latter are assumed fixed to compute the internal energy dependent rates $k(E)$ and the transitional modes are optimized by a variable factor in order to fit the TOF distributions (*vide infra*). Since many dissociations to molecular fragments and neutral single atom fragments often do not have a tight transition state, a loose TS can be computed by *ab initio* methods or DFT computations. The latter is obtained by stretching the breaking bond to 4-5 Å. The transitional frequencies of the loose TS are then used as start parameters for the fit of $k(E)$.

In the case of a single **fast dissociation** the rate constant $k(E)$ is larger than 10^7 s^{-1} . Every parent ion that has more internal energy than the dissociation limit dissociates. Therefore, no absolute rate information can be gained on the timescale of the experiment. Thus, for the calculation of the rate constants $k(E)$ the frequencies and rotational constants of the TS are not essential but nevertheless they are required from the program. If an additional dissociation channel comes up parallel to the first one, the ratio of the rate constants of the competing fragmentation channels is calculated (*vide infra*).

Calculation of the breakdown curves

With the computed rates the breakdown curves can be modeled. The breakdown curves, i.e. the fractional abundances of the threshold photoelectron signals as a function of energy are computed from the functions of the internal energy distribution $P(E)$ of the parent ion and the calculated dissociation rates $k(E)$. In a **fast dissociation**, all ions that have more energy than the dissociation limit will dissociate. With that assumption the fractional abundance of the parent signal BD_P in dependence of the photon energy $h\nu$ is calculated according to eq 2.4.20.^[61]

$$BD_P(h\nu) = \int_0^{E_0-h\nu} P(E, h\nu) dE \quad (2.4.20)$$

$P(E, h\nu)$ corresponds to the normalized internal energy distribution of the parent ion as a function of the internal energy for a specific photon energy. The respective fractional abundance of a fragment ion BD_D is given by the area of the energy distribution that exceeds the dissociation limit. The relation between the internal energy distribution and the shape of the breakdown curve is given in figure 2.4.2. From figure 2.4.2 and from eq. 2.3.2 can be deduced that the internal energy of the ion E_i is not only dictated by the difference of the photon energy and the ionization energy, but also from the internal thermal energy E_{th} of the parent ion, which is determined by the thermal energy distribution $P(E, h\nu)$. The thermal shift leads to the observation of fragments at lower energies than the zero Kelvin dissociation limit E_0 , as only a part of the parent molecules is still intact and will be detected with the mass of the parent. This percentage of the thermal energy distribution

can be calculated by integrating $P(E, h\nu)$ from 0 to $E_0 - h\nu$ and is marked in fig. 2.4.2 by the dashed lines. The percentage of the molecules that already will have exceeded E_0 is respectively calculated by integrating $P(E, h\nu)$ from $E_0 - h\nu$ to ∞ . With increasing photon energy the internal energy distribution is shifted to higher energies, which therefore leads to an increasing fragment ion signal BD_D . When $h\nu$ equals E_0 every parent cation dissociates and the fractional abundance of the latter goes down to zero. This means, that the dissociation gradient is a temperature dependent process since the sample temperature determines the width of the internal energy distribution and the width of the breakdown curve. Nevertheless, in a fast dissociation the appearance energy E_0 is found at the energy, where the parent ion signal has completely vanished and is therefore not influenced by the temperature.^[61] To find out whether the dissociation is fast or not can be done by analyzing the shape of the TOF peaks (*vide infra*). If they show a symmetric and narrow profile over the whole energy range in that the fragment is formed, it is a fast dissociation. If the peaks are broad and asymmetric in the low energy range and they narrow with increasing photon energy, the dissociation seems to be **slow** at low internal energies and gets faster with increasing energies. Slow dissociation means also that the time for dissociation is longer than the parent ion's TOF. This pronounced dependence of the dissociation rate $k(E)$ on the internal energy of the dissociating ion is called the *kinetic shift*.^[136–138] Close to the threshold the ion is metastable and does not dissociate completely during the time it spends in the acceleration region of the TOF mass spectrometer.^[139] The time scale for metastable dissociations is in the region $10^3 \text{ s}^{-1} < k(E) < 10^6 \text{ s}^{-1}$, meaning that a longer flight tube or a reflectron TOF-MS might allow the “slow” ions to dissociate. They do not fragment in the time τ_{max} , that is the maximum flight-time in that an ion has to dissociate to be recorded as a fragment ion. They are included in the breakdown by eq. 2.4.21:

$$BD_P(h\nu) = \int_0^{E_0-h\nu} P(E, h\nu) dE + \int_{E_0-h\nu}^{+\infty} P(E, h\nu) \cdot \exp(-k(E) \cdot \tau_{max}) dE \quad (2.4.21)$$

$$BD_D(h\nu) = \int_{E_0-h\nu}^{+\infty} P(E, h\nu) \cdot (1 - \exp(-k(E) \cdot \tau_{max})) dE. \quad (2.4.22)$$

The respective fractional abundance of the fragment ion $BD_D(h\nu)$ is given in eq. 2.4.22. If the dissociation includes a **slow parallel** channel, the fractional abundance of the second daughter fragment $BD_D(h\nu)$ is computed in dependence of the branching ratios of the parallel dissociating ions at a certain internal energy (eq. 2.4.23).

$$BD_D(h\nu) = \int_{E_0-h\nu}^{+\infty} P(E, h\nu) \cdot \underbrace{\frac{k_i(E)}{\sum_j k_j(E)}}_{\text{branching ratio}} \cdot (1 - \exp(-\sum_j k_j(E) \cdot \tau_{max})) dE \quad (2.4.23)$$

When a **fast parallel** dissociation channel opens up, it is more complicated to fit the appearance

energy for the second onset. The first onset is retrieved as described. The second onset can only be retrieved by the relative rates. Therefore the gradient of the breakdown curves is determined by the ratio of the rate constants, since the rate constants themselves are too fast to be measured, they are computed according to eq. 2.4.24:

$$\frac{BD_{D1}(h\nu)}{BD_{D2}(h\nu)} = \frac{N^\ddagger(E - E_{01})}{N^\ddagger(E - E_{02})}. \quad (2.4.24)$$

Here again the TS parameters are included. $N^\ddagger(E - E_{01})$ is the sum of internal energy states in the transition state for reaction 1 from 0 to $E - E_{01}$ and $N^\ddagger(E - E_{02})$ is the respective quantity for the second reaction. As already stated, no absolute rates can be determined in a fast dissociation due to the lack of experimental rate information. In order to fit the breakdown curves according to the branching ratios the TS-frequencies of one of the two fast channels need to be fixed, which means they are included with the computed values and the other TS_2 -frequencies are varied.

Computation of the TOF distributions

It was already mentioned that metastable ions dissociate slowly at low internal energies and the energy dependent dissociation rates $k(E)$ get faster with rising internal energy of the molecule (eq. 2.4.17). A fragment that is formed slowly will be formed at the end of the acceleration region in the ion TOF tube. Therefore it spent the most time in the acceleration region as the parent ion. Thus the formed fragment is only accelerated for a short distance and gets detected at long flight times. At higher internal energies the parent dissociates fast and the fragment ion is formed at the beginning of the extraction region. It gets therefore accelerated for a long time and is detected with a comparably short time-of-flight. As a result, a "TOF-distribution" TOF as function of the dissociation time τ of a parent molecule to the fragment ion is observed with a certain peak width. If a dissociation is fast or slow is related to the time scale of the experiment, thus the length of the ion flight tube. When a dissociation is slow in the time scale of the iPEPICO experiment, rates smaller than 10^3 s^{-1} do not lead to the detection of the fragment ion.

How are time-of-flight distributions modeled?

With the rates $k(E)$, calculated according to eq. 2.4.17, the time-of flight (TOF) distributions are computed. They carry the direct information of the unimolecular rate of the dissociation. For modeling the rates $k(E)$, the TOF channels i have to be correlated with the dissociation times τ . For a given dissociation time τ the $TOF(\tau)$ and also by numerical inversion the $\tau(TOF)$ functions are calculated. The fragment ion peak shape $Fr_i(h\nu)$ is computed according the following equation 2.4.25:

$$Fr_i(h\nu) = \int_{E_0-h\nu}^{+\infty} P(E, h\nu) \cdot (\exp(-k(E) \cdot \tau(TOF_i)) - (\exp(-k(E) \cdot \tau(TOF_{i+1}))))dE. \quad (2.4.25)$$

$Fr_i(h\nu)$ is the normalized height of the fragment ion peak for the channel i and $P(E_i, h\nu)$ is the normalized thermal energy distribution of the parent ion. $\tau(TOF_i)$ is the dissociation time corresponding to the time of flight of channel i . For a parallel dissociation the branching ratios and the sum of the dissociation rates are used to calculate $Fr_i(h\nu)$ that are summed up to calculate the TOF spectrum. The latter is then convoluted with a Gaussian distribution to consider broadening effects. By fitting the computed TOF distributions to the experimental TOF distributions at different photon energies a distinct $k(E)$ function is retrieved. The latter is then extrapolated to yield the dissociation limit E_0 . The experimentally determined $k(E)$ functions are then used to compute the breakdown curves.

When the S/N of the TOF distributions is not sufficient for a good fit, the rate information can also be evaluated from the center of gravity (CoG) of each TOF peak, which reveals the average channel number of a peak. The CoG is calculated at different photon energies based on the computed TOF distributions as a function of the dissociation time $TOF(\tau)$ according to the following equation:

$$CoG = \frac{\int_{\tau_{min}}^{\tau_{max}} \tau TOF(\tau) d\tau}{\int_{\tau_{min}}^{\tau_{max}} TOF(\tau) d\tau} \quad (2.4.26)$$

In comparison to fitting TOF-distributions, where the computed TOF-distributions are compared to the experimental ones, the integrals of the computed and experimental TOF distributions, which give the CoG, are compared. The CoG curve is then used to measure the asymmetry in peak and the dissociation rates, as it is applied in sect. 4.3.

Summary fitting procedure

The fitting procedure for single fast dissociations requires only to adjust E_0 iteratively by the help of the fractional abundance of the fragment BD_D (eq. 2.4.20). One way to improve the slope of the breakdown curves can be achieved by varying the temperature, which influences the internal energy distribution (eq. 2.4.18) of the parent molecule. Another way is to vary the weight of the errors of breakdown calculation and TOF calculation.

In a fast parallel pathway the second 0 K appearance energy E_{02} is determined by iteratively optimizing the latter and the TS frequencies of one of the two parallel channels.

In a slow dissociation, the computed $k(E)$ functions (eq. 2.4.17) are fitted to the TOF distributions (eq. 2.4.25), which yield the experimental $k(E)$ function. The latter is extrapolated according to the

RRKM approach (eq. 2.4.17) in order to get the dissociation onset E_0 . The experimentally gained $k(E)$ function and the extrapolated $k(E)$ function is then used to calculate the breakdown curves. This is done according to eq. 2.4.21 and 2.4.22. For a slow parallel fragmentation the breakdown curves are computed according to eq. 2.4.23. This is iteratively done and only the transition state frequencies of the dissociating ion (five for a loss of a neutral fragment with 3D rotations, four in loss of a linear fragment and two when an atom is lost) and the 0 K appearance energies E_0 are varied in order to reproduce the $k(E)$ function (eq 2.4.17). This procedure stops if the best match of the TOF distributions and the breakdown curves are achieved. Thereby the transitional frequencies of each TS are fitted by being scaled with a uniform factor.

3 Experiment

3.1 The VUV beamline at the SLS

3.1.1 Apparatus

The vacuum apparatus at the VUV beamline is shown in fig. 3.1.1. It consists of two differentially pumped vacuum chambers. The source chamber (SC) is operated at a pressure of $p(\text{SC}) = 4 \cdot 10^{-4}$ to $2 \cdot 10^{-6}$ mbar and the experimental chamber (EC) is operated at $p(\text{EC}) \leq 4 \cdot 10^{-6}$ mbar. The two chambers are linked by a “clockwork” valve. The latter enables to use a skimmer with an aperture of \varnothing 1 mm or a non-skimmed effusive aperture through a $\varnothing \sim 50$ mm hole. Both chambers are each pumped by a cryopump (Leybold COOLVAC) and additional turbomolecular pumps (Pfeiffer). Inside the source chamber the molecular source is placed. Different molecular sources (*vide infra*) can be connected, which depends on the nature of the experiment. A metal tube with a diameter of 6 mm is used as the gas line and is adapted to the SC by a flange. When low liquids with low volatility or solids are used, the sample reservoir is placed inside the SC. It is connected to the gas tube and is enclosed by a nozzle. The latter is either a short tubing from *Lenox Laser* with an orifice of $\varnothing(100-150)$ μm or a pinhole from *Plano*. The latter can be chosen with different diameters from 50 to 150 μm . When radicals are studied the pyrolysis source is mounted onto the nozzle. For liquid precursors with high a vapor pressure, the sample container is adapted to the gas tube outside the SC. Here the main advantage is that the sample can be changed without venting the machine. The molecular beam enters the SC by leaving the source through the nozzle. After that it reaches the EC in the z-direction, passing the skimmer and ending in the ionization spot close to the skimmer. The ionization spot displays the origin of the lab-frame coordinate system used here. The synchrotron light propagates through the gas filter along the x-axis into the EC. The electrodes for ion and electron extraction are placed in the EC along the y-direction, with the *Roentdek DLD40* VMI electron detector on the top. The WM-TOF-MS with the Jordan-MCP ion detector is mounted at the bottom of the flight tube. Herein the ions and electrons are accelerated in opposite direction in the 120 V cm^{-1} (also $40-80 \text{ V cm}^{-1}$ can be chosen) field vertical to the molecular beam propagation onto the detectors. The higher this voltage is, the lower the electron kinetic energy resolution, but the higher the mass resolution.

The specifications of any pumps, flanges and the monochromator can be found in the litera-

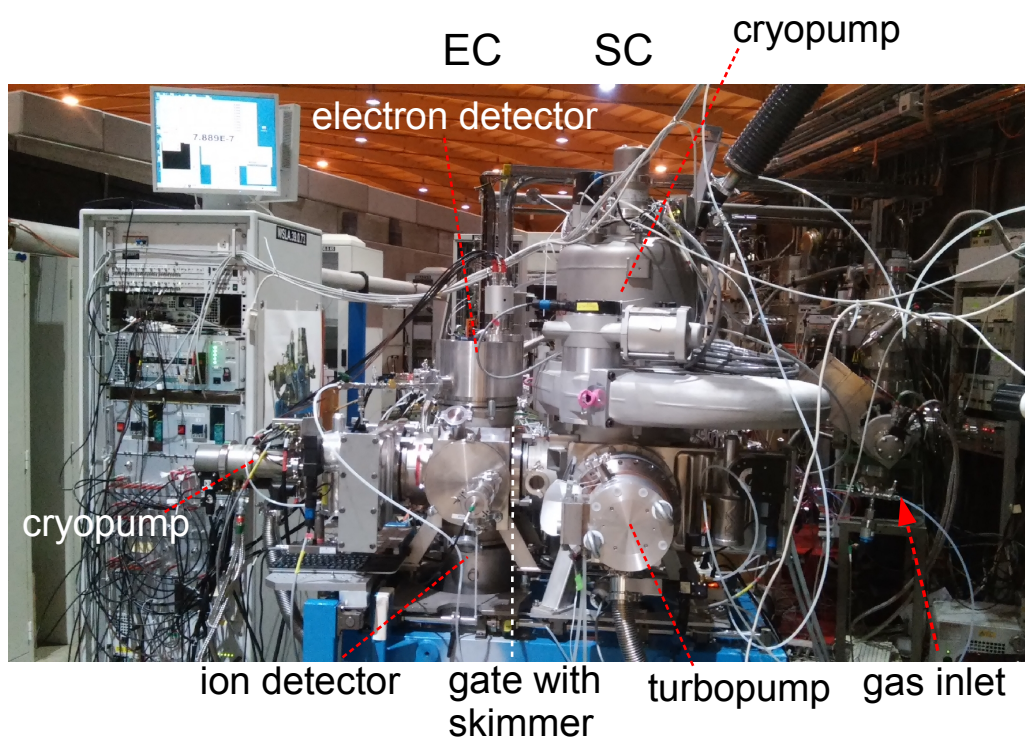


Figure 3.1.1: Vacuum apparatus of the VUV X04DB beamline at the SLS.

ture.^[86,100,107] The gas filter (GF), which is connected to the EC, consists of 8 differentially pumped sections. It is used to suppress higher harmonics radiation $\lambda = \lambda_0/m$ emitted from the bending magnet. The gas filter is either operated with pure Neon for photon energies from 14 eV to 21 eV or with a gas mixture of Neon (75%), Argon (24%) and Krypton (1%) in the energy range from 8 eV up to 14 eV. For lower photon energies a MgF_2 window that transmits radiation up to 10 eV, but transmits most efficiently in the range from 6 to 8 eV is used to filter off higher harmonics radiation. The working pressure of the GF covers the range from $10^{-9}/10^{-8}$ mbar for the section connected to the vacuum line of the storage ring and goes up to 10^{-6} mbar in the sections of the GF connected to the experimental chamber of the end-station apparatus. Since the EC and the gas filter are connected by a small aperture, the pressure gradient is chosen $p(\text{GF}) < p(\text{EC})$ to prevent the optical line from sample contamination.

3.1.2 Molecular sources and sample containers

The sample container for volatile liquids that is outside of the vacuum apparatus connected to the gas tube has been described in several PhD thesis previously (e.g. Patrick Hemberger^[140] and Christof Schon^[141]). Therefore only two molecular source layouts for solids will be presented in the following.

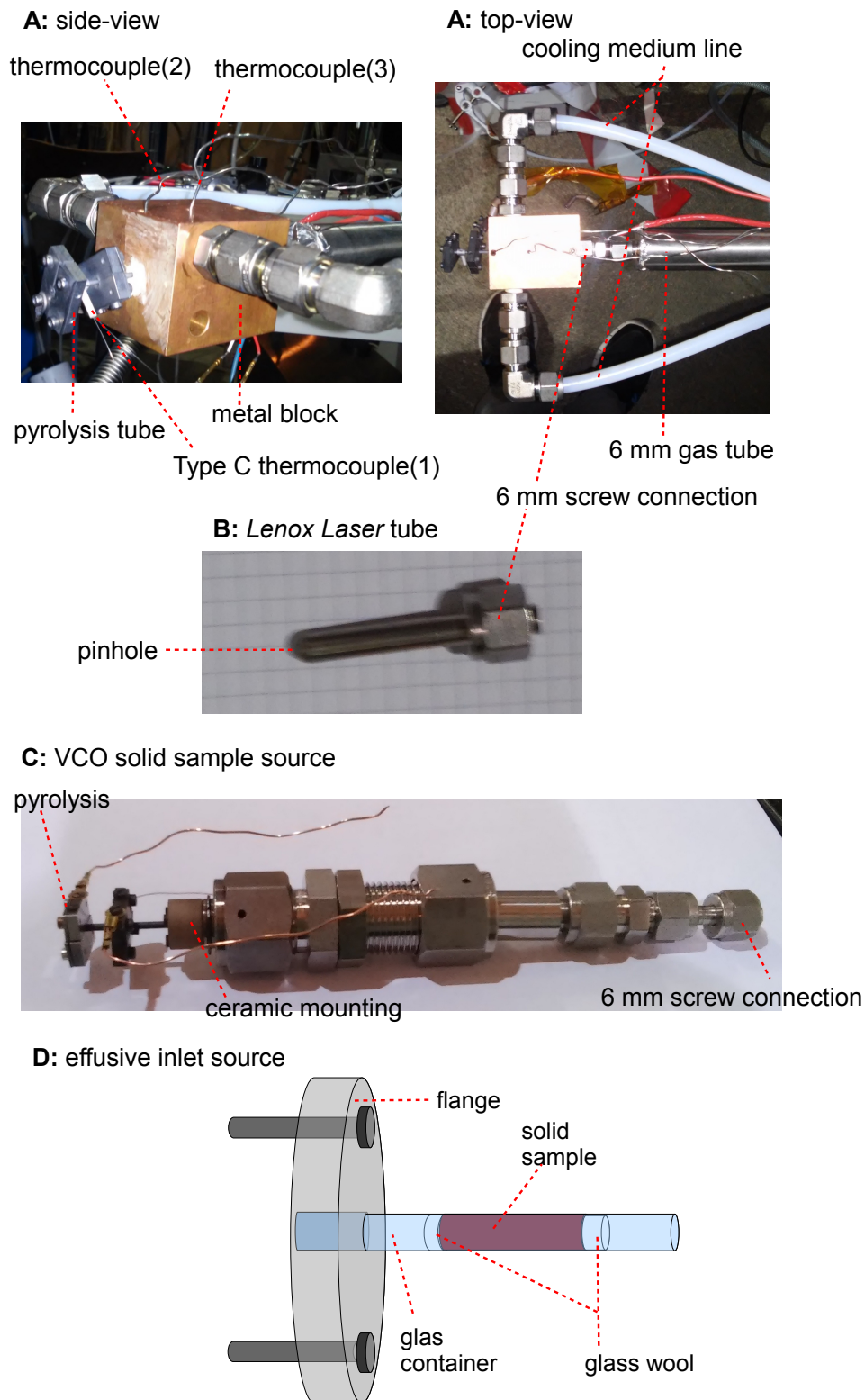


Figure 3.1.2: Molecular sources: **A)** sample container for solids with moderate/high vapor pressures **B)** *Lenox Laser* tube used in the source **A**, **C)** VCO solid sample source heated by a heating filament not shown in the picture **D)** effusive inlet source

In addition, an effusive inlet system for solids with very high melting points ($>150\text{ }^{\circ}\text{C}$), will be shown. For solid samples with melting points lower than $100\text{--}130\text{ }^{\circ}\text{C}$, the source shown in fig. 3.1.2, **A**, is used. It was designed by Patrick Hemberger at the VUV X04DB beamline.

A ca. 4 cm long metal tube (inner \varnothing 6 mm) with an orifice of $150\text{ }\mu\text{m}$ from *Lenox Laser* (fig. 3.1.2, **B**) is used as the sample container and nozzle in one device. The pinhole-tube is directly connected to the \varnothing 6 mm gas tube inside the source chamber. The tube is surrounded by a copper block with a water cycling system. The pyrolysis tube is mounted from the front side. Water is circulated by the *Huber Minichiller*. The latter can be operated from around $-5\text{ }^{\circ}\text{C}$ up to $90\text{ }^{\circ}\text{C}$, allowing to heat and to cool the sample. The temperature range can additionally be increased when operating the Minichiller with liquids of different melting and boiling points.

For solids with high molecular weight and low volatile liquids the molecular source, presented in fig. 3.1.2, **C**, reveals a neat sample container. It consists of three parts, which are all attached by *VCO* screw connections. In the front-part the *Plano* pinhole is fixed by a plunger. Outside, in a screwed ceramic connector the pyrolysis tube is mounted, which additionally can be glued inside the ceramic. The solid substance is filled in the middle part and closed by small pieces of glass wool at each side. The back part acts as the connection to the 6 mm gas tube. The whole molecular source is surrounded by one or two heating filaments from *Thermocoax*, which allow to heat the source up to $\sim 200\text{ }^{\circ}\text{C}$. In addition, low volatile liquids can also be soaked by glass wool and placed in this sample container.

If a solid sample is investigated effusively without pyrolysis and the melting point exceeds about $150\text{ }^{\circ}\text{C}$, the molecular source, presented in fig. 3.1.2, **D**, can be applied. A quartz tube is directly connected to the experimental chamber by a flange, adapted by a *Swagelok* tube fitting. For this purpose the source chamber and the experimental chamber are disconnected. The flange allows three stages of operation: 1) closed 2) closed to EC and open to the vacuum system for differential pumping of the sample and 3) open to the experimental chamber. The sample container is embraced by a heating ring, which is not shown in fig. 3.1.2. For steady sample flow and to prevent re-sublimation the entire sample should be in direct contact to the heater and not exceed the heated zone. To prevent the sample from getting lost in the heated space of the tube, some glass wool encloses the solid substance at each side.

3.2 General procedures in experimental analysis

Calibration of the monochromator

The monochromator is temperature sensitive. It should therefore be calibrated every day; after a beam-loss, after a change of gratings and before each new scan of an experiment. The calibration of the monochromator is usually performed on the resonances in argon. Ionization to the two first electronic states $^2P_{3/2}$ and $^2P_{1/2}$ of Ar^+ is observed at 15.760 eV^[142] and 15.938 eV. In the energy range between the two ionization potentials, a series of autoionization resonances exists, which converge to the $^2P_{1/2}$ state. The transitions are well known, very intense due to high photoionization cross sections and close in energy to each other, which makes a calibration with argon easy, fast and accurate. The photoelectron spectrum of argon is shown in fig. 3.2.1. It displays the energies of the 11s', the 12s' and the 13s' autoionization transitions, measured with the energy of the second harmonic radiation. The same scan is additionally performed with the fundamental photon energy. Thus, six energy values are obtained and used for calibration. The energies, observed for the 11s', 12s' and 13s' transitions, are taken to calculate the scan angle ϕ (compare eq. 2.2.5) according to eq. 3.2.1 for the current constant values of d, α and $\Delta\phi$.

$$E \propto \frac{1}{d \cdot \cos\alpha \cdot \sin(\phi + \Delta\phi)} \quad (3.2.1)$$

In the equation d stands for the number of lines per mm of the chosen grating, α is the incident angle and $\Delta\phi$ displays the offset of the scan angle, which is due to the motor movement of the monochromator. The literature energy values of the 11s', 12s' and 13s' transitions are 7.8812 eV, 7.8986 eV, 7.9109 eV in the second harmonic order, and 15.7639 eV, 15.7973 eV and 15.8219 eV in the first order.^[143] The differences between the energy values from literature and the experimentally observed ones are summed up to an overall error. The overall error is iteratively minimized by adjusting d, α and $\Delta\phi$, which are transcribed into the i²PEPICO software.

Mass calibration

The mass spectrometer is calibrated by a two point calibration. Particles of different masses and the same charge only differ in their time-of-flight when they are accelerated by a similar electric field and cover the same distance s to the detector (eq. 2.3.5). From this the relation of two different masses m_1 and m_2 and their TOF t_1 and t_2 are given in eq. 3.2.2 as follows:

$$\frac{m_1}{t_2^2} = \frac{m_2}{t_1^2}. \quad (3.2.2)$$

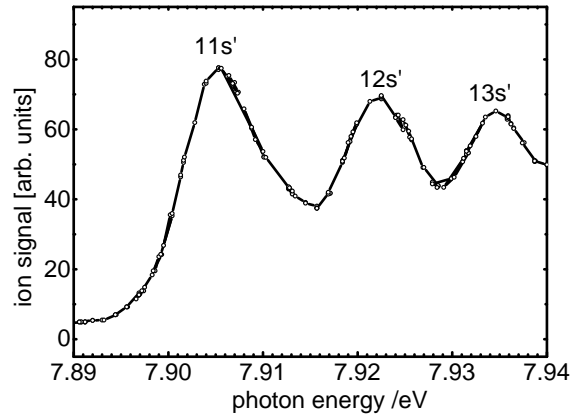


Figure 3.2.1: Photoion yield curve of argon used for energy calibration with second harmonic radiation.

The time of flight t is quadratic in the mass m , connected by the reference time t_0 , according to eq. 3.2.3

$$t = a\sqrt{m} + t_0. \quad (3.2.3)$$

The constant a includes several experimental parameters, i.e. voltages, the geometry of the extraction field and the distance of flight. The reference time t_0 is an empirical constant including several time-dependent offsets, e.g. cable delays.

From eq. 3.2.2 and eq. 3.2.3 follows for t_0 and for a :

$$t_0 = \frac{t_1 - t_2\sqrt{\frac{m_1}{m_2}}}{1 - \sqrt{\frac{m_1}{m_2}}} \quad a = \frac{t_1 - t_2}{\sqrt{m_1} - \sqrt{m_2}} \quad (3.2.4)$$

This approach enables to calculate the mass values in the range between m_1 and m_2 accurate, but does not reproduce the signal intensities correctly. This originates from the dependence of the time of flight from the square root of the mass, thus, not every time-of-flight interval dt is correlated to the same absolute value of the mass interval dm . Since this is not accounted for, mass calibration is performed in all regions of interests of the respective mass values.

4 Photoionization of hydrocarbon radicals

4.1 Butynyl radicals C_4H_5

The spectroscopic investigations on the small hydrocarbon radicals C_4H_5 has not been very extensive so far. Isomers of C_4H_5 were for example observed in the combustion of methyl methacrylate flames,^[144] in toluene flames,^[145] and in diverse fuel-rich flames.^[33] In addition, computations predict C_4H_5 radicals to play an important role in the unimolecular decomposition of dimethylfurane,^[146] and in the formation of soot.^[147] In the above mentioned experiments the radicals have been identified by PIMS. Therefore, spectroscopic information is scarce on the radicals and isomer identification has not yet been achieved. Beside several butadiene-yl isomers that are not discussed in this work, four different molecular structures of C_4H_5 radicals are known. These are 1-butyn-1-yl, 2-butyn-1-yl, 1-butyn-3-yl and 4-butyn-1-yl, shown in fig. 4.1.1. The two conjugated butynyl isomers 2-butyn-1-yl and 1-butyn-3-yl were investigated in this work. Among the butynyls, 2-butyn-1-yl and 1-butyn-3-yl are thermodynamically the most stable isomers and thus the ones preferably formed in combustion processes.

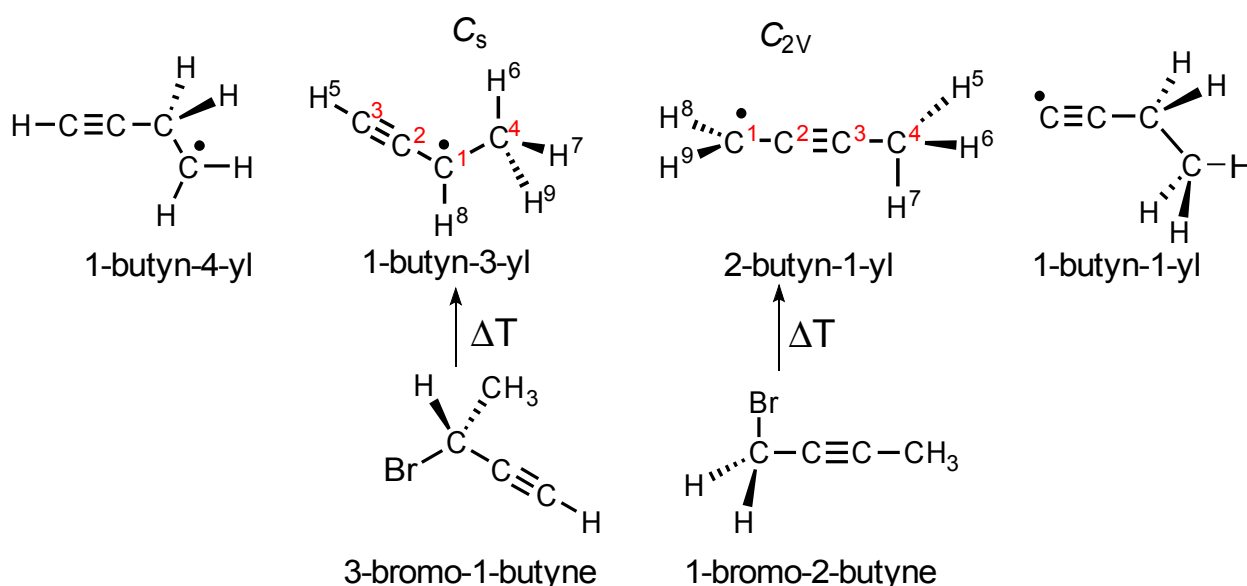


Figure 4.1.1: Survey of the C_4H_5 butynyl isomers and the precursors used in the pyrolysis experiment.

In this work the two radicals 2-butyn-1-yl and 1-butyn-3-yl were produced from the respective brominated precursor molecules, 1-bromo-2-butyne and 3-bromo-1-butyne (fig. 4.1.1). In addition, 2-butyn-1-yl was also observed in the pyrolysis of 3-bromo-2-methylpropene that was used to generate 2-methylallyl radical (*vide infra*).

1-Butyn-3-yl has C_S symmetry, whereas 2-butyn-1-yl is expected to transform according to C_{2V} symmetry because the terminal groups methyl and methylene can be treated as unhindered rotors. Computations on the CBS-QB3 level determined a transition state and failed to find the real minimum structure of 2-butyn-1-yl. The CBS-QB3 method uses the B3LYP/6-311g(2d,d,p) level for geometry optimization. The negative frequency of the obtained TS is the methyl torsion. This negative frequency indicates the critical mode from which the geometry change between the minimum structure and the transition state can be inferred. The minimum structure of 2-butyn-1-yl is presented by the staggered conformation **A** (fig. 4.1.2) at a dihedral angle H(5)-C(4)-C(2)-H(8) of 30° (for labeling of atoms see fig. 4.1.1). The transitional structure obtained with the CBS-QB3 computations is **B**. Here the H-atoms H(5) and H(9) are in an eclipsed position. The barrier to transfer conformation **A** into **B** is only 0.6 cm^{-1} . Since this value is about two orders of magnitude smaller than the precision that is used for the computation of ionization energies (80 cm^{-1} (1 meV)), the barrier was neglected in the present work. Thus, the computed zero point vibrational energy corrected electronic energy of the TS structure of the 2-butyn-1-yl radical (obtained on the CBS-QB3 level) is taken as the minimum energy of the molecule.

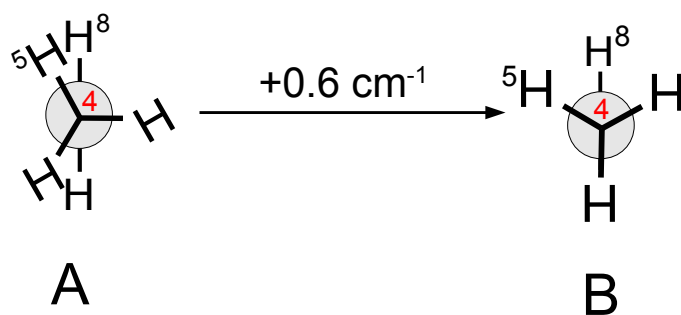


Figure 4.1.2: Newman projection of the minimum structure **A** and the transitional structure **B** of 2-butyn-1-yl. By rotation of the dihedral angle H(5)-C(4)-C(2)-H(8) about 30° **A** turns into **B** with a barrier of 0.6 cm^{-1} .

Temperature dependent precursor fragmentation

In a first set of experiments the temperature dependence of the qualitative and quantitative destruction of the brominated precursors has been examined. Figure 4.1.3 shows the Ms-TOF spectra of 1-bromo-2-butyne at 8.5 eV, 9.5 eV and 10.5 eV for three pyrolysis temperatures on the left. In the same figure on the right breakdown diagrams for each photon energy are depicted. The latter show the absolute abundances, as well as the fractional abundances of the prominent pyrolysis products versus the temperature. Figure 4.1.4 shows the same quantities of 3-bromo-1-butyne.

At 8.5 eV the only visible mass signal upon pyrolysis of 1-bromo-2-butyne and 3-bromo-1-butyne is $m/z=53$. $M/z=53$ corresponds to the signal of the C_4H_5 radicals. $M/z=53$ is produced with the highest amount by a pyrolysis temperature of 550 °C, as can be deduced from the breakdown curves at 8.5 eV of both precursors. At 9.5 eV both precursors at $m/z=132/134$, C_4H_5Br , are visible. At 450 °C, under medium pyrolysis conditions parts of the precursor $m/z=132/134$ are still retained and the major pyrolysis products are the radical isomers $m/z=53$. With increasing pyrolysis temperatures the precursor signal $m/z=132/134$ vanishes while the signal of $m/z=53$ decreases, too. Complementary to this observation the signal of $m/z=52$ increases. The latter reaches a maximum amount by 700 °C for both 1-bromo-2-butyne and 3-bromo-1-butyne. $M/z=52$ most likely corresponds to the formation of 1-buten-3-yne, C_4H_4 , that might be formed in an HBr-loss reaction. A further plausible carrier of $m/z=52$, cyclobutadiene, C_4H_4 , can be excluded. The latter has an IE of 8.16 eV.^[148] Therefore, it should be visible at 8.5 eV where no mass signal $m/z=52$ appears throughout the whole temperature range. A significant mass peak is observed at 9.5 eV and 1-buten-3-yne ionizes at 9.58 eV.^[149] In general, mass signals can be observed slightly below the adiabatic IE in pyrolysis experiments where large amounts of thermal energy lower the ionization onset. In the pyrolysis of 1-bromo-2-butyne at 9.5 eV tiny mass signals at $m/z=104/106$ and at $m/z=39$ are visible in the temperature range from 500 °C to 600 °C. $M/z=39$ is also observed in the pyrolysis of 3-bromo-1-butyne at equal conditions. $M/z=104/106$ corresponds to a species that differs in 28 atomic mass units from the precursor 1-bromo-2-butyne, $m/z=132/134$. The molecule has also the typical bromine isotopic pattern. However, a plausible molecular structure of $m/z=104/106$ cannot be derived from the precursor's structure. $Br-C_2H$ can be excluded, since it has an IE at 10.31 eV^[150] and the mass signal 104/106 is already observed at 8.5 eV. The signal at $m/z=39$ originates from a C_3H_3 isomer, probably the propargyl radical, linear C_3H_3 (IE=8.7 eV). The latter is the most stable neutral C_3H_3 isomer. In addition, with sufficient internal energy also the cyclic $C_3H_3^+$ will be detected. $c-C_3H_3^+$ is the energetically preferred isomer on the cationic C_3H_3 potential surface.^[151] At 10.5 eV and 20 °C both precursors undergo DPI to $m/z=53$. In doing so 3-bromo-1-butyne has already almost completely fragmented. The dissociative photoionization of the bromo-butyne isomers has already been examined by Bodi et al., who reported the 0 K appearance energies for 2-butyne-1-ylum ($AE_{0K}=10.375$ eV) and for 1-butyne-3-ylum cation ($AE_{0K}=10.284$ eV), respectively.^[152] Going to

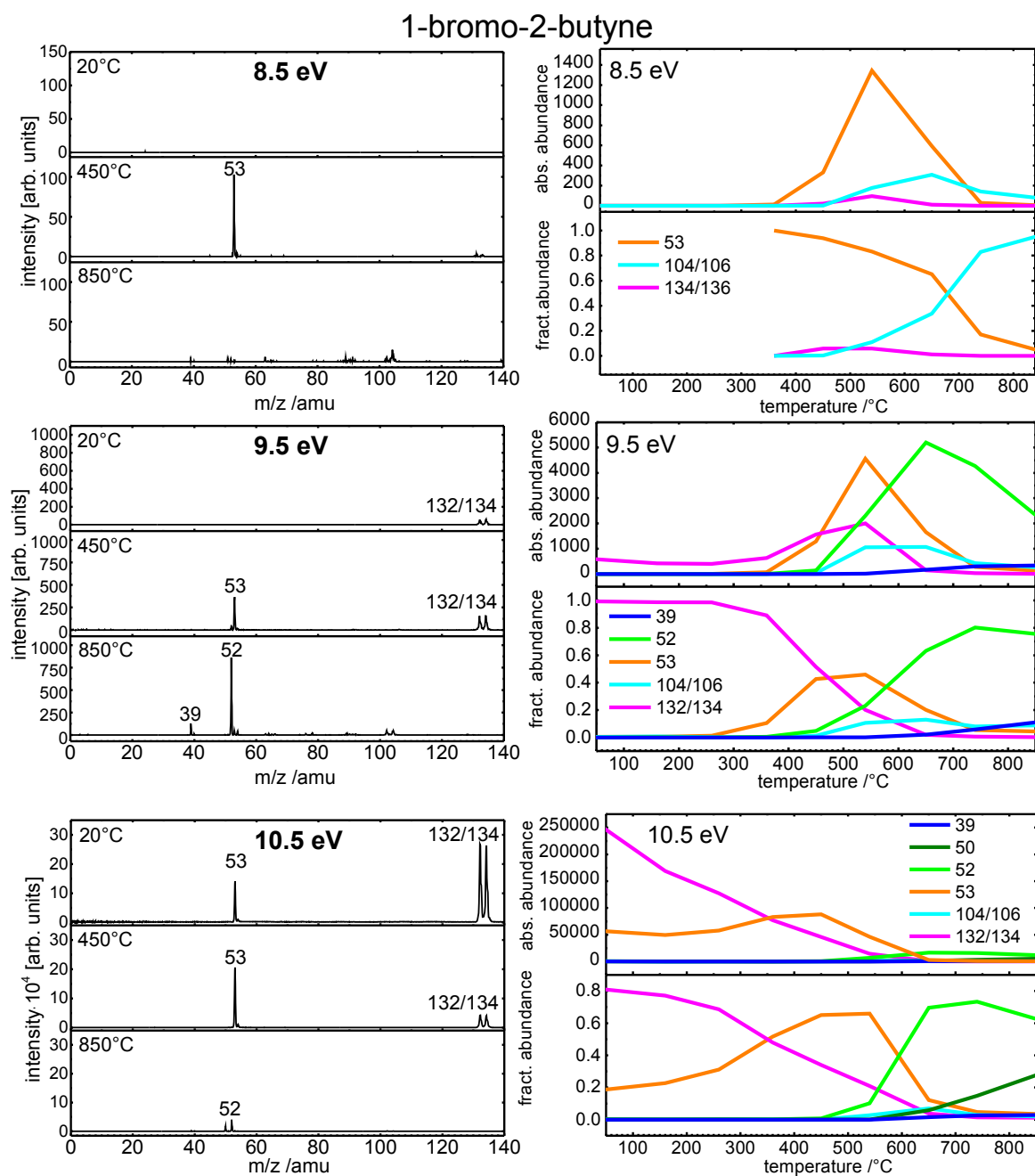


Figure 4.1.3: Ms-TOF spectra of 1-bromo-2-butyne in the temperature range from 20 °C to 800 °C at different photon energies are presented on the left. Breakdown diagrams showing the absolute and the relative abundance of the most prominent species versus the temperature ($T / ^\circ\text{C}$) are depicted for each photon energy on the right. The pure numbers display the mass signals m/z in amu.

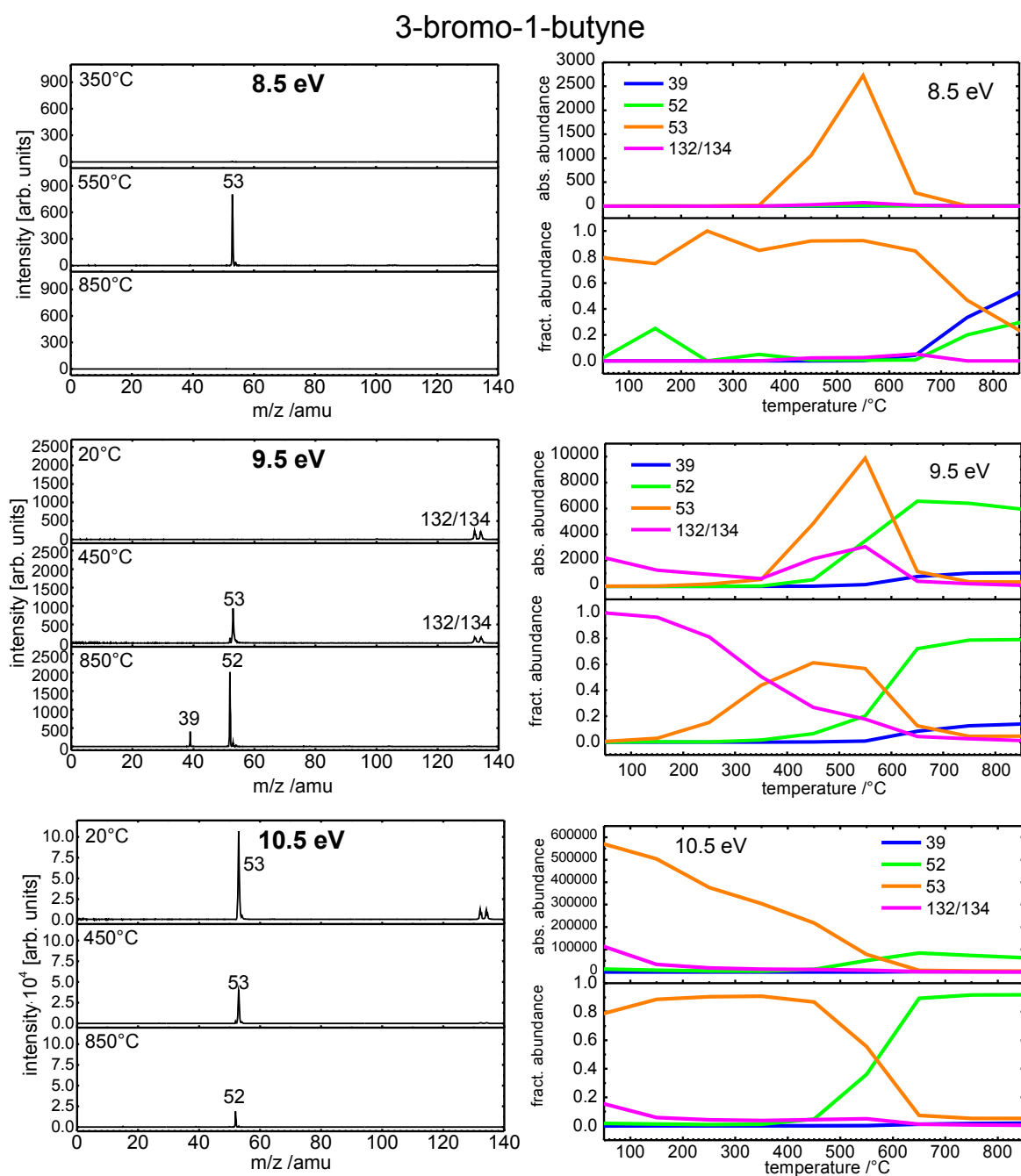


Figure 4.1.4: Ms-TOF spectra of 3-bromo-1-butyne in the temperature range from 20 °C to 850 °C at different photon energies (left). Breakdown diagrams, showing the absolute and the relative abundance of the most prominent pyrolysis products versus the temperature (T / °C) are depicted for each photon energy on the right. The numbers display the mass signals m/z in amu.

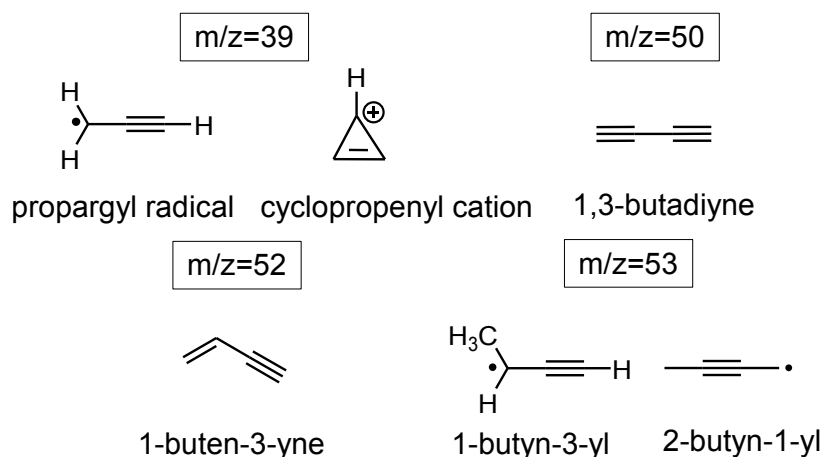


Figure 4.1.5: Scheme of the pyrolysis products, that are assumed to be formed from 1-bromo-2-butyne and 3-bromo-1-butyne.

high pyrolysis temperatures the saturated pyrolysis products $m/z=50$ and $m/z=52$, produced from 1-bromo-2-butyne, are the dominating. The two species have high IEs and are thus only visible in the TOF-MS at 10.5 eV. $m/z=50$ is supposed to correspond to 1,3-butadiyne and is only observed upon the pyrolysis of 3-bromo-1-butyne. In accordance to that, formation of the radical $m/z=53$ becomes less efficient and the signal $m/z=53$ vanishes at high temperatures. Unfortunately, the assignment of the formed pyrolysis products is more or less tentative, since no TPES, except for $m/z=53$ (section 4.1) were recorded as this was not the main goal of this study. Nevertheless, a scheme, embedding the most probable molecular structures of all formed molecules visible in fig. 4.1.3 and fig. 4.1.4, is shown in fig. 4.1.5. The structure of cyclopropenyl is shown as the cation, indicating, cyclopropenyl might preferably not be formed upon pyrolysis itself but in a rearrangement of the propargyl cation.

The best conditions for the formation of the $m/z=53$ radicals can be deduced from the pyrolysis scans. Thus, the temperature to record threshold photoelectron spectra of the C_4H_5 isomers was chosen 550 °C. With these conditions no other species are detected in the investigated energy range and the conversion to $m/z=53$ shows the highest efficiency for both 1-bromo-2-butyne and 3-bromo-1-butyne.

TPES of 1-butyn-3-yl and 2-butyn-1-yl

The threshold photoelectron spectra (TPES) and the Franck-Condon simulations of 2-butyn-1-yl (upper panel) and 1-butyn-3-yl (lower trace) are depicted in fig. 4.1.6.

The spectra were recorded with a step size of 5 meV and with an acquisition time of 120 s per data point. Since there are no other masses visible in the investigated energy range, all threshold photoelectrons without selection of the coincident ions were analyzed. The TPE-signal of 2-butyn-1-yl has been recorded from 7.8 eV to 8.6 eV and shows a peak at 7.94 eV followed by a shoulder at 8.04 eV.

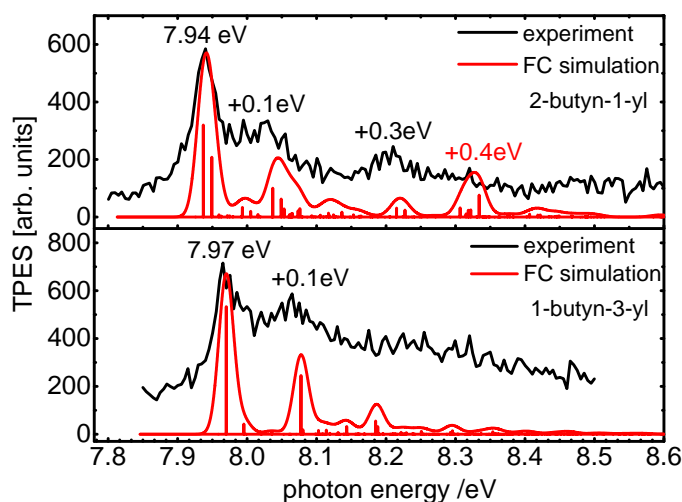


Figure 4.1.6: Ms-TPES of 2-butyn-1-yl (upper trace) and 1-butyn-3-yl (lower trace) with their respective Franck-Condon simulations.

A second less intense band is visible around 8.2 eV. The signal at 7.94 eV is assigned to the ionization energy IE_{ad} of 2-butyn-1-yl. This value has an estimated error of ± 0.02 eV. The spectrum of the second C₄H₅ isomer 1-butyn-3-yl (fig. 4.1.6, lower panel), recorded from 7.85 eV to 8.5 eV does not appear to be very different from the first one. The first peak, assigned to the ionization energy of 1-butyn-3-yl, is found at 7.97 eV. Again, an error of ± 0.02 eV is assumed. This peak is also accompanied by a shoulder at +0.1 eV. As stated above, dissociative photoionization of the precursors is not relevant for either butynyl isomer within the investigated energy range, however both spectra exhibit contributions of hot- and sequence bands at around 7.9 eV. The two spectra show some vibrational structure which can tentatively be assigned with the help of the Franck-Condon (FC) simulations (red line in fig. 4.1.6).

The simulation of 2-butyn-1-yl (fig. 4.1.6, upper panel) shows a band around +100 meV is mainly caused by mode ν_{16}^+ (computed 100 meV /806 cm⁻¹), a stretch of the two single bonds C(1)-C(2) and C(3)-C(4), and the combination of ν_{16}^+ with ν_{21}^+ (computed 12 meV /97 cm⁻¹). The discussed vibrations in the X⁺ ²B₁ cation ground state are visualized in figure 4.1.7 and the labeling of atoms

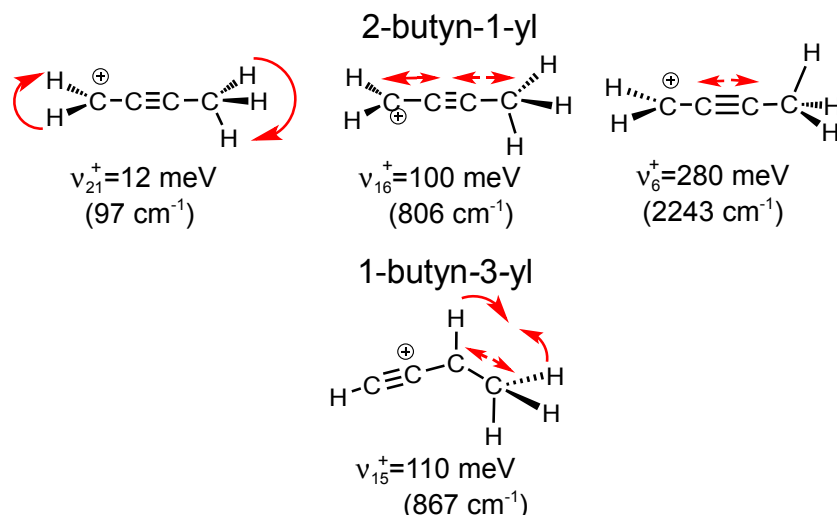


Figure 4.1.7: Active vibrations of 2-butyn-1-ylum and 1-butyn-3-ylum.

is given in figure 4.1.1. The band in the range of +300 meV is in the FC simulation described by v_6^+ (computed 280 meV / 2243 cm^{-1}), the C(2)-C(3) triple bond stretching vibration. Additionally, there is a band simulated at around +400 meV (3200 cm^{-1}) which is not distinguishable in the experimental spectrum.

The relative positions of the simulated bands of 1-butyn-3-yl also match the experimental spectrum quite well. The band around +100 meV is assigned to v_{15}^+ (computed to 110 meV / 867 cm^{-1}), which corresponds to the H₃C(4)-C(1) single bond stretching vibration. v_{15}^+ is in addition computed to contribute to the spectrum with the first overtone at around +220 meV (1750 cm^{-1}), which is barely visible as a shoulder in the spectrum. Both Franck-Condon stick spectra were convoluted with a Gaussian function of 25 meV full width at half maximum. In both molecules the internal rotations of the methyl groups are expected to cause broadening of the bands in the spectra. Since the harmonic approximation often fails for internal rotations, torsional modes are not always well represented in FC-simulations. Here only in the simulation of 2-butyn-1-yl the contribution of the methyl torsional mode v_{21}^+ is predicted well, while it does not appear in the simulated spectrum of 1-butyn-3-yl. Since the vibrational analysis is only tentatively possible, and some shortcomings in the simulations have been recognized the reference of vibrational activity on the geometry change upon ionization is tentative, too. The computations predict only small deviations in the geometries of both radicals upon ionization. The most significant change of 2-butyn-1-yl is caused by the torsional vibration v_{21}^+ . Thus, the dihedral angles H(7)-C(4)-C(1)-H(8) and H(7)-C(4)-C(1)-H(9) change both by 15 °, H(6)-C(4)-C(1)-H(8) and H(6)-C(4)-C(1)-H(9) increase by 19 °, each. In addition, the angle C(3)-C(4)-H(7) decreases by 6 ° and H(5)-C(4)-H(6) increases by 5 °. The greatest changes in bond lengths originate from v_{16}^+ which leads to an elongation of C(1)-C(2) and C(3)-C(4) about 3 pm each. The most distinct change in geometry of 1-butyn-3-yl is caused by the most intense active vibration v_{15}^+ , which leads to the decrease in C(1)-C(4) by 4.5 pm.

However, the similar shape of the spectra in fig. 4.1.6 leads one to consider isomerization in the pyrolysis as a possible side reaction. But not only the isomerization of the radicals, also the rearrangement of the precursors has to be taken into account. Figure 4.1.8 shows the plausible contributions to the formation of the two butynyl isomers. The precursor **a** which is used to form 2-butyn-1-yl can rearrange to the allene **b** which itself produces 1-butyn-3-yl upon pyrolysis. The other precursor **c** that is intended to generate 1-butyn-3-yl with active pyrolysis rearranges to **d**.

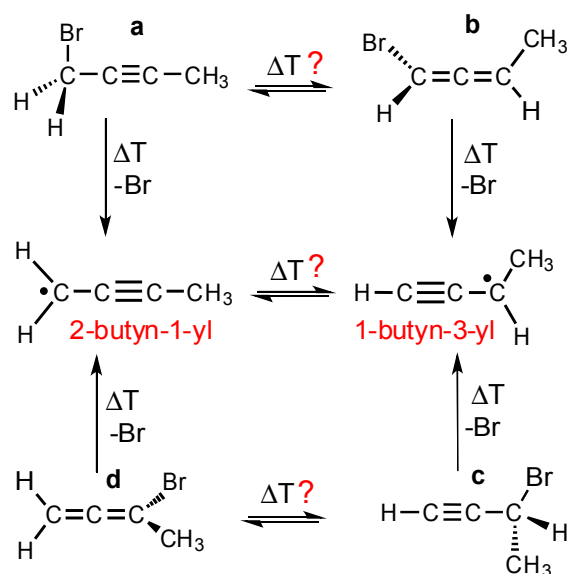


Figure 4.1.8: Supposed rearrangement of the precursors 1-bromo-2-butyne **a** to 1-methyl-3-bromo-allene **c** and 3-bromo-1-butyne **b** to 1,1-methyl-bromo-allene **d**. Precursor **a** and **d** form 2-butyn-1-yl upon pyrolysis and **c** and **b** generate 1-butyn-3-yl.

1,1-methyl-bromo-allene **d** most likely forms 2-butyn-1-yl upon pyrolysis. This assumption will be valid if the barriers for rearrangements of **a** to **b** and from **c** to **d** are low enough to be passed upon pyrolysis. In addition, the rearrangement of the radicals 2-butyn-1-yl and 1-butyn-3-yl to the respective other isomer might occur if this isomerization follows a low energetic reaction pathway. To find out, whether the proposed rearrangement shown in fig. 4.1.8 will lead to a mix of the two radicals, the barriers of the isomerization reactions were computed. Such rearrangement of a brominated propyne was already observed in a different TPEPICO experiment. In this experiment 1,3-dibromopropyne was used as a radical precursor upon pyrolysis and a mixture of mono-brominated radicals was yielded, originating from partial H-atom shift in the precursor and subsequent bromine loss.^[153] The rearrangement of both 1-bromo-2-butyne **a** and 3-bromo-1-butyne **b** are shown in fig. 4.1.9. Both reactions are predicted as 1,3-H-shifts which proceed via four membered transition states. The barrier of the isomerization of **a** to 1-bromo-3-methylallene **b** has a barrier of 3.88 eV (374 kJ/mol). The respective rearrangement of **c** to 1-bromo-1-methyl-allene **d** has been computed to 3.69 eV (356 kJ/mol). Both barriers are comparable to the strength of a C-H bond, which is

unlikely to break upon the chosen pyrolysis conditions. The computations were performed with the CBS-QB3 method.

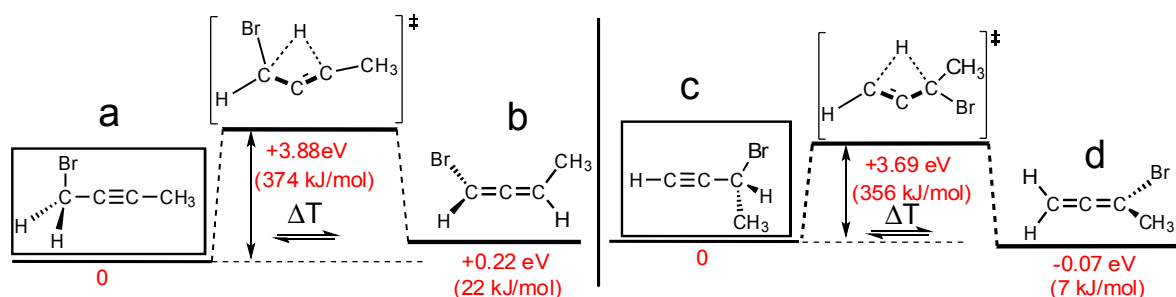


Figure 4.1.9: Isomerization of the precursors 2-bromo-1-butyne **a** to 1-methyl-3-bromo-allene **b** (left) and 3-bromo-1-butyne **c** to 1,1-methyl-bromo-allene **d** (right). The barriers of rearrangement of the bromo-butynes to the respective allenes are given in eV (kJ/mol) and are computed with the CBS-QB3 method.

The rearrangement from 2-butyne-1-yl to 1-butyne-3-yl is shown in fig. 4.1.10. The isomerization of 2-butyne-1-ylum to 1-butyne-3-ylum in the cation has been computed before and a complex reaction sequence was found.^[154] This work guided the computations on the CBS-QB3 level, which also predict a four step rearrangement on the neutral potential surface of C_4H_5 . Fig. 4.1.10 shows the complete reaction pathway from 2-butyne-1-yl (left) to 1-butyne-3-yl (right). In the first step the H(5)-atom of the $C(4)H_3$ moiety shifts to the α -C(3). From the intermediate I1, which is 4 meV (4 kJ/mol) lower in energy than 2-butyne-1-yl, the next transition state is passed. TS2 has a bent carbon chain and is 2.19 eV (211 kJ/mol) higher in energy than the starting molecule. Subsequently a four membered ring is formed (I2 in fig. 4.1.10). The highly strained cyclobutenyl is 0.99 eV (95 kJ/mol) higher in energy than 2-butyne-1-yl and opens again. The bond cleavage between C(3) and C(4) leads to the transition state TS3, 2.20 eV (212 kJ/mol) higher in energy than the reference structure. The intermediate I3 is the terminal radical 1-butyne-4-yl, 0.62 eV (60 kJ/mol) higher in energy than 2-butyne-1-yl. In I3 H(9) shifts from C(1) to C(4) to form the resonantly stabilized 1-butyne-3-yl. The transition state TS4, 2.06 eV (198 kJ/mol) higher in energy than 2-butyne-1-yl, is passed in this last rearrangement step. The transition state TS1 to the formation of the first intermediate was not located with the CBS-QB3 method. Nevertheless, computations on the M06L/6-311g(d,p) level yielded the energy for all of the transition states and intermediates, shown in fig. 4.1.10. Here TS1 is computed lower in energy than TS2 and TS3. In addition, the relation of all transition state and intermediate energies is the same like the ones obtained with the CBS-QB3 method. Thus, the relative energy position of TS1, as it is shown in fig. 4.1.10, can be assessed from the computations conducted on the M06L level. The CSB-QB3 method was nevertheless preferred, since it yields more accurate absolute energy values.

Although several reaction steps have to occur, the highest barrier is computed to 2.20 eV.

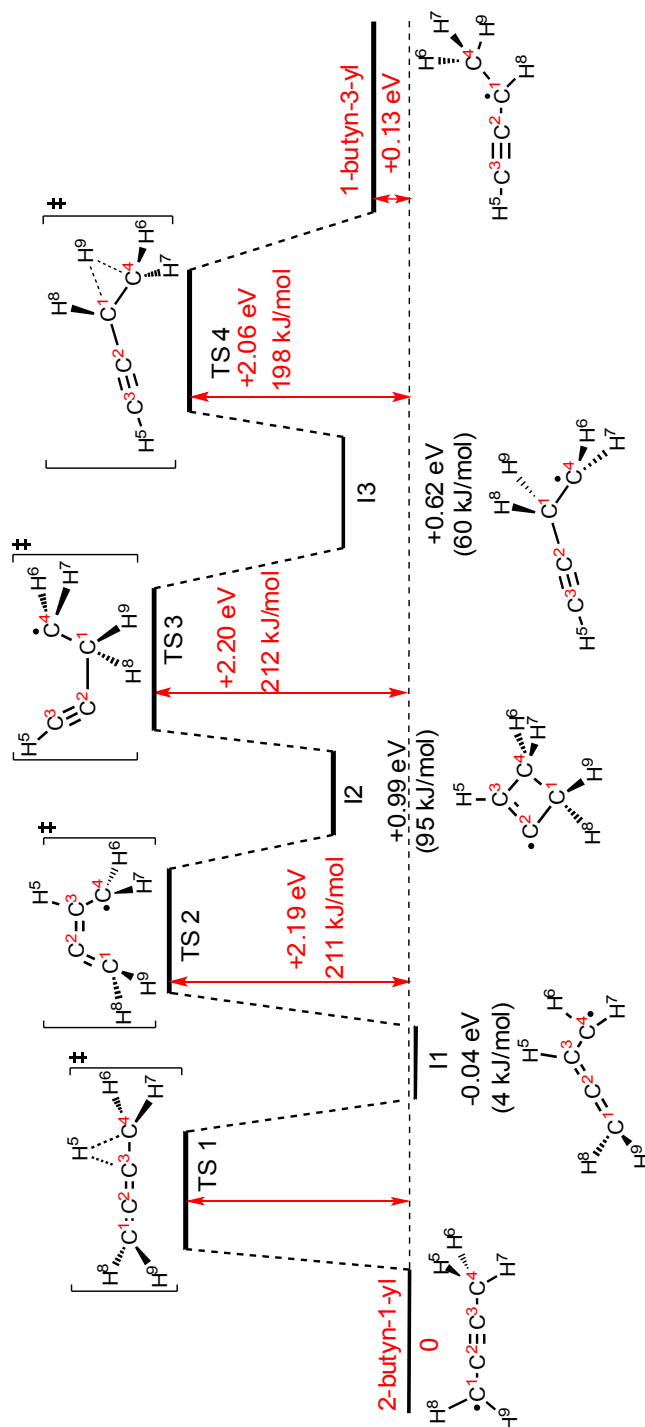


Figure 4.1.10: Isomerization of the radicals 2-butyn-1-yl and 1-butyn-3-yl. The reaction proceeds via four transition states (TS) and three intermediates (I). The energy difference of each TS and the intermediates is given referenced to the energetically preferred C₄H₅ isomer 2-butyn-1-yl in eV (kJ/mol).

This value is moderate so that at pyrolysis temperatures of 550 °C a small degree of isomerization cannot be excluded. Since 2-butyn-1-yl and 1-butyn-3-yl differ only by 13 meV (12 kJ/mol) in their absolute energies, the rearrangement is not supposed to produce a dominant product. The direct loss

of bromine and formation of the radical from each precursor is computed to 2.76 eV (267 kJ/mol) for 1-bromo-2-butyne and to 2.67 eV (258 kJ/mol) for 3-bromo-1-butyne, respectively. Since the barriers for precursor rearrangement (fig. 4.1.9) are significantly higher than those for the radical rearrangement and the formation of the radical itself by bromine loss, the precursor isomerization can be ignored.

From the computations can be inferred that to some extent each radical isomer might isomerize. The TPE spectra of 2-butyne-1-yl and 1-butyne-3-yl are therefore expected to include both isomers. Nevertheless, since the origin bands are found at 7.94 eV and 7.97 eV at slightly different energies, each spectrum is dominated by one isomer. This interpretation might also give a further explanation for the broadening in the spectrum of 1-butyne-3-yl.

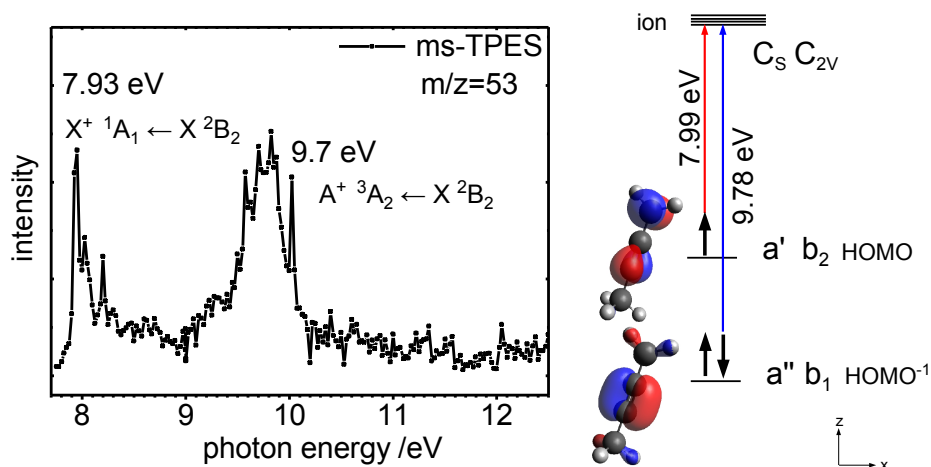


Figure 4.1.11: Ms-TPES of 2-butyne-1-yl up to 9.8 eV, including the transitions to the singlet and the triplet cation. On the right, the frontier molecular orbitals of the two ionization processes are visualized, assuming the validity of Koopman's theorem.

At higher photon energies the first excited state of the 2-butyne-1-yl cation is detected. The spectrum of 2-butyne-1-yl up to 12 eV, recorded with a step size of 20 meV and an acquisition time of 150 s per data point is presented in figure 4.1.11. The spectrum includes the two first ionization energies of 2-butyne-1-yl: the transition $X^+ \ ^1A_1 \leftarrow X \ ^2B_2$ at 7.93 eV that was precisely discussed in fig. 4.1.6, and the transition $A^+ \ ^3A_2 \leftarrow X \ ^2B_2$ to the triplet cation. For clarification of the orbitals' and electronic states' symmetry, the frontier molecular orbitals of 2-butyne-1-yl are shown in fig. 4.1.11 on the right. For their simplified representation the validity of Koopman's theorem is assumed. The band at 9.7 eV refers to the transition to the triplet cation. However, no detailed vibrational activity can be assigned. The computed value of 9.78 eV (TD-DFT) for this transition is in very good agreement with the experimental one, too.

As already indicated, an important point should be considered when discussing deviations of computed and experimental spectra. Some features of a molecule might not be appropriately represented by theory conducted on a comparably low cost level, like applied here. This is especially the case for molecules that have methyl and methylene groups which perform internal rotations. In the performed Franck-Condon simulations the internal rotations are treated like harmonic vibrations. The different potentials of the harmonic oscillator (A), the hindered rotor (B) and the unhindered rotor (C) are revealed in fig. 4.1.12. Whether such a motion is either best represented by a free rotor, a hindered rotor or an oscillator depends on the observed energy range and the molecule itself. In general, the treatment of an internal rotation depends on the barrier height. This implies, at low energies the motion is similar to a vibration, while at energies above the barrier height the motion turns into a free rotation. A simple solution to the problem of internal rotations does therefore not exist.^[54]

In the case of 2-butyn-1-yl the vibration ν_{21}^+ corresponds to an internal rotation. Unfortunately, both terminal groups, methyl and methylene, are moving simultaneously. Thus, the rotational barrier of this motion cannot be easily determined. Nevertheless, it is sure that the treatment of this internal rotation as a harmonic vibration is not appropriate. Especially the band at +0.4 eV in the computed spectrum of 2-butyn-1-yl (fig. 4.1.6, upper panel) gives an indication for the last stated assumption. The computed band gains high intensity through the contribution of the torsional mode ν_{21}^+ , whereas the spectrum lacks this feature.

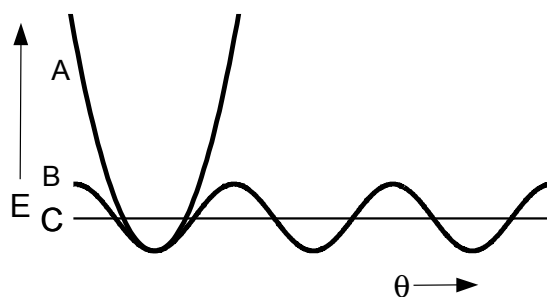


Figure 4.1.12: Potentials of the harmonic oscillator (A), the hindered rotor (B) and the free rotor (C).

However, there exist methods to account for internal rotations in harmonic vibrational analysis, while Pitzer and Gwinn^[155] were the first who developed an approach to calculate accurate energy levels and thermodynamic functions for molecules with internal rotation.

4.2 Methylallyl radicals C_4H_7

The radicals of the composition C_4H_7 exist as four different isomers. Three of them can be considered to be methylated allyl radicals, as shown in fig. 4.2.1. The allyl position of a $C=C$ double bond is a preferred position to form comparably stable radicals and carbocations. This characteristic was observed to dictate especially the processes in the combustion of biodiesel.^[156, 157] The latter contains e.g. fatty acid esters, compounds with double bonds that preferentially lose H-atoms in the α -position to the $C=C$ double bonds, forming intermediates that can be described as alkylated allyl radicals. The smallest alkylated allyl radicals are methylallyl isomers. The influence of an adjacent methyl group on several properties of the neutral and cationic allyl moiety is also of interest. Isomers of C_4H_7 have been observed in methyl methacrylate flames^[144] and in the combustion of several fuel-rich flames, too. The methylallyl (MA) radicals have been in the focus of several spectroscopic studies. They were investigated by conventional photoelectron spectroscopy,^[158] high-resolution zero kinetic energy (ZEKE) photoelectron spectroscopy,^[69] in UV absorption studies^[159] and by resonance-enhanced multiphoton ionization (REMPI) experiments.^[160, 161] The photodissociation dynamics have been explored by H-atom photofragment Doppler spectroscopy.^[68, 70] The ps time-resolved dynamics of the 3s Rydbergstate were investigated in the Fischer group,^[162] and is described in detail in the PhD thesis of Jörg-Viktor Herterich.^[163]

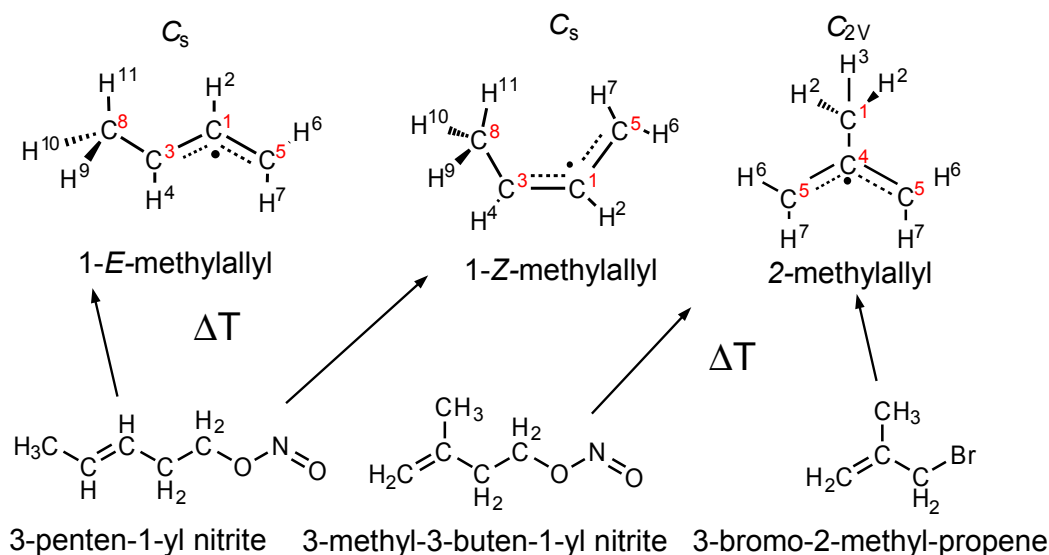


Figure 4.2.1: Scheme of the C_4H_7 isomers and their precursor molecules.

In this work the methylallyl radicals were generated upon pyrolysis of different precursors which are also shown in fig. 4.2.1. 3-penten-1-yl-nitrite and 3-methyl-3-buten-1-yl nitrite were synthesized according to the procedures of the literature. The synthesis is described in the appendix. 3-bromo-2-methylpropene was purchased from Sigma Aldrich and used without further purification. All of the

three liquid substances have sufficient vapor pressures. Therefore the molecular source for volatile liquids was used in the experiment. The bromide was seeded in 0.5-1.0 bar of argon whereas the two nitrites were seeded in 2-2.5 bar of argon. The aim of this work was to characterize the ionic structures of all three C₄H₇ isomers and in addition to explore the dissociative photoionization of 2-methylallyl (2-MA).

Temperature dependent precursor fragmentation

A) 3-penten-1-yl nitrite and 3-methyl-3-buten-1-yl nitrite

Figure 4.2.2 shows on the left mass spectra of 3-penten-1-yl nitrite, recorded at different photon energies and different temperatures. In addition, the fractional and the absolute signals of the most prominent masses are plotted versus the temperature for each photon energy on the right. The mass spectra at 25 °C will be discussed in section 4.2. The prominent pyrolysis products of 3-penten-1-yl nitrite is $m/z=55$. It corresponds to the mass signal of the two conformers 1-*E*- and 1-*Z*-methylallyl. The two C₄H₇ isomers were identified by their ms-TPES, discussed in the following section. At 9.5 eV the signal of $m/z=55$ is dominant at low pyrolysis temperatures and decreases rapidly up to 700 °C. Complementary to this, $m/z=54$ is formed and increases with rising temperatures. The mass signal $m/z=54$ originates from butadiene, C₄H₆, that is most likely formed by H-atom loss from $m/z=55$. Butadiene has been identified by the TPE signal of $m/z=54$ (fig. 4.2.4, upper panel). All TPE spectra shown in figure 4.2.4 were recorded at a pyrolysis temperature of 450 °C, with a step size of 5 meV and an acquisition time of 60 s per data point. Starting around 230 °C a further signal at $m/z=110$ appears. It reaches a maximum at 430 °C and decreases up to 550 °C where it completely vanishes. The mass signals at $m/z=95$ and $m/z=81$ rise by about 450 °C, slightly higher than $m/z=110$. The two species $m/z=95$ and $m/z=81$ show the same gradient in dependence of the temperature as $m/z=110$, but are less intense. $m/z=110$ most probably corresponds to the dimer of the 1-MA radicals, 2,2-octadiene, C₈H₁₄. The formation of the dimer is, in addition to the formation of butadiene $m/z=54$, the second reason why the radical production is suppressed at higher pyrolysis energies. $m/z=95$ and $m/z=81$ are only visible when the dimer of the radical is formed, thus they are supposed to be formed in a subsequent dissociation of $m/z=110$. The ms-TPES of $m/z=110$ (fig. 4.2.4, middle panel) shows a broadened band without any vibrational activity. The molecular structure of the dimer is 2,2-octadiene, C₈H₁₄, shown in fig. 4.2.3, which has a computed IE of 8.94 eV (CBS-QB3) and is therefore in reasonable agreement with the experimentally observed IE_{ad} at 8.7 eV in the TPES. This value is assigned with the help of two linear functions, shown in green and red in the same graph, which can be used for assignment of the adiabatic ionization energy. The signal increases in the energy range from 8.63 eV to 8.7 eV with the same shallow slope (green dashed line), indicating that hot and sequence bands are contributing to the signal.

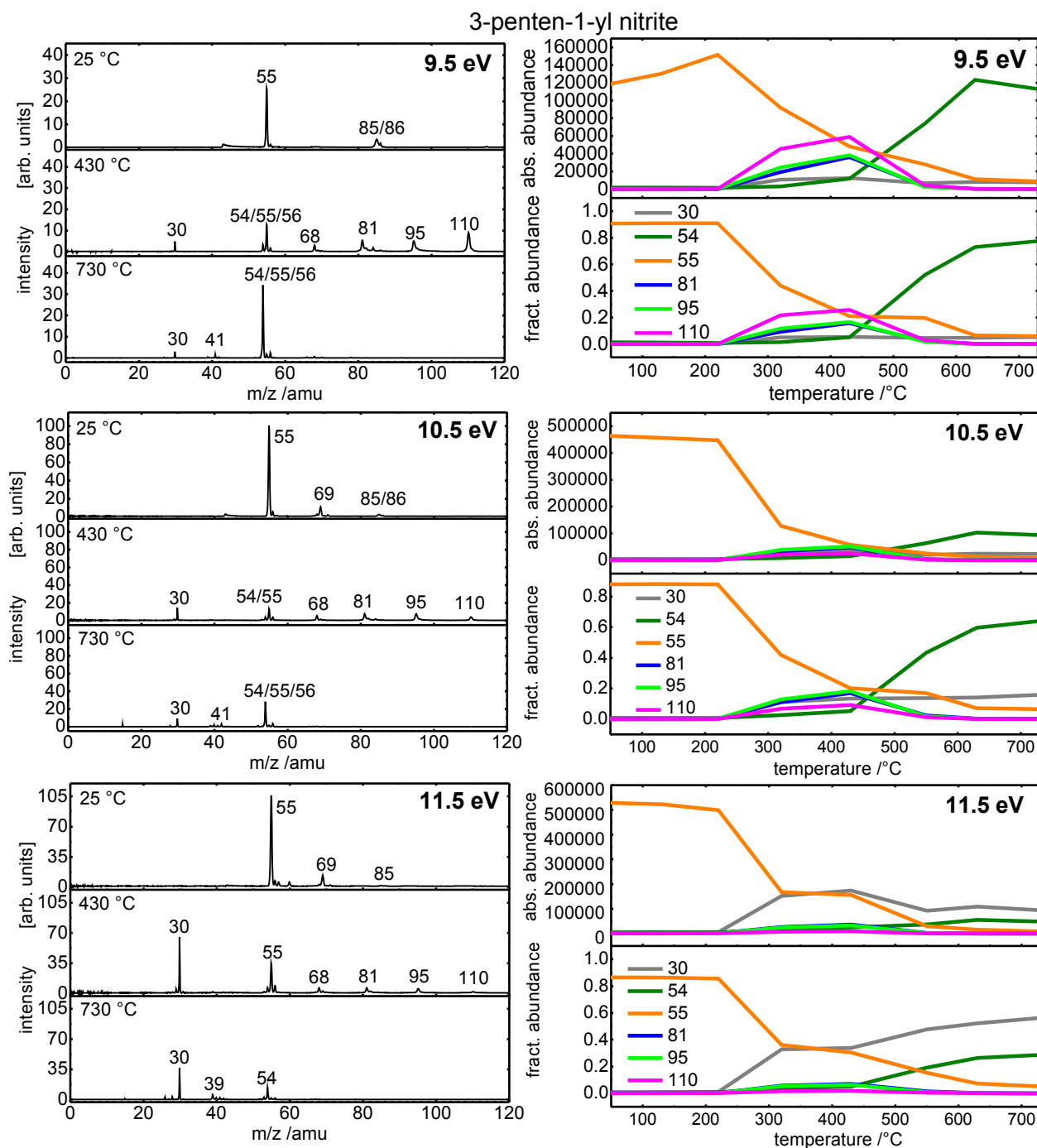


Figure 4.2.2: TOF mass spectra of 3-methyl-3-buten-1-yl nitrite for a temperature set from 25 °C to 730 °C at different photon energies (left). On the right breakdown diagrams with the absolute and relative abundances of the most prominent pyrolysis products versus the temperature ($T / ^\circ\text{C}$) at each photon energy are presented. The numbers denote the mass signals m/z in amu.

At 8.7 eV the slope increases and stays constant up to an energy of 8.9 eV (red dashed line), where the maximum TPE signal is found. The energy, at which the change in slopes is observed can be assigned to the IE_{ad} , at 8.7 eV. Considering the difficulty in finding the point where the slopes change, an error of ± 0.05 eV is reliable. The maximum signal at 8.9 eV can be assigned to the vertical ionization energy. In contrast to the ms-TPES of 110, the respective mass-selected signals of $m/z=95$ and $m/z=81$ show both a very gradual and unstructured shape (fig. 4.2.4, middle panel). Since $m/z=95$ and $m/z=81$ start to rise in the same energy range like $m/z=110$, they might be most likely formed in parallel fragmentation pathways in the DPI of $m/z=110$. However, the background photoelectron signal (not shown here) shows a similar development as the TPE signals of $m/z=95$ and $m/z=81$. Thus, another origin of the two mass signals might be further thermal decomposition of the dimer $m/z=110$. In either case, $m/z=95$, C₇H₁₁, corresponds to a methyl loss from the dimer and $m/z=81$, C₆H₉, to the loss of C₂H₅. Proposed molecular structures of C₇H₁₁ and C₆H₉ are shown in fig. 4.2.3. Here they are depicted as fragments of the DPI. At temperatures above 600 °C no more radicals $m/z=55$ are produced. Consequently, neither the dimer $m/z=110$ nor the respective fragments $m/z=95$ and $m/z=81$ are observed. At about 230 °C small amounts of $m/z=30$ are visible. The species has been identified as NO from the ms-TPES (fig. 4.2.4, lower panel). At 730 °C also $m/z=41$, corresponding to the allyl radical, C₃H₅, is formed. All identified and assumed pyrolysis products of 3-penten-1-yl nitrite are shown in fig. 4.2.3 (left row). At 10.5 eV the mass spectra of 3-penten-1-yl nitrite and their temperature depending development (fig. 4.2.2) look similar to those recorded at 9.5 eV. The radicals $m/z=55$ are formed up to 550 °C, which then turn preferably into the formation of $m/z=54$. The ratio of radical signal $m/z=55$ to dimer signal $m/z=110$ increases. Nevertheless, the amount of $m/z=95$ and $m/z=81$ is greater than the signal at $m/z=110$. This observation argues for the dissociative photoionization of the dimer to the masses 95 and 81. In addition, the signal of NO is larger than at 9.5 eV, too.

At 11.5 eV the signal of the 1-MA radicals at $m/z=55$ forms similarly with increasing temperature as at lower energies. However, $m/z=54$ is still produced at higher temperatures but $m/z=30$ dominates the signal intensities. The reversed intensities of $m/z=54$ and $m/z=30$ at 11.5 eV compared to 10.5 eV are probably originating from a second molecule that contributes to the signal at $m/z=30$. At 10.88 eV^[164] formaldehyde, CH₂O, is ionized and thus contributes to the increase in the signal of $m/z=30$. The dimer $m/z=110$ is only barely visible, like its fragments $m/z=95$ and $m/z=81$.

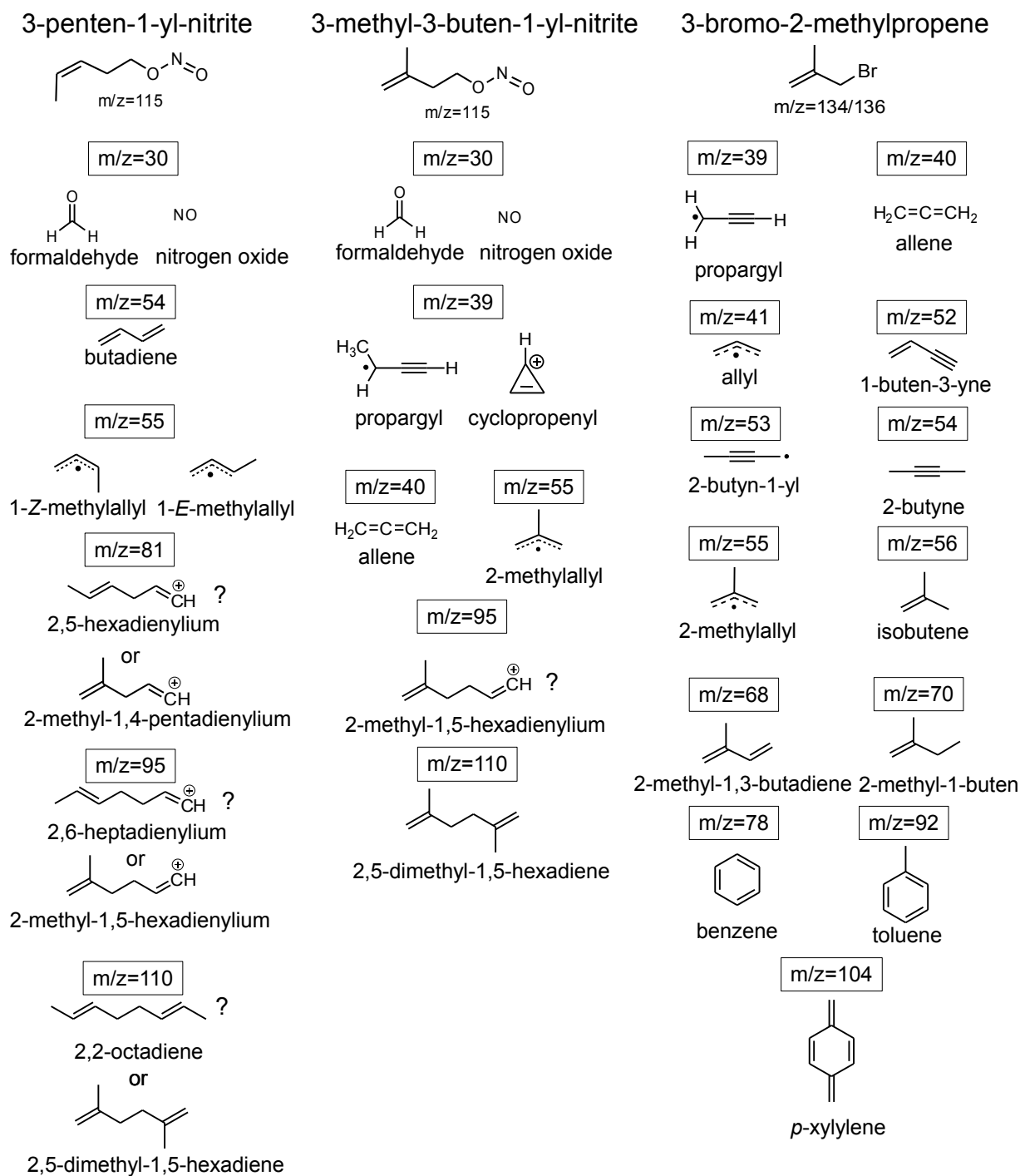


Figure 4.2.3: Pyrolysis products of the precursor molecules 3-penten-1-yl nitrite (left), 3-methyl-2-buten-1-yl nitrite (middle) and 3-bromo-2-methylpropen (right).

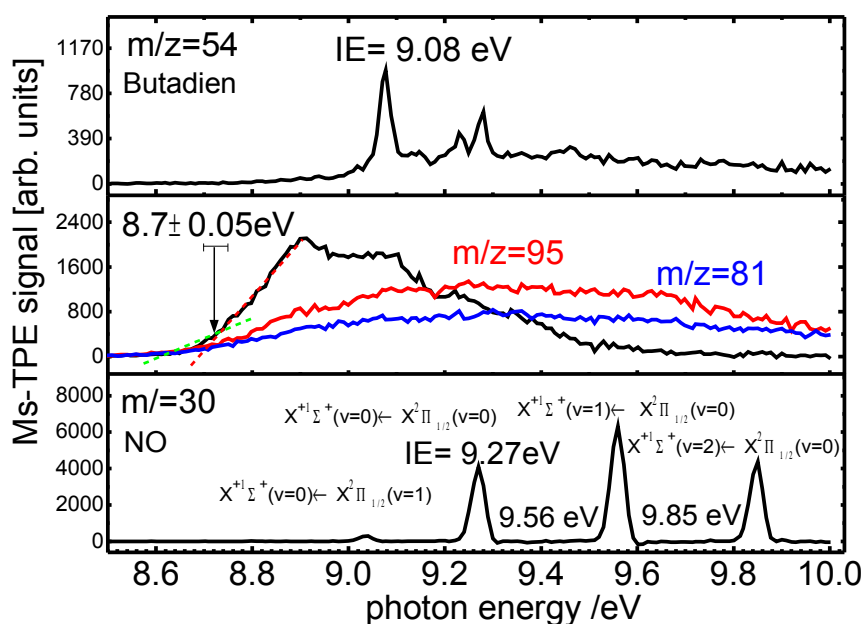


Figure 4.2.4: Ms-TPE spectra of the pyrolysis products $m/z=54$ (upper panel), $m/z=110$ (middle panel) and $m/z=30$ (lower panel) formed from 3-penten-1-yl nitrite. In addition, the ms-TPES of the mass signals $m/z=95$ and $m/z=81$ are shown in the lower panel.

The MS-TOF and breakdown graphs of 3-methyl-3-buten-1-yl nitrite recorded at different temperatures and photon energies are shown in fig. 4.2.5. The precursor for the 2-methylallyl radical is expected to show a similar behavior to 3-penten-1-yl upon temperature dependent decomposition. At 9.4 eV the formation of the 2-methylallyl radical at $m/z=55$ dominates the low temperature range. The signal $m/z=55$ then decreases around 400 °C and finally vanishes at a pyrolysis temperature of 800 °C. In contrast to 3-penten-1-yl nitrite, the dimer $m/z=110$ is already formed at around 100 °C. This might be caused by a higher concentration of the 2-MA radicals originating from a higher vapor pressure of the precursor or from inaccuracies in measuring the temperature. With higher concentrations of the radicals bimolecular reactions leading to the formation of the dimer is preferred.

The fragment $m/z=95$, formed from the DPI of the dimer is visible in small amounts and shows a similar development like the dimer signal. Fragment $m/z=81$ is not visible. When the radical signal $m/z=55$ decreases, the molecule at $m/z=39$ is preferably formed. Furthermore, above 500 °C NO ($m/z=30$) develops a large signal intensity. At 10.5 eV, when the signal of the 2-MA radical decreases at about 600 °C, the formation of the species at $m/z=40$ is dominating. All other mass signals $m/z=110$, $m/z=95$ and $m/z=30$ are rather small. At 11.5 eV the intensities of $m/z=30$ and $m/z=40$ are greater than the one of $m/z=55$. Only small amounts at $m/z=95$ are observed. They indicate that the dimer $m/z=110$ is nearly completely fragmented. All products formed from 3-methyl-3-buten-1-yl nitrite upon pyrolysis are shown in fig. 4.2.3 in the middle row. The TPE signals of the masses, visible in fig. 4.2.5, except $m/z=55$, are depicted in fig. 4.2.6.

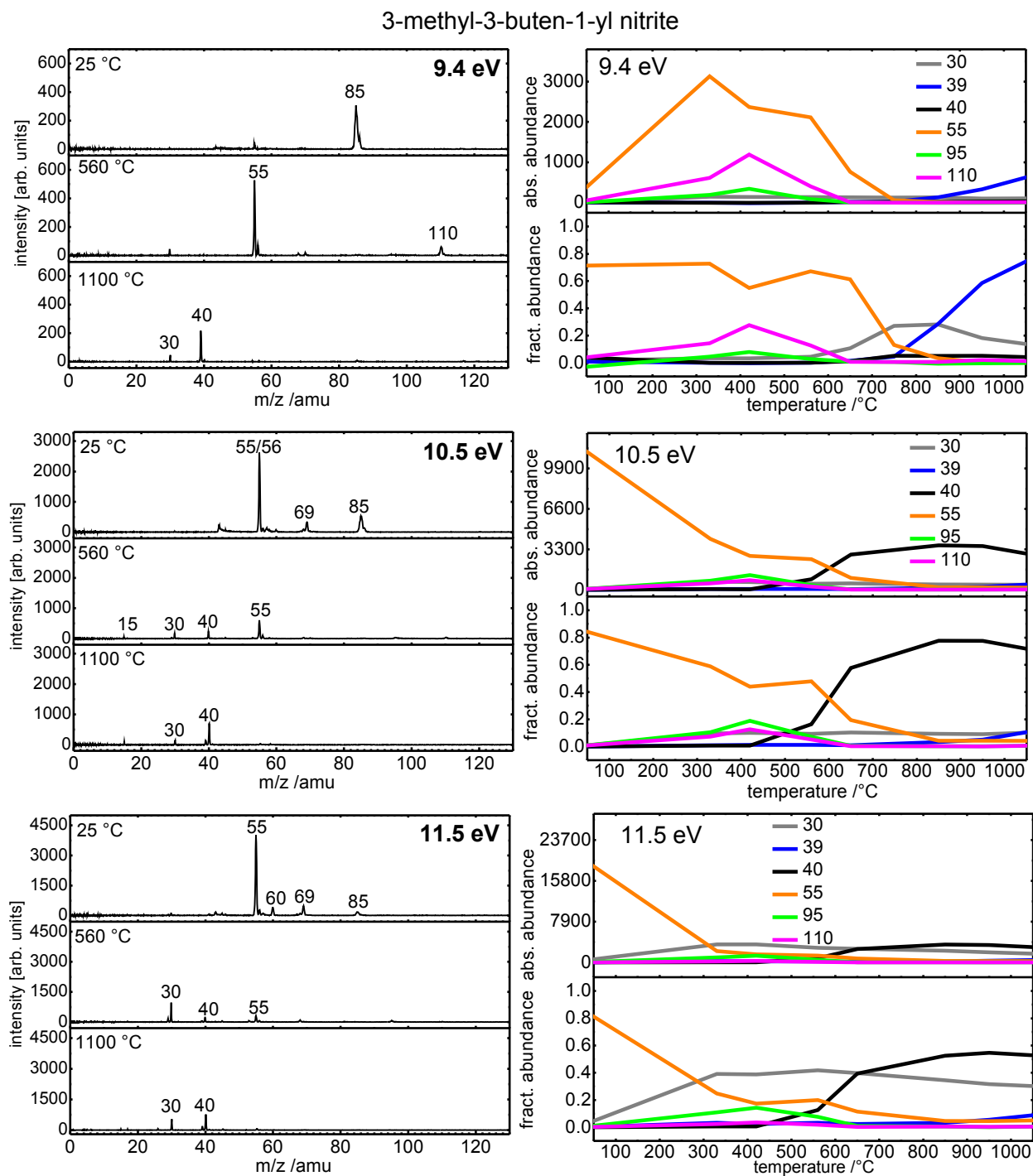


Figure 4.2.5: TOF mass spectra of 3-methyl-3-buten-1-yl nitrite for a temperature set from 25 °C to 1100 °C at different photon energies. In addition breakdown plots showing the absolute and relative abundances of the most prominent pyrolysis products versus the temperature (T / °C) are depicted for each photon energy. The pure numbers display the mass signals m/z in amu.

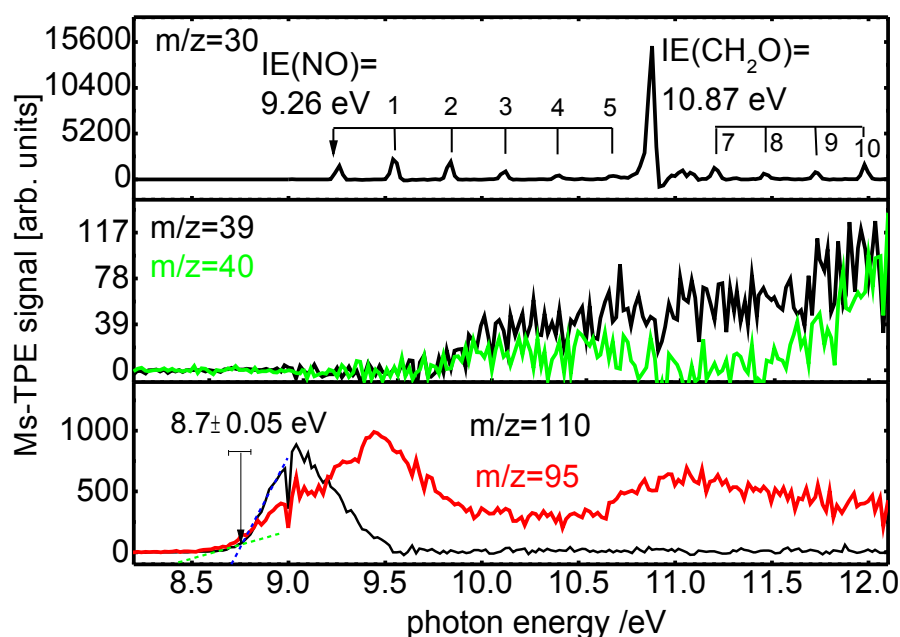


Figure 4.2.6: Ms-TPES of the products formed in the pyrolysis of 3-methyl-3-buten-1-yl nitrite. The dip in the spectrum at 9.0 eV seems to be an absorption in the gas filter.

$m/z=30$ is identified as NO and formaldehyde, which are both visible in the TPES in the first panel of fig. 4.2.6. Identification of the mass signals at $m/z=39$ and $m/z=40$ based on their TPE signal is not significant. The TPES of $m/z=39$ and $m/z=40$ are shown in the middle panel of fig. 4.2.6. Instead of a unique vibrational structure the signals of both masses show an unstructured slope at 9.7 eV, indicating that $m/z=39$ and $m/z=40$ are fragments formed in a DPI process. Thus, molecular structures of the fragments of $m/z=39$ and $m/z=40$ can only be supposed. The most probable structure for $m/z=39$ is the propargyl radical, C_3H_3 (see sec. 4.1). $m/z=40$, C_3H_4 , either corresponds to allene (IE=9.62 eV^[165]) or cyclopropene (IE=9.67 eV^[149]), whereas allene is the energetically preferred C_3H_4 isomer. The formation of propyne can be excluded, since propyne ionizes at 10.37 eV^[164] and $m/z=40$ is visible at 9.4 eV. The molecule with the mass signal $m/z=110$ is expected to be formed in a bimolecular reaction of the radical $m/z=55$, similar to $m/z=110$ obtained in the pyrolysis of 3-penten-1-yl nitrite. The ms-TPES of $m/z=110$, shown in fig. 4.2.6 in the lower panel, looks similar to the ms-TPES of $m/z=110$, shown in fig. 4.2.4. The dip in the spectrum at 9.0 eV is supposed to originate from an absorption resonance in the gas filter. Since different radical isomers of C_4H_7 are formed from the precursors 3-penten-1-yl nitrite and 3-methyl-3-buten-1-yl nitrite, at first glance also different dimer isomers, C_8H_{14} , are expected to be generated. The computed ionization energy of the dimer 2,2-octadiene (fig. 4.2.3, left column), corresponding to the head-to-head dimerization product of 1-MA, is 8.94 eV. The IE of the dimer 2,5-dimethyl-1,5-hexadiene, shown in the middle column is computed at 8.80 eV. This value deviates from the experiment by 0.1 ± 0.05 eV, while the computed IE of 2,2-octadiene at 8.94 eV has a difference of

0.24 ± 0.05 eV to the experimental value, when an error in the experimental IE_{ad} of 8.7 ± 0.05 eV is considered. Consequently, based on the computed IEs, none of the two different dimers can be excluded to be the one that is formed, since none of the computed IEs is clearly outside a reasonable range for the error between theory and experiment. However, since 2,5-dimethyl-1,5-hexadiene constitutes the head-to-head dimerization product of 2-MA and is about 120 meV more stable than the direct dimer of 1-MA, it seems as if the different C_4H_7 isomers form the same dimer 2,5-dimethyl-1,5-hexadiene, C_8H_{14} . In addition, the development of the ms-TPES of $m/z=95$ looks similar for both precursors (fig. 4.2.4, middle panel and fig. 4.2.6, lower panel), giving another indication for two similar fragments $m/z=95$. To conclude, the both dimers cannot reliably be identified to be identical. The TPES for both species is nearly similar, but the unstructured shape and the long onset does not permit to retrieve unique features of one of the two molecules 2,5-dimethyl-1,5-hexadiene and 2,2-octadiene.

To conclude from the pyrolysis scans, the most efficient pyrolysis conditions for the generation of 1-MA and 2-MA will be found at moderate temperatures around 450-500 °C.

B) 3-bromo-2-methylpropene

As a second precursor 3-bromo-2-methylpropene, C₄H₇Br, was used to generate the 2-MA radical. The mass spectra of 3-bromo-2-methylpropene at different energies and temperatures are shown in fig. 4.2.7. At 9.0 eV and 100 °C no mass signals are visible in the TOF-MS. This means, that neither the precursor 3-bromo-2-methylpropene nor pyrolysis products of the latter are ionized. At 400 °C sufficient thermal energy is available to produce the radical m/z=55. At higher pyrolysis temperatures (750 °C) plenty of pyrolysis product are formed. These are the mass signals at m/z=39, displaying the largest signal, and small mass signals at m/z=40, m/z=41, m/z=53, m/z=54 and m/z=55. Furthermore, small signals are observed at m/z=68, m/z=78, m/z=92 and m/z=104. At 10.0 eV the precursor m/z=134/136 is visible. With little pyrolysis power (100 °C) only small amounts of it are converted to m/z=55. The amount of radical production increases at 400 °C, whereas 3-bromo-2-methylpropene is still visible. At 750 °C m/z=134/136 has completely vanished, but also the radical signal m/z=55 has dramatically decreased. In contrast, all the pyrolysis products, already observed at 9.0 eV and 750 °C, are visible again. The mass signals m/z=39, m/z=40 and m/z=52, m/z=54 are the most intense ones. At 11.0 eV the dissociative photoionization (*vide infra*) has set in. The precursor signal at m/z=134/136 has nearly completely vanished, already at low pyrolysis energies. At higher pyrolysis powers, the most intense species is m/z=40. All other masses, observed before under rough pyrolysis conditions are visible, too.

Threshold photoelectron spectra (appendix, sec. 8) were recorded for most of the species. The spectra show, that the molecule at m/z=39 is the propargyl radical, C₃H₃. M/z=40 corresponds to allene, C₃H₄, and m/z=41, C₃H₅, is the allyl radical. One more radical is observed at m/z=53, 2-butyne-1-yl C₄H₅ (*vide supra*). M/z=54 corresponds to 2-butyne, the saturated analogous molecule of 2-butyne-1-yl. M/z=55 is the 2-methylallyl radical, C₄H₇, whose threshold photoelectron spectrum will be presented in sec. 4.2. The reactive 2-MA radical is supposed to abstract an H-atom in a bimolecular reaction at higher pyrolysis powers. Thus, m/z=56 is formed, which refers to the formation of isobutene. The mass signals at m/z=68 and m/z=70 correspond to the closed shell molecules 2-methyl-1,3-butadien and 2-methyl-1-buten. The mass signal at m/z=78 displays once more the combustion relevance of the propargyl radical, since m/z=78 corresponds to benzene. The latter is formed from two propargyl molecules. One further mass, not visible in the TOF-MS in fig. 4.2.7, but clearly identified by its TPE signal is HBr at m/z=80/82. M/z=92 corresponds to toluene, a product of a bimolecular reaction of the allyl radical. The mass signal at m/z=104 corresponds to the one further cyclic product, which is supposed to be formed in a bimolecular reaction in the pyrolysis. From the TPES of the species m/z=104 (shown in the appendix, 8) the IE at 7.85 eV^[166] was found, which identified the molecule as *p*-xylylene, C₈H₈. The detection of benzene, toluene and *p*-xylylene in the pyrolysis of 3-bromo-2-methylpropene reveals the relevance of the small hydrocarbon radicals, like allyl, propargyl methylallyl in the formation of aromatics

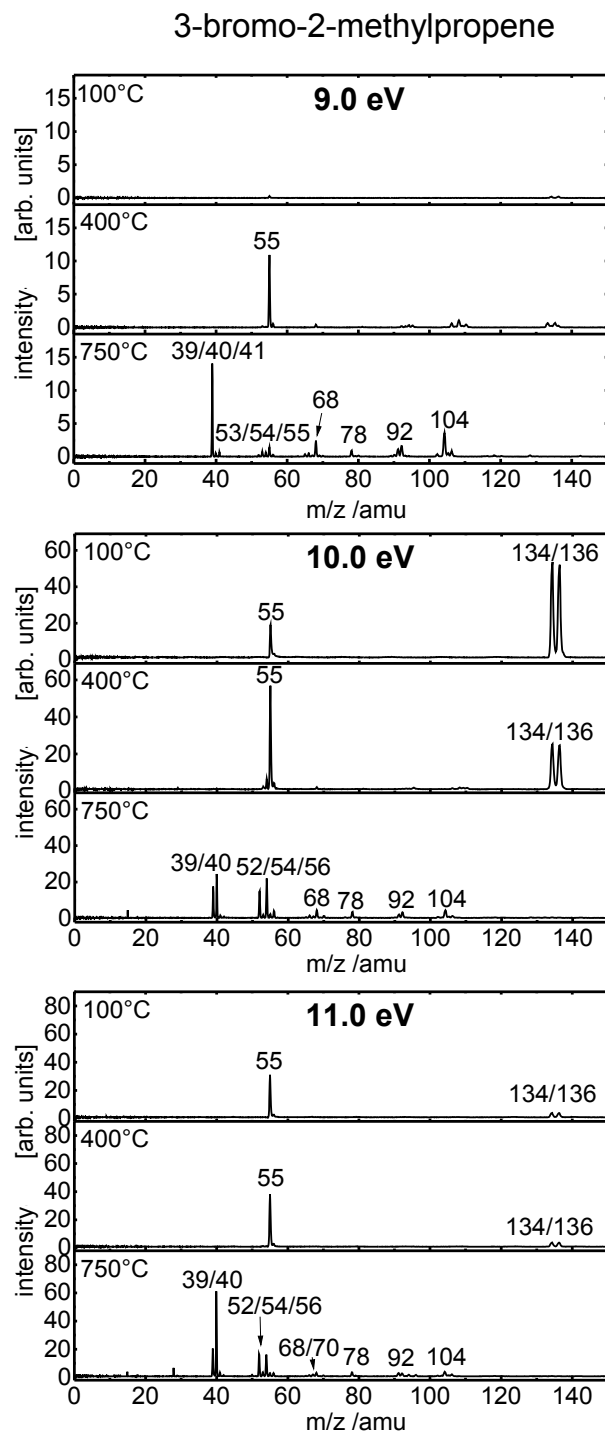


Figure 4.2.7: TOF mass spectra of 3-bromo-2-methylpropene at different photon energies and different temperatures. The numbers in the graphs denote the masses m/z /amu.

and further cyclic hydrocarbons. All pyrolysis products are displayed in figure 4.2.3. 3-bromo-2-methylpropene should also be pyrolyzed at medium temperatures (450 °C), to achieve a good ratio of 2-MA radical to precursor and to prevent the formation of further pyrolysis products.

Dissociative photoionization of the precursor molecules

A) 3-penten-1-yl nitrite and 3-methyl-3-buten-1-yl nitrite

As stated above, the two nitrite precursors are not visible in the MS-TOF spectra (fig. 4.2.2 and fig. 4.2.5, 25 °C). The reason can either be a large geometry change upon ionization and therefore small Franck-Condon factors. Another reason could be a dissociative ground state of the nitrite cations, as indicated by the computations. They predict the loss of NO in the cationic ground state for both 3-penten-1-yl nitrite and 3-methyl-3-buten-1-yl nitrite. Accordingly, the dissociative photoionization of both nitrite precursors cannot be evaluated exactly in a breakdown diagram. To assess at which energies the precursor produces the fragments $m/z=55$ can be retrieved from the onset of $m/z=55$ in the ms-TPES. The complete dissociative photoionization of the precursors 3-penten-1-yl nitrite and 3-methyl-3-buten-1-yl nitrite is shown in fig. 4.2.8. The scans were recorded without pyrolysis, with a step size of 20 meV and 50 meV and an acquisition time of 60 s per data point for 3-penten-1-yl nitrite and 3-methyl-3-buten-1-yl nitrite, respectively.

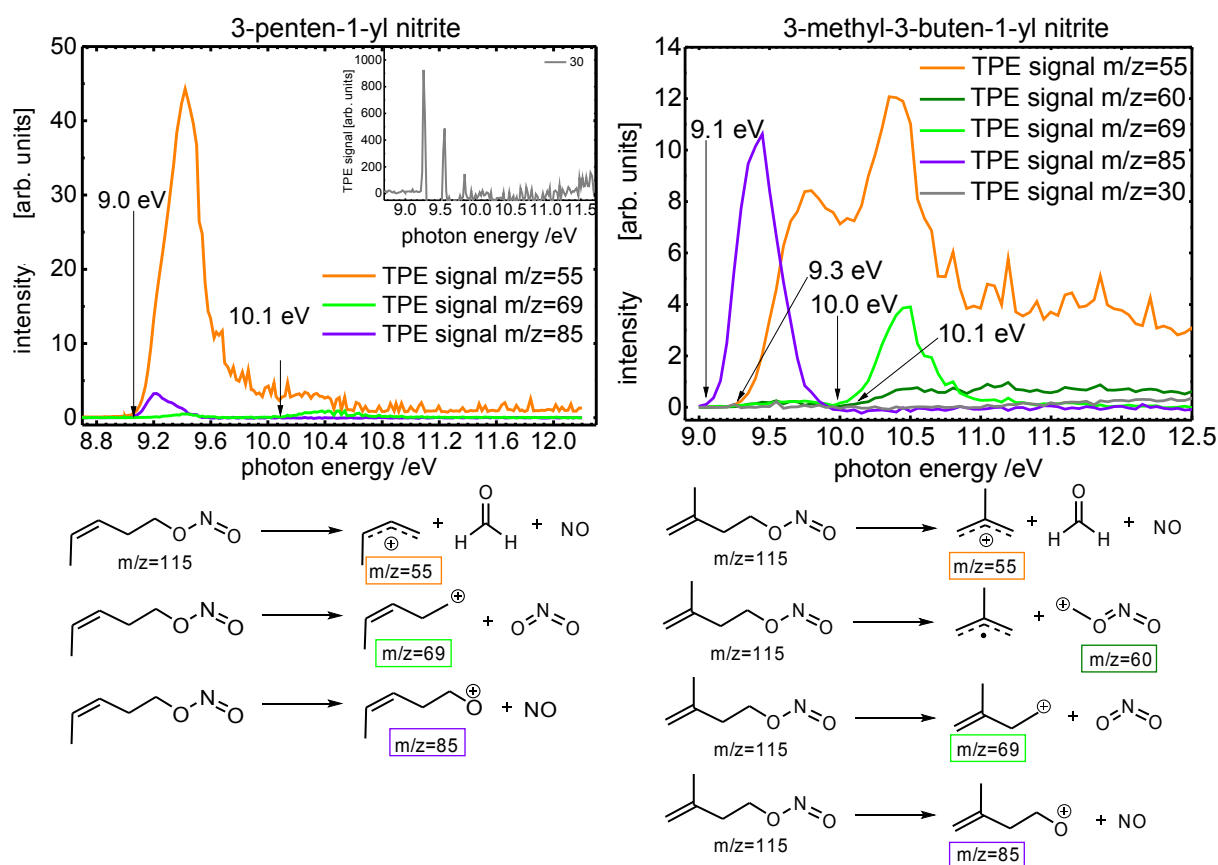


Figure 4.2.8: Dissociative photoionization of 3-penten-1-yl nitrite (left) and 3-methyl-3-buten-1-yl nitrite (right). Both precursors ($m/z=115$) are not visible. Below each graph the reaction for each fragment is depicted.

The TPE spectrum of 3-penten-1-yl nitrite is shown in fig. 4.2.8 on the left-hand side. In the mass spectra at 25 °C in fig. 4.2.2 the mass signals of the fragments $m/z=55$, $m/z=69$ and $m/z=85$ are detected. At 9.0 eV the threshold photoelectron signal of the fragment $m/z=55$ increases steeply, which turns into a steeply decreasing signal at 9.4 eV. $M/z=55$ corresponds to the 1-MA cations, which are formed with formaldehyde and NO as the neutral counterparts. The second parallel fragmentation channel is also observed to set in at 9.0 eV. In this pathway the pent-2-en-1-oxonium cation, $m/z=85$ is observed in small amounts. Even smaller is the intensity of the fragment $m/z=69$, the pent-2-en-1-yl-ium, which is observed at around 10.1 eV. A tiny mass signal at $m/z=30$, which is not visible in the TOF-MS in fig. 4.2.2, is additionally observed. Interestingly, the fragment $m/z=30$ is not formed in the DPI. This is indicated by the threshold photoelectron spectrum, depicted in the inset of the left graph in fig. 4.2.8. The inset shows the TPES of NO. Thus, the precursor already decomposes as a neutral molecule and loses NO, which gives another explanation for the precursor's absence in the mass spectra. The described DPI channels are visualized below the left graph in fig. 4.2.8.

The mass spectra of 3-methyl-3-buten-1-yl nitrite at 25 °C (fig. 4.2.5) show similar mass signals like 3-penten-1-yl nitrite: no precursor $m/z=115$ and signals for the fragments at $m/z=55$, $m/z=69$ and $m/z=85$. Furthermore, a fragment with $m/z=60$ is formed. The ms-TPES of the fragmentation is shown in figure 4.2.8 on the right-hand side. The first channel of $m/z=85$ comes up at 9.1 eV. This fragment corresponds to the 2-methyl-1-buten-oxonium ion, produced by the loss of NO. At around 9.3 eV the fragment of $m/z=55$ arises most likely from the sequential dissociation of $m/z=85$. By around 10.0 eV and 10.1 eV the fragments $m/z=69$ and $m/z=60$ appear. $M/z=60$ most probable displays the cation ONOC_3H_7 and $m/z=69$ is 2-methyl-1-buten-yl-ium formed by the loss of NO_2 . The fragmentation pathways are in addition shown below the TPE spectra in fig. 4.2.8 on the right-hand side. From the two scans the DPI onsets of the methylallyl cations can be deduced to 9 eV and 9.3 eV for 1-MA and 2-MA, respectively. Even when a red shifted dissociation onset of 0.3-0.5 eV for medium amounts of pyrolysis energies is taken into account, the evaluation of the TPE spectra of the 1-MA and the 2-MA radicals should not be influenced by the DPI of the precursors below ≈ 8.5 eV.

B) 3-bromo-2-methylpropene

The precursor 3-bromo-2-methylpropene was additionally investigated without pyrolysis. Three TOF mass spectra, recorded without pyrolysis at 9.80 eV, 11.0 eV and 12.2 eV are depicted in figure 4.2.9. They show that the bromide fragments in one single pathway to the fragment $m/z=55$ up to an internal energy of 12.2 eV. The fragment formed with $m/z=55$ is the 2-MA cation.

To evaluate the appearance energy of 2-methylallyl cation, a scan, covering the ionization and the dissociation onset of 3-bromo-2-methylpropene was recorded with a step size of 15 meV and an

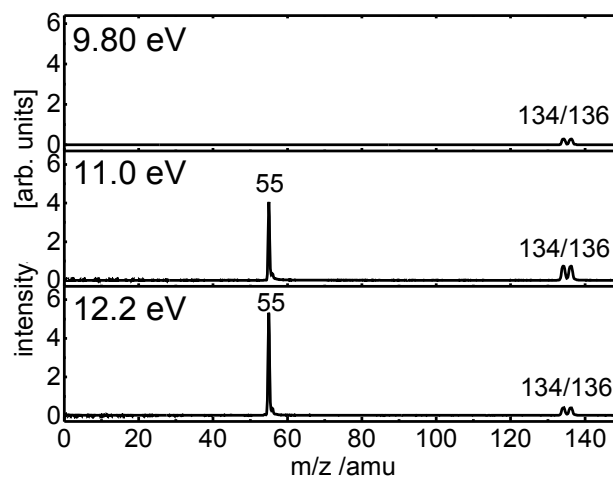
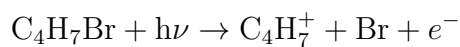


Figure 4.2.9: Mass spectra of 3-bromo-2-propene without pyrolysis at 9.80 eV (upper panel), 11.0 eV and 12.2 eV (lower panel).

acquisition time of 150 s per data point. The TPE spectra of all masses (black), of the parent $m/z=134/136$ (red) and the fragment $m/z=55$ (blue) are shown in fig.4.2.10 in the graph on the left hand side. The TPE signal sets in at 9.4 eV and a first band is visible around 9.52 eV. Thus, the ionization energy of 3-bromo-2-methylpropene is assigned to 9.45 eV. This value is in very good agreement with the computed value at 9.47 eV. However, as can be deduced from the spectrum a large error bar of ± 0.05 eV is estimated for the value of the IE_{ad} based on the procedure of assignment (described in fig. 4.2.4, *vide supra*)

The spectrum shows some vibrational structure in two further bands and supposedly reaches a first excited state in the cation around 10.2 eV. The ms-TPE signal of $m/z=134/136$ (red) vanishes and indicates the dissociation of the molecule. The next intense transition, visible in the TPES of all masses at 10.5 eV, displays the transition to a further excited state in the parent cation which crosses a potential surface of C₄H₇⁺. Thus, the precursor fragments to $m/z=55$ according to the following equation:



The fractional abundance of the mass-selected TPE signals of the parent and the daughter fragment is depicted in the breakdown diagram in fig. 4.2.10 on the right-hand side. The relative signal of the parent starts to decrease at 10 eV and reaches zero around 10.4 eV. Since the dissociation is fast in the time scale of the experiment, which can be deduced from the symmetric $m/z=55$ fragment peaks in the TOF mass spectra (fig. 4.2.9), the shape of the breakdown diagram depends only on the thermal energy distribution of the neutral parent 3-bromo-2-methylpropene. Thus, the breakdown diagram can be fitted according to eq. 2.4.20 (sec. 2.4.5).

The appearance energy of the 2-MA cation is determined to 10.38 eV at 17 °C. According to eq. 2.4.8 (sec. 2.4.2), the AE_{0K} can be computed with quantum chemistry from the sum of the dissociation

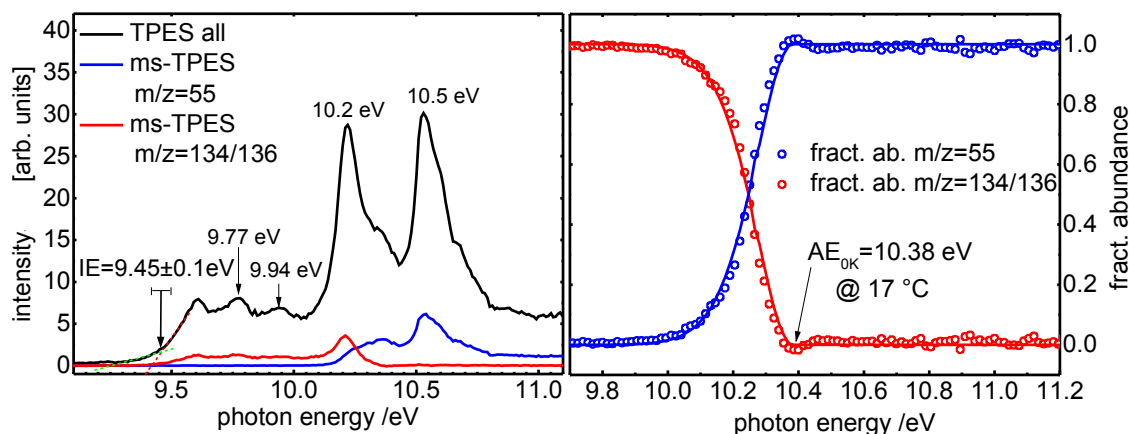


Figure 4.2.10: Non mass-selected and mass-selected TPE spectra of $m/z=134/136$ and $m/z=55$ (left) and the corresponding breakdown diagram of 3-bromo-2-methyl-propene (right).

products and the neutral parent molecule:

$$AE_{0K} = \Delta H_f^0(C_4H_7^+) + \Delta H_f^0(Br) - \Delta H_f^0(C_4H_7Br).$$

The derived value is 10.74 eV on the CBS-QB3 level, obviously higher than the experimental one. To conclude from the determined appearance energy, the contribution of the fragment $m/z=55$ from the precursor's DPI to the radical signal can be excluded up to energies of ≈ 9.7 eV, even when the internal energy of the parent is taken into account.

Some further information can be retrieved from the breakdown diagram. Since the the loss of bromine does not have a reverse barrier, the bond dissociation energy in the cation of 3-bromo-2-methylpropene can be retrieved. Scheme 2.3.2 in sec. 2.3.1 illustrates how this can be done. The ΔBDE of $(C-Br)^+$ in $C_4H_7Br^+$ is calculated according :

$$\begin{aligned} \Delta BDE(C_4H_7 - Br)^+ &= \Delta H_f^0(C_4H_7^+) + \Delta H_f^0(Br) - \Delta H_f^0(C_4H_7Br^+) \\ &= AE_{0K}(C_4H_7^+) - IE(C_4H_7Br). \end{aligned}$$

Thus, with the obtained IE of 9.45 eV and the retrieved AE_{0K} at 10.38 eV the bond dissociation energy of the C-Br bond in the cation is determined to 0.98 eV (95 kJ/mol). Computations yield a value of 1.27 eV (122.5 kJ/mol) for the C-Br bond in the cation. Unfortunately, the agreement between theory and experiment is non satisfying for the appearance energy and the bond dissociation energy.

TPES of 1-*E*-methylallyl and 1-*Z*-methylallyl and 2-methylallyl

The precursor 3-penten-1-yl nitrite used to generate 1-MA seems to preferentially form the *Z*-conformation. However, the absolute energy difference between the *E*- and *Z*-conformations of the formed 1-MA radicals is marginal, the *E*-conformer is 3 meV (0.3 kJ/mol) lower in energy than the *Z*-conformer and the rotational barrier for isomerization is only 0.67 eV (65 kJ/mol). Thus, with a pyrolysis temperature of 450 °C, both the *E*- and the *Z*-conformer are formed, as it has been observed before.^[158] The mass-selected TPE spectrum (black line) of the two 1-MA radicals is depicted in figure 4.2.11 and fig. 4.2.12. At around 7.25 eV the TPE signal starts to rise, reaching the first peak in the spectrum at 7.48 eV. This peak is assigned to the adiabatic ionization energy of 1-*E*-methylallyl, based on the best agreement with the Franck-Condon simulation. The error of this value is estimated to ± 0.02 eV. The computed IE for 1-*E*-methylallyl is 7.54 eV, 0.11 eV lower than for 1-*Z*-methylallyl (7.65 eV). A comparison of the experimental and computed IEs is given in table 4.1.

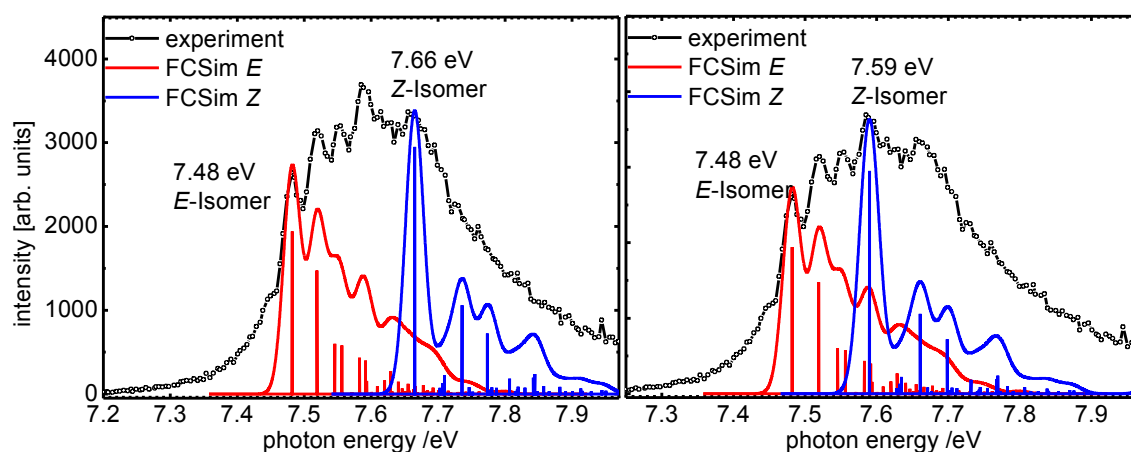


Figure 4.2.11: Franck-Condon simulations of 1-*E*- and 1-*Z*-methylallyl differently superimposed with the experiment. Left: IE of 1-*Z*-MA at 7.48 eV and IE of 1-*E*-MA determined to 7.66 eV, Right: IE of 1-*Z*-MA at 7.48 eV and IE of 1-*E*-MA determined to 7.59 eV.

Three further peaks are observed, showing increasingly higher intensities. The most intense peak in the spectrum appears at 7.59 eV. In the previous reported conventional PES, the first peak was observed at 7.49 eV and the most intense one at 7.67 eV.^[158] Since in this work the contribution of the two different isomers was not considered, these peaks were assigned to the adiabatic and the vertical IE, respectively. Fig. 4.2.11 shows two different simulations of the spectrum, assuming different IEs for 1-*Z*-MA. On the left-hand side, the IE of 1-*Z*-MA is set to 7.66 eV and in the graph on the right-hand side to 7.59 eV, whereas the IE_{ad} of the *E*-isomer is retained at 7.48 eV in both cases. When the 0-0 transition of the *Z*-isomer is shifted to 7.59 eV, a better agreement between experiment and simulation is achieved. Nevertheless, the agreement of simulation and experiment up to 8 eV is not entirely satisfactory in either convolution shown in fig. 4.2.11. The high intensity

of the TPE signal in this energy range might be attributed to activity in the torsional modes of the CH_3 groups. The participation of autoionizing states can be neglected since the conventional PES study shows very similar relative signal levels and shape. In addition no excited states on the singlet and triplet surface were found in the same energy range.

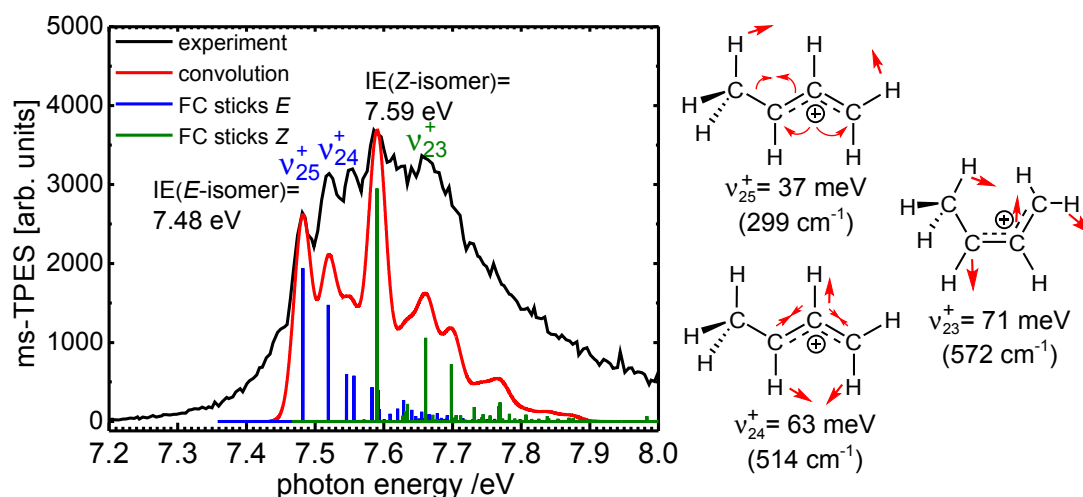


Figure 4.2.12: Ms-TPEs of 1-*E*-MA and 1-*Z*-MA. The blue FC sticks represent 1-*E*-methylallyl and the green simulation originates from the respective *Z*-isomer. The convolution of the combined stick spectra was done with 25 meV fwhm.

The peak at 7.59 eV is assigned to the IE_{ad} of 1-*Z*-MA, based on the best match with the combined FC-simulation of the two isomers, depicted in fig. 4.2.12. The error of IE_{ad} is again assumed to be ± 0.02 eV. The relative ratio of the presence of two isomers cannot be concluded easily from the weight of the two simulations, which was chosen 1:1.5 of 1-*E*-MA:1-*Z*-MA. This is why the Franck-Condon factors only relate on the intensity of one transition, but not on the entire ionization probability. The ionization probability is given by the ionization cross section of a molecule. Thus, when assessing total or relative amounts of ionization processes the total ionization cross sections have to be known. The peaks at 7.52 eV (+40 meV) and 7.55 eV (+60 meV) correspond to the modes ν_{25}^+ (computed 37 meV / 299 cm^{-1}) and ν_{24}^+ (computed 63 meV / 514 cm^{-1}) of the *E*-isomer. ν_{25}^+ is assigned to the C(3)-C(1)-C(5) bending motion and ν_{24}^+ to the C-C stretching vibration (bonds C(3)-C(1) and C(1)-C(5)). For labeling of atoms see fig. 4.2.1. The band around +70 meV, with respect to the IE_{ad} of the *Z*-isomer at 7.66 eV reveals the mode ν_{23}^+ (computed 71 meV / 572 cm^{-1}) of 1-*Z*-MA, a wagging mode of C(3) and C(1). The change in geometry upon ionization is not very distinct. Since the HOMO of both conformers is mainly localized on the allyl-moiety (vide infra), the active vibrations upon one-photon ionization and the geometry changes are concentrated on the C(3)-C(1)-C(5) carbon chain. The most significant geometry change in the *E*-conformer is found in the C(3)-C(1)-C(5) angle, which decreases by 6°. The respective angle in the *Z*-conformer

decreases by 5°. In addition, the C(3)-C(8) bond decreases in both conformers by 4 pm.

Figure 4.2.13 shows the ms-TPES of 2-MA (black) in the range from 7.7 eV to 12.0 eV. The Franck-Condon simulation of the transitions to the singlet cation X⁺ ¹A₁ (red) and to the triplet cation A⁺ ³A (blue) are also displayed in the graph. A first peak is observed at 7.83 eV, followed by the most intense peak in the spectrum at 7.88 eV, which is assigned to the adiabatic ionization energy of 2-MA. This value includes an error of ±0.01 eV and matches the computed IE of 7.93 eV quite well.

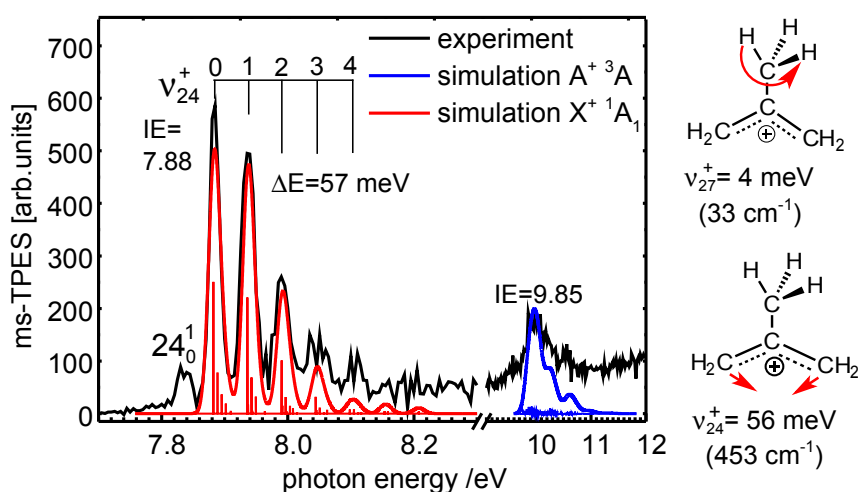


Figure 4.2.13: Ms-TPES of 2-MA. The red line reveals the FC simulation for the transition X⁺ ¹A₁ ← X ²A₂ to the singlet cation and the blue simulation represents the transition A⁺ ³A ← X ²A₂ to the triplet cation.

The vibrational progression with a spacing of 57 meV is assigned to the totally symmetric bending mode ν_{24}^+ (computed 56 meV / 453 cm⁻¹). The ν_{24}^+ is broadened by a combination with even quanta of the methyl torsion ν_{27}^+ that is computed with a wavenumber of 33 cm⁻¹. The peak at 7.83 eV is assigned to the hot band 24₀¹ with a computed energy of 484 cm⁻¹ for the respective bending mode in the radical. The hot band has a fwhm of 30 meV, 10 meV larger than the 0-0 transition. Thus, the hot band is also significantly broadened by the rotational activity of the methyl group in the radical or from contribution of hot and sequence bands. However, the simulation does not include the vibrational activity in the neutral molecule. The band at 9.85 eV is assigned to the transition to the triplet cation. Its shape is represented quite well by the FC simulation. In the ZEKE-spectra of Gasser et al.^[69] a value of 450 cm⁻¹ for the ν_{24}^+ vibration was observed. However, no ionization energy was obtained for 2-MA, but a value of 63530 cm⁻¹, corresponding to 7.877 eV, was reported for the d⁷-isotopologue. This value is very similar to the 7.88 eV obtained for 2-MA in the present experiments. In addition, the excitation of two further non totally symmetric modes in the 2-MA cation were observed up to 64700 cm⁻¹ (8.02 eV). Since a [1+1'] scheme via intermediate

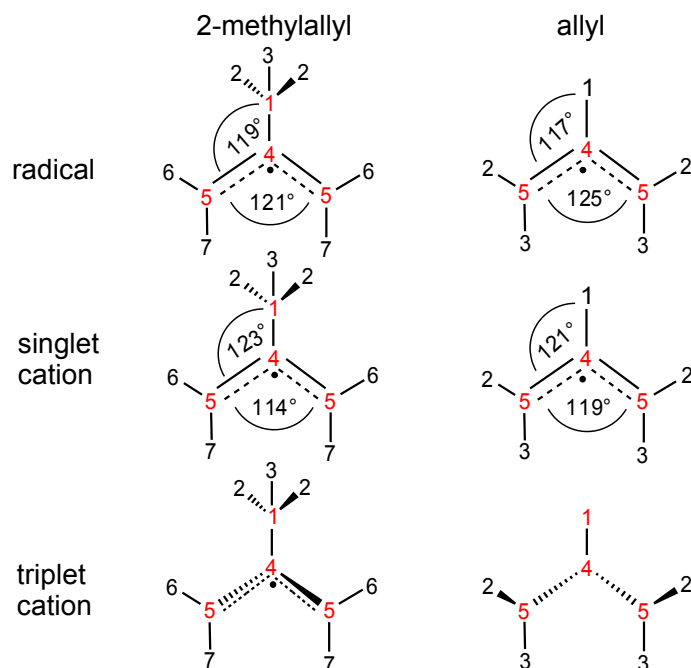


Figure 4.2.14: Geometries of allyl and methylallyl.

Rydberg-states was employed, only the fundamental of the C-C-C bending mode was observed in the ZEKE-spectra.

The geometry does also not change significantly for 2-MA upon ionization to the singlet cation. Here, the most pronounced difference between the cation and the radical is observed in the two angles C(5)-C(4)-C(5) and C(5)-C(4)-C(1), which decrease by 7° and increase by 4° , respectively (see fig. 4.2.1 for atom labels). The bond lengths are more or less retained. In contrast, the geometry obtained for the triplet cation changes significantly in comparison to the neutral molecule and to the singlet cation. The symmetry is reduced from C_{2v} in the neutral and in the singlet cation to C_2 in the triplet cation. The CH_2 moieties move out of the molecular plane, leading to a decrease of the dihedral angle $d(\text{H}(3)\text{-C}(1)\text{-C}(4)\text{-C}(5))$ by about 65° . In addition, the bond C(4)-C(5) increases by 5 pm and C(1)-C(4) decreases by 5 pm. The change in angles is not very pronounced.

In comparison, the C(5)-C(4)-C(5) angle decreases in the singlet cation in allyl by 6° , slightly smaller than for 2-MA. The angle C(5)-C(4)-H(1) increases by 4° , which is the same difference obtained for 2-MA. The changes in bond lengths of allyl are negligibly small as for 2-methylallyl. Upon the transition to the triplet cation, the symmetry in allyl is reduced from C_{2v} to C_s . The three C-atoms are moving out of the molecule's plane and the two pairs of H-atoms point in the same direction.

The decrease of the angle C(5)-C(4)-C(5) and the respective increase of the angle C(5)-C(4)-C(1)/H(1) is in the same range for both molecules upon ionization to the singlet cation, which leads to the response in the C(5)-C(4)-C(5) bending motion, visible in the TPE spectra of both

molecules. Furthermore, the angle of the carbon chain in allyl and its singlet cation is more widened compared to the methylated radical and its respective cation. From this can be inferred that the methyl group reveals a greater steric demand compared to the H-atom leading to the reduction in the C(5)-C(4)-C(5) angle in 2-methylallyl.

With the IE of 2-MA the respective ΔBDE of (C-Br) in the neutral precursor molecule C₄H₇Br can be calculated from the following equation:

$$\begin{aligned}\Delta BDE(C_4H_7 - Br) &= \Delta H_f^0(C_4H_7) + \Delta H_f^0(Br) - \Delta H_f^0(C_4H_7Br) \\ &= AE_{0K}(C_4H_7^+) - IE(C_4H_7).\end{aligned}$$

Since the adiabatic ionization energy of the 2-MA radical is obtained ($IE_{ad}=7.88$ eV) and the appearance energy is observed at 10.38 eV, the C-Br bond dissociation energy in the neutral molecule is determined to be 2.5 eV (241 kJ/mol). The respective computed value for the C-Br bond dissociation energy in the neutral molecule is found at 2.81 eV (271 kJ/mol). The large discrepancy between the computed and the experimentally derived value shows again a non-satisfying agreement between theory and experiment. Of course, the error in the computed bond dissociation energies is larger compared to the error of the computed ionization energy and the appearance energy, since it includes the error propagation of the latter two. The discrepancy between the experimental values for the neutral (2.5 eV) and the cation (0.98 eV) implies that the bonding order decreases significantly upon ionization while the C-Br bond length shortens by 2 pm. This effect can be explained by the relative energies of the formed products. The dissociation on the neutral potential energy surface results in two radicals (bromine and C₄H₇), whereas on the ion surface a closed shell ion and a radical are generated. The latter process needs less energy.

At the end of this section the ms-TPES of allyl is shown for comparison. The spectrum was recorded with a step size of 5 meV and an acquisition time of 300 s per datapoint and is depicted in fig. 4.2.15. The spectrum, obtained with the TPEPICO technique, has already been reported.^[167,168] Allyl and 2-methylallyl transform according to C_{2v} symmetry. Thus, the TPES of 2-MA appears very similar to the one of allyl. The C-C-C bending mode was previously reported to be 52 meV (420 cm⁻¹) and is observed at 440 cm⁻¹ in the present experiments for allyl. This bending motion is as expected very close in energy to the respective bending motion in 2-MA, observed at 460 cm⁻¹. Compared to allyl, even the methyl torsion does not significantly broaden the vibrational peaks in the spectrum of 2-MA. The 1-MA conformers cannot likely be compared to the spectrum of allyl because the 1-MA isomer's spectra interfere. In addition, they transform according to C_s symmetry, which allows for diverse vibrational activity upon one-photon excitation. A further band in the TPES of allyl starts to rise at 9 eV and has a maximum signal at 9.9 eV. This band is supposed to be the transition to the triplet cation A⁺ ³A". However, computations predict a value at 10.23 eV with B3LYP/6-311g(d,p)

and at 10.64 eV with the CBS-QB3 method. Since this is a significant deviation between the experimental finding and the CBS-QB3 value, in addition the excitation energy to the first excited singlet cationic state was computed with TD-DFT to +5 eV above the ionization threshold and can therefore be excluded to contribute to this band.

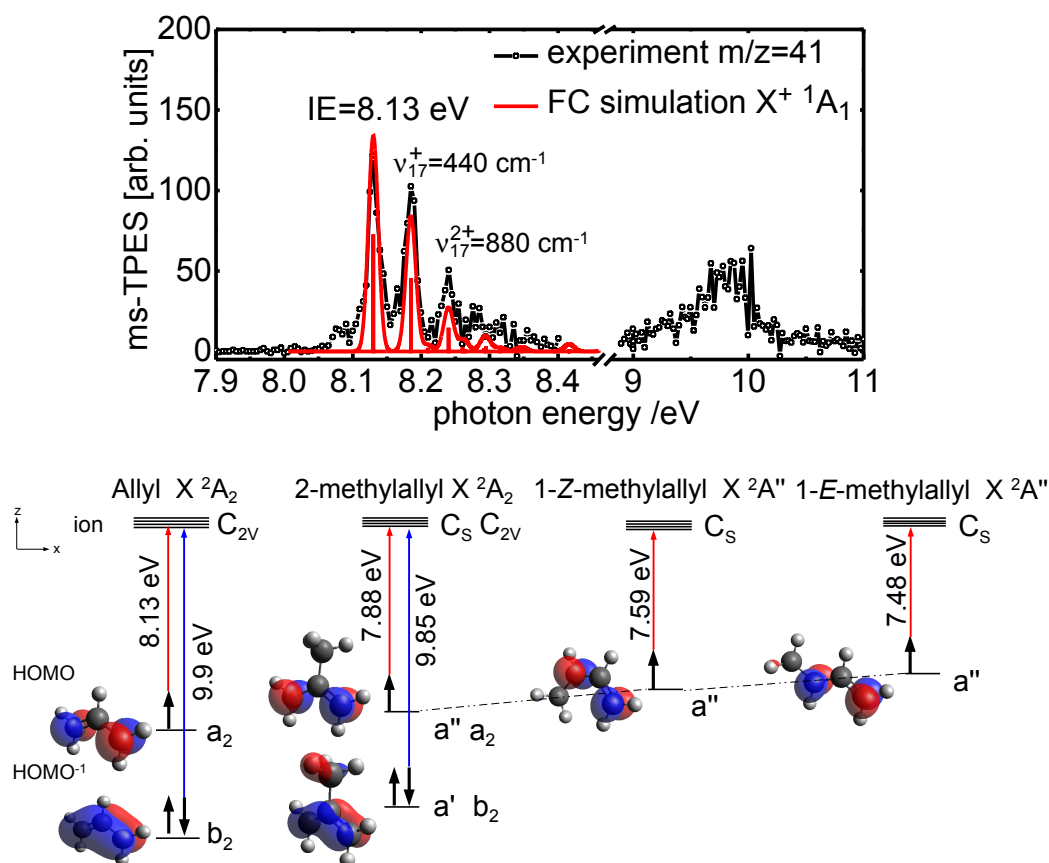


Figure 4.2.15: Ms-TPES of the allyl radical and the frontier molecular orbitals of the 1-methylallyl isomers, 2-methylallyl radical compared to the allyl radical. The computed energies for the ionization to the singlet cations and the triplet cations are given along the red and blue arrows.

In comparison to the methylallyl isomers, allyl has the highest IE at 8.13 eV and the energetically most stabilized HOMO. 2-MA owes the highest IE_{ad} among the methylated allyl isomers. Thus, the SOMO energies increase in the order 2-MA < 1-Z-MA < 1-E-MA (fig. 4.2.15), assuming the validity of Koopman's theorem.^[169] Even from the Valence-Bond (VB) structure can be inferred that the radical center of the allyl radical is localized at one of the terminal atoms C(5), as represented by the conjugated structures in fig. 4.2.16, a.

The additional methyl group attached to the radical center C(5) of allyl forms 1-methylallyl and causes hyperconjugation between the σ_{C-H} bonds of the methyl group and the $2p_z$ orbital of allyl (fig. 4.2.16, b). This means further electron density is pushed into the single occupied molecular

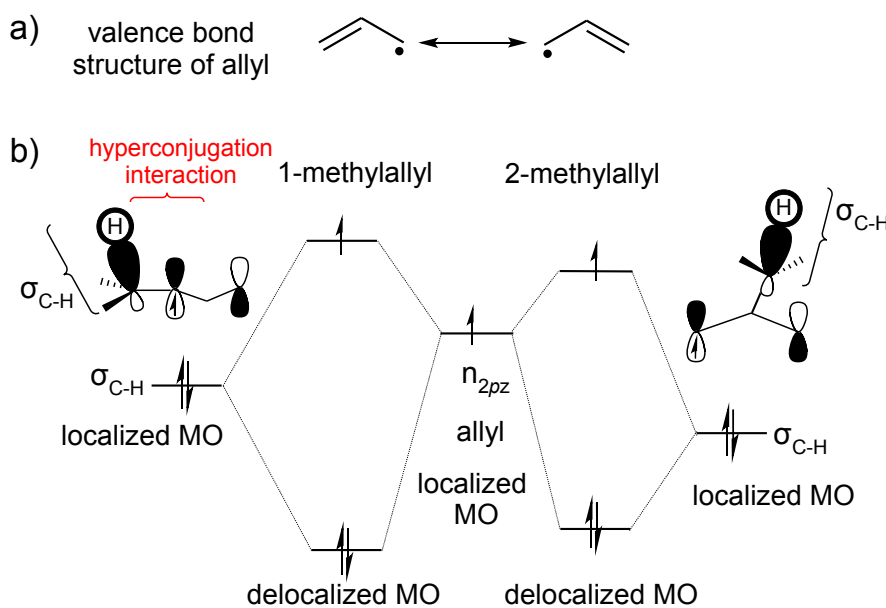


Figure 4.2.16: a) Valence bond structures of allyl. b) Molecular orbital schemes of 1-methylallyl and 2-methylallyl. Hyperconjugation between the radical center in allyl and the σ_{C-H} bond of the methyl group attached in the 1- position leads to the increase in the resulting SOMO of the 1-methylallyl radical.

orbital (SOMO) of 1-methylallyl, leading to the respective increase in the energy of the latter. In 2-methylallyl the CH₃ group is connected to the central C(4) atom instead to the formal radical center C(5). Consequently, the destabilization is less pronounced in 2-MA than in 1-MA, as it is predicted by the order of HOMO energies, presented in fig. 4.2.15.

Dissociative photoionization of 2-methylallyl

It has already been explained in sec. 2.3.1 and shown for 3-bromo-2-methylpropene (sec. 4.2), that the DPI of a molecule can be used to retrieve thermochemical data like bond dissociation energies. This is especially interesting for radicals, since it is very challenging to get access to this information for selectively produced radicals. The threshold photoelectron spectra of 1-MA (*vide supra*) imply that the investigation of the dissociation of the two conformers 1-MA might be problematic. The two conformers are not only indistinguishable in the mass signal, but also quite similar and interfering in their TPE signals. Thus, the investigation of their dissociations would not be unambiguous. For this reason, only the DPI of 2-MA was intended to be studied in detail. The possible fragmentation pathways of 2-MA comprise the loss of an H atom, leading to a variety of product fragments $C_4H_6^+$. Furthermore, 2-MA can eliminate H_2 and in addition loose CH_3 by forming $C_3H_4^+$ isomers. To retrieve BDEs, only direct fragmentation without rearrangements and reverse reaction barriers upon dissociation have to occur. This means that the loss of CH_3 will provide access to the dissociation energy of the $C_{allyl}-CH_3$ bond. A survey of the potential $C_3H_4^+$ fragments that might be formed by the loss of CH_3 are presented in fig. 4.2.17. Also the loss of an H-atom is supposed to occur in a direct way without a dissociation barrier. But since several H-atoms are present in the molecule, such an experiment is again insufficient to retrieve a BDE. This problem can be circumvented when using deuterated isotopologues. The loss of H_2 inevitably includes rearrangement reactions to form a stable fragment. The main challenge to observe 2-MA's DPI originates from the fact that it is not exclusively formed from neither precursor. It has been deduced from the pyrolysis scans of the precursors 3-methyl-3-buten-1-yl nitrite (fig. 4.2.5) and 3-bromo-2-methylpropene (fig. 4.2.7) that 2-MA appears as the only pyrolysis product only in the mass spectrum at the threshold of ionization. When sufficient amounts of radical should be produced from the brominated precursor, the pyrolysis conditions are not strong enough to convert the precursor completely. The latter then forms the 2-MA cation via DPI, starting above 10 eV (*vide supra*). For this reason, 3-bromo-2-propene was not used to investigate 2-MA's DPI. 3-methyl-3-buten-1-yl nitrite is supposed to be converted completely already under mild pyrolysis temperatures, as can be deduced from the mass spectra at 9.4 eV and 560 °C. Here, a intense mass signal at $m/z=55$ is visible and furthermore no fragments of the precursor's DPI that are visible at 25 °C are observed. So the dissociative photoionization of the precursor will not be problematic, but the dimer $m/z=110$ might fragment to $m/z=55$. In addition, $m/z=40$, which is expected to be a fragment in the DPI of 2-MA, is already present upon pyrolysis of the precursor.

Therefore not only the fact, that the mass signal at $m/z=55$ might still be formed from different other molecules, but also that the mass signals of 2-MA's hypothetical fragments of the DPI are formed in the pyrolysis of the precursor, has to be considered. Furthermore, the expected fragments of 2-MA ($m/z=40$, $m/z=53$, and $m/z=54$) can also be formed from the higher masses $m/z=110$ and

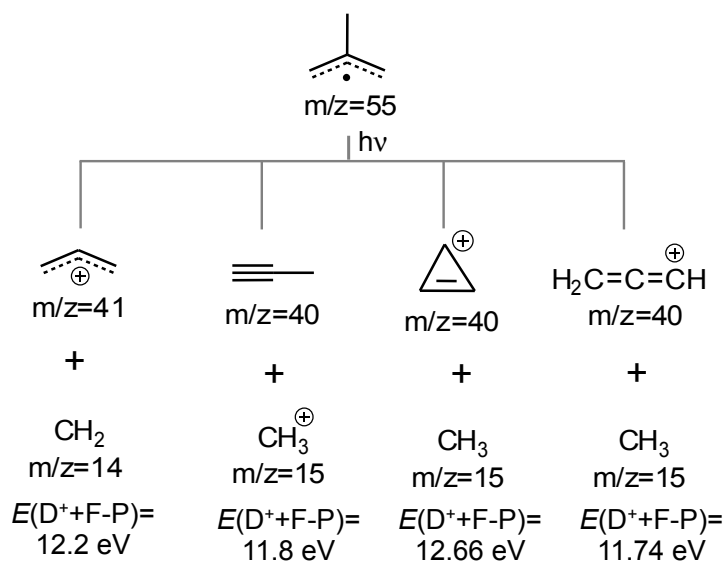


Figure 4.2.17: Theoretical products in the CH₃ loss channel of 2-MA. Below the products the difference between the product energies, corresponding to the daughter D^+ and the neutral fragment F and the neutral parent P are denoted.

$m/z=95$. Because of this circumstances, a double imaging experiment was conducted. In simplified theory, the origin of a species' formation (pyrolysis or DPI) can be obtained from its arrival position on the ion detector. A product formed in the pyrolysis will be in the central elliptic spot of the detector, since the species is to some extent cooled in the molecular beam and gains mainly some translational energy in the direction of the beam. A fragment, originating from a DPI will carry the excess energy of this process as kinetic energy and therefore hit the detector away from the center. However, the two images shown in fig. 4.2.18 illustrate that the signal intensities were very low. The left image was recorded at a pyrolysis temperature of 480 °C at 12 eV. The red ellipse highlights the part of the image, where the masses of the molecular beam are expected to be positioned.

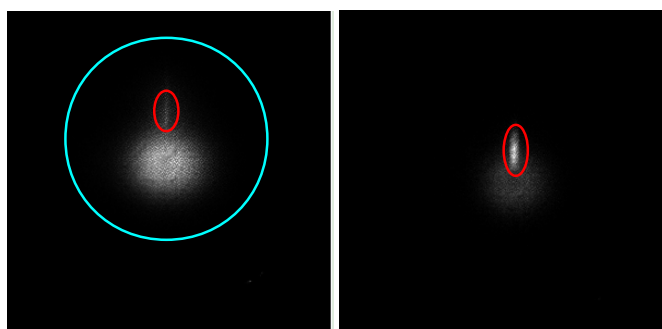


Figure 4.2.18: Ion images of 3-methyl-3-penten-1-yl nitrite (a) and of argon (b). The image a) was recorded at 12 eV and with a temperature of 480 °C.

The signal in this area is very intense in the argon image b). The blue circle in image a) should ideally

incorporate the signal that stems from DPI. The intense spot in the middle of the image is expected to carry the thermal background, which is very low in the argon image. Thus, an evaluated scan is not shown, since the images display a very low signal to noise ratio, not permitting to retrieve any useful data. Nevertheless, the energy range in which the DPI of the 2-MA radical is expected, was additionally observed with the iPEPICO experiment without ion imaging. The TPE signals depicted in fig. 4.2.19 were recorded at 300 °C (upper panel) and 600 °C (lower panel) pyrolysis temperatures in the energy range from 10 eV to 13.5 eV with step sizes of 50 meV and acquisition times of 180 s. Both scans show that the ms-TPES of $m/z=55$ is low below 10.5 eV, rises then again and vanishes up to 13.5 eV. The rise at 10.5 eV might originate from a second excited state in the cation or from the DPI of another fragment, not plotted in the spectra of fig. 4.2.19. The decrease at 13 eV is not expected to originate from the DPI of the 2-MA cation, since no additional fragment appears.

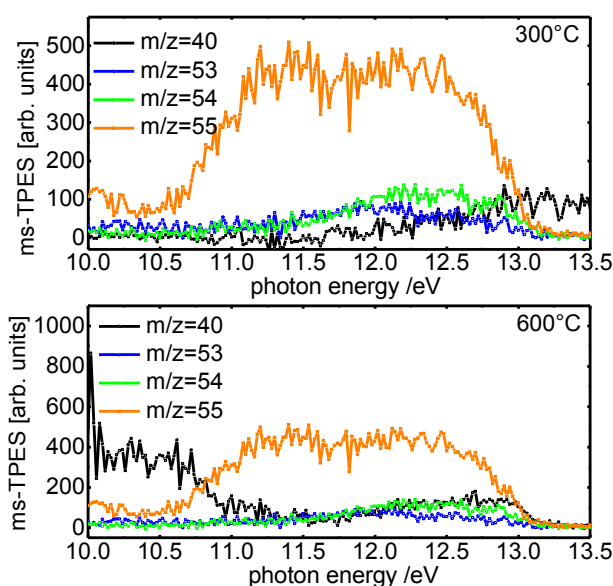


Figure 4.2.19: High energy scan of the TPES of $m/z=55$.

In comparison, the dissociative photoionization of allyl was tentatively investigated to show a main H_2 loss channel with the formation of the fragment $C_3H_3^+$. Nevertheless, the same challenges present in the DPI of 2-MA were present. The precursor used to generate allyl was not completely destroyed by pyrolysis and therefore fed the allyl signal channel, making a breakdown diagram impossible to evaluate.^[168] All in all, the DPI of a radical formed upon pyrolysis is very difficult to elucidate when the precursor is not fully converted upon pyrolysis. There exist many perturbing and interfering signals, which make it challenging to analyze the signals. Because of the different origins of the same masses, an double imaging experiment might be promising for the future, if higher signal levels can be obtained.

Conclusion and summary

Two C₄H₅ isomers and three C₄H₇ isomers were generated by pyrolysis from different precursors. Comparably low volatile bromine precursors were utilized to generate the two radicals 2-butyne-1-yl and 1-butyne-3-yl. A TPES was obtained for each isomer and the adiabatic ionization energies of both isomers were measured. In addition, the spectra were analyzed for the vibrational activity upon ionization based on the Franck-Condon simulations. A low signal/noise ratio and rotational broadening induced by the activity in the methyl and methylene groups causes broad bands and some deviations from the computed spectra. Computations implied that the rearrangement of the two radicals in the tubular reactor cannot be excluded because a low isomerization barrier was observed. The C₄H₇ isomers 1-methylallyl and 2-methylallyl were generated from 3-penten-1-yl nitrite and 3-methyl-3-buten-1-yl nitrite, respectively. In addition, 3-bromo-2-methyl-propene was used to generate 2-methylallyl. Especially the nitrite precursors with their very large vapor pressures yielded even with a dilution of 0.2 % in the carrier gas high signal intensities. The TPES of 1-MA includes both conformers, 1-*E*-isomer and the 1-*Z*-isomer. With the help of a combined Franck-Condon simulation both IE_{ad} were assigned and further vibrations were identified. From the ms-TPES of 2-MA the IE_{ad} of the radical was retrieved and the vibrational activity in the cation was identified. The dissociative photoionization of 2-MA was not successfully carried out, because too many perturbing factors were present. Especially the dimer, which could not be suppressed even for high dilution of sample, contributes to the signal m/z=55 by DPI. The double imaging experiment, which was performed to circumvent the problem of different origins of one mass signal, was not working constantly by this time.

The experimental data are in good agreement with the computed values. The experimentally determined and the computed adiabatic ionization energies of all discussed isomers C₄H₅ and C₄H₇ are summarized in table 4.1. All computed ionization energies show the same tendency to overestimate the experimental value by about 0.05 eV, which is a satisfying result.

molecule	IE _{ad} (experiment)	IE _{ad} (CBS-QB3)
2-butyne-1-yl	7.94±0.02 eV	7.99 eV
1-butyne-3-yl	7.97±0.02 eV	8.02 eV
1- <i>E</i> -methylallyl	7.48±0.02 eV	7.52 eV
1- <i>Z</i> -methylallyl	7.59±0.02 eV	7.64 eV
2-methylallyl	7.88±0.01 eV	7.93 eV

Table 4.1: Ionization energies derived from the experiment and computed on the CBS-QB3 level of theory.

4.3 Fluorenyl radical $C_{13}H_9$

The resonantly stabilized π -conjugated radical fluorenyl, $C_{13}H_9$, is proposed as one further important radical in the combustion of hydrocarbon fuels. Fluorene, $C_{13}H_{10}$ a polycyclic aromatic molecule, is observed in the combustion of premixed toluene flames.^[145] The further fragmentation of fluorene yielding fluorenyl in an H-atom abstraction can be expected to be easily occurring in a combustion process. Moreover, a mass signal at $m/z=165$, which can be assigned to fluorenyl, was observed in the combustion of an ethylbenzene flame.^[32] In addition, theoretical studies predict the formation of the fluorenyl radical from *o*-benzyne, C_6H_4 and benzyl (C_7H_7).^[170] Fluorenyl has 13π electrons and is thus a polycyclic aromatic molecule. Further interests stems from the fact that ions of polycyclic aromatic hydrocarbon are assumed to be carrier of diffuse interstellar absorptions bands (DIB) and unidentified infrared bands (UIB).^[45,46] Although fluorenyl is not a "real" PAH because it has 13 instead of 14π electrons, it is proposed to be the carrier of the DIB at 488.2 nm, since a strong visible band at 494.6 nm was observed in fluorenyls optical absorption.^[171] Another absorption band was detected in the UV range at 283.1 nm.^[172] Besides, fluorenyl has been in the focus of further spectroscopic investigations. The infrared spectrum^[171] and the preresonance Raman transitions^[172] were obtained in an Ar-Matrix by either photolysis or electron impact dissociation of fluorene as the precursor. The adiabatic IE of fluorenyl has been determined to 7.03 eV by electron impact ionization.^[173]

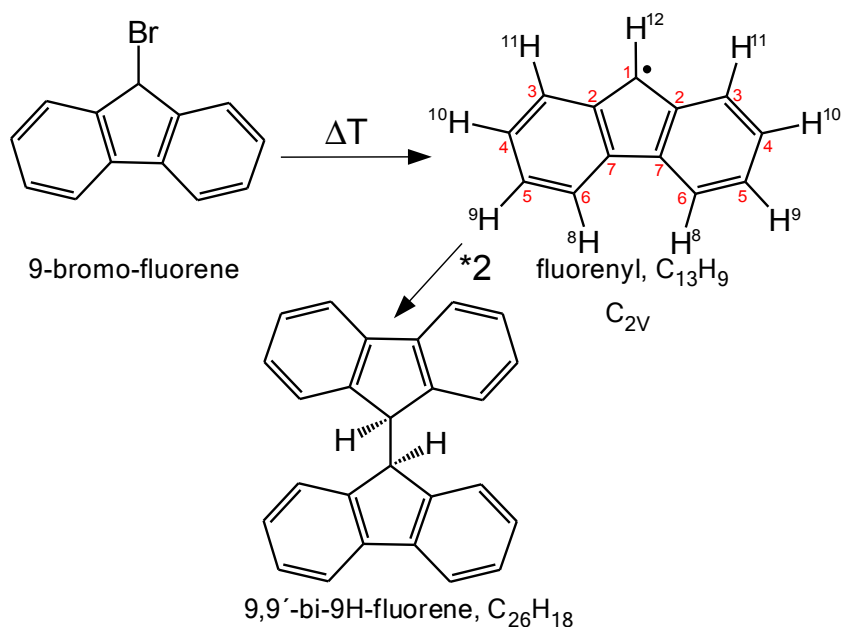


Figure 4.3.1: Pyrolysis of 9-bromofluorene to 9-fluorenyl radical and dimerization of the radical.

In the present experiments fluorenyl was generated by pyrolysis from 9-bromo-fluorene according to the scheme, presented in fig. 4.3.1. The solid sample was heated to 175 °C in the oven source, described in the PhD Thesis of Christof Schon.^[141] In his description the source was attached to a pulsed valve, which was not used. Instead, the oven was directly connected to the faceplate with the pinhole, which was in addition heated with a heating filament. As it turned out, the experiment was challenging because the signal, which was very low due to the low vapor pressure of the solid substance, was not observed to stay constant for a time longer than one hour. In addition, the substance was quickly re-sublimating so that the pinhole was frequently blocked.

Mass spectra and photoionization of the precursor

The mass spectra, recorded with and without pyrolysis were used to check the efficiency of pyrolysis (fig. 4.3.2, left). The TOF mass spectra were recorded with an acquisition time of 60 s. At 7.0 eV (upper panel), when pyrolysis is turned on, a small mass signal at $m/z=165$ is visible. This signal corresponds to the fluorenyl radical. At 8.7 eV (middle panel) without pyrolysis, beside the mass signal of the precursor at $m/z=244/246$, a tiny signal at $m/z=166$ appears. The latter corresponds to fluorene, C₁₃H₁₀, which is present as an impurity in the commercial 9-bromofluorene precursor sample. As visible in the inset of the middle panel in fig. 4.3.2, without pyrolysis and at 9.20 eV the signal at $m/z=166$ has almost vanished and the fluorenyl cation $m/z=165$ is formed from dissociative photoionization of 9-bromofluorene.

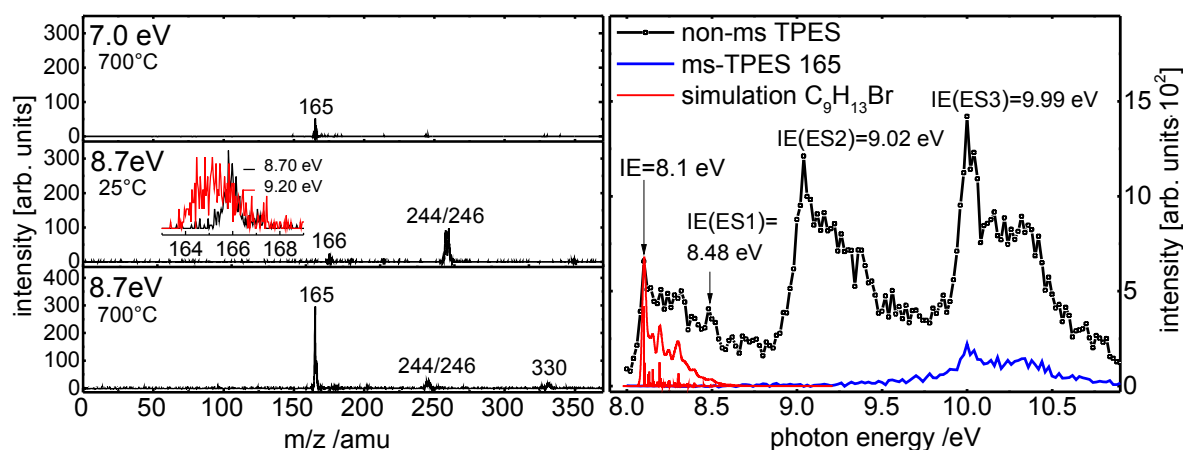
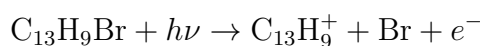


Figure 4.3.2: TOF- mass spectra (left) and threshold photoelectron spectrum (right) of 9-bromofluorene.

At a pyrolysis temperature of 900 °C the precursor is not yet completely converted to $m/z=165$, which displays the only fragment upon thermal treatment. Applying higher pyrolysis temperatures over a few hours is unfavorable, because the pyrolysis tube's lifetime shortens. Thus, for the radical generation a temperature around 900 °C was chosen. Because of incomplete pyrolysis at this

temperature, the photoionization and dissociative photoionization of the precursor was examined first. On the right-hand side of figure 4.3.2 the threshold photoelectron spectrum (TPES) without pyrolysis is depicted. All threshold electrons were collected, i.e. no mass selection was applied. A value of 8.10 eV was determined for the IE_{ad} of the precursor 9-bromo-fluorene ($C_{13}H_9Br$). A Franck-Condon simulation to the ground state cation is shown as red line. It displays vibrational activity in the cation up to an energy around 8.5 eV. Excited electronic states of the $C_{13}H_9Br$ cation are visible at 8.48 eV, 9.02 eV and 9.99 eV. TD-DFT computations yielded energies for the excited states of the cation at 8.58 eV, 9.20 eV and 9.9 eV, in good agreement with the observed transitions in the spectrum. However, spin-orbit splitting was ignored in these computations. Above 9.5 eV the precursor starts to fragment, loses Br and forms the fragment $m/z=165$, fluorenyl cation. This is visualized by the blue line in the same graph, which displays the mass-selected TPES of $m/z=165$. The daughter signal appears in the same mass channel as the radical of interest and can thus be incorrectly assigned to the desired reactive intermediate. This process is observed according the following equation:



In order to elucidate the DPI of the precursor a breakdown curve was recorded as shown in figure 4.3.3 (left).

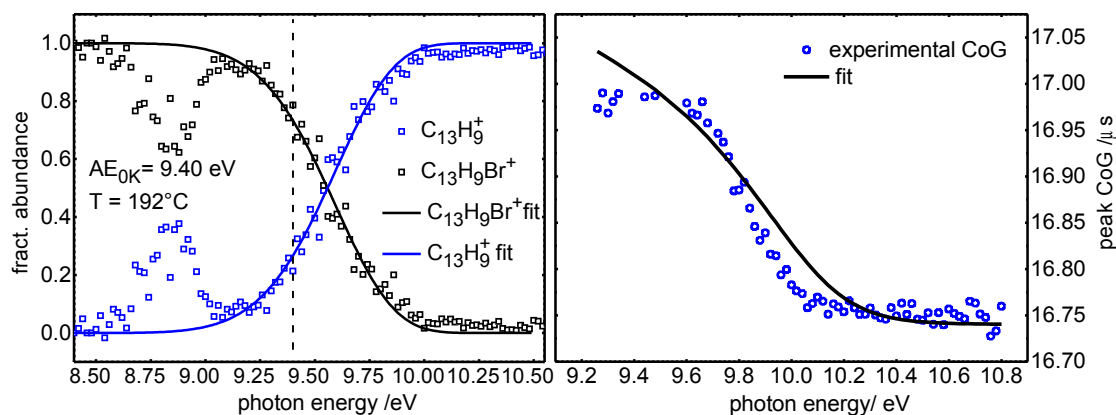


Figure 4.3.3: Breakdown diagram of 9-bromofluorenone (left) and center-of-gravity curve (right) of the TOF mass peak $m/z=165$.

The latter displays the fractional abundances of the parent signal ($C_{13}H_9Br^+$, black squares) and the fractional abundance of the daughter fragment's ($C_{13}H_9^+$, blue squares) TPE signal versus the photon energy. As visible in figure 4.3.3 (right), there is a “peak” in the daughter ion signal and a corresponding “dip” in the parent ion fractional abundance between 8.55 eV and 9.10 eV. This feature is caused by fluorene, which has been identified from the mass spectra (fig. 4.3.2, left, middle panel). This mass spectrum in the inset in fig. 4.3.2 (left, middle panel) reveals that the mass signal of the fluorenyl ion ($m/z=165$) with its asymmetric TOF peak shape due to the kinetic shift encloses

the mass signal of fluorene ion ($m/z=166$). As a consequence, the threshold photoelectron signal of the fluorenyl fragment contains threshold photoelectrons of fluorene because an excited electronic state of the fluorene cation becomes accessible at 8.92 eV.^[174] The corresponding feature in the breakdown diagram is therefore not related to the dissociative photoionization of 9-bromo-fluorene. For this reason the data points between 8.55 eV and 9.10 eV were disregarded in the analysis.

The asymmetric peak shape of the fluorenyl fragment ion (C₁₃H₉⁺) thus reveals the dissociation channel to be slow, which leads to a kinetic shift of the observed fragmentation threshold (see section 2.4.5). To include the kinetic shift in the analysis of AE_{0K} of fluorenyl fragment ion, the breakdown diagram and the time-of-flight distributions have to be modeled simultaneously. Due to the small signal-to-noise ratio, TOF peak shape fitting was impractical for the rate calculations. Instead, the center-of-gravity (CoG) of the fragment ion peak as a function of the photon energy was modeled to get the experimental rates $k(E)$. The fit was performed with the program MinimalPEPICO. The input file for the fit is given in the appendix. The fitted CoG curve is shown in figure 4.3.3 on the right. Deviations of the fit from the experimental data at higher flight times can be explained by the contribution of fluorene to the signal. For the rate calculations the SSACM model (sec. 2.4.5) was applied. To achieve a good fit to the experimental data the density of states was adjusted by deleting several low-frequency modes of the products. This approach has been discussed in the literature.^[61,175,176] The experimental rate curve was extrapolated to the 0 K appearance energy, where the rate vanishes and a value of 9.4 eV for AE_{0K} was obtained. The simplified empirical adjustment chosen is justified by the perturbation of the signal from fluorene impurities, the unknown temperature in the beam, and the main interest in the radical rather than the precursor. The temperature of 192 °C obtained from the fit correlates with the sample temperature of around 175 °C and indicates limited cooling in the molecular beam experiment. A more accurate determination of the appearance energy requires an extensive study of the precursor dissociative photoionization that was beyond the scope of this work. In addition the AE_{0K} was computed by quantum chemistry, according to eq. 2.4.8 (sec. 2.4.2):

$$AE_{0K} = \Delta H_f^0(C_{13}H_9^+) + \Delta H_f^0(Br) - \Delta H_f^0(C_{13}H_9Br).$$

The electronic energies were taken from the size consistent CBS-QB3 computations. A value of 9.37 eV for AE_{0K} was obtained, in good agreement with the value of 9.4 eV derived from the experiment. Taking into account the IE and the AE_{0K} of C₁₃H₉Br the C-Br bond dissociation energy of the ion can be calculated to be 1.3 eV (125 kJ/mol). In the experiments with active pyrolysis the precursor fragmentation does not contribute to the radical signal below 9 eV, contributing for thermal lowering of the 0 K onset at 9.4 eV.

TPES of fluorenyl

Figure 4.3.4 shows the TPE signal of fluorenyl as a function of the photon energy. Because the mass spectrum depicted in figure 4.3.2 on the left side in the upper panel shows only one peak at $m/z=165$ in the relevant energy range, all threshold photoelectrons were taken into account and no mass-selection was employed. The signal rises at a photon energy of about 6.60 eV and reaches a maximum at 7.01 eV. This value is assigned to the adiabatic ionization energy. A similar value of 7.03 eV was yielded from an electron impact ionization experiment, although in general, an electron impact ionization measurement does not depict a method as powerful as photoionization for establishing ionization energies.^[177] The IE_{ad} computed with the CBS-QB3 composite method is 7.17 eV. Above 7.01 eV the TPE signal decreases slowly, but no individual vibrational features can be resolved. The red line displays a Franck-Condon (FC) simulation that is based on the geometries, force constants and vibrational frequencies (unscaled) computed at B3LYP/6-311g(d,p) level of theory. The Franck-Condon factors (red sticks) were subsequently convoluted with a Gaussian function (fwhm=100 meV). Both the fluorenyl radical as well as the cation possess C_{2v} symmetry. Upon ionization from the $X \ ^2B_1$ neutral ground state to the closed shell $X^+ \ ^1A_1$ state of the cation mainly the two totally symmetric in-plane bending modes ν_{58}^+ and ν_{47}^+ are supposed to be active. They are depicted in figure 4.3.4 on the right hand-side and computed to 27 meV /218 cm^{-1} and 81 meV /658 cm^{-1} , respectively. Furthermore, the first overtone of ν_{58}^+ and a combination band $\nu_{58}^+ \nu_{47}^+$ can be expected to appear. As evident from the dashed lines, the transitions can tentatively be associated with some of the features visible in the spectrum.

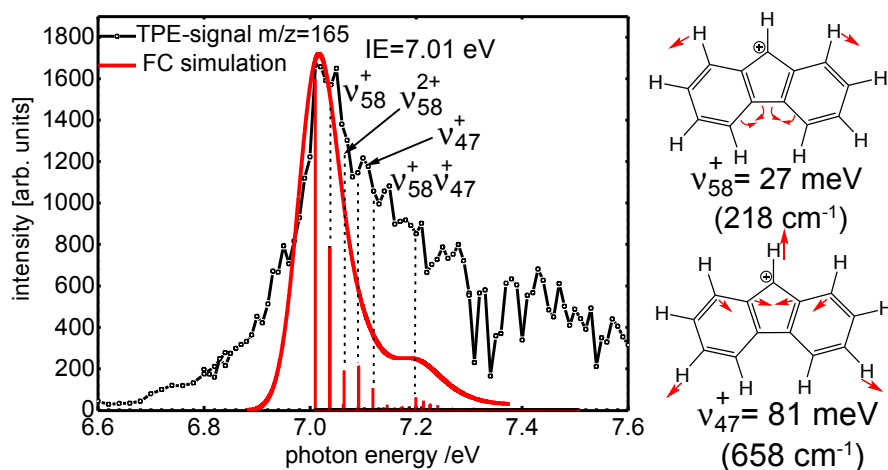


Figure 4.3.4: Threshold photoelectron spectrum of fluorenyl radical $C_{13}H_9$ (black). The red line displays the FC simulation. On the right the most pronounced vibrations are displayed.

Although the overall agreement between experiment and simulation is reasonable, there are some deviations visible on the low and high energy side. The former is most likely due to the fact that hot and sequence band transitions are not simulated. Since the temperature of pyrolytically generated radicals in a continuous beam is known to be not significantly lower than the applied pyrolysis temperature^[57] a considerable fraction of radicals is produced in rotationally and vibrationally excited states. In particular the presence of sequence bands can be expected. The deviations on the high energy side might be explained by a geometry change upon ionization that is more pronounced than expected from theory. The most pronounced change in geometry is associated with the C(7)-C(7) bond in the five-membered ring. For labeling of atoms see fig. 4.3.1. A difference of around 2 pm was computed by B3LYP/6-311(2d,d,p). The C(2)C(1)C(2) angle is predicted to change by 1.4° (B3LYP/6-311g(d,p)). Since the overall computed geometry change is small, alternative explanations to account for the broad shoulder on the high energy side were investigated. Dissociative photoionization of the precursor can be excluded below 9 eV as discussed above. Dissociative photoionization of the fluorenyl dimer, which is detected at higher energies, can be excluded as well because the IE_{ad} of the dimer is determined to be at 7.69 eV, above the IE_{ad} of the monomer (*vide infra*). A further possibility is the presence of a second C₁₃H₉ isomer, originating from a rearrangement in the pyrolysis. Moreover other brominated fluorene isomers might appear as contamination in the precursor synthesis, e.g. 1-, 2-, 3- or 4-bromofluorene. For that reason the corresponding fluorenyl radicals 1-,2-,3- and 4-fluorenyl of these precursors and three further possible C₁₃H₉ radical rearrangement products, 1H-benz[f]indenyl (b) and 1H-benz[e]indenyl (c) have been investigated theoretically. The energy diagram showing the structures of the isomers and all calculated ionization energies is given in figure 4.3.5. All isomers are higher in energy than fluorenyl or the calculated IE_{ad} (B3LYP/6-311g(d,p)) values are higher (isomers c-g). Thus, another conclusion might be that the computations underestimate the geometry change upon ionization.

$$\begin{aligned}\Delta BDE(C_{13}H_9 - Br) &= \Delta H_f^0(C_{13}H_9) + \Delta H_f^0(Br) - \Delta H_f^0(C_{13}H_9Br) \\ &= AE_{0K}(C_{13}H_9^+) - IE(C_{13}H_9).\end{aligned}$$

With the ionization energy of fluorenyl determined here, a BDE of the C-Br bond in neutral 9-bromofluorene can be determined through a thermochemical cycle (sec. 2.3.1, fig. 2.3.2). With the radical IE_{ad} of 7.01 eV and AE_{0K}(C₁₃H₉Br, C₁₃H₉⁺) = 9.4 eV, the BDE of the C-Br bond of the neutral is determined to be (9.4 eV – 7.01 eV) around 2.4 eV, corresponding to 230 kJ/mol. Compared to the cation's BDE with 1.3 eV (125 kJ/mol), the neutral possesses almost twice as much bond energy, while the bond length only changes by about 2 pm. This relation of a significantly decreased C-Br BDE while the bond length shortens upon ionization has been observed for C₄H₇Br (sec. 4.2, sec. 4.2), too. The reason for this behavior might be the same, like found before. The dissociation

in the neutral bromide requires more energy than dissociation in the cation.

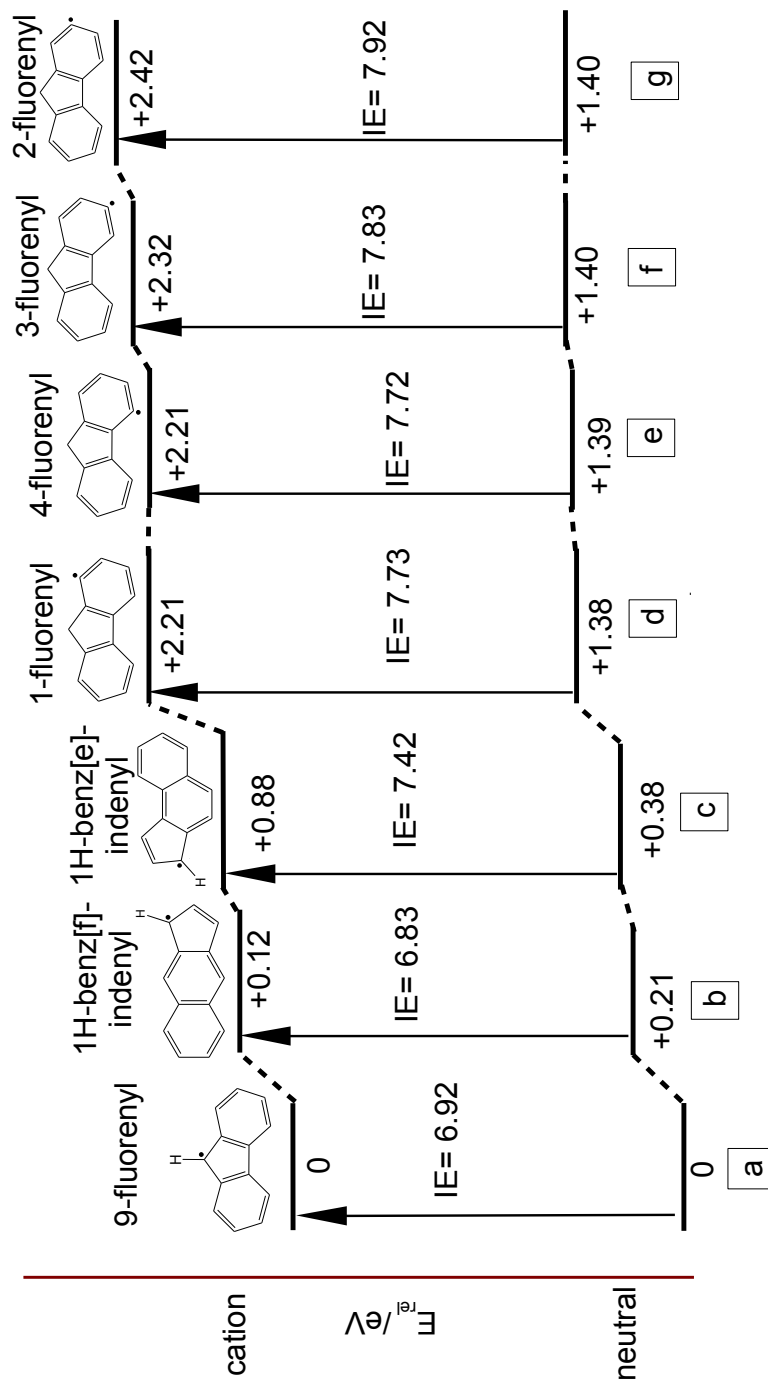


Figure 4.3.5: Energy diagram of the different C₉H₁₃ isomers. The numbers in the lower part represent the relative energy (eV) with respect to 9-fluorenyl.

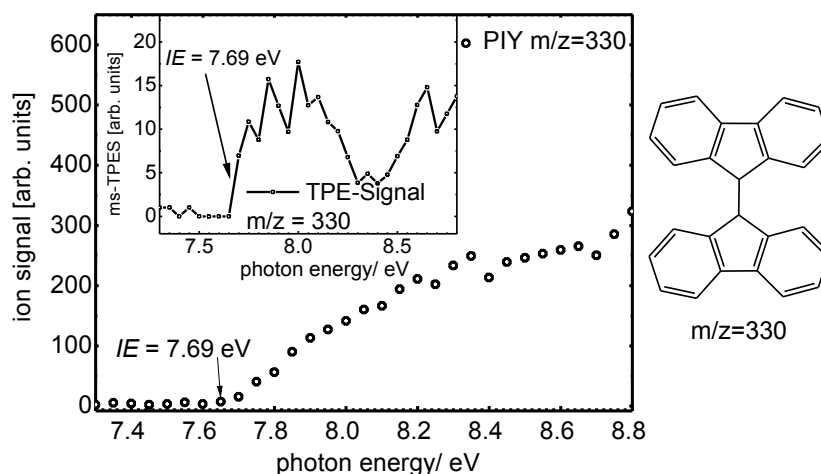


Figure 4.3.6: PIY curve and ms-TPES of the mass signal $m/z=330$.

The mass spectra with active pyrolysis (figure 4.3.2,) reveal an interesting mass peak at $m/z=330$ that can be assigned to a fluorenyl dimer. Reactions of radicals occur because the pyrolysis tube can be considered as a chemical reactor, as it was also observed for the methylallyls, C_4H_7 , before. Previous work by IR/UV double resonance spectroscopy indicated that such dimerization reactions show a remarkable selectivity.^[178] Figure 4.3.6 shows the PIY curve and the ms-TPES of the molecule with $m/z=330$. From the experimental data the IE_{ad} is assigned to be $7.69 \pm 0.04 \text{ eV}$.

The structures and the ionization energies of nine stable dimer structures ($C_{25}H_{18}$) (shown in fig. 4.3.7) were computed by DFT, using the $\omega B97XD$ functional and the 6-311++g(d,p) basis set. Although several further dimer structures exist, which were also intended to be computed, many of them did not show an equilibrium structure neither in the neutral form nor in the cation. The isomer revealing the best match is obtained for the direct dimer 9,9'-bi-9H-fluorene (figure 4.3.1), where both fluorenyl moieties are connected by the carbon atom C(1) in the five-membered ring. Besides, the resonance stabilization of the radical would permit dimerization to occur also at every other C-atom of the molecule. The calculated value of 7.79 eV is in excellent agreement with the experimental one of 7.69 eV. Moreover, the calculations revealed that 9,9'-bi-9H-fluorene is the most stable neutral fluorenyl dimer structure.

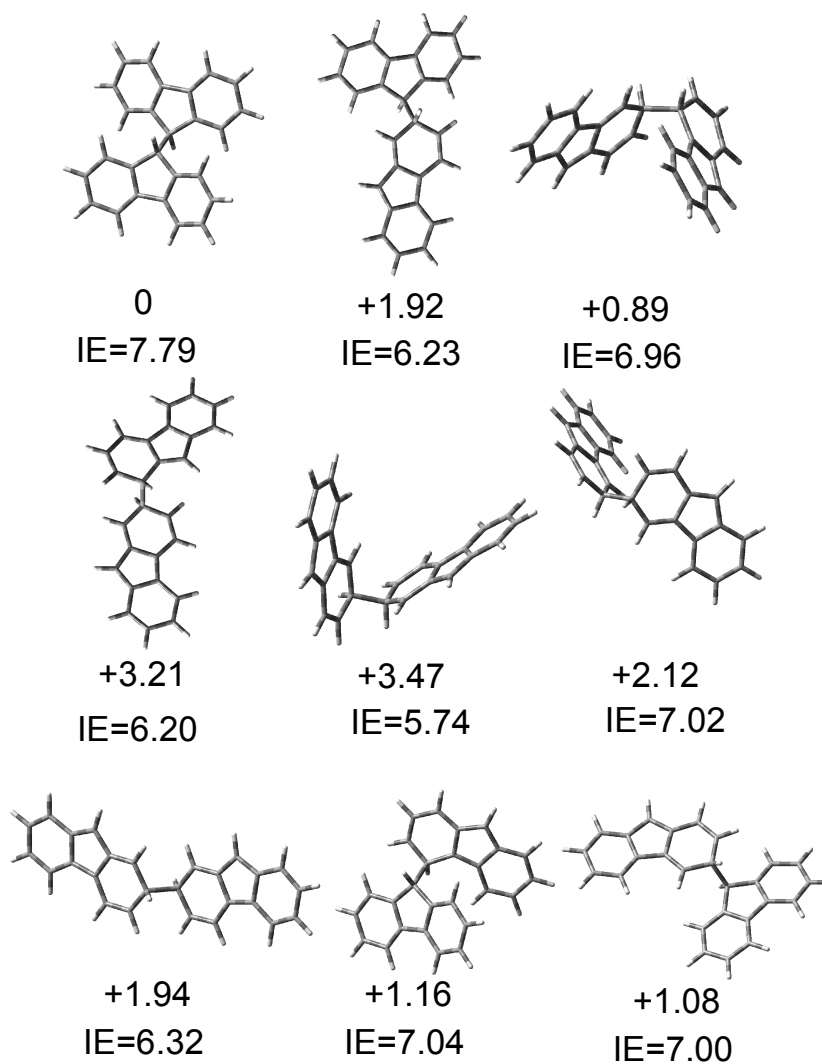


Figure 4.3.7: Computed dimers, $C_{26}H_{18}$ of the fluorenyl radical. The first number gives the relative energy (eV) referenced to the most stable isomer (0 eV, upper row, left side) and below the IE (eV) is depicted.

4.4 Benzhydryl $C_{13}H_{11}$ and diphenylmethylene $C_{13}H_{10}$

The $C_{13}H_{11}$ radical, is similar to fluorenyl a π -conjugated molecule with 13π electrons in the neutral radical and 12π electrons in the closed shell cation. The respective carbene, $C_{13}H_{10}$, has 14π electrons. In contrast to fluorenyl radical, which is fused at the C(7)-C(7) bond to a polycyclic aromatic hydrocarbon, the two benzene rings in all of the four species (benzhydryl, diphenylmethylene (dpc) and their respective cations) are not in one plane. Thus, all molecules are of C_2 symmetry. This means that each of the molecules has two separated aromatic moieties, which are not in full conjugation to the carbenic, the radical and the cationic center. Similar to the mass signal at $m/z=165$, which might be assigned to fluorenyl, also a mass signal at $m/z=167$ was observed in an ethylbenzene flame,^[32] making both radicals potential suspects as reactive intermediates in combustion processes. Further computational studies on the ring-growth mechanism of *o*-benzyne with benzyl radical show that the benzhydryl radical is expected to be the most stable $C_{13}H_{11}$ isomer on the product potential energy surface for this reaction.^[170] The radical and the carbene have already been extensively studied by various spectroscopic techniques. Those comprise also electron impact ionization experiments of dpr, yielding an IE_{ad} of 7.32 eV. Several photochemical studies were performed in glassy matrices as well as in the gas phase. The absorption spectrum of benzhydryl was reported in several experiments^[179,180] and also transient absorption and emission were examined for several electronic states of dpr. In the last stated experiments dpr was studied as an adsorbate on zeolites,^[179] in solution,^[181,182] or in silica gel.^[183]

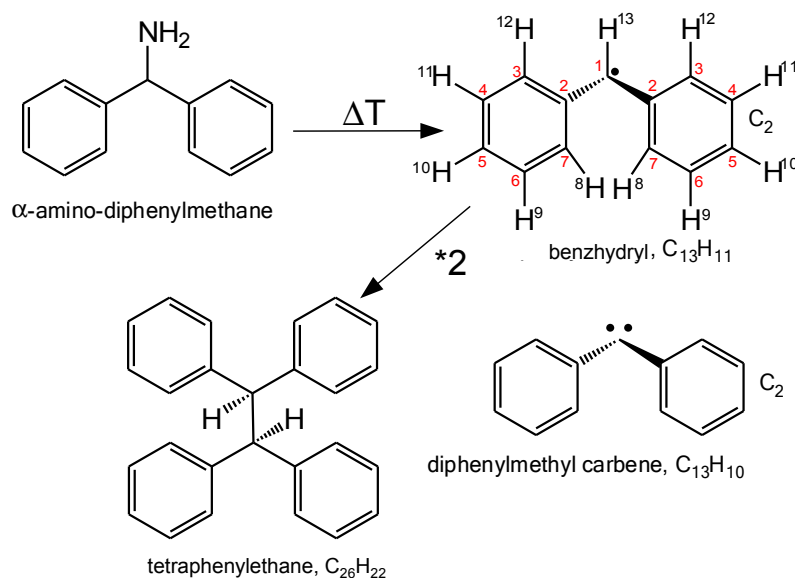


Figure 4.4.1: Pyrolysis of α -amino-diphenylmethane.

Diphenylmethylene (dpc) has gained attention similar to the radical. Several electron paramagnetic resonance (EPR) experiments in different rigid matrices^[184–187] as well as electron double resonance

experiments^[188] revealed that the triplet carbene is the ground state multiplicity. Excitation, absorption and emission spectra were recorded as well.^[189] Moreover the first excited triplet state of the diphenylmethylene was examined by time-resolved EPR,^[190] by absorption^[191] and fluorescence spectroscopy.^[192] Recent experiments performed on dpc in the *Sander* group reversed the ground state multiplicity of the carbene from triplet to singlet, when the dpc interacts with hydrogen in a dpc-H₂O/HOCH₃ complex.^[193,194]

In the presented experiment benzhydryl radical and diphenylmethylene were generated from pyrolysis of α -amino-diphenylmethane (adpm), as depicted in figure 4.4.1. The liquid substance was purchased from Sigma Aldrich and used without further purification. A piece of glasswool was soaked by the substance and placed in the molecular source for solids (fig. 3.1.2). The source was heated to 120 °C.

Mass spectra and fragment analysis

The mass spectra, presented in fig. 4.4.2 on the left hand-side were recorded without pyrolysis at three different photon energies. At 8.50 eV (upper panel) the precursor molecule at $m/z=183$ is still intact. At 9.25 eV (middle panel) a closer inspection reveals that additionally $m/z=182$ is formed. At higher photon energies the parent molecule dissociates and the dominant fragments are $m/z=105$ and $m/z=106$. Furthermore, small contributions are visible at $m/z=167$. In addition, mass signals at $m/z=43$ and $m/z=58$ are detected, which are supposed to stem from a contamination of acetone ($m/z=58$) in the molecular source, which fragments to acetyl ($m/z=43$).

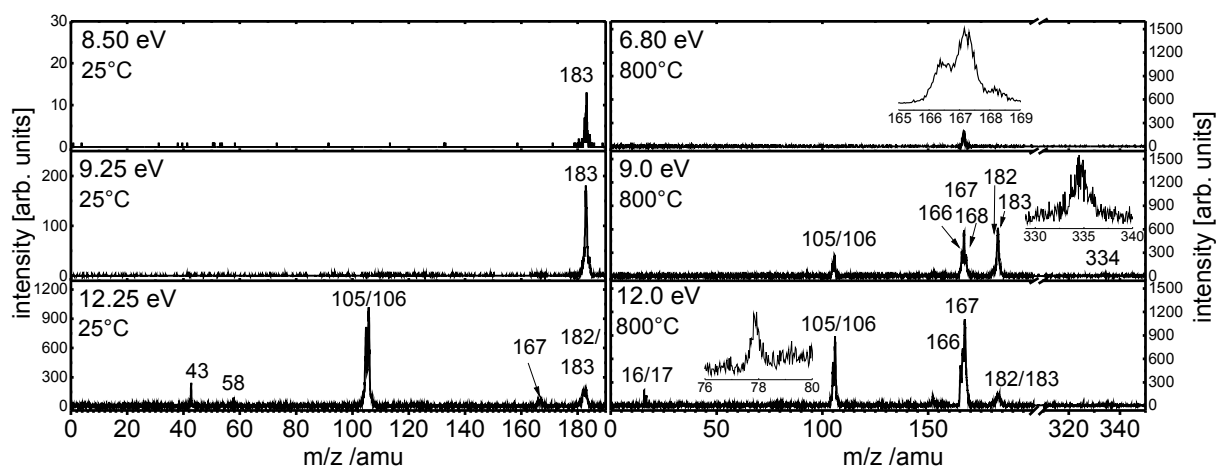


Figure 4.4.2: TOF-MS of α -amino-diphenylmethane without pyrolysis (left) and at a pyrolysis temperature of 800 °C (right). All mass spectra were recorded with an acquisition time of 60 s.

All pyrolysis fragments proposed are shown in figure 4.4.3 on the right hand-side. The TOF-mass spectra on the right hand-side of fig. 4.4.2 were recorded with a pyrolysis temperature of 800 °C at different photon energies. At 6.80 eV (upper panel) the only mass signal is observed

at $m/z=166/167$. The inlet confirms that beside masses 166 and 167 also a small contribution of $m/z=168$ is visible. At 9.0 eV the masses 166/167/168 and two mass peaks at $m/z=105$ and $m/z=106$ appear in addition to the precursor signal at $m/z=183$ and $m/z=182$. Furthermore, small contributions at $m/z=334$ can be observed. At 12.0 eV three additional mass signals at $m/z=16$, $m/z=17$ and $m/z=78$ are observed. The signals at $m/z=105/106$ and $m/z=166/167$ have become larger and $m/z=183$ has decreased.

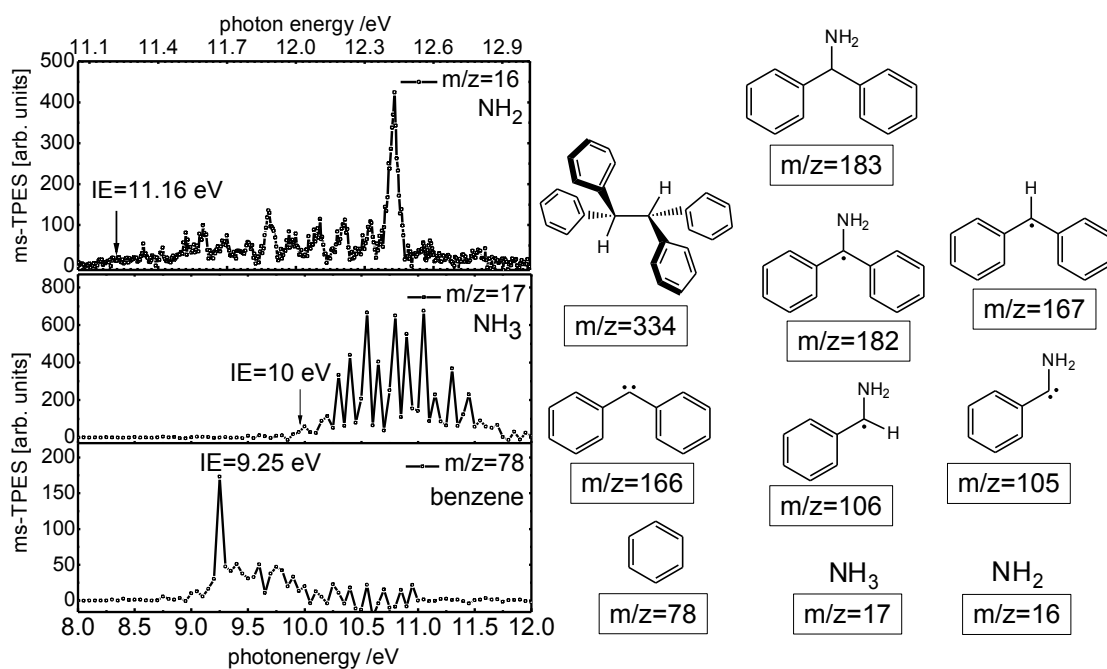


Figure 4.4.3: Ms-TPES of further pyrolysis products NH_2 , NH_3 and benzene, generated from adpm. On the right hand-side the proposed pyrolysis products of adpm are depicted.

However, even at 800 °C no full conversion of the precursor is achieved, since $m/z=183$ is still visible. The three overlapping mass peaks at $m/z=166-168$ correspond to the mass signals of diphenylmethylene, $C_{13}H_{10}$ ($m/z = 166$) and the signal at $m/z=167$ can be assigned to benzhydryl, $C_{13}H_{11}$. The signal at $m/z=168$ is supposed to be the ^{13}C isotopologue of $m/z=167$. This can be inferred from the relative intensities of the mass signals in the inlet at 6.8 eV in fig. 4.4.2. While benzhydryl formation is associated with cleavage of NH_2 ($m/z=16$), the carbene is generated in the pyrolysis tube together with NH_3 ($m/z=17$) as the second product. The signals at $m/z=105$ and $m/z=106$ might be assigned to the aminobenzyl radical, $C_7H_5NH_2$, and benzylimine, $C_7H_6NH_2$ generated by benzene, C_6H_6 ($m/z=78$) and phenyl (C_6H_5) abstraction of the precursor (fig. 4.4.3). Phenyl, $m/z=77$ is not visible in the TOF mass-spectra, presented in fig. 4.4.2. The formation of NH_2 ^[195] NH_3 ^[196] and benzene^[164] is also validated by the mass-selected threshold photoelectron spectra, depicted in fig. 4.4.3 on the left. The ms-TPES of the masses $m/z=166/167$ and $m/z=334$ will be discussed in detail in subsec. 4.4. Unfortunately, ms-TPES of aminobenzyl radical ($m/z=106$) and benzylimine ($m/z=105$) were not recorded.

Dissociative photoionization of α -amino-diphenylmethane

As stated above, a mass signal at $m/z=167$ is observed without pyrolysis (fig. 4.4.2, left, lower panel). Thus, the dissociative photoionization of the precursor was also studied to elucidate a possible contribution to the radical and carbene signal (*vide infra*). In figure 4.4.4 on the left hand-side, the most prominent channels of the DPI of adpm are depicted in a breakdown diagram. At about 10.4 eV adpm ($m/z=183$) starts to lose a hydrogen atom. Thus, the mass channels $m/z=182$ and $m/z=183$ cannot be separated because the peaks are broadened by the kinetic shift. Therefore the $m/z=182$ H-loss channel is not shown in figure 4.4.4, but is indicated by the slight signal increase of the combined $m/z=182/183$ signal (black) at about 10.45 eV. At around 9.3 eV the parallel loss of phenyl radical (C_6H_5) and benzene (C_6H_6), leads to the fragment ions with $m/z=106$ (red) and $m/z=105$ (blue). As both fragments are generated in a slow dissociation process the mass peaks overlap at threshold, leading to a challenging analysis.

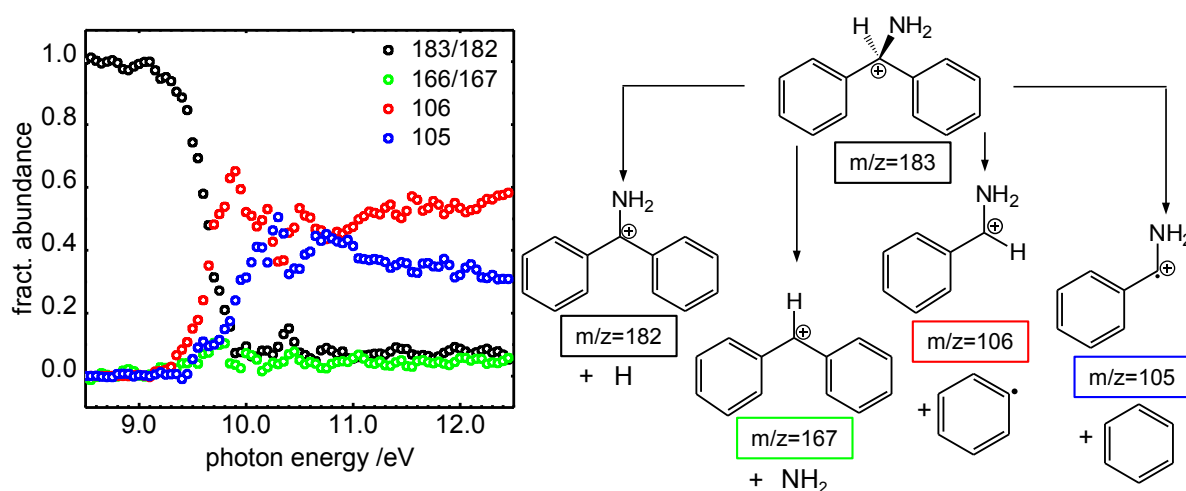


Figure 4.4.4: Dissociative photoionization of adpm. On the left the fragmentation channels are shown in a breakdown plot up to 12.5 eV. On the right the respective molecular structures are presented.

The most important dissociative photoionization channels for the experiments on the reactive species described in the next subsection are loss of NH_2 and NH_3 , respectively. However, neither $C_{13}H_{11}^+$, corresponding to the benzhydryl cation ($m/z=167$), nor $C_{13}H_{10}^+$, the cation of diphenylmethylene ($m/z=166$), are formed with significant intensity (green) in the investigated energy range. Only a small signal is visible at around 9.8 eV. Therefore the dissociative photoionization of the precursor to $C_{13}H_{11}^+$ and $C_{13}H_{10}^+$ is of minor importance and can be ignored in the analysis of the radical and carbene data below.

Ms-TPES of diphenylmethyl radical and diphenylmethylene

It was shown from the mass spectra in fig. 4.4.2 on the right hand-side, that the mass peaks of diphenylmethylene and benzhydryl overlap from $m/z=166$ to $m/z=168$. Since the ^{13}C satellite of the carbene ($m/z=166$) will also contribute to the signal at $m/z=167$, full mass-selectivity is difficult to achieve. In the investigated energy range the mass signals from $m/z=166$ to $m/z=168$ are present. When all threshold electrons are recorded and the signal thus contains contributions from all of the three masses. Figure 4.4.5 on the left shows the threshold photoelectron spectrum of the adpm pyrolysis products from 6.0 eV to 8.2 eV. On the right of fig. 4.4.5 the signal within a narrow mass gate is depicted. The carbene signal was integrated from $m/z=165.3$ to $m/z=166.3$, the radical signal from $m/z=166.7$ to $m/z=167.7$. Narrowing the integration intervals leads to a quickly deteriorating signal to noise ratio. Despite this, different onsets for both species can be identified. One can recognize that the TPE signal of the radical starts to rise at around 6.3 eV, whereas the carbene signal increases at slightly higher photon energy of 6.6 eV. However, contributions from the carbene ^{13}C isotopologue to the radical signal cannot be avoided.

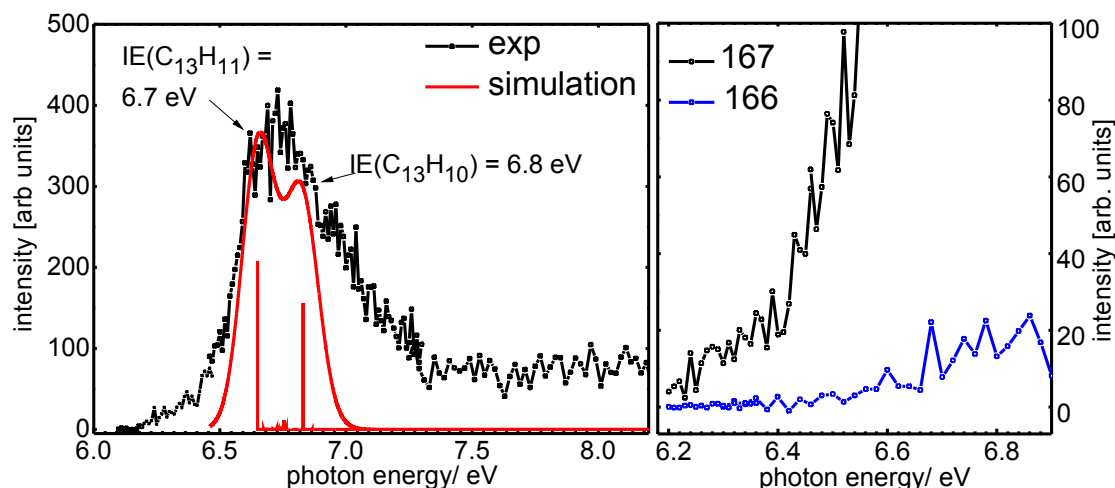


Figure 4.4.5: Ms-TPES of benzhydryl ($C_{13}H_{11}$) and *t*-diphenylmethylene ($C_{13}H_{10}$). The red line displays the Franck-Condon simulation of both the radical and the triplet carbene.

DFT computations on at the B3LYP/6-311(2d,d,p) level of theory reveal only a small geometry change upon photoionization for both species. The structures of the radical, and the carbene and their corresponding cations were all found to have C_2 symmetry. The overall geometry changes upon ionization for both the radical and the triplet (*t*)-carbene are rather small. The most significant changes of the radical are found in the C(1)-C(2) bond that shortens by 1.8 pm. The change in angles and dihedral angles is not larger than 1.6° for the radical and its respective cation. The most pronounced geometry change upon ionization of the *t*-carbene is also found in the decrease of the bond C(1)-C(2) and in the dihedrals C(7)C(2)C(1)C(2) and C(3)C(2)C(1)C(2), which increase

and decrease by 5° , respectively. Thus the $v''=0$ to $v^+=0$ transition is expected to dominate the spectrum. To simulate the spectrum the computed geometries were used and the ionization energy of radical and carbene were varied until the best fit to the experimental spectrum was achieved. We assumed relative intensities of 3:2, based on the mass spectrum at 6.80 eV (fig. 4.4.2, right, upper panel). The relative intensity accounts for the difference in both the particle density and the ionization cross section. From the best fit to the experimental spectrum (red line in figure 4.4.5) we extract an $IE_{ad}=6.7$ eV for the radical and $IE_{ad}=6.8$ eV for the triplet carbene. For comparison the calculations predict the IE_{ad} of benzhydryl to be at 6.60 eV (CBS-QB3). The IE_{ad} of triplet diphenylmethylene is calculated to be at 6.77 eV (CBS-QB3). The TPE band is much broader than expected for two diagonal transitions. However, the torsional motion of the two benzene moieties act as internal rotors in the neutral as well as in the cationic species. In addition, the torsional motion in the dihedral angle C(7)C(2)C(1)C(2) is for all species computed not larger than a few 50 cm^{-1} and thus expected to be excited in the neutral as well as in the cationic species, but not activated in the simulation. Therefore several vibrationally excited states will be populated in the neutral and transitions from all of them contribute to the TPE-spectrum. Such contributions were not accounted for by the FC simulation. As a consequence the bands in the simulated spectrum are actually found narrower than the experimental ones. In principle, contribution from the singlet diphenylmethylene should be taken into account as well. The total energy (CBS-QB3) of the singlet carbene is calculated to be 0.10 eV above the triplet carbene, with an IE_{ad} of 6.67 eV. Nevertheless, in the simulation its contribution to the spectrum is neglected. The presence of two independent fit parameters (two ionization energies) leads to error bars of around 100 meV associated with the IE_{ad} . However, the IE_{ad} of benzhydryl of 6.7 eV derived from our data is significantly lower than the value reported in the literature. The earlier IE_{ad} with a value of 7.32 eV was based on electron impact ionization mass spectrometry^[197] and is clearly outside the error bars of the data presented in figure 4.4. Accordingly, the conclusion from the experiment presented here is that a significant downward revision of the ionization energy of benzhydryl is warranted.

At higher photon energies (fig. 4.4.2, right, middle panel) also the dimer of benzhydryl ($m/z=334$) is detected. The photoion yield curve and the TPES (figure 4.4.6) deliver an ionization energy of 8.13 eV. An error of ± 0.04 eV is expected to be associated with this value, based on the step size of 20 meV between two data points. Again a selected number of possible isomers were investigated computationally. Their structures and relative and/or ionization energies are summarized in fig. 4.4.7. For most of the structures the computations failed to derive the ionic structure and no IE was retrieved. Thus only the relative energy of the neutral molecule referenced to the absolute energy of the most stable neutral isomer is denoted.

For tetraphenylethene, the product of a direct dimerization at the radical centers, an IE of 7.99 eV was obtained by DFT, using the ω B97XD functional. The absolute energies for a number of other isomers were calculated to be higher, making a contribution to the spectrum in figure 4.4.6

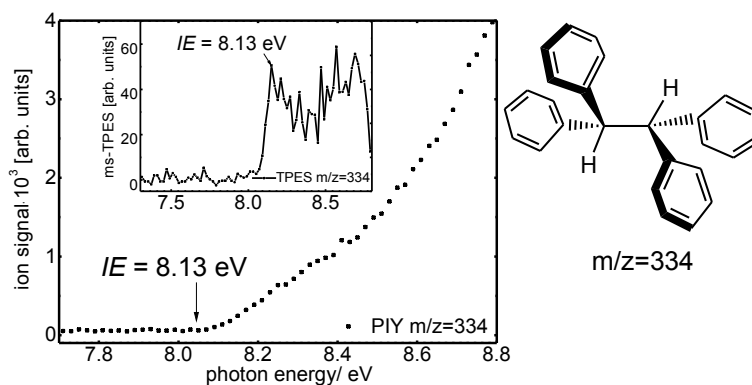


Figure 4.4.6: PIY curve and ms-TPES of the dimer, $C_{26}H_{22}$.

improbable. Note that no dimerization product of the carbene diphenylmethylene is visible in the mass spectrum. Since the diphenylmethyl radical might play a role in combustion chemistry as discussed in the introduction, its dimer might be also an intermediate on the way to the formation of polycyclic hydrocarbons, the precursors of soot.

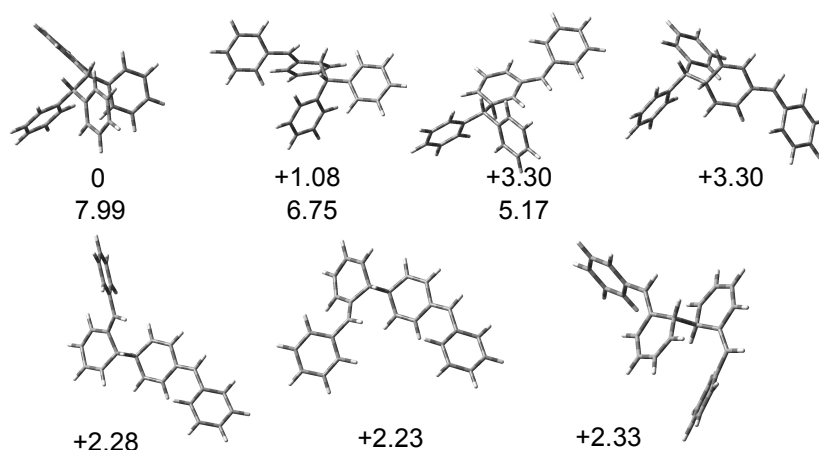


Figure 4.4.7: Computed structures, relative energies and ionization energies (IE) of the dimers $C_{26}H_{22}$. The energy (eV) is given referenced to the most stable obtained isomer tetraphenylethane (upper row, left). For the isomers 4-7 no IE was computed.

Conclusion and summary

Three π -conjugated molecules fluorenyl, $C_{13}H_9$, diphenylmethylene $C_{13}H_{10}$ and diphenylmethyl, $C_{13}H_{11}$ were generated by pyrolysis from different precursors. Since both precursors were not completely converted at the applied pyrolysis temperature, the dissociative photoionization of both molecules was investigated first. The DPI of 9-bromofluorene, used as precursor for generation of fluorenyl, was examined, yielding an $AE_{0K}(C_{13}H_9Br, C_{13}H_9^+) = 9.4$ eV. It can be concluded from this value that a contribution to the radical signal can be neglected. The DPI of the α -aminodiphenylmethane, the precursor of $C_{13}H_{10}$ and $C_{13}H_{11}$ did not show significant contributions

in the mass channel of $C_{13}H_{10}^+$ and $C_{13}H_{11}^+$ and was thus not analyzed in detail. The threshold photoelectron spectra of the carbene and the two radicals were recorded and adiabatic ionization energies, which are summarized in table 4.2, were retrieved. The two TPE spectra, the one of fluorenyl and the spectrum of $C_{13}H_{11}$ enclosing the spectrum of $C_{13}H_{10}$, did not show distinct vibrational structures due to insignificant changes in geometries upon ionization. The simulated spectra and the experimental ones are in good agreement but are deviating to minor extent, since the contributions of internal rotations, hot and sequence bands is not included in the computed spectra. The signal intensities for both precursors and the formed species upon pyrolysis were comparably low, originating from the low vapor pressure of the precursor molecules. Furthermore the dimers $C_{26}H_{18}$ and $C_{26}H_{22}$ of the two radicals were detected and from their photoion yield curves and ms-TPES the adiabatic ionization energies were retrieved. The experimental values are in good agreement with the computed data and are summarized in table 4.2.

molecule	AE_{0K} (CBS-QB3)	AE_{0K} (experiment)
$C_{13}H_9Br$, $C_{13}H_9^+$	9.37 eV	9.4 eV
molecule	IE_{ad} (CBS-QB3)	IE_{ad} (experiment)
$C_{13}H_9$	7.01 ± 0.02 eV	7.17 eV
<i>t</i> - $C_{13}H_{10}$	6.8 ± 0.02 eV	6.77 eV
$C_{13}H_{11}$	6.7 ± 0.02 eV	6.60 eV
$C_{26}H_{18}$	7.69 ± 0.04 eV	7.79 eV
$C_{26}H_{22}$	8.13 ± 0.02 eV	7.99 eV

Table 4.2: Computed (CBS-QB3) and experimental values of AE_{0K} and IE_{ad} for $C_{13}H_x$ ($x=9,10,11$) isomers and their dimers.

5 Photoionization of $C_{14}H_{10}$, $C_{18}H_{12}$ and $C_{22}H_{16}$

Many Polycyclic aromatic hydrocarbons are not yet spectroscopically characterized and the IEs of the three closed shell polycyclic aromatic hydrocarbon 1,2-Dihydropyrylene (DHP), $C_{14}H_{10}$, 1-(Phenylethynyl)naphthalene (1-PEN), $C_{18}H_{12}$, and 1,2,7,8-Tetrahydrocyclopenta[fg,op]-tetracene (THCT), $C_{22}H_{16}$, were not known before. In the present work they were investigated by threshold photoelectron spectroscopy and they are presented in fig. 5.0.1. As it was discussed in the introduction, PAH are important intermediates in combustion processes. In fig. 1.0.1 (sec. 1), 1-ethynynaphthalene and acenaphthalene are shown, which are central products in the first steps of hydrogen-abstraction-and- C_2H_2 -addition to benzene. Thus, in a subsequent HACA reaction DHP and also 1-PEN can be easily formed. This means, that DHP, 1-PEN and THCT are central PAH structures in a possible mechanism on the way to the formation of soot.

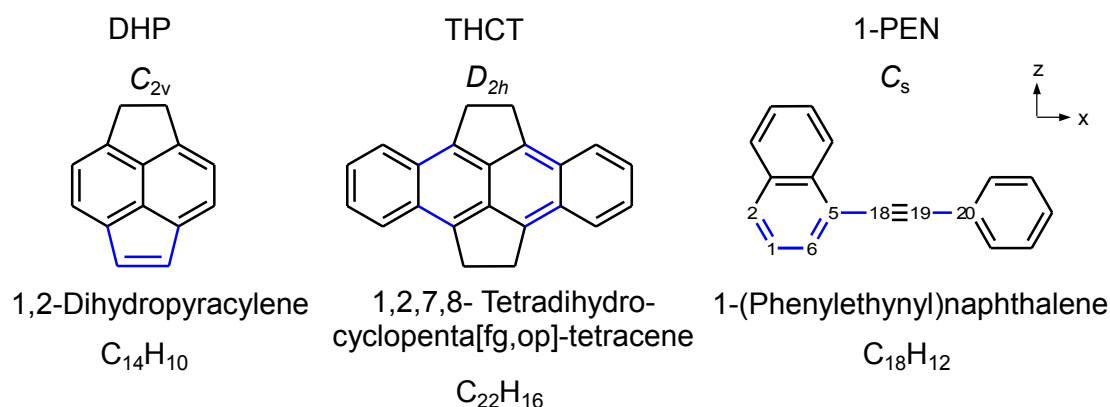


Figure 5.0.1: Molecular structures of the investigated polycyclic aromatic hydrocarbon molecules DHP, 1-PEN and THCT.

PAH with aliphatic side chains are in addition suggested to be the reason for high amounts of H-rich polycyclic aromatic hydrocarbon observed in soot.^[198] 1-PEN has been observed as the dimerization product of phenylpropargyl radicals, C_9H_7 , and is thus supposed to be an important PAH in combustion.^[178] Since PAH are generally assumed to be the carrier of DIBs, especially those with aliphatic

side chains have been proposed to be the reason for some infrared emission.^[199] Moreover, also in synthetical chemistry, 1-PEN was used to prepare larger polycyclic aromatic hydrocarbon.^[200] Beyond, DHP and THCT reveal non-regular moieties of graphene, carbon-nanotubes and fullerenes.^[201] Understanding their electronic properties is therefore important.

All molecules are solid substances which were synthesized by Johannes Auerswald in the group of Prof. Dr. Anke Krüger and transferred to the gas phase by an effusive inlet source (sec. 3.1.2). The PAH were examined by photoionization for two reasons. To investigate excited states in the neutral molecules via multiphoton ionization, the IE_{ad} has to be known. This value is most reliably retrieved from a (threshold) photoelectron spectrum. Moreover, intermediates in soot formation are often detected in flame-online mass spectrometry. The reliable assignment to a structure is only possible when ionization energies and ionic structures are known.

5.1 TPES of 1,2-Dihydropyrylene

The TPES of DHP is shown in figure 5.1.1. The solid sample was heated to 130 °C. Since, as expected, no other mass signal was visible in the investigated energy range, all photoelectrons were analyzed. The spectrum was recorded with an acquisition time of 90 s per data point and a step size of 10 meV. The Franck-Condon simulation, given in red with a fwhm of 25 meV is in good agreement with the experimental spectrum, but nevertheless deviates in some details. The first peak at 7.72 eV is assigned to the adiabatic ionization energy. It is computed to be 7.38 eV on the B3LYP/6-311g(d,p) level, somewhat lower than the experimental value. Three further peaks accompany the IE_{ad} at +70 meV, +120 meV and +170 meV. The first peak at +70 meV can be assigned to ν_{57}^+ , the in-plane stretching vibration along the z-axis (see fig. 5.0.1 for Cartesian coordinate system). This mode is computed to +60 meV / 482 cm⁻¹. Figure 5.1.2 shows the discussed active vibrations in the DHP cation. The peak following at +120 meV is more difficult to assign, since the corresponding simulated peak is predicted at +140 meV. It is dominantly caused by the two modes ν_{35}^+ and ν_{33}^+ , which reveal the C=C double bond stretching vibration in the annealed five-membered ring and the C-C stretching mode in the naphthalene moiety along the z-axis, respectively. The two modes are computed to 127 meV (1024 cm⁻¹) and 137 meV (1101 cm⁻¹), respectively. The simulated peak at +140 meV is supposed to correspond to the experimental peak at 7.84 eV. Therefore, the vibrations of the simulated peak might be computed too high in energy. This in turn can originate from deviating computed absolute geometry parameters in the cation, which correspond to these modes or it can originate from coupling with the first excited cationic state ²D₁.

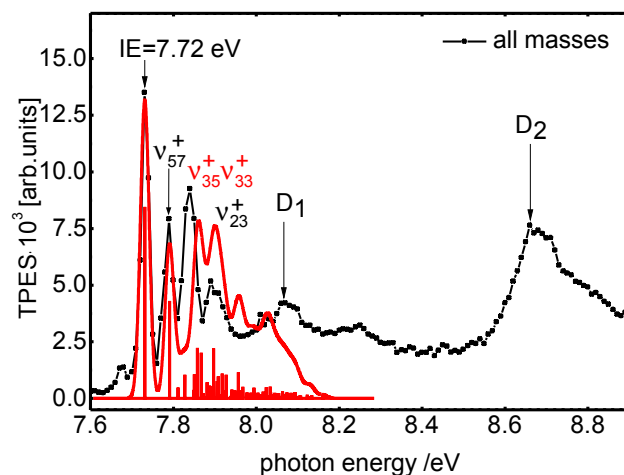


Figure 5.1.1: Threshold photoelectron spectrum of DHP (black line) and the simulated spectrum with a convolution (red line). The IE, several vibrations (v_n^+) and two excited cation doublet states (D_1 and D_2) are assigned.

The geometry changes that induce mode v_{35}^+ and mode v_{33}^+ have been described above and are highlighted in fig. 5.0.1. The overestimation of the frequencies in the computations can originate from an error in the computed bond lengths. With bond lengths computed to short the force-constants are overestimated, which subsequently leads to the prediction of higher frequencies.

The less intense experimental peak at +170 meV is also deviating from the simulated one in intensity. However, it can be assigned to mode v_{23}^+ , an in-plane deformation mode that is computed to 166 meV (1340 cm^{-1}). An additional peak is predicted by the simulation but not distinguishable in the spectrum at 7.96 eV. At 8.06 eV and 8.67 eV two more bands are visible that are most likely corresponding to excited states in the cation. The computed value for the first excited state in the cation is predicted at +0.65 eV above the ionization threshold, somewhat in between the two observed bands in the experiment. The geometry change upon ionization is most pronounced in the annealed five-membered ring with the C_2H_2 bridge. Here the $C=C$ double bond is predicted to increase by 8 pm, whereas the $C-C$ bonds, that connect the C_2H_2 bridge with the naphthalene moiety decrease by 6 pm. The respective bonds are visualized in blue in figure 5.0.1.

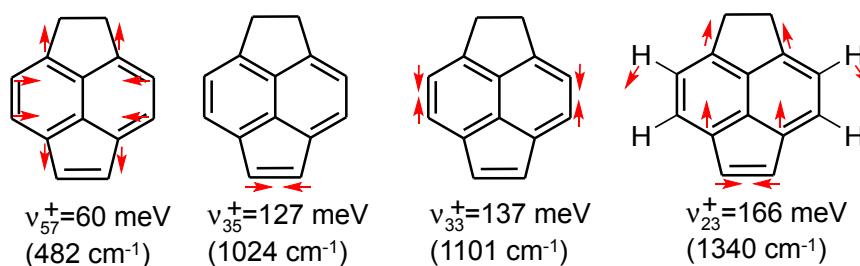


Figure 5.1.2: Active vibrations (v_n^+) of 1,2-dihydropyrycene upon ionization.

5.2 TPES of 1-(Phenylethynyl)naphthalene

The TPES of 1-PEN (black) is shown together with the Franck-Condon simulation of the cation ground state and the first excited state cation in figure 5.2.1. It was recorded with photon energy steps of 20 meV and an acquisition time of 5 min per data point. The signal starts to rise at 7.50 eV and the first maximum is reached around 7.6 eV. One further broad band is visible at around 7.8 eV. The computed IE_{ad} is 7.63 eV (CBS-QB3) and vertical excitation energies in the cation to higher electronic states are computed to +0.30 eV and +0.72 eV. The simulation of the transition to the ground state cation allows to retrieve a more accurate IE. The Franck-Condon factors were convoluted with a Gaussian function of 70 meV fwhm, which represents the best match with the experimental spectrum with an IE_{ad} of 7.58 eV. The two simulation show that several vibrations are active upon ionization to both cationic states but no dominant progression is observed. In addition, the bands are broadened due to a high amount of internal energy because an effusive beam was applied. The simulation of the transition to the first excited cationic state matches best when an origin of 7.76 eV assumed. To assign rather an intense vibration of the ground state cation is not plausible since the FC simulation does not indicate one.

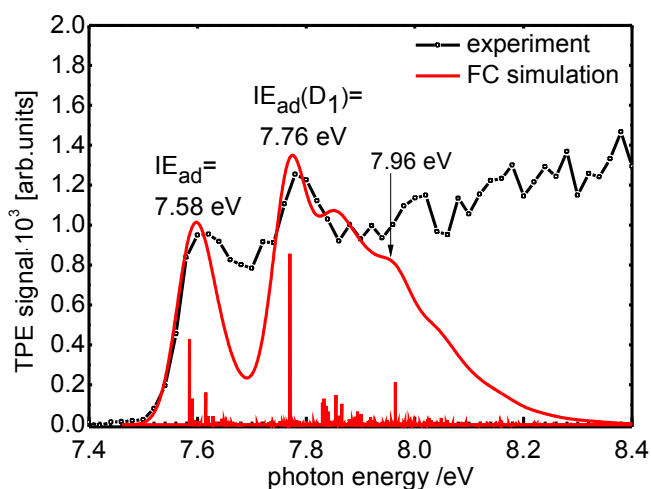


Figure 5.2.1: Threshold photoelectron spectrum of 1-PEN (black line) and the simulated spectrum presented in red.

Further vibrational assignment is not feasible because of the broad and unstructured spectrum. The bonds that change upon ionization to the cationic ground state are also highlighted in blue in fig. 5.0.1. The bonds C(1)-C(2) and C(5)-C(6) both increase by 2 pm and 3 pm, respectively, while the related bond C(1)-C(6) decreases by 2 pm. The two bonds C(5)-C(18) and C(19)-C(20) decrease by 3.2 pm and 2.5 pm and develop partially double bond character. The acetylenic bond C(18)-C(19) only increases slightly by 1.3 pm.

At higher photon energies further excited cationic states are detected up to 16 eV. Above, the

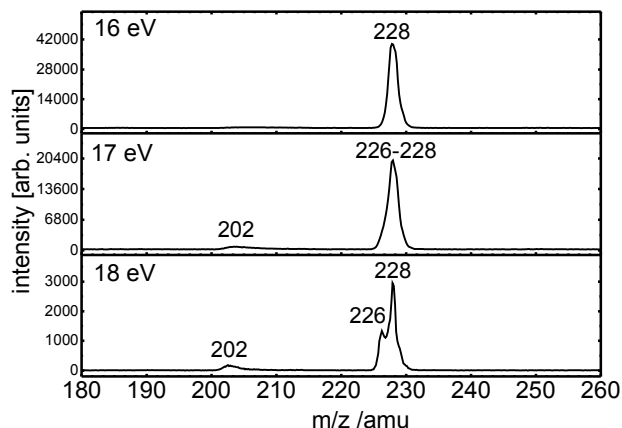


Figure 5.2.2: TOF-mass spectra of 1-PEN from 16 eV to 18 eV.

dissociative photoionization sets in around 17 eV. The TOF mass peak of 1-PEN at $m/z=228$ gets broadened because of the loss of H_2 (fig. 5.2.2, upper panel). Thus, also the mass signal at $m/z=226$ contributes to the signal at $m/z=228$. In addition a small broad signal at $m/z=202$ is detected, indicating to the loss of C_2H_2 . At 18 eV (fig. 5.2.2, middle panel) the signal at $m/z=202$ has grown slightly and two distinct peaks at $m/z=226$ and $m/z=228$ are visible. Note that the exit slits were reduced vertically to achieve a better mass resolution at the cost of the total signal intensity. Thus the peaks of $m/z=226$ and $m/z=228$ are resolved.

5.3 1,2,7,8-Tetrahydrocyclopenta[fg,op]-tetracene

Figure 5.3.1 shows the TPE spectrum of THCT recorded in the energy range from 6.3 eV to 7.3 eV with a photon energy step size of 10 meV and an acquisition time of 8 min per data point. The first and most intense peak is detected at 6.40 eV and is assigned to the adiabatic ionization energy of the molecule. It is accurate to within 20 meV. DFT computations yield an ionization energy of 6.02 eV, significantly lower than the experimental value. The red sticks represent the FC-factors for the various transitions into the ion, based on the optimized geometries of the neutral molecule and the ground state cation. The full red line displays the FC simulation with a full width at half maximum of 30 meV. As visible, it represents the low energy part of the spectrum rather well. There are two more bands at 6.58 eV and 6.78 eV that correspond to transitions into vibrational fundamentals of the cation.

However, they are not due to individual transitions, but rather to several overlapping ones that can be identified with the help of the FC simulation. The band at 6.58 eV is dominated by a C-H bend with a computed wavenumber of 1200 cm^{-1} and several in plane deformation modes with ring breathing character and computed wavenumbers between 1269 cm^{-1} - 1690 cm^{-1} . The modes are visualized in figure 5.3.2. Ring breathing vibrations often appear in photoelectron spectra of

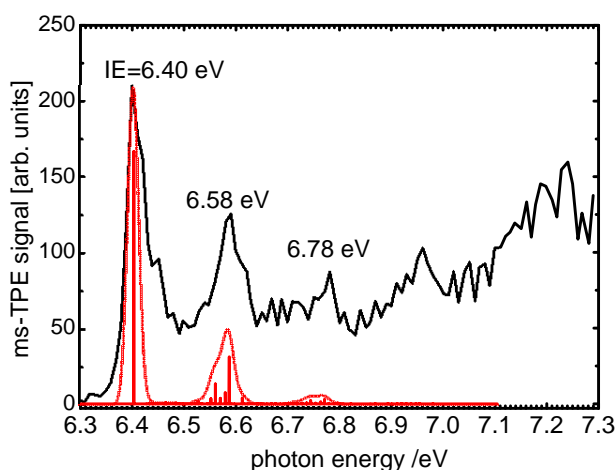


Figure 5.3.1: Ms-TPES of THCT. The adiabatic ionization energy is assigned to 6.40 eV.

aromatic compounds, because the bond order decreases upon removal of a binding electron from a π -orbital located on the aromatic ring. Overtones and combination bands of those modes also contribute to the second band at +0.38 eV (6.78 eV). Overall only limited vibrational activity is visible, indicating that the geometry change upon ionization is small. Due to the temperature of the molecule hot- and sequence-band transitions are expected to occur. Most likely, they are responsible for the broadening of the bands that is evident from a comparison with the simulation. A hot band is for example visible roughly 0.08 eV below the IE. As visible, the signal intensity starts to increase again at around 6.9 eV. Two further bands around 7 eV and 7.2 eV appear that are not matched by the simulations. Most likely, these correspond to transitions into excited states in the cation. The first excited state of the cation was computed to appear at +1.3 eV above the IE, significantly higher than the experimentally observed one. The geometry change upon ionization is rather insignificant: the most pronounced one is the elongation of the four equivalent C-C bonds in the naphthalene moiety by 2 pm. The respective bond is highlighted in blue in figure 5.0.1.

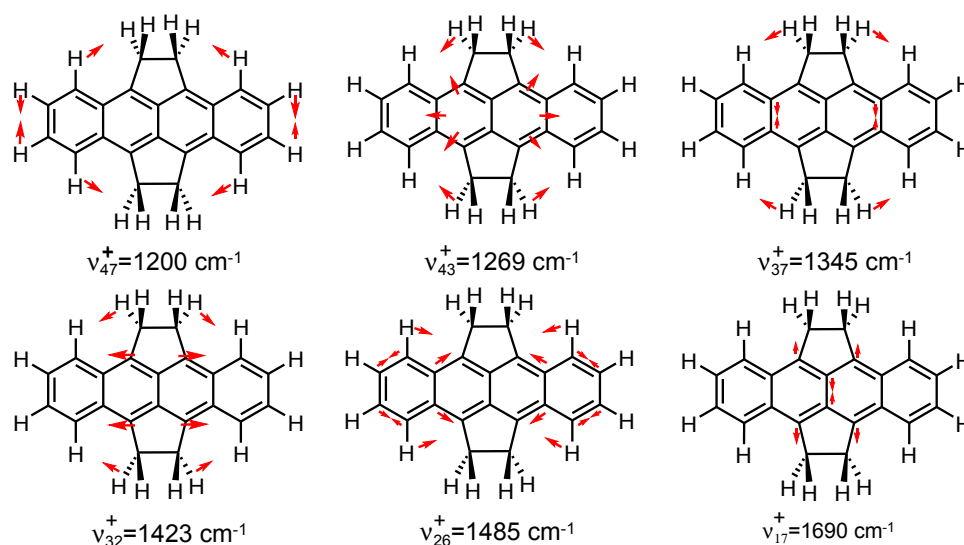


Figure 5.3.2: Vibrations (v_n^+) of 1,2,7,8-tetrahydrocyclopenta[fg,op]-tetracene.

Conclusion and summary

Three solid polycyclic aromatic hydrocarbon were investigated by VUV synchrotron radiation photoionization. Their threshold photoelectron spectra were analyzed and compared to the simulations. The adiabatic ionization energies were assigned and deviate from the computed values. The latter are predicted to be at least 0.4 eV lower than the experimentally observed values. However, it is well known that DFT computations performed with the B3LYP functional underestimate ionization energies.^[43] The more accurate CBS-QB3 method was not applied for all molecules since the cost in computational time is too high. Furthermore, vibrations were tentatively assigned. Moreover, several excited cationic states were observed for all three molecules. As expected for large highly conjugated molecules the excited cationic states were all observed close to the first ionization energy. However, the TD-DFT computations of the latter deviate significantly with the experimental values.

molecule	$IE_{ad}(\text{experiment})$	$IE_{ad}(\text{B3LYP}/6\text{-}311\text{g}(\text{d},\text{p}))$
$\text{C}_{14}\text{H}_{10}$	7.38 ± 0.02 eV	7.72 eV
$\text{C}_{18}\text{H}_{12}$	7.58 ± 0.05 eV	7.08 (7.63 eV ^a)
$\text{C}_{22}\text{H}_{16}$	6.4 ± 0.02 eV	6.02 eV

Table 5.1: Computed (B3LYP/6-311(g,p)) and experimental values for IE_{ad} of the investigated PAH. ^aCBS-QB3

6 Diazomeldrum's acid and its pyrolysis products

Diazomeldrum's acid (DMA) is an interesting molecule for different reasons: diazo-compounds are good precursors for reactive intermediates relevant in combustion and in astrochemistry.^[57,202,203] In a further context DMA reveals a model compound in the chemistry of the photochemically or thermally induced Wolff rearrangement (WR) (fig. 6.0.1).^[204] Because the photochemical aspects of this molecule have not yet been discussed in the introduction, they will be presented in the following section. When DMA undergoes a WR, 2,2-dimethyl-4,6-dioxo-1,3-dioxan-5-ylidene (fig. 6.0.1, carbene) and subsequently 2,2-dimethyl-5-carbonyl-1,3-dioxolan-4-one (fig. 6.0.1, ketene) are supposed to be formed. The WR proceeds via the formation of a carbene which further rearranges to a ketene, as it is shown in figure 6.0.1. N_2 is the thermodynamically most stable fragment that can be produced from the molecule in a thermally or a photochemically induced decomposition, while a reactive carbene is formed simultaneously. These characteristics of α -diazo-carbonyl compounds are for example utilized in deep UV positive photoresists,^[205] whereupon diazonaphthoquinones (DNQ) are widely applied. The working principle of a positive photoresist can be summarized as follows. The α -diazo-carbonyl compound is coated onto a substrate and exposed to light through a mask. The light induced Wolff rearrangement forms a ketene, which reacts with a suitable solvent (H_2O , MeOH) to form a soluble carboxylic acid or ester, which gets dissolved. The exposed regions of the substrate can then be selectively prepared by etching or metallization, which only works on the exposed regions and the photoresist is finally stripped.

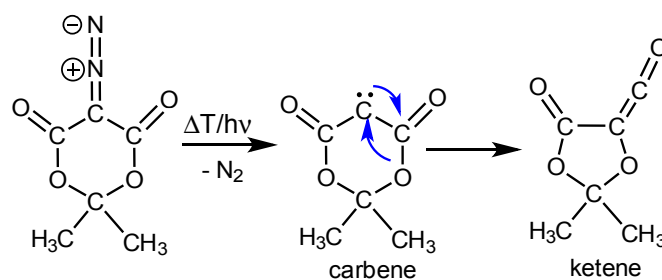


Figure 6.0.1: Reaction scheme of the Wolff rearrangement (WR) of diazomeldrum's acid (DMA).

Dominantly motivated by its ability to undergo this photochemically induced rearrangement reaction DMA has been part of several spectroscopic studies. Those comprise infrared spectroscopy,^[206] photolysis^[206–213] and thermolysis experiments^[209–213] in the liquid phase and laser ablation reactions on DMA doped polymer matrices.^[214–217] The studies mainly showed that DMA loses N₂ and undergoes a *Wolff rearrangement* (WR), a typical chemical rearrangement in α -diazo carbonyl compounds under thermal or photochemical treatment.

Time-resolved experiments on the rearrangement dynamics^[218–220] in the liquid phase and recently in the gas phase^[221] pointed out that the rearrangement's mechanism most likely proceeds with the loss of N₂ in a concerted way. This observation is also predicted by computational studies.^[209, 210, 222] A concerted rearrangement normally occurs very fast. Thus, the reaction in DMA is observed to happen on the femtosecond (fs)-timescale. However, indication for the formation of the carbene as a reactive intermediate upon fragmentation has also been found.^[219, 220] A pyrolysis experiment at 350 K showed that N₂ is cleaved from the molecule nearly completely leading to the main products of this reaction: acetone (m/z=58), N₂ (m/z=28), CO₂ (m/z=44). These molecules are expected to be the products of the dissociating ketene, that is formed in the WR. Thus, the WR is also proposed to occur upon pyrolysis.^[223]

As a consequence, in this work, DMA was investigated for two independent reasons: the thermal decomposition of DMA was probed by photoionization to identify the formed species and the dissociative photoionization was investigated on the purpose to observe the photochemical fragmentation in the DMA cation. In the experiments, the solid sample of DMA (5-diazo-2,2-dimethyl-1,3-dioxane-4,6-dione), purchased from TCI Europe (CAS 727-63-5), was used without further purification. The substance was heated in the molecular source shown in fig. 3.1.2, **C** up to 135 °C. The computed structure (ω B97xD/6-311g(d,p)) of DMA which has C_S symmetry is presented in fig. 6.0.2.

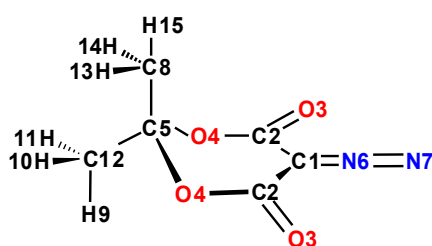


Figure 6.0.2: Structure of diazomeldrum's acid DMA with labels. The neutral molecule and the cation transform according to C_S symmetry.

6.1 Photoionization and dissociative photoionization of DMA

Figure 6.1.1 shows the TPE spectrum of DMA (grey), analyzed for all threshold electrons, in the energy range from 9.5 eV to 12.0 eV. The ms-TPES of $m/z=170$ (black) with the FC simulation (red) is shown up to 10.6 eV in the inset of fig. 6.1.1. Both spectra were recorded with a step size of 10 meV and an acquisition time of 80 s per data point. The dip in the spectrum at 10.03 eV is caused by a resonant absorption of krypton, used in the gas filter. The ionization energy (IE) is obtained from the first peak in the spectrum at (9.68 ± 0.02) eV, which is in good agreement with the computed value of 9.70 eV (CBS-QB3).

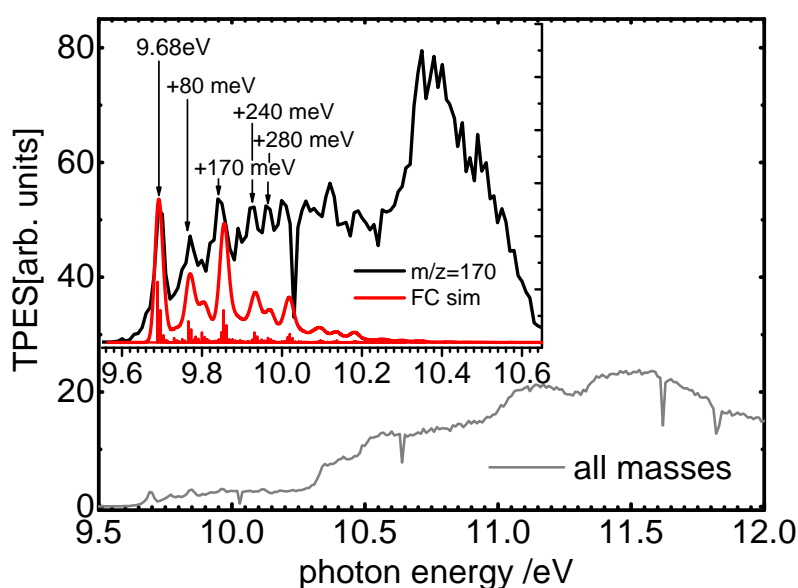


Figure 6.1.1: Threshold photoelectron spectrum of DMA (grey) in the energy range from 9.5-12.0 eV and the expanded view into the mass-selected spectrum (black) of DMA with the FC simulation (red) in the energy range from 9.55 eV to 10.6 eV in the inset. The spectrum has been recorded with a step size of 10 meV and an acquisition time of 80 s per data point.

Several vibrational bands appear in the spectrum, which are well represented by the Franck-Condon simulation shown as a red line in the inset of figure 6.1.1. Analysis of the FC factors shows that each band is due to a group of close-lying active modes. Most of them are very low intense (less than 7% of the intensity of the 0-0 transition). For that reason, only the most prominent vibrations (visualized in figure 6.1.2) of each band are assigned. The 0-0 transition is accompanied by a low-wavenumber progression of the mode ν_{48}^+ with a computed energy of 7 meV / 56 cm^{-1} , representing the bending motion of the C=N=N unit. It cannot be resolved in the spectrum. The breathing of the entire molecule causes the excitation of ν_{31}^+ (computed to 76 meV / 620 cm^{-1}), visible as the band at around +80 meV. The most intense transition at +170 meV is assigned to ν_{16}^+ (computed to 165 meV / 1333 cm^{-1}). The latter is best described by the stretching of the C-O bonds in the

ring. The most prominent vibrational activity in the band at +240 meV is due to the combination of the modes ν_{31}^+ and ν_{16}^+ . The bands at higher energies +280 meV and +320 meV originate from various further vibrational modes of the cation, as a result of the considerable change of several bond lengths and angles upon ionization. The C_s symmetry of the neutral molecule is retained upon ionization.

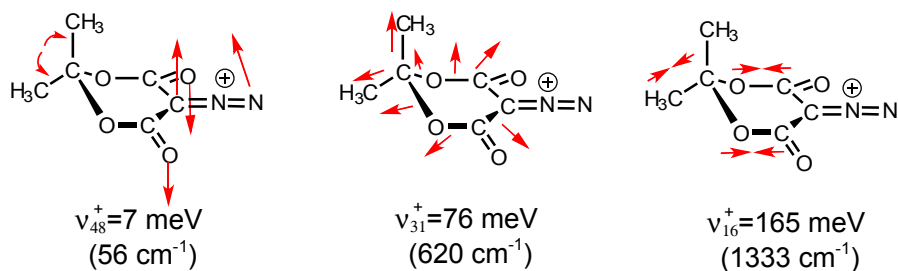


Figure 6.1.2: Most prominent vibrational modes in the DMA cation.

The six-membered ring shows an envelope-like structure with the $\text{C}(5)(\text{CH}_3)_2$ -moiety being allocated above the ring plane. For labeling of atoms see fig 6.0.2. The most pronounced geometry changes according to $\omega\text{B97xD/6-311g(d,p)}$ computations comprise the elongation of the $\text{C}(1)\text{-C}(2)$ bond by about 4 pm and the decrease of the $\text{C}(2)\text{-O}(4)$ bond by about 4 pm. The $\text{C}=\text{N}$ double bond has a length of 132 pm in the neutral and increases by 3 pm upon ionization, thus developing partial single bond character in the cation. Furthermore the $\text{C}(5)\text{-O}(4)$ bond increases by about 2 pm. In addition, the angle ($\text{C}(1)\text{-C}(2)\text{-O}(3)$) decreases about 5° and ($\text{O}(4)\text{-C}(2)\text{-O}(3)$) widens about 5° . Astonishingly, DFT computations with the B3LYP functional showed a distorted geometry for the DMA cation.

The deviation of the experimental and the simulated intensities in the spectrum of DMA can be explained with transitions originating from vibrationally excited neutral molecules. They contribute with hot bands to each transition. The threshold photoelectron (TPE) signal increases further beyond 10.2 eV, but the structure disappears. Most likely the signal is due to an electronically excited state in the DMA cation. In addition, in the non mass-selected TPES the signal rises further up to 12.0 eV (figure 6.1.1), which presumably originated from further excited states in the cation. However, since the structure is not very pronounced, no assignment is possible.

The mass selected TPE signal of DMA (black, inlet in fig 6.1.1) vanishes at around 10.65 eV. This means that further increase in the non mass-selected TPE signal (grey, fig. 6.1.1) by around 10.6 eV is associated with the fragmentation in the DMA cation. The fragmentation of the DMA cation is depicted in the breakdown diagram (6.1.3), which shows the fractional abundance of the parent

ion and the daughter fragments in coincidence with threshold electrons as a function of the photon energy.

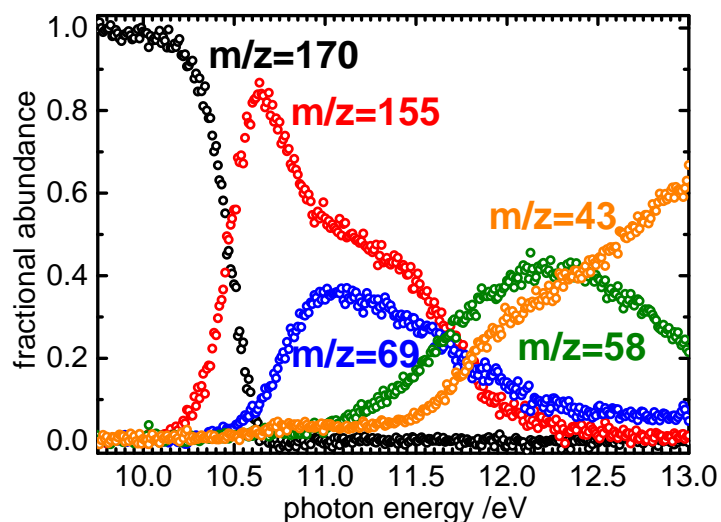


Figure 6.1.3: Breakdown diagram of the dissociative photoionization of DMA. The spectrum was recorded with a step size of 10 meV and with an acquisition time of 80 s per data point. In the energy range up to 13.0 eV four different fragment cations of $m/z=155$, $m/z=69$, $m/z=58$ and $m/z=43$ emerge.

The parent signal $m/z=170$ (black) starts to decrease at around 10.2 eV, while the first daughter fragment, $m/z=155$ appears, which corresponds to a methyl loss. At slightly higher energies a second parallel dissociation channel, $m/z=69$ (blue) emerges. Simultaneously, $m/z=155$ has already started decreasing at around 10.65 eV and the decrease slows at around 10.95 eV. When the parent signal $m/z=170$ has completely disappeared at 10.7 eV, a third dissociation channel at $m/z=58$ (acetone cation) opens up at around 11 eV. Around 12 eV the $m/z=155$ signal vanishes, because a sequential reaction channel to $m/z=43$ opens up, corresponding most likely to the acetyl cation. The signal at $m/z=69$ also starts to decrease at around 11 eV, but does not completely disappear. Below 12 eV $m/z=43$ originates either from a direct fragmentation of DMA or from a secondary decomposition of the initially formed fragment ion $m/z=155$. However, above 12 eV the acetyl signal at $m/z=43$ increases further, which can be explained by the sequential decomposition of the acetone fragment ion. Acetone is known to undergo dissociative photoionization to the acetyl cation. This respective appearance energy $AE_{0K}((CH_3)_2O, CH_3O^+)$ is observed at 10.56 eV^[224] which is 0.86 eV above the IE of acetone at 9.70 eV.^[225]

To elucidate the molecular structure of the fragment cations and the characteristics of the DPI (parallel or consecutive), computations were performed. In the first step a methyl loss occurs, forming the $m/z=155$ daughter ion. When performing relaxed redundant coordinate scans on the B3LYP/6-311g(d,p) level of theory for the loss of the C(8) methyl group and the C(12) methyl group,

iso-energetic transition states are obtained and the abstraction of either the C(8)- or the C(12)-methyl group leads to an identical product geometry of $m/z=155$. But, as evident from fig. 6.0.2, the two methyl moieties are not equivalent. The CBS-QB3 computations for the located TS yield an energy of 10.48 eV (fig. 6.1.4, structure B) referenced to the total energy of neutral DMA. The product energies of the cation $m/z=155$ and the methyl radical are computed to 10.50 eV, which is shown in the same figure as structure C. Thus, a barrier-less decomposition pathway is

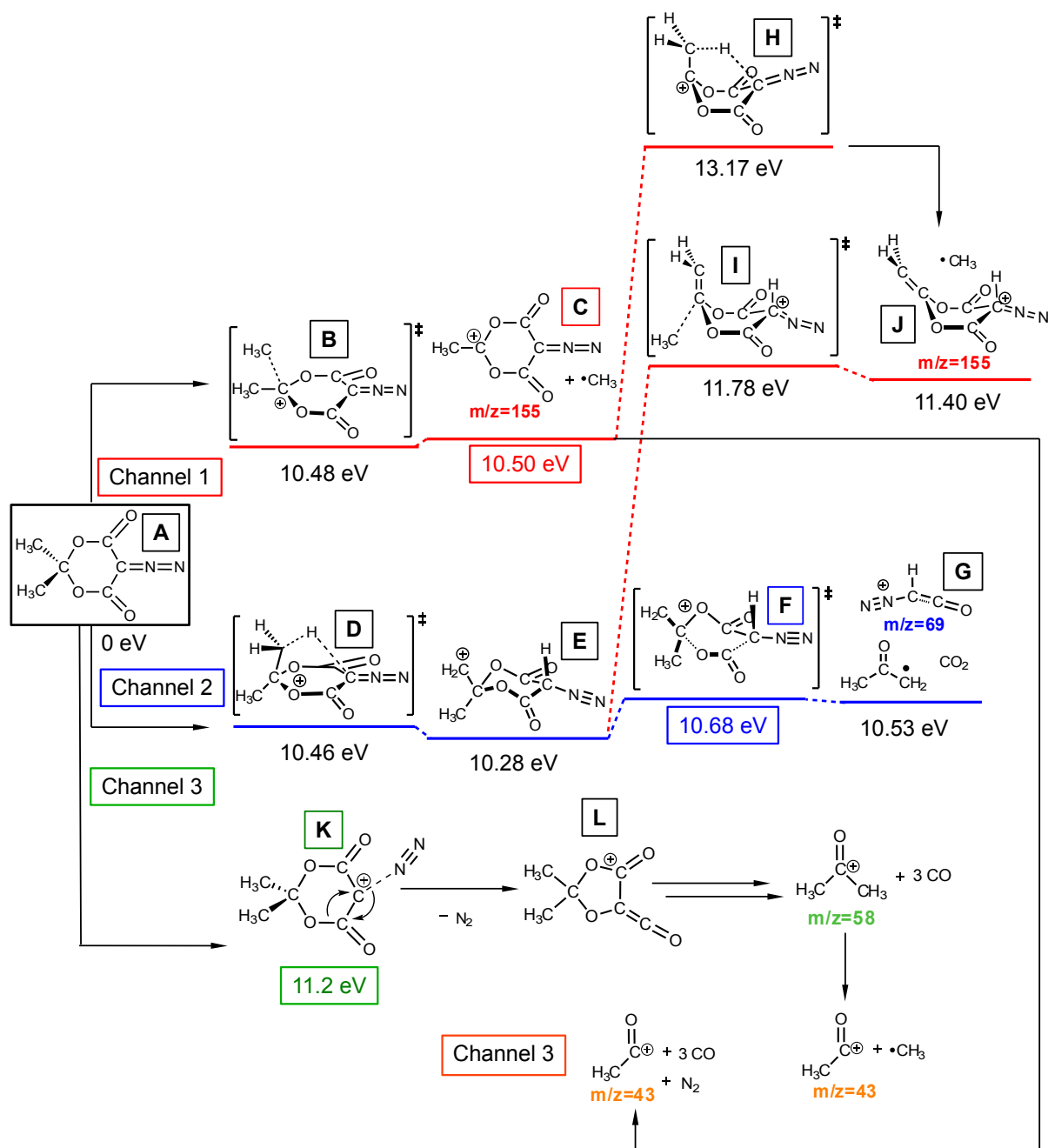


Figure 6.1.4: Schematic overview of the dissociation pathways in the DMA cation with the computed energies (CBS-QB3).

predicted and the appearance energy AE_{0K} is therefore computed to 10.50 eV. This value is calculated according to eq. 2.4.8, which corresponds to the difference of the product energies and the absolute energy of neutral DMA.

In contrast, B3LYP computes the TS with an energy of 10.05 eV referenced to the total energy of neutral DMA, while the product energies of the cation $m/z=155$ and the methyl radical are found at 9.93 eV (not shown in fig. 6.1.4). As a consequence a small reverse barrier of 0.12 eV (11.6 kJ/mol) is predicted.

The fast decrease of the signal $m/z=155$ at 10.65 eV can have two reasons: either the fragment dissociates further in a sequential reaction to $m/z=69$ or the signal drops because $m/z=69$ increases in a parallel process. To elucidate whether $m/z=69$ is generated in a parallel or a consecutive dissociation the identity of $m/z=69$ has to be clarified first. Two moieties of $m/z=68$ O(3)-C(2)-C(1)-C(2)-O(3) and N₂C(1)-C(2)-O(3) are present in the parent cation, thus the fragment $m/z=69$ has to be of the general composition N₂C₂OH or C₃O₂H. However, the formation of the $m/z=69$ cannot be associated with a simple bond breaking in the parent leading to N₂C₂OH or C₃O₂H. For both channels an H-atom shift has to occur in the parent cation prior the dissociation. To find the correct fragment cation all possible structures of mass 69 and the accompanying neutral fragments were computed. All computed structures are shown in fig. 6.1.5, **a-k**. The energy values stated in fig. 6.1.5 below each fragment represent the energy difference between the sum of products and neutral DMA. The sum of products includes the energy of the respective cation fragment and the neutral fragments that are simultaneously formed in the dissociation of the DMA cation. In addition, the energy values stated in fig. 6.1.5 correspond to the AE_{0K} of the respective fragment $m/z=69$, if the fragmentation does not have a reverse barrier. The computed preliminary AE_{0K} should have a value in the range of the fragments' $m/z=69$ (blue) appearance in the breakdown diagram (fig. 6.1.3), which is from 10.5 eV to 12.0 eV. Following this criterion, it is obvious that structures **d** and **e**, as well as the structures **j-n** (not highlighted in figure 6.1.5) can be ignored. Within these boundary conditions a search for the transition states of the H-atom migration to the rearranged parent cation that dissociates further to the appropriate fragment with $m/z=69$ **a-c** and **f-i** was conducted. The computed values are derived by subtracting the neutral molecules' zero point corrected electronic energy $E_0(P)$ from those of the transition state of the reaction $E_0(TS^+)$ to the fragment ion and the neutral fragment. Channel 2 in fig. 6.1.4 shows the most likely mechanism for the generation of fragment $m/z=69$. It includes a rearrangement initiated by an H-atom shift in the parent ion to C(1) with a transition state (fig 6.1.4, structure **D**) that is 10.46 eV higher in energy than the neutral parent. Any other H-atom shift to O(3),N(7) or C(2), which inevitably has to occur to form the fragments **a**, **c** and **g-i**, either has a transition state higher in energy than the one to C(1) or the relaxed PES scan leads to a distortion of the DMA cation. When the TS **D** is

passed, the fragments $m/z=69$ **b** or **f** (fig. 6.1.5) can be formed.

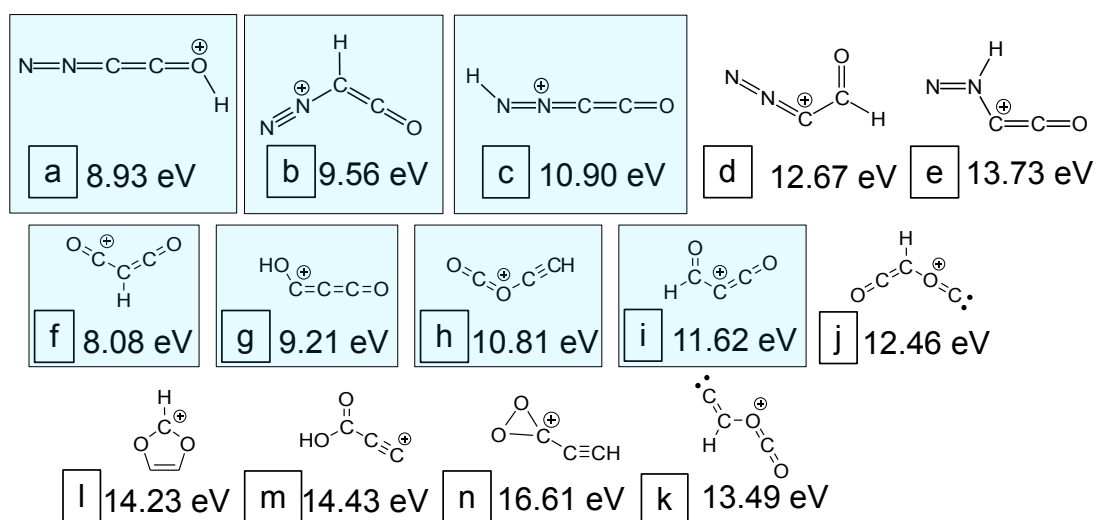


Figure 6.1.5: Computed structures of the compositions C_3O_2H and N_2C_2OH of the DPI channel to the fragment cation $m/z=69$. Energy values are preliminary appearance energies $AE_{0K}(\text{calc.})$, revealing the sum of the cationic fragment $m/z=69$ and the respective neutral fragments referenced to the neutral parent molecule DMA.

The rearrangement leads to a chair-like conformer **E** (fig. 6.1.4). The latter is computed to be (10.28 ± 0.02) eV higher in energy than neutral DMA. The dissociation of the $m/z=155$ isomer **E** to fragment **b** (figure 6.1.5) is computed to be significantly lower in energy than the competing dissociation pathway to fragment **f**. Thus, **E** dissociates to the fragment cation N_2CHCO^+ and the neutral fragments CO_2 and $CH_3(C=O)CH_2$ (**G** in fig. 6.1.4). Since there is a reverse barrier of 0.15 eV for this reaction, the experimentally observed AE_{0K} corresponds to the formation of the transition state **F** of the dissociation reaction at 10.68 eV. In addition, it has to be checked that a sequential dissociation via the fragment $m/z=155$ to $m/z=69$ is not energetically preferred over the parallel one. Thus, any H-atom shift, relevant for the formation of $m/z=69$ from $m/z=155$, has been computed, too. The lowest transition state has been located at 13.17 eV, which is significantly higher in energy than the parallel pathway in Channel 2 and is shown as structure **H** in figure 6.1.4. To conclude from this computations, the parallel pathway to $m/z=69$ is the one preferably observed. As visible in the breakdown diagram, the decrease of $m/z=155$ slows down at about 11 eV. It has to be considered that a second isomer of $m/z=155$ might be formed from the rearranged parent cation $m/z=170$ **E** (fig. 6.1.4). At higher internal energies isomer **E** might also loose CH_3 and form a $m/z=155$ isomer, that is shown as structure **J** in figure 6.1.4. The dissociation reaction to **J** passes the TS **I** (fig. 6.1.4) at 11.78 eV. This value corresponds to the appearance energy of the $m/z=155$

isomer **J**. Considering a thermal shift, which causes the fragment to be observed at lower energies than computed (sect. 2.4.5) the formation of **J** is a relevant explanation for the different slopes in the fractional abundance of $m/z=155$ (fig. 6.1.3, red). When the parent signal $m/z=170$ has completely vanished at around 10.7 eV, the channel to fragment $m/z=58$ (green) rises (fig. 6.1.3). This daughter fragment can neither be formed from the fragment $m/z=155$, nor from $m/z=69$. So it has to be formed in an additional parallel fragmentation from the parent cation. Mass 58 corresponds to the acetone cation. The thermodynamically most favored neutral fragments, formed simultaneously, are N_2 and 3 CO. It has already been stated that when N_2 is cleaved from the neutral molecule, acetone and CO are the main products and might be explained by a WR initiated reaction.^[223] A three dimensional potential energy surface, illustrating the elongation of the C(1)=N(6) bond while the C(1)-O(4) bond is shortened, is shown in fig. 6.1.6. The de-diazotation reaction, breaking of the C(1)=N(6) bond, lies roughly 2 eV higher in energy than the DMA^+ and attempts to optimize the carbene ion structure failed. Upon shifting the oxygen atom O(4) to the carbene carbon atom C(1), while the C(1)=N(6) bond is kept constant, the potential energy decreases and the ketene (fig 6.1.4, structure **L**) is formed. The landscape of the potential energy surface suggests a concerted reaction pathway (white arrows in figure 6.1.6). Roughly 1.5 eV internal energy is needed to reach the saddle point, instead of 2 eV for the N_2 loss coordinate and subsequent rearrangement. The ketene undergoes a further dissociation to acetone, which proceeds without a reverse barrier. Interestingly the WR does only play a role at higher internal energies of DMA^+ , whereas in the neutral it is the most prominent reaction. In the breakdown diagram acetone is observed as the direct product of the WR after an internal energy of +1.5 eV (144 kJ/mol) is deposited in the parent cation.

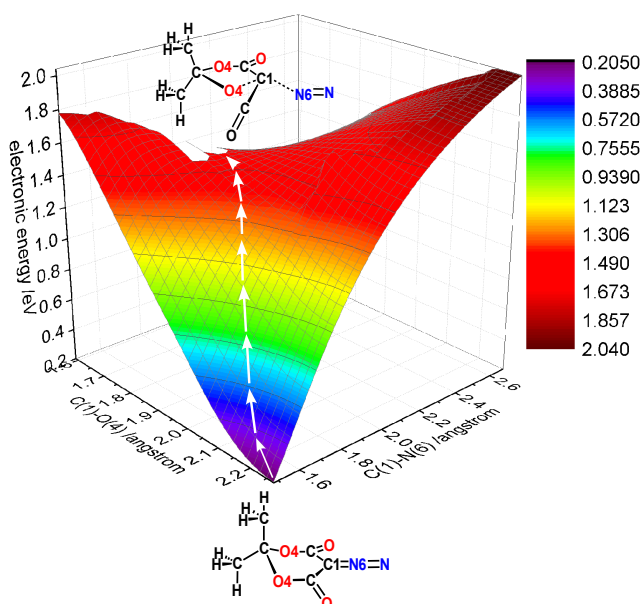


Figure 6.1.6: 3D PES for the loss of N_2 and the concerted rearrangement of the carbene to the ketene in the Wolff rearrangement. At 0 eV the DMA^+ cation is shown and in the region of the transition state the most likely transition state structure is depicted.

This is remarkable, since the C(1)=N(6) bond length is computed to increase upon ionization and therefore the stability of the C(1)=N(6) bond is supposed to decrease. Because the WR in the cation to the ketene needs more energy than the subsequent dissociation to the acetone fragment, the appearance energy of $m/z=58$ is computed to the WR's energy at 11.2 eV.

The fragment $m/z=43$ corresponds to the formation of the acetyl cation. Below 12 eV $m/z=43$ originates either from a direct fragmentation of DMA or from a secondary decomposition of the initially formed fragment ion $m/z=155$, because from $m/z=69$ no fragment with $m/z=43$ can be formed. However, above 12 eV the acetyl signal at $m/z=43$ increases further and originates from the sequential decomposition of the acetone fragment. Due to this ambiguous origin of $m/z=43$ no detailed computations on its formation were performed. The appearance energy is influenced by several mechanistic steps, making it difficult to fit the breakdown data to a statistical model. So only the low energy channels were modeled employing RAC-RRKM statistical rate theory (sec. 2.4.4/2.4.5).

To fit the data, the program *mPEPICO* (2.4.4 and 2.4.5) was applied. Some more details, including the input-file for the *mPEPICO* program and a list of all the computed data and their format in the input file, are presented in the appendix. The modeled TOF-distributions, from which the energy dependent rate information is retrieved and the breakdown diagram are presented in fig. 6.1.7. From the modeled experimental data we derived appearance energies for the first two fragment ions to be 10.65 eV and 10.72 eV for $m/z=155$ and 69, respectively. The experimental numbers agree well with the quantum chemical computations (see table 6.1), supporting the assumed reaction mechanisms. The reverse barrier in dissociation channel 1, predicted by computations on the B3LYP/6-311g(d,p) level, was not considered in the analysis of the methyl loss channel, since its impact is supposed to be negligibly small. In addition, the BDE of the C-C bonds can be tentatively determined to 0.82 eV (79 kJ/mol). Since the dissociation channel 2 includes transition states with a reverse barrier, a bond dissociation energy cannot be derived from the AE_{0K} of $m/z=69$.

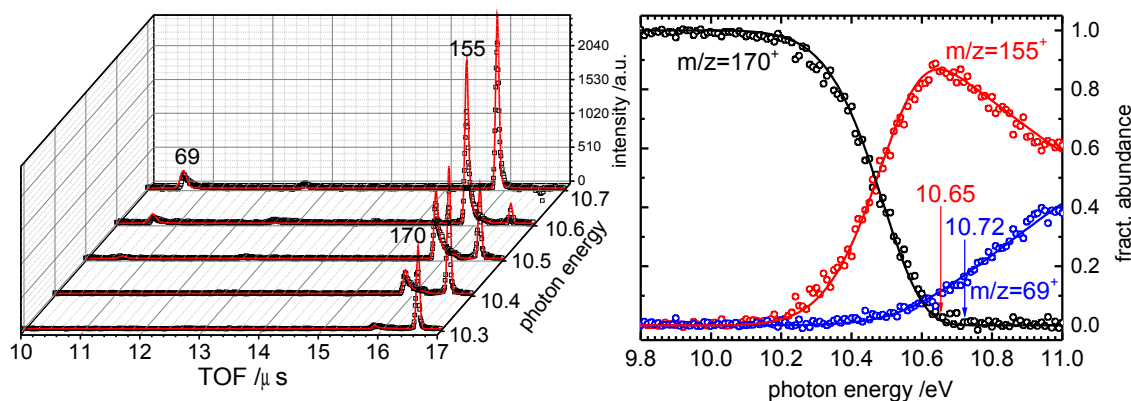


Figure 6.1.7: TOF-distributions (left) and breakdown fit of the the low energy channels $m/z=155$ and $m/z=69$ (right).

6.2 Thermal decomposition upon pyrolysis

The decomposition upon pyrolysis at 350 K was observed to yield N_2 , CO and acetone as the main products. The products were interpreted as an indication for the Wolff rearrangement.^[223]

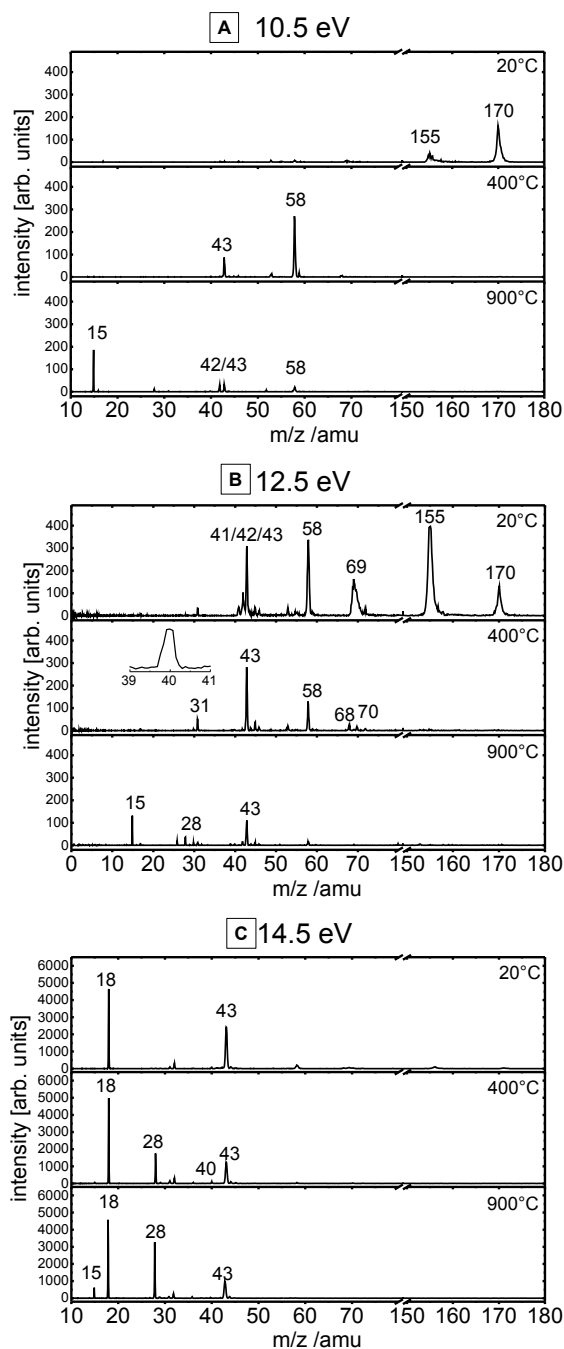


Figure 6.2.1: TOF-MS at 10.5 eV, 12.0 eV and 14.5 eV recorded at different pyrolysis temperatures.

In a first set of pyrolysis experiments the temperature dependence on the decomposition behavior of DMA has been examined (fig. 6.2.1). Mass spectra at 10.5 eV (A), 12.5 eV (B) and at 14.5 eV (C) were recorded at each photon energy for the temperatures 20 °C, 400 °C and 900 °C. At 10.5 eV (fig. 6.2.1, A) and 20 °C the precursor $m/z=170$ partially undergoes DPI to $m/z=155$, but is completely converted to pyrolysis products already at 400 °C since no precursor signal $m/z=170$ is visible anymore. Here the masses 58 and 43 are the dominant products. In contrast at 900 °C $m/z=15$ comes up, the mass peaks of 58 and 43 are getting smaller and $m/z=42$ emerges. In the mass spectrum B at 12.5 eV at 20 °C further fragments of the precursor's ($m/z=170$) DPI are visible: $m/z=155$, $m/z=69$, $m/z=58$ and the masses 41/42/43. At 400 °C the precursor signal has vanished and in addition $m/z=31$ comes up and small traces at $m/z=68$ and $m/z=70$ are visible. At 900 °C $m/z=15$ and the masses 26, 28, 30 and 42 are formed upon thermal treatment. At 14.5 eV (mass spectra C) in addition to the products observed for lower photon energies, mass 18 and mass 28 show significant peaks at any temperature. The signal of $m/z=43$ has increased in contrast to the low energy spectra and mass 58 has completely vanished. A tiny signal of $m/z=40$ becomes visible at 400 °C.

Analysis of pyrolysis products by mass-selected TPES

In order to identify the species visible in the spectra of fig. 6.2.1, the TPE signals were evaluated. For some species no data including the ionization onsets, were collected. Thus, they were not identified. In addition, the TPE spectra of some pyrolysis products discussed below are well known from the literature. Consequently, the latter were not evaluated in this work.

The dominant pyrolysis product at low photon energies is $m/z=58$, which corresponds to acetone. The photoelectron spectrum and the ionization energy at 9.70 eV of acetone is very well known.^[225,226] The acetyl cation ($m/z=43$) is produced upon dissociative ionization of vibrationally and rotationally hot acetone. The appearance energy AE_{0K} (acetone, H_3C-CO^+) is known to be $AE_{0K}=10.56$ eV.^[224] The signal in the mass spectrum visible at 10.5 eV can be explained by the increased thermal energy distribution in the neutral, which leads to a red shift of the fragmentation threshold. At 20 °C, both the signals of acetone and ($m/z=58$) acetyl ($m/z=43$) originate from the DPI of the precursor $m/z=170$. $M/z=15$ is assigned to methyl CH_3 that is formed upon higher pyrolysis temperatures. Masses 42 and 41 are supposed to be the products of the H-loss and H_2 -loss from the acetyl cation. All masses at any photon energy at 20 °C are fragments of the precursor's DPI that has been discussed previously (6.1). The masses 30, 31 and 36 were not identified, since their TPE signals were of insufficient quality. $M/z=18$ and $m/z=32$ correspond to H_2O and O_2 . The latter can be a product of pyrolysis, but most likely both molecules are residuals in the experimental chamber. $M/z=28$, visible at higher temperatures at 14.5 eV, indicates the cleavage of CO from the DMA molecule. N_2 can be excluded as the carrier of $m/z=28$, since it has an ionization energy of 15.60 eV.

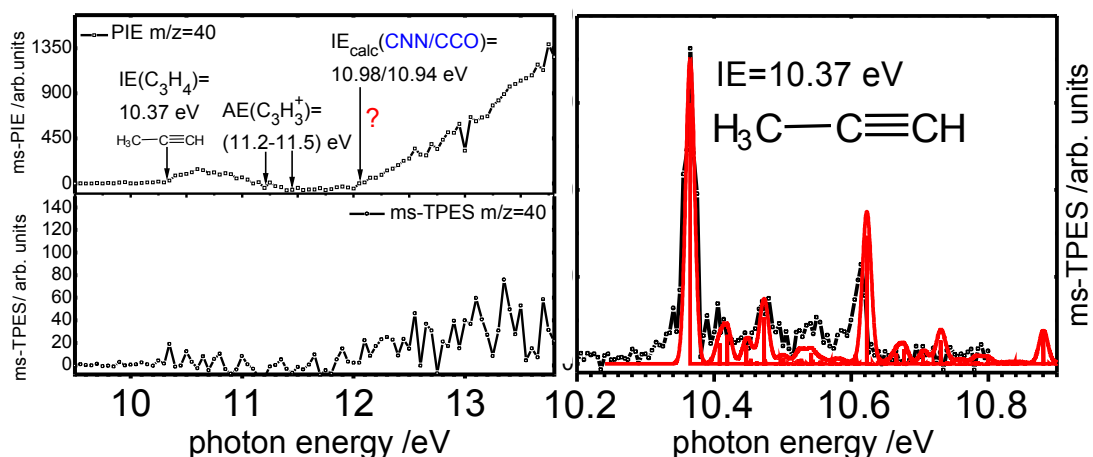


Figure 6.2.2: TPES and PIY curve of the pyrolysis product $m/z=40$. The ms-PIY curve and the ms-TPES in the energy range from 9.5 eV up to 13.8 eV has been recorded with step size of 50 meV and with an acquisition time of 120 s per data point. The TPES on the right was recorded from 10.2 eV to 10.9 eV with a step size of 5 meV with an acquisition time of 60 s per point.

The signal of $m/z=40$ can be of different origins: at low photon energies the very tiny signal of mass 40 (visible in the inlet in B, 400 °C in fig. 6.2.1) is identified as propyne, $\text{CH}_3\text{C}\equiv\text{CH}$. This is confirmed by the TPES in figure 6.2.2 (right). This spectrum has been recorded at a pyrolysis temperature of 500-600 °C, a step size of 5 meV and with an acquisition time of 60 s per data point. The total photoionization cross section of propyne ($2.3 \cdot 10^{-17} \text{ cm}^2 @ 10.5 \text{ eV}$ ^[227]) is observed twice as large as the one of acetone ($1.1 \cdot 10^{-17} \text{ cm}^2 @ 10.5 \text{ eV}$ ^[228]). Therefore, the very small ratio of propyne's mass signal compared to the signal at $m/z=58$ in the mass spectra at 10.5 eV/400 °C points at the huge amounts of acetone, that are formed in the pyrolysis. The mass-selected PIY curve and the mass selected TPES, that are shown in the upper and the lower panel of fig. 6.2.2 on the left were recorded with a step size of 50 meV and with an acquisition time of 120 s per data point. The PIY signal of 40 increases around 10.4 eV according to the ionization threshold of propyne and decreases at 11.5 eV. Propyne is known to lose an H-atom in the DPI around 11.58 eV,^[229] in agreement with the observations in fig. 6.2.2. The signal $m/z=40$ rises again intensively at around 11.9 eV, indicating that a different species than propyne might be the carrier of mass 40. Two further plausible pyrolysis products corresponding to mass 40 are the species $\text{C}=\text{N}=\text{N}$ and $\text{C}=\text{C}=\text{O}$. The ionization energies of both species are computed (CBS-QB3) to 10.98 eV (CNN) and to 10.94 eV (CCO). The second onset in the PIE in figure 6.2.2 is at 11.8 eV, nearly 1 eV higher than the computed IE of the two molecules. Concluding from these values, CNN and CCO are not visible in the spectra. The intensity of the second rise, in comparison to the first onset in the PIE, also appears more typical for a fragment formed in a DPI process. Unfortunately the TPE signal in this energy region (fig. 6.2.2, lower panel) shows a poor S/N so that no additional information is retrieved.

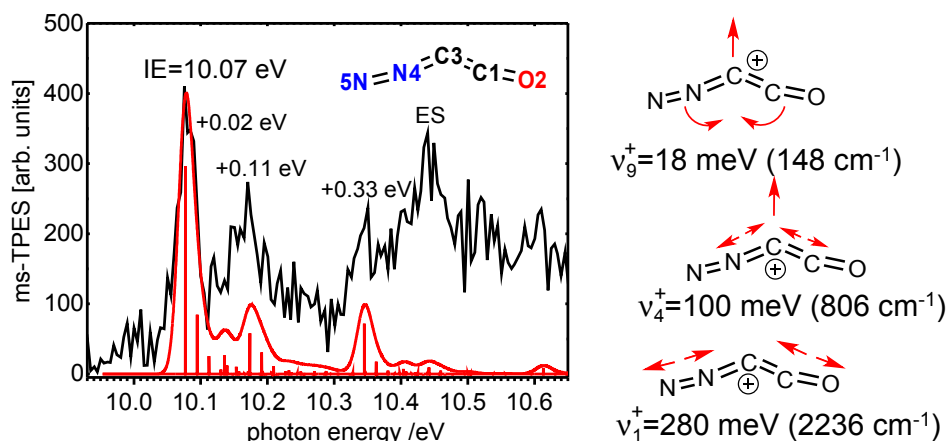


Figure 6.2.3: Ms-TPES of the fragment $m/z=68$ $\text{N}=\text{N}=\text{C}=\text{C}=\text{O}$, 2-diazoethenone and Franck-Condon simulation (fwhm=25 meV). The molecular structure of 2-diazoethenone is shown in the inset and the most important vibrations that are excited in the cation upon ionization are presented on the right hand-side.

A tiny $m/z=68$ signal is visible at 10.5 eV with mild pyrolysis conditions. It has already been shown in fig. 6.1.5 that two moieties of $m/z=68$, $\text{N}=\text{N}=\text{C}=\text{C}=\text{O}$ and $\text{O}=\text{C}=\text{C}=\text{C}=\text{O}$, are present in the DMA molecule. The ms-TPES of $m/z=68$ is shown in figure 6.2.3 and has been recorded with a step size of 5 meV and with an acquisition time of 300 s per data point at a pyrolysis temperature of 200 °C. Since 1,2-propadiene-1,3-dione C_3O_2 ($\text{O}=\text{C}=\text{C}=\text{C}=\text{O}$) is well investigated and possesses an IE of 10.6 eV,^[230] it can be ruled out as the major carrier of the spectrum. However the calculated IE (CBS-QB3) of 2-diazoethenone $\text{N}=\text{N}=\text{C}=\text{C}=\text{O}$ (see inset in fig. 6.2.3) is 10.07 eV and matches the experimental onset in the ms-TPES (fig. 6.2.3). For a comparison of experimental and computational results see table 6.1. In addition a Franck-Condon simulation was carried out and agrees well with the lower energy part of the spectrum, confirming the assignment of 2-diazoethenone as the carrier of the spectrum. In addition, the by-products in the formation of $\text{N}=\text{N}=\text{C}=\text{C}=\text{O}$ are the thermodynamically stable molecules acetone and CO_2 (*vide infra*).

According to the FC simulation the 0-0 transition is broadened by a symmetric N(4)-C(3)-C(1) bending mode ν_9^+ , which cannot be resolved because of its low energy of around +20 meV (computed 18 meV / 148 cm^{-1}). Mode ν_9^+ appears also with its first and second overtone at higher energies. The band around +110 meV (computed 100 meV / 806 cm^{-1}) is dominated by ν_4^+ , the C(3)=N(4) and the C(3)=C(1) double bond stretching vibration (for labeling of atoms see the structure in Figure 6). The band at around +330 meV (computed 280 meV / 2236 cm^{-1}) is assigned to ν_1^+ , a symmetric stretch of the N(5)=N(4) and the C(1)=O(2) bonds. The vibrations are visualized on the right hand side of fig. 6.2.3. The signal rises again at around 10.45 eV. Since this rise is not reflected by the FC simulation, the band at 10.48 eV is assigned to the first excited state in the radical cation. TD-DFT/B3LYP computations indeed locate the first excited state at +0.44 eV (10.52 eV) above the ionization threshold. The molecule transforms according to C_s symmetry as

neutral molecule and in the cation. The bent structure is indicated by the inlet of figure 6.2.3. Upon ionization the length of the N=N bond does not change significantly, the N(4)=C(3) double bond increases by 3 pm, C(1)=O(2) decreases by 3 pm and C(3)=C(1) increases by 6 pm during ionization. In addition the C(3)-C(1)-O(2) and C(3)-N(4)-N(5) angles decrease by 3.7 ° and 3.3 ° respectively, and C(1)-C(3)-N(4) decreases by 10.6 °. Up to photon energies of 14.0 eV the PIE signal of $m/z=68$ (not shown here) does not vanish. Consequently, the DPI of the molecule was not observed in this work.

The temperature of the experiment (200 °C) provides considerable energy for rearrangement reactions upon pyrolysis. Thus, isomerization of pyrolysis products always have to be considered in the analysis of mass selected TPES. For completeness and to be sure that no other isomer of N_2C_2O and C_3O_2 is coincidentally formed, the ionization energies of further possible structures were computed, too (fig. 6.2.4).

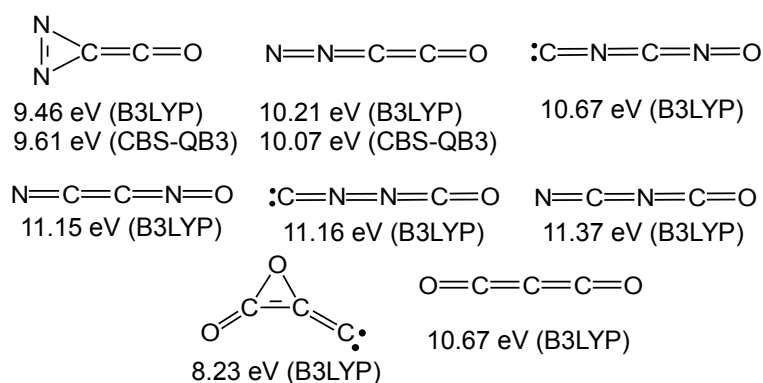


Figure 6.2.4: Schematic overview of the possible structures $m/z=68$.

From the computations can be inferred that presumably no other structure of $m/z=68$ has an IE to contribute to the the spectrum in the observed energy range. However, it has to be taken into consideration that in the energy range of 10.5-10.6 eV the intensity in the threshold electron signal is high. Thus, if a different pyrolysis product with $m/z=68$ contributed to the spectrum in this energy range, the intensity of the TPE signal, originating from the excited state at 10.45 eV of 2-diazoethenone might be too high to recognize the onset of the further species. Thus, the contribution of C_3O_2 with an IE at 10.6 eV cannot be excluded at higher energies.

It is somehow surprising that the molecule $N=N=C=C=O$ is formed in the pyrolysis as a stable product. Since N_2 is a thermodynamically favorable decomposition product, the formation of 2-diazoethenone demonstrates the strength of the C=N bond in the parent molecule. 2-diazoethenone has not yet been directly observed experimentally. Only tentative hints on the *in situ* formation in a reaction of phosgene and diazomethane have been achieved by IR spectroscopy.^[231] Such small chain molecules that are shown in fig. 6.2.5 are expected to be present in the interstellar clouds. They are

assumed to be formed in ion-neutral or radical-radical reactions of C_2H , probably the most abundant hydrocarbon radical in the interstellar space,^[232] with other different abundant stable molecules like N_2O ,^[233] NH_3 ,^[234] HCN or H_3CCN .^[235] These reactions are nearly barrierless and hence of potential importance in those regions.^[233] Among the presented structures of the potentially formed molecules, the survey in fig. 6.2.5 shows also $C=C=N=N=O$, an isomer of 2-diazoethenone, which is predicted to be a stable species formed in the reaction of C_2H and N_2O after H-atom loss from the initial product.

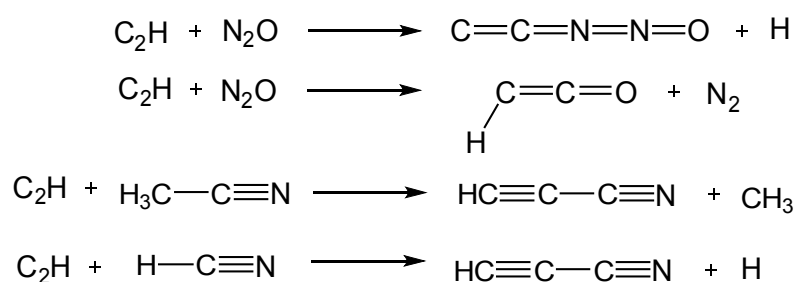


Figure 6.2.5: Examples of astrochemical relevant species, related to 2-diazoethenone. The presented molecules are expected to be formed in bimolecular reactions of C_2H and N_2O / HCN / H_3CCN in interstellar clouds.

It appeared furthermore astonishing that the diazocarbene $C=N=N$ and ketenylidene radical $C=C=O$, both further interesting species that are assumed to be reactive intermediates in combustion processes,^[236–238] were not detected in the present experiments. Both ionization energies were computed with CBS-QB3 to 10.95 eV (CCO) and 10.98 eV (CNN) and they were also expected to be formed upon thermal decomposition of DMA. However, a formation of these species cannot be excluded from the present experiments, since no TPES was recorded at higher pyrolysis temperatures than 600 °C, where the two molecules are expected to be formed.

Another small mass signal barely visible in the mass spectra (fig. 6.2.1) is $m/z=70$. The ms-TPES of $m/z=70$ has been recorded at a pyrolysis temperature of 200 °C with a step size of 10 meV and an acquisition time of 120 s per data point and is depicted in figure 6.2.7 and 6.2.8. The most plausible compositions of $m/z=70$ are $N_2C_2OH_2$ and $C_3O_2H_2$ that might be formed by two H-atom shifts in the parent molecule. When $N_2C_2OH_2$ is formed, the respective other pyrolysis products are $CO_2 + H_3CH(=O)$ or $O_2 + CO + HC\equiv C-CH_3$. With the formation of $C_3O_2H_2$ the further molecules formed at the same time are $N_2 + O_2 + HC\equiv C-CH_3$. For the reason of stable product formation for both structures $N_2C_2OH_2$ and $C_3O_2H_2$, none of these two general compositions can be excluded instantly. Thus, in order to identify the carrier of the peak, the ionization energies of 31 different structures of the compositions $N_2C_2OH_2$ and $C_3O_2H_2$ were calculated (fig. 6.2.6).

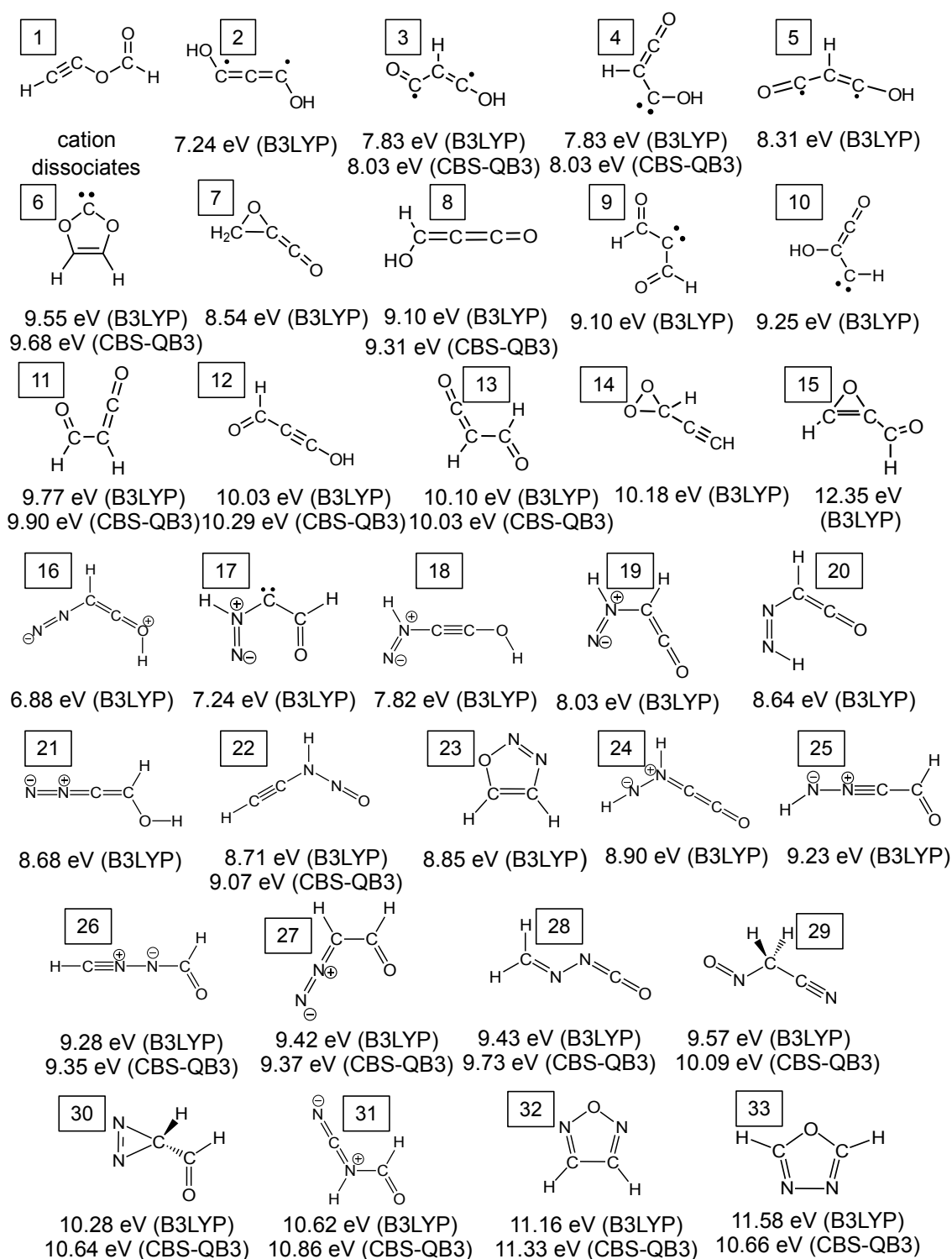


Figure 6.2.6: Structures and ionization energies of the computed isomers of $m/z=70$ with the molecular compositions $C_3O_2H_2$ and $N_2C_2OH_2$.

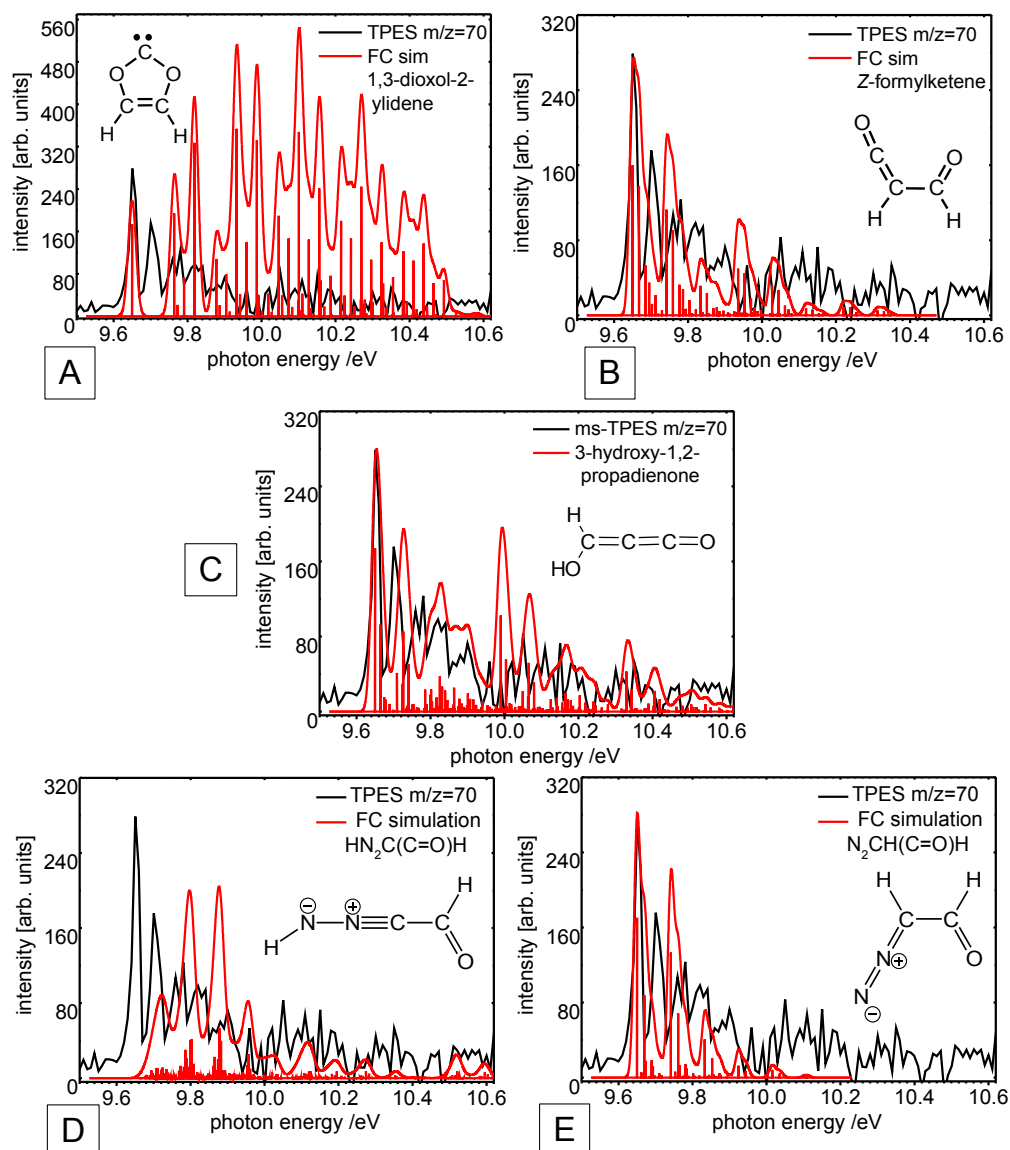


Figure 6.2.7: Ms-TPES of $m/z=70$ with five different FC simulations.

The IEs as well as the simulated threshold photoelectron spectra of the computed structures were compared to the experimental data. The TPES, shown in fig. 6.2.7 and fig. 6.2.8, shows the first peak at 9.65 eV, which is assigned to the ionization energy of $m/z=70$. One of 31 computed species (fig. 6.2.6, 6) has the IE at 9.68 eV, which is in agreement with the experimental value. However, the convolution of the FC simulation of 1,3-dioxol-2-ylidene, (fig. 6.2.6, 6) disagrees with the experimental spectrum (fig. 6.2.7, A).

Hence, the other fragments (fig. 6.2.6) with the least deviating predicted IEs were considered. Their Franck-Condon simulations were superimposed with the experimental spectrum, as shown in fig. 6.2.7. The simulation's 0-0 transition was shifted to the experimental 0-0 transition at 9.65 eV. The simulations of the $m/z=70$ isomers Z-formylketene (IE=9.90 eV, 11 in fig. 6.2.6), 3-hydroxy-

1,2-propadienone (IE=9.31 eV, 8 in fig. 6.2.6), HN₂C(CHO) (IE=9.23 eV, 25 in fig. 6.2.6) and N₂CH(CHO) (IE=9.37 eV, 27 in fig. 6.2.6) are presented in the graphs **B-E** in figure 6.2.7. None of the simulations shows an acceptable agreement with the experimental spectrum.

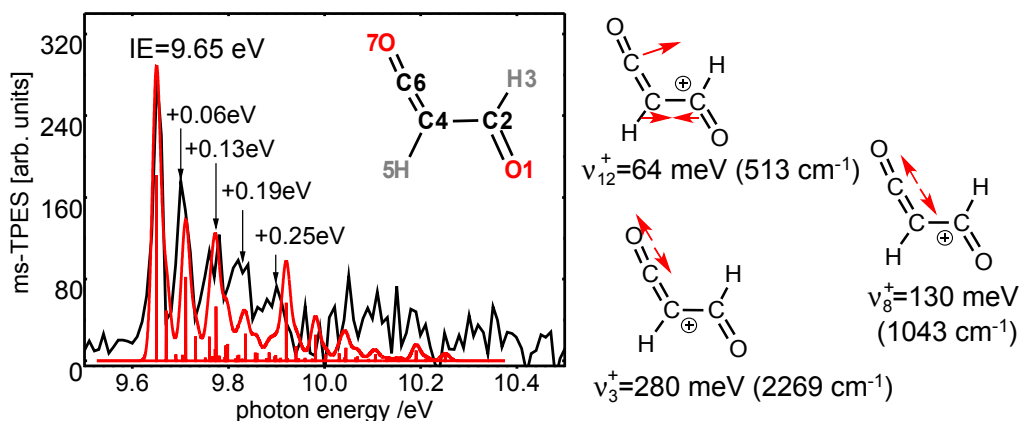


Figure 6.2.8: Ms-TPES of *E*-formylketene. In the inset the molecular structure and on the right hand side the most pronounced vibrations upon ionization of *E*-formylketene are visualized.

Finally, the molecular structure which gave the best match is *E*-formylketene, shown in the inset of figure 6.2.8. A Franck-Condon simulation based on the computations is also depicted in the figure. The spectrum agrees well with the simulations. The first peak at 9.65 eV is assigned to the IE_{ad} with an assumed error of ± 0.02 eV. The peak at around +60 meV (computed $v_{12}^+ = 64$ meV / 513 cm⁻¹) corresponds to the excitation of the C(2)-C(4) stretching mode (for labeling of atoms see the structure in fig. 6.2.8). The C(4)=C(6) double bond stretching vibration, (computed $v_8^+ = 130$ meV / 1043 cm⁻¹) explains the feature at around +130 meV. The combination band of the two modes v_{12}^+ and v_8^+ is responsible for the peak at +190 meV. The band around +250 meV can finally be characterized as a O(7)=C(6) stretching mode and is calculated to be $v_3^+ = 280$ meV / 2269 cm⁻¹. There is a significant change in geometry upon ionization: The C(4)=C(6) double and C(2)-C(4) single bond increase by 6 pm and 4 pm, respectively. The O(1)-C(2)-H(3) and H(3)-C(2)-C(4) angles increase by 3.4 ° and 3.2 ° and as a consequence the O(1)-C(2)-C(4) angle decreases by 6.6 °. Surprisingly an IE of 10.03 eV was computed by CBS-QB3 beyond the expected uncertainty of ± 0.04 eV and significantly higher than the experimental value of 9.65 eV. However, also G4, MP2 and G4MP2 computations yielded values of 10.02 eV, 10.03 eV and 10.00 eV, as summarized in table 6.1. In addition, among all of the 31 computed N₂C₂OH₂ and C₃O₂H₂ isomers, *E*-formylketene is the one with the lowest energy and shows the best agreement between computed and experimental spectrum. Therefore the spectrum is assigned to this structure, despite the discrepancy with the calculated IE_{ad}.

E-formylketene has been detected before by pyrolysis and photolysis of α -diazoketones and α -diazoaldehydes.^[239–241] Because of its high reactivity and its ability to perform unusual rearrange-

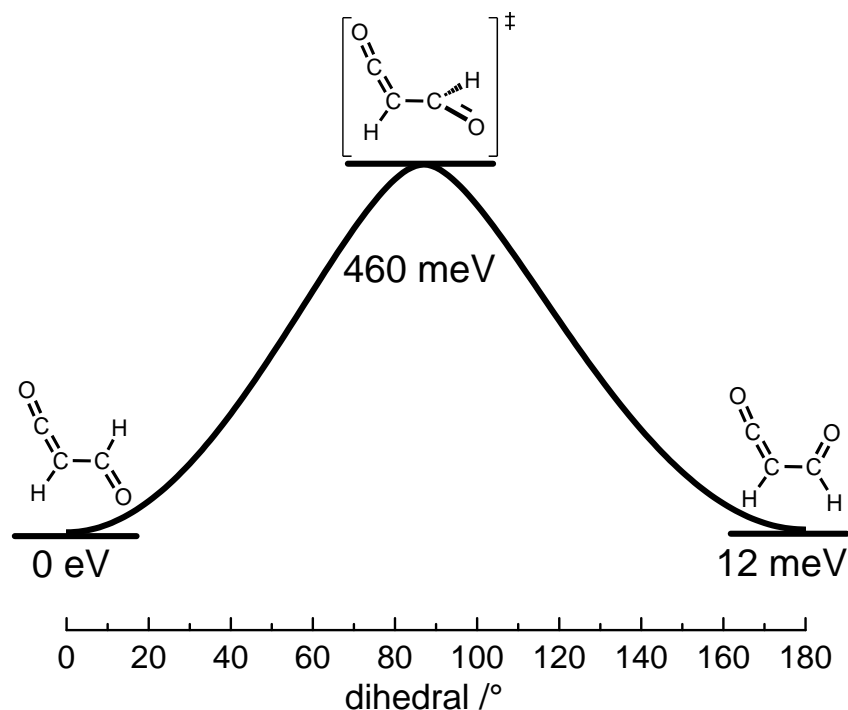


Figure 6.2.9: Energy diagram for the isomerization of formylketene in dependence of the dihedral angle H(5)C(2)C(4)O(1).

ments it is interesting from a theoretical point of view.^[242–244] Maier and Reisenauer first reported the photochemical generation of *Z*- and *E*-formylketene by IR spectroscopy.^[240] Earlier work in matrices yielded a mixture of both formylketene conformers, *E* and *Z*.^[245] Since the experimental investigations on this molecule are challenging, it has been in the focus of several theoretical studies. Computations of the preferred conformation of formylketene yield contradictory results.^[245–248]

Recent computations, performed on the B3LYP/6-311++G(d,p) level, showed that the *E*-conformer is slightly more stable than the *Z*-conformer. Although the relative stability of the *E* isomer is not significant, the rotational barrier is high compared to a C-C single bond rotation caused by the conjugation of the ketene and the formyl moiety.^[247] Fig. 6.2.9 shows that the barrier from the *E* to the *Z* conformation is computed (B3LYP/6-311g(d,p), not zero point corrected) to be 460 meV (44 kJ/mol), presumably low enough to be passed upon pyrolysis temperatures of 200 °C. In comparison, butadiene has a rotational barrier of 310 meV (B3LYP/6-311g(d,p), not zero point corrected).

The experimental observation of the pure *E*-conformer formed upon pyrolysis of DMA on the one hand seems to agree with theory and confirms that the *E*-conformer is lower in energy than the *Z*-conformer. Though, the low rotational barrier for isomerization seems to contradict the fact that the *E*-conformer is selectively produced.

Conclusion and summary

The threshold photoelectron spectrum of diazomeldrum's acid was observed by photoelectron photoion coincidence and the ionization energy and vibrational structure was obtained. Furthermore the dissociative photoionization of DMA was investigated. Three parallel fragmentation channels and one further fragment, being produced in both a parallel and a sequential pathway, were observed. The two low energetic fragmentation channels were fitted to a RRKM model and appearance energies were retrieved. The third channel was identified to include the Wolff rearrangement. The latter leads by subsequent dissociation and further rearrangement steps to the formation of acetone.

DMA was also investigated under pyrolysis conditions. From the analysis of the mass-selected threshold photoelectron spectra three thermal fragmentation pathways can be derived for the pyrolysis of DMA, summarized in fig. 6.2.10.

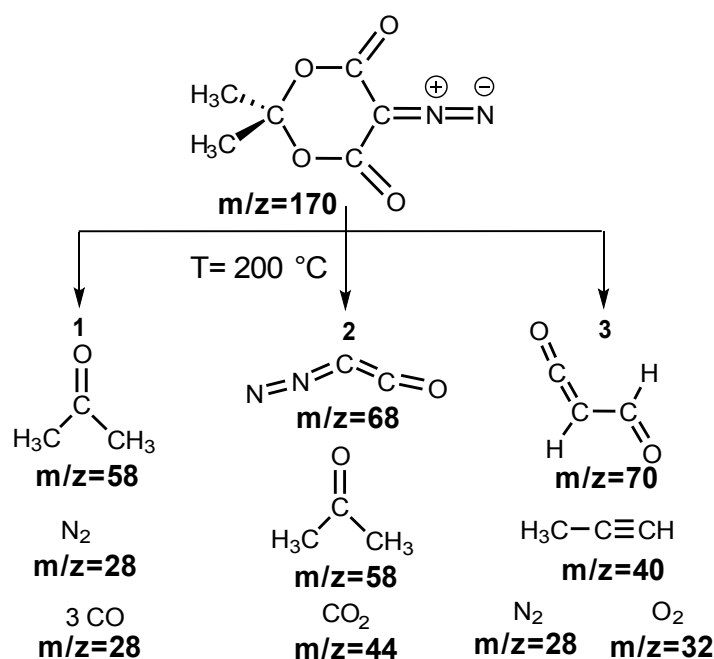


Figure 6.2.10: Fragmentation pathways of DMA upon pyrolysis at 200 °C. The 1st channel has been known to the literature,^[223] whereas the 2nd channel describes the fragmentation without the loss of N_2 . The third pathway includes a rearrangement prior the dissociation to high reactive formylketene.

The first pathway includes the formation of acetone ($m/z=58$) and CO ($m/z=28$) as pyrolysis products, emerging after a WR reaction induced by the loss of N_2 (scheme 3, left). From the signal intensities of acetone and CO in the mass spectra we can also qualitatively conclude that this fragmentation channel is the dominant process upon pyrolysis of DMA, as has been observed before.^[223] The second fragmentation channel leads to 2-diazoethenone ($m/z=68$), CO_2 ($m/z=44$) and ace-

tone. The third fragmentation pathway, shown on the right hand side in fig. 6.2.10 is associated with the loss of nitrogen from DMA, the formation of *E*-formylketene ($m/z=70$), oxygen ($m/z=32$) and propyne ($m/z=40$). Most of the fragments were identified by their TPES. 2-diazoethenone and *E*-formylketene have not yet been analyzed by photoionization. A peak at $m/z=142$, referring to the direct fragmentation product of N_2 from DMA, cannot be detected at any photon energy or pyrolysis temperature. The same is observed for the ketene intermediate. Nitrogen-loss leads immediately either via WR to acetone and CO or by further decomposition to $m/z=70$. From the mass spectra in fig. 6.2.1 can be inferred without knowing the cross sections of 2-diazoethenone and *E*-formylketene that acetone is formed in large excess upon pyrolysis. This observation and the huge signal of CO points at the dominance of fragmentation pathway 1 in fig. 6.2.10. Astonishingly, the two species CNN and CCO were not observed upon pyrolysis up to 600 °C. The All retrieved appearance energies and ionization energies and the computed values are summarized in table 6.1.

fragment	$AE_{0K}(\text{fit})$	$AE_{0K}(\text{CBS-QB3})$
$m/z=155$	10.65 eV	10.50 eV
$m/z=69$	10.72 eV	10.69 eV
molecule	$IE_{ad}(\text{experiment})$	$IE_{ad}(\text{experiment})$
diazomeldrum's acid	9.68 ± 0.02 eV	9.70 eV
<i>E</i> -formylketene	9.65 ± 0.01 eV	10.03 eV
2-diazoethenone	10.07 ± 0.01 eV	10.07 eV

Table 6.1: Appearance energies AE_{0K} computed on the CBS-QB3 level of theory and derived from a fit of the experimental data. Ionization energies IE_{ad} computed at the CBS-QB3 level of theory and derived from the experimental data.

7 Summary

The present work covers gas phase VUV-valence photoionization experiments of hydrocarbon radicals, three polycyclic aromatic hydrocarbon molecules and the decomposition of diazomeldrum's acid. The reactive intermediates were generated by vacuum flash pyrolysis from stable molecules. Most of these precursors were commercially available, while preparative synthesis was also employed for the others. The radicals and carbenes were examined in a continuous molecular beam. Therefore different molecular sources, depending on the molecule's vapor pressure, were applied. The PAH were synthesized in the Krüger group (Department of Organic Chemistry, University of Würzburg) and transferred to the gas phase by heating the solid sample and producing an effusive beam. The molecules were ionized by monochromatic Synchrotron radiation, supplied from a bending magnet beamline at the *Swiss Light Source* in Villigen/Switzerland. A threshold photoelectron photoion coincidence (TPEPICO) experiment was applied, which enables to correlate ions and threshold photo- electrons from the same ionization event. Thus, ions are detected in a TOF mass spectrum and integration over the mass signal and assigning the corresponding electron yields the threshold photoelectron spectrum of the respective molecule or fragment. From the threshold photoelectron spectra, the ionization energy of the molecule was derived. In addition, the vibrational structure of the ion and the geometry change upon ionization was assigned with the help of quantum chemical computations. Based on the latter, the ionization energy was validated and a simulation of the TPES was carried out, which enabled comparison of experiment and computations. In the following, the detailed results are presented.

1. The C_4H_5 radicals 2-butyn-1-yl and 1-butyn-3-yl were selectively produced from brominated precursor molecules. The IE_{ad} of 2-butyn-1-yl was derived to 7.94 ± 0.02 eV and IE_{ad} of 1-butyn-3-yl was found at 7.97 ± 0.02 eV. A rearrangement of the two isomers to the respective other cannot be excluded, since an isomerization barrier of 2.20 eV (212 kJ/mol) was computed. In addition, an excited cationic state was obtained at 9.7 eV for 2-butyn-1-yl.
2. Three C_4H_7 isomers 1-*E*-methylallyl, 1-*Z*-methylallyl and 2-methylallyl were generated from nitrite precursors and 3-bromo-2-methylpropene. The two conformers 1-*E*-MA and 1-*Z*-MA were both assigned in a combined TPE spectrum. Their IE_{ad} were determined to 7.48 ± 0.01 eV and 7.59 ± 0.01 eV, respectively. From the threshold photoelectron spectrum of 2-MA the $IE_{ad} = 7.88 \pm 0.01$ eV was assigned. The triplet cationic state of 2-MA was observed at 9.85 eV.

3. The two large hydrocarbon radicals fluorenyl, $C_{13}H_9$, and benzhydryl, $C_{13}H_{11}$, as well as the carbene diphenylmethylen, $C_{13}H_{10}$, were produced from the precursors 9-bromofluorene and α -amino-diphenylmethane. The ionization energies of the radicals were determined to be $IE_{ad}(\text{fluorenyl})=7.01\pm 0.02$ eV and $IE(\text{benzhydryl})=6.7$ eV. The IE_{ad} of benzhydryl was therefore downward revised with respect to a former value. The carbene signal was not separable from the radical signal, due to the small difference in mass units. In the same spectrum the IE of the carbene was assigned to 6.8 eV. Additionally, the dimers of the two radicals were observed to be formed in small amounts. The IE_{ad} of the fluorenyl dimer, $C_{26}H_{18}$, was assigned to 7.69 ± 0.04 eV and the respective value was obtained to 8.13 ± 0.04 eV for the dimer of diphenylmethyl, $C_{26}H_{22}$. Both dimers were computed to be products of direct dimerization.
4. Three polycyclic aromatic hydrocarbon DHP ($C_{14}H_{16}$) 1-PEN ($C_{18}H_{22}$) and THCT ($C_{22}H_{16}$) were investigated in an effusive beam. The ionization energies were determined to $IE_{ad}(\text{DHP})=7.38\pm 0.02$ eV, $IE_{ad}(\text{1-PEN})=7.58\pm 0.05$ eV and $IE_{ad}(\text{THCT})=6.40\pm 0.02$ eV.
5. In the thermal decomposition upon pyrolysis of DMA three dominant decomposition pathways were observed. The first includes the Wolff rearrangement and leads to the formation of acetone, N_2 and 3 CO. In the second pathway the formation $N=N=C=C=O$, 2-diazoethenone, acetone and CO_2 is found. The third channel again includes a rearrangement which leads to the formation of *E*-formylketene, $C_3O_2H_2$, propyne, CH_3CCH , N_2 and O_2 . Among the products were the two reactive molecules 2-diazoethenone and *E*-formylketene, which were isomer selectively observed for the first time in the present experiments. The IE_{ad} of 2-diazoethenone was determined to 10.07 ± 0.01 eV and the respective value of *E*-formylketene was assigned to 9.65 ± 0.01 eV. The decomposition of diazomeldrum's acid ($m/z=170$) was in addition observed in the cation. The IE_{ad} of the parent molecule was determined to 9.68 ± 0.02 eV. The dissociative photoionization yielded four different fragment ions to be formed up to an internal energy of ≈ 3.3 eV. The first fragmentation is the loss of CH_3 , yielding the fragment cation $m/z=150$ with an AE_{0K} fitted to 10.65 eV. The second dissociation channel proceeds parallel to the first one and is initiated by an H-atom shift. The rearranged cation fragments to N_2C_2OH ($m/z=69$) with an appearance energy determined to 10.72 eV from a fit. The third channel sets in with roughly 1.5 eV of internal excess energy, again parallel to the two other pathways. It is initiated by the Wolff rearrangement, which produces in a subsequent rearrangement and dissociation reaction acetone, $(CH_3)_2CO$ ($m/z=58$) as the third fragment cation. The AE_{0K} of acetone is determined to 11.2 eV. The acetyl cation ($m/z=43$) is observed as a further fragment. It is supposed to be formed from different origins: in an additional direct fragmentation channel of the parent cation, in the consecutive fragmentation of the fragment $m/z=155$ and in the consecutive methyl loss from acetone.

8 Zusammenfassung

Die vorliegende Arbeit befasst sich mit VUV Valenz-Photoionisations-Experimenten, welche in der Gasphase an verschiedenen Kohlenwasserstoffradikalen und drei polyzyklischen aromatischen Kohlenwasserstoffen (PAH) durchgeführt wurde. Des Weiteren wurden die Pyrolyseprodukte der Diazomeldrumsäure mit dem genannten Experiment untersucht. Die reaktiven Intermediate wurden im Vakuum mittels Flash-Pyrolyse aus stabilen Vorläufermolekülen erzeugt. Die meisten dieser waren kommerziell erhältlich, wobei auch einige Moleküle selbst im Würzburger Chemielabor synthetisiert wurden. Die erzeugten Radikale und Carbene wurden in einem kontinuierlichen Molekularstrahl expandiert. Um den Vorläufer in die Gasphase zu überführen, wurden verschiedene Molekular-Quellen eingesetzt. Die Auswahl erfolgte dabei in Abhängigkeit des Dampfdrucks des Vorläufermoleküls. Die Polyzyklischen Aromaten (PAH) wurden in der Arbeitsgruppe von Prof. Dr. Anke Krüger im Institut für Organische Chemie der Universität Würzburg synthetisiert. Die PAH wurden in einer Feststoffmolekularquelle geheizt und in einem effusiven Molekularstrahl expandiert. Die Ionisation aller Spezies erfolgte mit monochromatischem VUV-Synchrotronlicht, das an der Bending-Magnet Beamline an der *Swiss Light Source* in Villigen/Schweiz erzeugt wird. Das Schwellenphotoelektronen-Photoionen-Koinzidenz (TPEPICO) Experiment wurde zur Detektion und Analyse der Ionisationsprozesse angewendet. Dieses Experiment ermöglicht es massenselektierte Ionen und Schwellenphotoelektronen des selben Ionisationsereignisses zu korrelieren. Die Ionen wurden in einem Time-of-Flight Massenspektrometer detektiert. Durch Integration des Massensignals und anschließende Auswertung des zugeordneten Schwellenphotoelektronen-Signals erhält man das Schwellenphotoelektronen-Spektrum (TPES) des Moleküls bzw. Fragments. Aus den TPE-Spektren konnten Ionisierungsenergien bestimmt werden und mit Hilfe von Franck-Condon-Simulationen sowohl die Schwingungsstruktur im Kation, als auch die Geometrieänderung, hervorgerufen durch die Ionisation, analysiert werden. Berechnete Ionisierungsenergien wurden zusätzlich mit den experimentellen Daten verglichen. Im Folgenden werden die einzelnen Ergebnisse aufgelistet.

1. Die beiden C_4H_5 Radikale 2-Butin-1-yl und 1-Butin-3-yl wurden selektiv von den entsprechenden bromierten Vorläufermolekülen erzeugt. Die IE_{ad} von 2-Butin-1-yl wurde zu 7.94 ± 0.02 eV und die IE_{ad} von 1-Butin-3-yl zu 7.97 ± 0.02 eV bestimmt. Die Umlagerung jedes Isomers in das entsprechend andere kann nicht ausgeschlossen werden, da eine Isomerisierungsbarriere von 2.20 eV (212 kJ/mol) berechnet wurde. Die Höhe der Barriere ist unter gewählten Pyrolysebedingungen sehr wahrscheinlich überwindbar. Des Weiteren wurde im 2-Butin-1-yl Kation

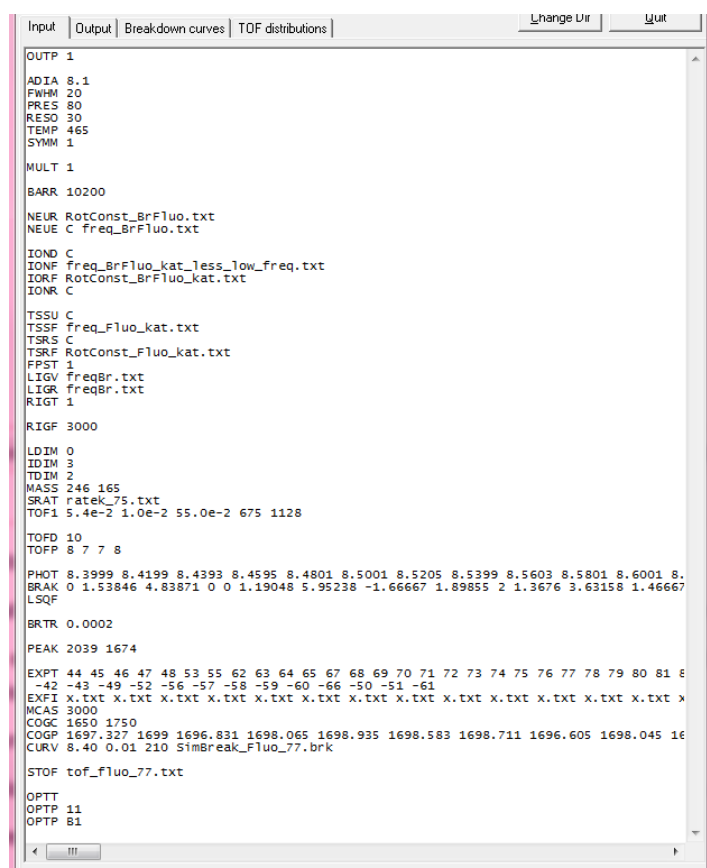
- ein angeregter Zustand bei 9.7 eV detektiert.
- Die drei C_4H_7 Isomere 1-*E*-Methylallyl, 1-*Z*-Methylallyl und 2-Methylallyl wurden aus den jeweiligen Nitrit-Vorläufern und aus 3-Brom-2-Methylpropen dargestellt. Die beiden Konformere 1-*E*-Methylallyl and 1-*Z*-Methylallyl wurden aufgrund des geringen Unterschieds ihrer Ionisierungsenergien in einem TPE-Spektrum gemeinsam nachgewiesen. Ihre IE_{ad} wurden bei 7.48 ± 0.01 eV und 7.59 ± 0.01 eV gemessen. Aus dem Schwellenphotoelektronen-Spektrum von 2-Methylallyl wurde die IE_{ad} zu 7.88 ± 0.01 eV bestimmt. Der erste Triplett-Zustand von 2-Methylallyl wurde bei 9.85 eV detektiert.
 - Die beiden Kohlenwasserstoffradikale Fluorenyl, $C_{13}H_9$, und Benzhydryl, $C_{13}H_{11}$, sowie das Carben Diphenylmethylen, $C_{13}H_{10}$, wurden von den Vorläufern 9-Brom-Fluoren and α -Amino-Diphenylmethan erzeugt. The Ionisierungsenergien der beiden Radikale wurden zu $IE_{ad}(\text{Fluorenyl}) = 7.01 \pm 0.02$ eV und $IE_{ad}(\text{Benzhydryl}) = 6.7$ eV bestimmt. Die IE_{ad} von Benzhydryl wurde nach unten korrigiert. Der bislang bekannte Wert der Ionisierungsenergie liegt weit über dem Wert, der aus diesem Experiment erhaltenen wurde. Da sich das Carben und das Benzhydryl Radikal nur um eine Masseneinheit unterscheiden, konnten die Schwellenphotoelektronen-Signal der beiden Spezies nicht separiert werden. Im selben Spektrum wurde neben der IE von Benzhydryl auch die IE des Carbens detektiert und zu 6.8 eV bestimmt. Zusätzlich wurden die entsprechenden Dimere von Fluorenyl und Benzhydryl in geringen Anteilen beobachtet. Die IE_{ad} von Fluorenyl-Dimer, $C_{26}H_{18}$, wurde bei 7.69 ± 0.04 eV gemessen und der entsprechende Wert für das Dimer von Benzhydryl, $C_{26}H_{22}$, bei einer Energie von 8.13 ± 0.04 eV gefunden. Beide Dimere sind Berechnungen zu Folge die Produkte direkter Dimerisierung in der Pyrolyse.
 - Drei polycyclische aromatische Kohlenwasserstoffe, DHP ($C_{14}H_{16}$) 1-PEN ($C_{18}H_{22}$) und THCT ($C_{22}H_{16}$) wurden in einem effusiven Molekularstrahl untersucht. Die Ionisierungsenergien wurden zu $IE_{ad}(\text{DHP}) = 7.38 \pm 0.02$ eV, $IE_{ad}(\text{1-PEN}) = 7.58 \pm 0.05$ eV und $IE_{ad}(\text{THCT}) = 6.40 \pm 0.02$ eV bestimmt.
 - Bei der thermischen Spaltung von Diazomeldrumsäure wurden eine Reihe von Pyrolyseprodukten beobachtet, die in drei verschiedenen Pfaden gebildet werden. Aus dem ersten Kanal gehen nach einer Wolff Umlagerung die Produkte Aceton, N_2 and 3 CO hervor. Im zweiten Pfad werden $N=N=C=C=O$, 2-Diazoethenon, Aceton und CO_2 gebildet. Der dritte Pfad thermischer Spaltung wird durch eine Umlagerung initiiert, welche zur Bildung von *E*-Formylketen, $C_3O_2H_2$ führt. Zusätzlich werden dabei Propin, CH_3CCH , N_2 and O_2 gebildet. Unter den Pyrolyseprodukten wurden die zwei bislang noch nicht selektiv untersuchten Moleküle 2-Diazoethenon und *E*-Formylketen gefunden. Die IE_{ad} von 2-Diazoethenon wurde zu 10.07 ± 0.01 eV bestimmt und der entsprechende Wert für *E*-Formylketen bei 9.65 ± 0.01 eV gemessen. Die Fragmentierung im Kation der Diazomedrumsäure ($m/z=170$) wurde zusätzlich untersucht. Die IE_{ad} des Muttermoleküls wurde zu 9.68 ± 0.02 eV bestimmt. Die Analyse der dissoziativen Pho-

toionisation bis zu einer internen Energie von ≈ 3.3 eV zeigte die Bildung vier verschiedener Fragmente. Der erste Kanal beschreibt den Verlust von CH_3 , wobei das Fragmention $m/z=150$ mit einer Auftrittenergie AE_{0K} zu 10.65 eV gefittet wurde. Der zweite Dissoziationskanal verläuft parallel zum Ersten und wird durch einen H-Atom Shift im Muttermolekül eingeleitet. Das umgelagerte Molekül dissoziiert zu $\text{N}_2\text{C}_2\text{OH}$ ($m/z=69$) mit einer Auftrittenergie, die aus einem Fit zu 10.72 eV bestimmt wurde. Der dritte Kanal setzt mit ungefähr 1.5 eV interner Überschussenergie parallel zu den beiden niedrigerenergetischen Dissoziationspfaden ein. Der dritte Kanal wird durch eine Wolff-Umlagerung eingeleitet, aus welcher in einer weiteren Umlagerung mit anschließender Dissoziationsreaktion Aceton, $(\text{CH}_3)_2\text{CO}$ ($m/z=58$), als drittes Fragmention hervorgeht. Die AE_{0K} von Aceton wurde bei 11.2 eV detektiert. Als viertes Fragment wird das Acetyl-Kation, ($m/z=43$) beobachtet. Es wird vermutlich aus verschiedenen Kanälen gebildet: zum einen durch eine weitere direkte Fragmentierung des Muttermoleküls und des Weiteren in einer sequenziellen Dissoziation des Fragments $m/z=155$. Des Weiteren kann auch der Methylverlust von Aceton-Kation zur Bildung des Acetyls ($m/z=43$) führen.

Appendix

Modelling of the breakdown diagram of 9-bromo-fluorene

The current version of the program *mPEPICO* is version *MiniPEPICO_v187.h*. A general description of all keywords is given in a document available as supporting information to the publication of the program. In the following the input, shown in fig. 8.0.1 is explained. The theoretical process of the fitting procedure for fast, slow and/or parallel dissociations is presented in 2.4.5.



```
Input | Output | Breakdown curves | TOF distributions | Lchange Uir | Lquit
-----|-----|-----|-----|-----|-----
OUTP 1
ADIA 8.1
FWHM 20
PRES 80
RESO 30
TEMP 465
SYMM 1

MULT 1
BARR 10200
NEUR RotConst_BrFluo.txt
NEUE C Freq_BrFluo.txt

IOND C
IONF Freq_BrFluo_kat_less_low_freq.txt
IORF RotConst_BrFluo_kat.txt
IONR C

TSSU C
TSSF Freq_Fluo_kat.txt
TSRS C
TSRF RotConst_Fluo_kat.txt
FPST 1
LIGV freqBr.txt
LIGR freqBr.txt
RIGT 1

RIGF 3000

LDIM 0
IDIM 3
TDIM 2
MASS 246 165
SRAT ratek_75.txt
TOF1 5.4e-2 1.0e-2 55.0e-2 675 1128

TOFD 10
TOFP 8 7 7 8

PHOT 8.3999 8.4199 8.4393 8.4595 8.4801 8.5001 8.5205 8.5399 8.5603 8.5801 8.6001 8.6205
BRAK 0 1.53846 4.83871 0 0 1.19048 5.95238 -1.66667 1.89855 2 1.3676 3.63158 1.46667
LSQF

BRTR 0.0002
PEAK 2039 1674

EXPT 44 45 46 47 48 53 55 62 63 64 65 67 68 69 70 71 72 73 74 75 76 77 78 79 80 81 82
-42 -43 -49 -52 -56 -57 -58 -59 -60 -66 -50 -51 -61
EXPI x.txt x.txt x.txt x.txt x.txt x.txt x.txt x.txt x.txt x.txt x.txt x.txt x.txt x.txt x.txt x.txt
MCAS 3000
COGC 1650 1750
COGP 1697.327 1699 1696.831 1698.065 1698.935 1698.583 1698.711 1696.605 1698.045 1698.045 1698.045
CURV 8.40 0.01 210 SimBreak_Fluo_77.brk

STOF tof_fluo_77.txt

OPTT
OPTP 11
OPTP 81
```

Figure 8.0.1: Inputfile for the breakdown fit for the DPI 9-bromo-fluorene with the program *MiniPEPICO_187.h*.

In general, lines that begin with a space character are commented out. All *.txt*-files that are named in the input have to be placed in the same directory like the input file.

OUT 1 : an output file will be generated, the higher the number, the more information will be written in the file

ADIA 8.1 : the experimental adiabatic ionization energy in eV of the parent molecule has to be written here

FWHM 20: the resolution of the electron energy in cm^{-1} , means the minimum value with which slow/zero kinetic energy electrons are selected on the electron image, 80 is default.

PRES 80 : photon energy resolution in cm^{-1} , for the 600 /mm grid 80 is default

RESO 30 : is the ion energy resolution/step size in cm^{-1} with which the calculations of the rate constants are performed

TEMP 465 : the sample temperature in K

SYMM 1: here the degeneracy factor is written for each channel separated by space character. Since only one bromine atom is lost, only one non-degenerate channel is present

MULT 1 : gives the number of dissociation channels of the parent. If one of the daughter ions fragments further, its own subsequent dissociation channels will be written in the second number and so on.

BARR 10200 : the value is the barrier height for the dissociation channel in cm^{-1} . The barrier for the fragmentation is determined by the transition state of the dissociation. Here the *ab initio*/DFT computed value of the barrier of the TS is taken as starting values and are fitted during the different runs of the procedure. The calculated value then acts as the new starting value. In the case of the bromine loss from 9-bromo-fluorene, no real TS exists. Thus a loose TS was computed by stretching the C-Br bond to 4.5 Å. This value was taken fixed while optimizing the molecule to a TS.

NEUR : the name of the text file that includes the rotational constants in GHz of the neutral parent molecule is written here.

NEUE C : file name of the neutral parent's frequencies; C means calculate the density of states.

IOND C : the parent ion's density of states $\rho(E)$ will be calculated.

IONF : the text file that includes all frequencies in cm^{-1} of the parent cation is named here.

IORF :the parent ion's rotational constants in GHz

IONR C: the rotational density of states of the parent cation will be calculated

TSSF : the names of the text files that include the transition state frequencies are written here. Since no real TS exists and the loose TS is somewhat to the products, the frequencies of the product, i.e. of the fragment cation are taken.

TSSU C : the number of states for the "TS" will be calculated from vibrational frequencies (of the fragment).

TSRF : the names of the text files that include the “transition state” rotational constants. Again, these are the rot constants of the fragment ion.

TSRS C : calculate the rotational density of states for the “transition state”.

FPST 1 : SSACM is used for rate calculation. If “2” is stated or the keyword is not used, then all rates are calculated by the RRKM statistical approach

LIGV : neutral ligand’s vibrational frequencies are listed in this text file (only necessary in SSACM calculations or sequential dissociations). This file contains one “0” for the bromine atom.

LIGR : neutral ligand’s rotational constants are listed in this text file(only necessary in SSACM calculations or sequential dissociations). This file contains one “0” for bromine, thus the same file as in LIGV can be applied.

RIGT 1: states which functional form of the energy dependence of the rigidity factor in the SSACM calculation should be applied. The option is either “0” for: $e^{-E/c}$, with the excess internal energy E and the constant c , the rigidity factor, which is chosen in the RIGF card, second option “1”: $(1+(E/c)^2)^{-2/3}$ function

RIGF 3000 : gives the constant for the calculation of the rigidity factor

LDIM 0 : states the rotational dimension of the neutral product (Br). This is only applied for SSACM calc., or in any sequential dissociation

IDIM 3 : states the rotational dimension of the product ion (only necessary in SSACM/ sequential dissociations

TDIM 2: translational degrees of freedom for product energy calculations

BRTR 0.002 : the error for the TOF distributions is weighted 500 times more than the error for the breakdown curve. The function to be optimized is: $\langle \text{TOF error} \rangle + x \cdot \langle \text{breakdown error} \rangle$

MASS 246 165 : the masses of the parent and the fragment are listed.

SRAT rate_k_29.txt : the calculated rates are saved in the text file named here.

TOF1 5.5e-2 1.0e-2 55.0e-2 675 1065 : value one and two are the lengths (in m) of the two acceleration regions, value three: length of the field-free region, values four and five: voltage differences (in V) in the two acceleration regions.

PHOT : photon energies in eV for which the breakdown data is added

BRAK : the breakdown data, i. e. the fractional abundances, for each daughter fragment are listed in %. For every daughter fragment the line has to start with BRAK.

MCAS 3000 : the number of active channels in the multi-channel analyzer. The number can be retrieved from the number of points that are written in each TOF.

PEAK 2039 1674: gives the peak positions of the parent and the first daughter fragment in mass channels.

TOFP : parent peak left and right half gaussian FWHM in channels, there are two values for each side contributing to a “peak in the peak” shape. But normally the two values for each side left and right can be the same.

TOFD : The daughter ion peaks FWHM in channels.

EXPT : the “TOF distributions” that are listed under EXFI (x.txt files) should be calculated for the respective photon energies that are listed here in the same order as under EXFI. Each photon energy is given with the number it is listed under PHOT.

EXFI : all file names of the TOF distributions are listed here. Since no TOF distributions are fitted, “dummy” files x.txt have to be added, which only contain a row of the number zero

COGC 1650 1750 : Center of mass positions of the daughter(s) and the parent in channel numbers.

COGP : experimental center of mass position in channel numbers

CURV 8.40 0.01 210 SimBD_dma_29.brk : the first value is the photon energy from that the calculation of the breakdown curve starts, the second value constitutes the step size of the calculation the third value is the number of points to be calculated and then the name of the file in which the breakdown curve is saved follows.

STOF : saves the calculated TOF distributions to the file named here.

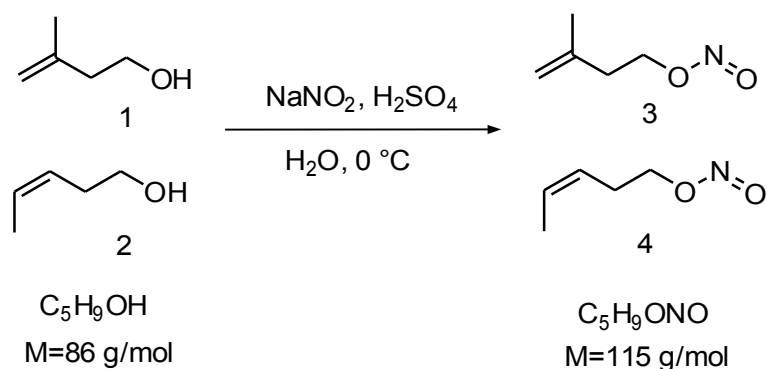
OPTT : the parameter stated under OPTP are optimized

OPTP 15: the 5 lowest transition state frequencies are optimized for TS1.

OPTP B1: the barrier heights B of the transition state TS1 is optimized.

Synthesis of 3-methyl-3-buten-1-yl nitrite and 1-penten-1-yl nitrite

The synthesis was performed according to the procedure described in the literature.^[70]



NaNO₂ (12.0 g, 0.174 mol) was dissolved in water (20.5 mL) and cooled to 0 °C. 3-methyl-3-buten-1-ol **1** (*Sigma Aldrich*) (10.0 g, 11.8 mL, 0.116 mol) was added and after that H₂SO₄ (30%, ρ=1,215 g/mL, 26.5 mL) was added dropwise. The reaction mixture was stirred in the dark for 90 min under argon. A solution of NaHCO₃ (0.4 g) and NaCl (3 g) in water (10 mL) was added to stop the reaction. The product phase was washed three times with the same solution. The crude product was distilled at 85 mbar/ 31 °C to give 11.5 g (99.7 mmol, 86 %) pure cyan blue 3-methyl-3-buten-1-yl nitrite **3**.

To prepare 1-penten-1-yl nitrite **4** in a similar procedure, H₂SO₄ (30%, 19.1 mL) was added during 60 min dropwise to a solution of NaNO₂ (8.8 g, 127 mmol) and *cis*-3-pentene-1-ol **2** (*ABCR Chemicals*) (9.2 mL, 7.85 g, 89 mmol) in water (6 mL). After stirring for 90 min at 0 °C under argon in the dark the yellow product was separated with four 5 mL portions of a solution of NaCl (7.8 g) and NaHCO₃ (1 g) in water (50 mL). Again, the product phase was washed with the salt solution for several times and dried over sodium sulfate. A distillation of the crude product at 83 mbar (32-34 °C) yielded 7.92 g (71.2 mmol, 80 %) of the yellow product.

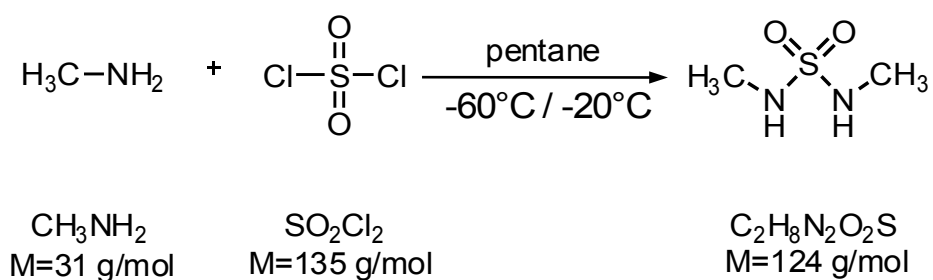
¹H-NMR (3-methyl-3-buten-1-yl nitrite, 400 MHz, CDCl₃) δ= 4.81-4.73 (m, 2H, CH₂CH₂ONO), 2.48-2.37 (t, 2H, CH₂CH₂ONO), 1.77 (s, 3H, CH₃) ppm.

¹H-NMR (1-penten-1-yl nitrite, 400 MHz, CDCl₃) δ= 5.63-5.58 (m, 1H, CH₃CH=CH), 5.42-5.39 (m, 1H, CH₃CH=CH), 4.74 (t, 2H, CH₂ONO), 2.53-2.46 (m, 2H, CH₂CH₂ONO), 1.64-1.61 (m, 3H, CH₃) ppm.

Synthesis of N,N'-dimethylsulfamide

N,N'-dimethylsulfamide was synthesized on the purpose for the synthesis of azomethane. The latter compound was used as a precursor for the production of the methyl radical, CH_3 , upon pyrolysis. This synthesis was done in a cooperation with *Christian Alcaraz*, who intends to re-investigate the electronically excited states in CH_3^+ by velocity map double (ion-electron) imaging.

The synthesis was performed according to a procedure described by *Ohme et al.*^[249]



Ca. 40 mL (88 mmol) of methylamine (*ABCR Chemicals*) were condensed in a 500 mL three-neck round bottom-flask at $\approx -90^\circ\text{C}$. 125 mL of cold pentane were added. A solution of 4.5 mL (5.5 g, 40 mmol) sulfonyl chloride (*Sigma Aldrich*) in 50 mL of pentane was added drop wise over a few (2-3) hours to the stirred reactant. By the first drop the reaction starts very powerfully while gaseous clouds (Cl_2 , SO_2) fill the entire apparatus, which was held open by a CaCl_2 dry tube throughout the procedure. The reaction was held at -60°C by the beginning of adding SO_2Cl_2 and was intended to rise not higher than to -20°C when sulfonyl chloride was completely added. The stirred reaction was slowly warmed to room temperature. It is recommendable to use a mechanic stirrer, since the magnet stirrer has not enough power to stir in between the formed precipitate. When the flask was opened to evaporate the pentane, gas was still formed, indicating the reaction was not yet over in the precipitate. The tough precipitate was therefore stirred by hand with a spatula, until no more gas was formed. Pentane was evaporated and the yellow-brownish-white precipitate was used for a Soxhlet extraction in diethylether. The extraction was running for 16-18 h and the ether was evaporated to yield a light orange product. (4 g, 30 mmol, 75 %)

$^1\text{H-NMR}$ (400 MHz, CDCl_3) $\delta = 4.32$ (s, 2H, NH_2), 2.72 (s, 6H, CH_3)

Ms-TPES of the pyrolysis products of 3-bromo-2-methylpropene

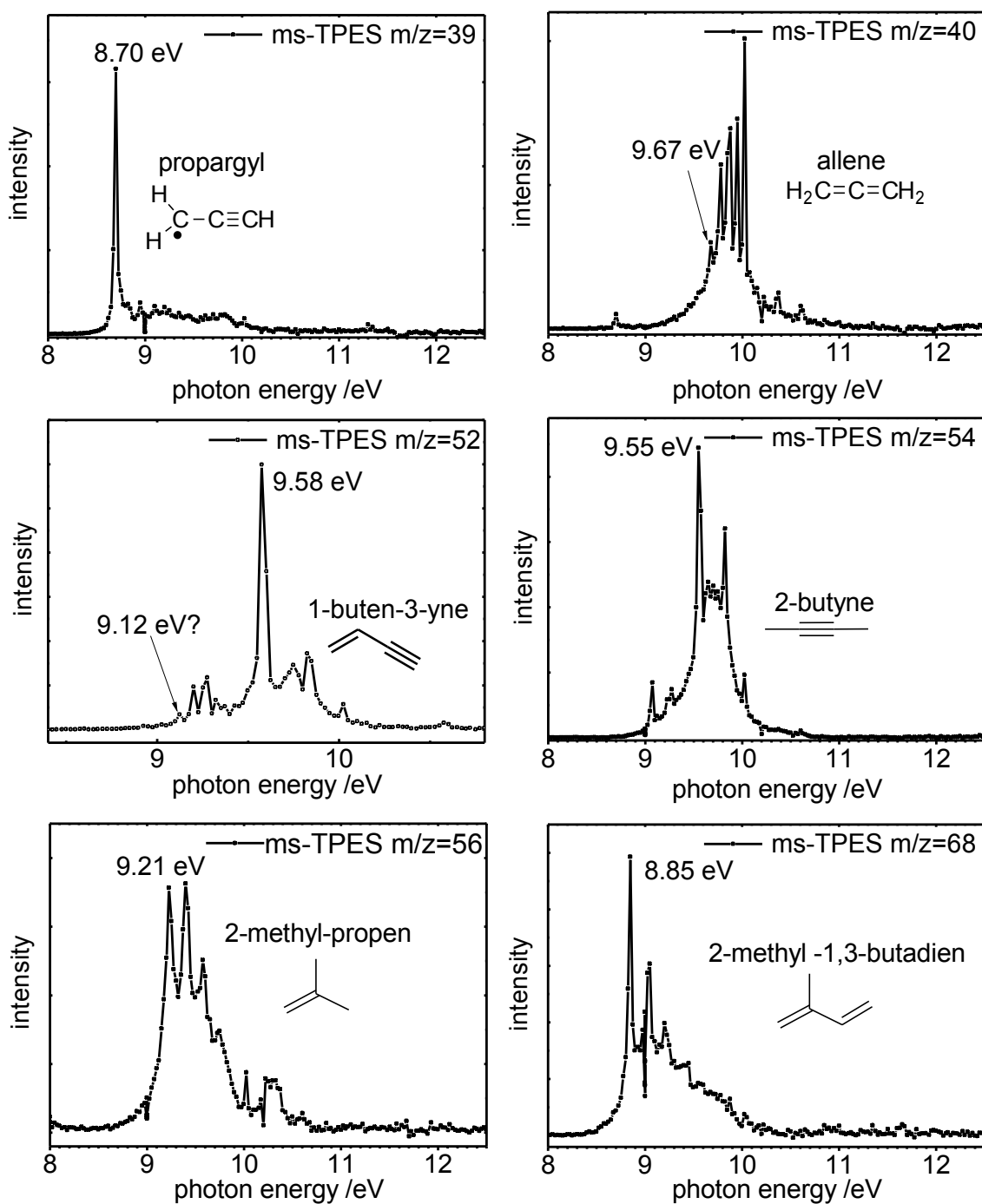


Figure 8.0.2: Ms-TPES of the pyrolysis products of 3-bromo-2-methyl-propene at m/z=39, m/z=40, m/z=52, m/z=54 and m/z=56 and m/z=68 at 650 °C pyrolysis temperature.

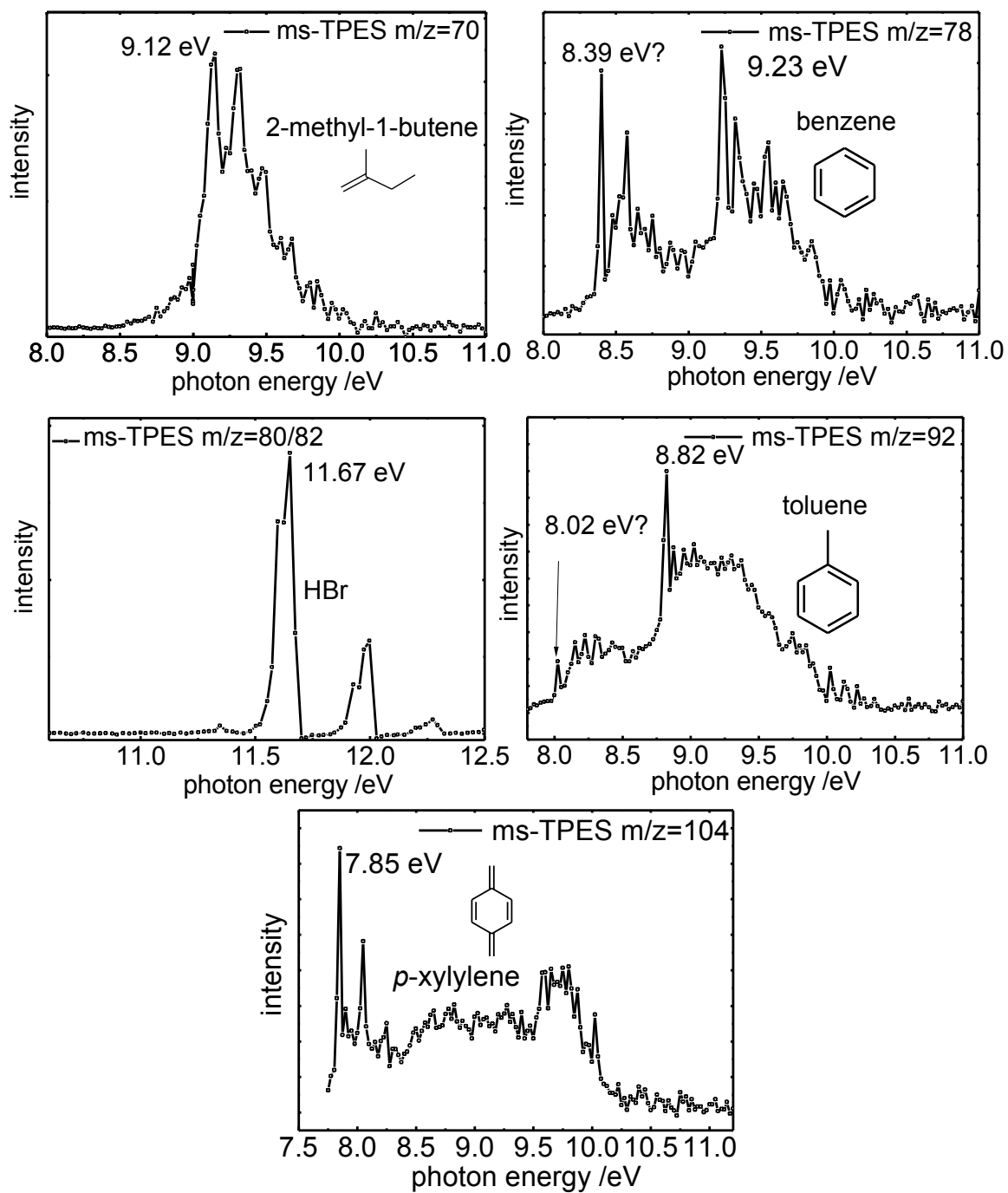
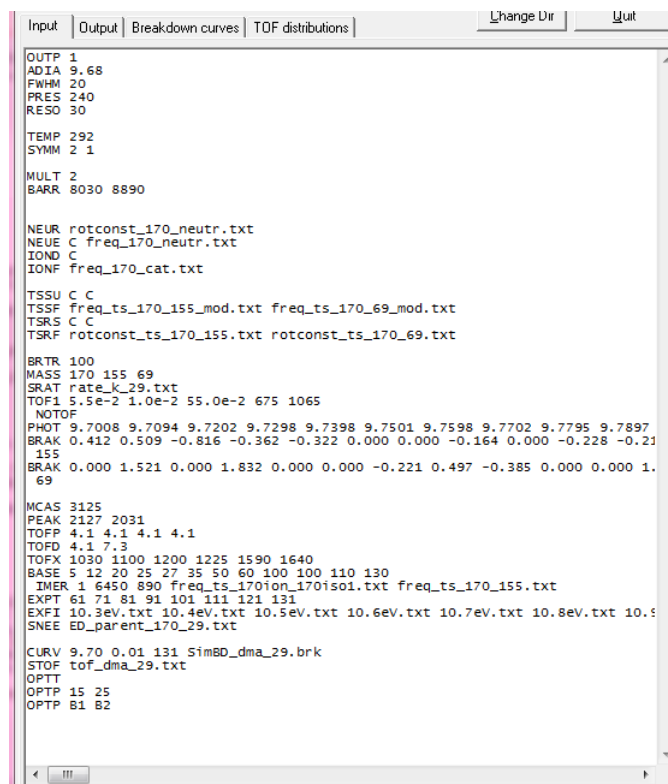


Figure 8.0.3: Ms-TPES of the pyrolysis products of 3-bromo-2-methyl-propene at $m/z=70$, $m/z=78$, $m/z=80/82$, $m/z=92$, and $m/z=104$ (650 °C pyrolysis temperature).

Modelation of the breakdown diagram of DMA

In the following the input that is shown in fig. 8.0.4 for the fitting procedure of the DPI of DMA (6.1) is explained.



```
Input | Output | Breakdown curves | TDF distributions | Change Dir | Quit
-----
OUTP 1
ADIA 9.68
FWHM 20
PRES 240
RESO 30

TEMP 292
SYMM 2 1

MULT 2
BARR 8030 8890

NEUR rotconst_170_neutr.txt
NEUC C freq_170_neutr.txt
IOND C
IONF freq_170_cat.txt

TSSU C C
TSSF freq_ts_170_155_mod.txt freq_ts_170_69_mod.txt
TSRS C C
TSRF rotconst_ts_170_155.txt rotconst_ts_170_69.txt

BRTR 100
MASS 170 155 69
SRAT rate_k_29.txt
TOF1 5.5e-2 1.0e-2 55.0e-2 675 1065
NOTOF
PHOT 9.7008 9.7094 9.7202 9.7298 9.7398 9.7501 9.7598 9.7702 9.7795 9.7897
BRAK 0.412 0.509 -0.816 -0.362 -0.322 0.000 0.000 -0.164 0.000 -0.228 -0.21
155
BRAK 0.000 1.521 0.000 1.832 0.000 0.000 -0.221 0.497 -0.385 0.000 0.000 1.
69

MCAS 3125
PEAK 2127 2031
TOFP 4.1 4.1 4.1 4.1
TOFD 4.1 7.3
TOFX 1030 1100 1200 1225 1590 1640
BASE 5 12 20 25 27 35 50 60 100 100 110 130
IMER 1 6450 890 freq_ts_170ion_170is01.txt freq_ts_170_155.txt
EXPT 61 71 81 91 101 111 121 131
EXFI 10.3eV.txt 10.4eV.txt 10.5eV.txt 10.6eV.txt 10.7eV.txt 10.8eV.txt 10.9
SNEE ED_parent_170_29.txt

CURV 9.70 0.01 131 SimBD_dma_29.brk
STOP tof_dma_29.txt
OPPT
OPTH 15 25
OPTH 81 82
```

Figure 8.0.4: Inputfile for the breakdown fit of the DPI of DMA with the program MiniPEPICO_187.h.

OUT 1 : an output file will be generated

ADIA 9.68 : the experimental adiabatic ionization energy in eV of the parent molecule has to be written here

FWHM 20: the resolution of the electron energy in cm^{-1} , means the minimum value with which slow/zero kinetic energy electrons are selected on the electron image, 80 is default.

PRES 240 : photon energy resolution in cm^{-1} , for the 600 /mm grid 80 is default

RESO 30 : is the ion energy resolution/step size in cm^{-1} with which the calculations of the rate constants are performed

TEMP 292 : the sample temperature in K

SYMM 2 1: here the degeneracy factor is written for each channel separated by space character. The first reaction that is observed here is the loss of methyl from the DMA molecule. There are two chemical non-equal methyl groups, that are computed to lead to the same product, when detached.

MULT 2 : gives the number of dissociation channels of the parent. If one of the daughter ion fragments further, its own further dissociation channels will be written in the second number and so on.

BARR 8030 8890 : the two values are the barrier heights for the two dissociation channels in cm^{-1} . The barriers for the fragmentations are determined by the transition states of the dissociation. Here the *ab initio*/DFT values of the barriers are taken as starting values and were fitted during the different runs of the procedure. The new calculated value then acted as the new starting value.

NEUR : the name of the text file that includes the rotational constants in GHz of the neutral parent molecule is written here.

NEUE C : file name of the neutral parent's frequencies; the *C* means calculate the density of states.

IOND C : the parent ion's density of states $\rho(E)$ shall be calculated.

IONF : the text file that includes all frequencies in cm^{-1} of the parent cation is named here.

TSSF : the names of the text files that include the transition state frequencies for the *TS1*, *TS2*... are written here.

TSSU C C : states the transition state number of states for the two channels will be calculated from vibrational frequencies.

TSRF : the names of the text files that include the transition state rotational constants for the *TS1*, *TS2*... are written here.

TSRS C C : calculate the rotational density of states for each transition state.

BRTR 100 : the breakdown curve is weighted 100 times more than the TOF distribution when the error of the calculation is calculated.

MASS 170 155 69 : the masses of the parent and the fragments are listed.

SRAT rate_k_29.txt : the calculated rates are saved in the text file named here.

TOF1 5.5e-2 1.0e-2 55.0e-2 675 1065 : value one and two are the lengths (in m) of the two acceleration regions, value three: length of the field-free region, values four and five: voltage differences (in V) in the two acceleration regions.

PHOT : photon energies in eV for which the breakdown data is added

BRAK : the breakdown data, i. e. the fractional abundances, for each daughter fragment are listed in %. For every daughter fragment the line has to start with BRAK.

MCAS 3123 : the number of active channels in the multi-channel analyzer. The number can be retrieved from the number of points that are denoted in a TOF-file

PEAK : gives the peaks of the parent and the first daughter fragment in mass channels.

TOFP : parent peak left and right half gaussian FWHM in channels, there are two values for each side contributing to a “peak in the peak” shape. But normally the two values for each side left and right can be the same.

TOFD : The daughter ion peaks FWHM in channels.

TOFX : if there are mass peaks in the TOF that are not evaluated in the fit. Here three ranges (channels) are excluded: from 1030 to 1100...

BASE : correcting the baseline of the TOF distributions. The first value will be added to every channel in the 1st TOF listed in EXFI and so on...

EXPT : the TOF distributions that are listed under EXFI should be calculated for the respective photon energies that are listed here in the same order as under EXFI. Each photon energy is given with the number it is listed under PHOT.

EXFI : all file names of the TOF distributions are listed here. The integer in a file contains the number of counts in channel 0...up to the channel number stated in MCAS

SNEE : save the thermal energy distribution under the file name that is states here.

CURV 9.70 0.01 131 SimBD_dma_29.brk : the first value is the photon energy from that the calculation of the breakdown curve starts, the second value constitutes the stepsize of the calculation the third value is the number of points to calculate and then the name of the file, where the breakdown curve is saved follows.

STOF : saves the calculated TOF distributions to the file named here.

OPTT : the parameter stated under OPTP are optimized

OPTP 15 25: the lowest 5 transition state frequencies are optimized for the TS1 and for TS2.

OPTP B1 B2: the barrier heights B of the two transition states TS1 and TS2 are optimized.

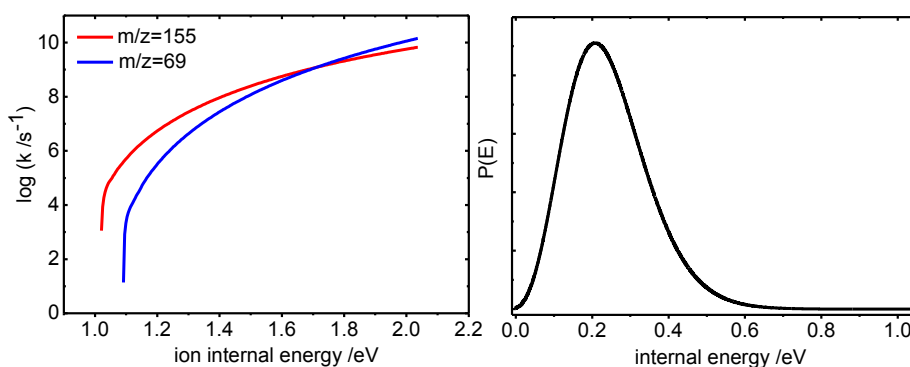


Figure 8.0.5: Energy dependent dissociation rates $k(E)$ of the fragments $m/z=155$ and $m/z=69$ in the DPI of DMA (left) and the internal energy distribution of the neutral parent DMA (right).

List of Figures

1.0.1	HACA scheme/ PAH formation.	2
2.1.1	Molecular beam expansion	8
2.1.2	Scheme of the pyrolysis source	10
2.2.1	Scheme of a synchrotron	15
2.2.2	Bending magnet and insertion devices	16
2.2.3	Front-end of the VUV beamline	17
2.2.4	Monochromator grating	18
2.3.1	Photoionization schemes	20
2.3.2	DPI scheme and breakdown diagram.	22
2.3.3	Photoionization transitions of CO	24
2.3.4	Delay line detector	27
2.3.5	Ion and electron spectrometer	28
2.3.6	Electron images with circle and ring for TPE selection	30
2.4.1	Potential energy curves of a dissociating TS	38
2.4.2	Dissociative photoionization in dependence of the parent cation's thermal energy.	40
3.1.1	Vacuum apparatus at VUV X04DB beamline	48
3.1.2	Molecular sources	49
3.2.1	Photoion yield curve of argon.	52
4.1.1	C_4H_5 isomers and their precursors.	53
4.1.2	Newman projection of 2-butyne-1-yl	54
4.1.3	Pyrolysis scans of 1-bromo-2-butyne.	56
4.1.4	Pyrolysis scans of 3-bromo-1-butyne.	57
4.1.5	Pyrolysis fragments of 1-bromo-2-butyne and 3-bromo-1-butyne.	58
4.1.6	Ms-TPES of 2-butyne-1-yl and 1-butyne-3-yl.	59
4.1.7	Vibrations of 2-butyne-1-ylum and 1-butyne-3-ylum.	60
4.1.8	Scheme of the precursor C_4H_5Br and radical C_4H_5 rearrangement.	61
4.1.9	Rearrangement of the two bromo-butyne.	62
4.1.10	C_4H_5 isomerization pathway	63

4.1.11	TPES 2-butyn-1-yl of the singlet and triplet cation	64
4.1.12	Potentials of the free rotor, the hindered rotor and the harmonic oscillator.	65
4.2.1	C ₄ H ₇ isomers and their precursor molecules.	66
4.2.2	Pyrolysis scans of 3-penten-1-yl nitrite.	68
4.2.3	Pyrolysis products of the precursors of 1-MA and 2-MA.	70
4.2.4	Ms-TPES of pyrolysis products of 3-penten-1-yl nitrite.	71
4.2.5	Pyrolysis scans of 3-methyl-3-buten-1-yl nitrite.	72
4.2.6	Ms-TPES of the pyrolysis products of 3-methyl-3-buten-1-yl nitrite.	73
4.2.7	Pyrolysis scans of 3-bromo-2-methylpropene	76
4.2.8	DPI of 3-penten-1-yl nitrite and 3-methyl-3-buten-1-yl nitrite	77
4.2.9	MS-TOF of 3-bromo-2-methylpropene without pyrolysis.	79
4.2.10	Breakdown diagram of 3-bromo-2-methyl-propene.	80
4.2.11	Different convolutions of FC simulations with ms-TPES of 1-MA.	81
4.2.12	Ms-TPES of 1- <i>E</i> -MA and 1- <i>Z</i> -MA	82
4.2.13	Ms-TPES of 2-MA	83
4.2.14	Geometries of allyl and 2-methylallyl	84
4.2.15	TPES of the allyl radical and MOs.	86
4.2.16	Molecular orbitals of methylallyl	87
4.2.17	Survey of theoretical DPI products of 2-MA.	89
4.2.18	Ion images of 3-methyl-3-penten-1-yl nitrite (a) and of argon (b).	89
4.2.19	High energy scan of the TPES of m/z=55	90
4.3.1	Pyrolysis of 9-bromofluorene to 9-fluorenyl radical.	92
4.3.2	TOF- mass spectra and TPES of 9-bromofluorene.	93
4.3.3	BD diagram of 9-bromofluorenone and CoG-curve of fluorenyl cation.	94
4.3.4	Threshold photoelectron spectrum of fluorenyl radical, C ₁₃ H ₉	96
4.3.5	Energy diagram of the different C ₉ H ₁₃ isomers.	98
4.3.6	PIY curve and ms-TPES of the mass signal m/z=330.	99
4.3.7	Computed dimers, C ₂₆ H ₁₈ of the fluorenyl radical.	100
4.4.1	Pyrolysis of α -amino-diphenylmethane.	101
4.4.2	TOF-MS of α -amino-diphenylmethane.	102
4.4.3	Ms-TPES of further pyrolysis products from adpm.	103
4.4.4	Dissociative photoionization of adpm.	104
4.4.5	Ms-TPES of the benzhydryl (C ₁₃ H ₁₁) and <i>t</i> -diphenylmethylene (C ₁₃ H ₁₀).	105
4.4.6	PIY curve and ms-TPES of the dimer, C ₂₆ H ₂₂	107
4.4.7	Potential dimers of diphenylmethyl.	107
5.0.1	Molecular structures of the investigated PAH.	109

5.1.1	Threshold photoelectron spectrum of DHP.	111
5.1.2	Vibrations of DHP	111
5.2.1	Threshold photoelectron spectrum of 1-PEN	112
5.2.2	TOF-mass spectra of 1-PEN	113
5.3.1	Ms-TPES of THCT.	114
5.3.2	Vibrations of THCT	115
6.0.1	Wolff rearrangement of DMA	117
6.0.2	Labeled structure of DMA	118
6.1.1	Threshold photoelectron spectrum of DMA	119
6.1.2	Vibrations of the DMA cation.	120
6.1.3	Breakdown diagram of the DPI of DMA.	121
6.1.4	DPI pathways in DMA	122
6.1.5	Structures of $C_3O_2H^+$ / $N_2C_2OH^+$	124
6.1.6	3D PES for a DPI pathway in DMA	125
6.1.7	TOF-distributions and breakdown fit of the channels to $m/z=155$ and $m/z=69$	126
6.2.1	TOF-MS of DMA at different pyrolysis temperatures.	127
6.2.2	TPES and PIE curve of the pyrolysis product $m/z=40$	129
6.2.3	Ms-TPES of 2-diazoethenone	130
6.2.4	Schematic overview of the possible structures $m/z=68$	131
6.2.5	Astrochemical relevant molecules related to 2-diazoethenone	132
6.2.6	Structures and IEs of the computed $C_3O_2H_2$ and $N_2C_2OH_2$ isomers.	133
6.2.7	Ms-TPES of $m/z=70$: Different isomers of the formula $N_2C_2OH_2$ and $C_2O_3H_2$	134
6.2.8	Ms-TPES of <i>E</i> -formylketene	135
6.2.9	Energy diagram <i>E</i> -formylketene	136
6.2.10	Fragmentation pathways of DMA upon pyrolysis at 200 °C.	137
8.0.1	Inputfile DPI-Fit 9-bromofluorene	145
8.0.2	Ms-TPES of pyrolysis products of 3-bromo-2-methylpropene(a)	151
8.0.3	Ms-TPES of pyrolysis products of 3-bromo-2-methylpropene(b)	152
8.0.4	Inputfile DPI-Fit DMA	153
8.0.5	$k(E)$ Fit of the DMA fragments and thermal energy distribution of DMA	155

List of Tables

2.1	BDE for radical precursors	13
4.1	Ionization energies C_4H_5 and C_4H_7	91
4.2	AE_{0K} and IE_{ad} for $C_{13}H_x$ ($x=9,10,11$) isomers and their dimers	108
5.1	IE_{ad} for three PAH.	115
6.1	AE_{0K} and IE_{ad} of DPI and pyrolysis fragments of DMA.	138

Bibliography

- [1] M. Lang, F. Holzmeier, P. Hemberger, I. Fischer, *J. Chem. Phys. A*, 2015, **119**, 3995–4000.
- [2] M. Lang, F. Holzmeier, I. Fischer, P. Hemberger, *J. Phys. Chem. A*, 2013, **117**, 5260–5268.
- [3] P. Constantinidis, M. Lang, J. Herterich, I. Fischer, J. Auerswald, A. Krueger, *J. Phys. Chem. A*, 2014, **118**, 2915–2921.
- [4] M. Lang, F. Holzmeier, I. Fischer, P. Hemberger, *J. Phys. Chem. A*, 2014, **118**, 11235–11243.
- [5] M. Gomberg, *Ber. Dtsch. Chem. Ges.*, 1900, **33**, 3150–3163.
- [6] M. Gomberg, *J. Am. Chem. Soc.*, 1900, **22**, 757–771.
- [7] T. T. Tidwell, in *Encyclopedia of Radicals in Chemistry, Biology and Materials*, John Wiley & Sons, Ltd, 2012.
- [8] J. Hioe, H. Zipse, in *Encyclopedia of Radicals in Chemistry, Biology and Materials*, John Wiley & Sons, Ltd, 2012.
- [9] G. Cohen, Y. Riahi, S. Sasson, in *Encyclopedia of Radicals in Chemistry, Biology and Materials*, John Wiley & Sons, Ltd, 2012.
- [10] L. Valgimigli, D. A. Pratt, in *Encyclopedia of Radicals in Chemistry, Biology and Materials*, John Wiley & Sons, Ltd, 2012.
- [11] N. E. Geacintov, V. Shafirovich, in *Encyclopedia of Radicals in Chemistry, Biology and Materials*, John Wiley & Sons, Ltd, 2012.
- [12] L. J. Ignarro, *Angew. Chem., Int. Ed.*, 1999, **38**, 1882–1892.
- [13] P. H. Wine, J. M. Nicovich, in *Encyclopedia of Radicals in Chemistry, Biology and Materials*, John Wiley & Sons, Ltd, 2012.
- [14] T. Owen, *Nature*, 2005, **438**, 756–757.
- [15] J. H. Waite, H. Niemann, R. V. Yelle, W. T. Kasprzak, T. E. Cravens, J. G. Luhmann, R. L. McNutt, W.-H. Ip, D. Gell, V. De La Haye, I. Müller-Wordag, B. Magee, N. Borggren, S. Ledvina, G. Fletcher, E. Walter, R. Miller, S. Scherer, R. Thorpe, J. Xu, B. Block, K. Arnett, *Science*, 2005, **308**, 982.

- [16] J. Lalevée, J. P. Fouassier, in *Encyclopedia of Radicals in Chemistry, Biology and Materials*, John Wiley & Sons, Ltd, 2012.
- [17] J. Pérez-Prieto, M. A. Miranda, in *Encyclopedia of Radicals in Chemistry, Biology and Materials*, John Wiley & Sons, Ltd, 2012.
- [18] C. Alcaraz, D. Schröder, I. Fischer, in *Encyclopedia of Radicals in Chemistry, Biology and Materials*, John Wiley & Sons, 2012.
- [19] M. Sarobe, L. W. Jenneskens, A. Kleij, M. Petroutsas, *Tetrahedron Lett.*, 1997, **38**, 7255–7258.
- [20] H. Richter, J. B. Howard, *Prog. Energy Combust. Sci.*, 2000, **26**, 565.
- [21] ed. M. S. Platz, R. A. Moss, J. Maitland Jones, *Reviews of Reactive Intermediate Chemistry*, Wiley & Sons, Inc. New York, 2007.
- [22] S. E. Stein, J. A. Walker, M. M. Suryan, A. Fahr In *23rd Symp. (Int.) Combust.*, pp. 85–90.
- [23] M. Frenklach, F. Wang, *Proc. Combust. Inst.*, 1991, **21**, 1559.
- [24] H. Böhm, H. Jander, D. Tanke, *Symp. (Int.) Combust.*, 1998, **27**(1), 1605 – 1612.
- [25] D. S. N. Parker, R. I. Kaiser, B. Bandyopadhyay, O. Kostko, T. P. Troy, M. Ahmed, *Angew. Chem. Int. Edit.*, 2015, **54**, 5421–5424.
- [26] B. Shukla, M. Koshi, *Combust. Flame*, 2011, **158**, 369 – 375.
- [27] K. Kohse-Höinghaus, B. Atakan, A. Lamprecht, G. Gonzalez Alatorre, M. Kamphus, T. Kasper, N.-N. Liu, *Phys. Chem. Chem. Phys.*, 2002, **4**, 2056–2062.
- [28] M. Frenklach, *Phys. Chem. Chem. Phys.*, 2002, **4**, 2028–2037.
- [29] C. A. Taatjes, S. J. Klippenstein, N. Hansen, J. A. Miller, T. A. Cool, J. Wang, M. E. Law, P. R. Westmoreland, *Phys. Chem. Chem. Phys.*, 2005, **7**, 806–813.
- [30] C. A. Taatjes, N. Hansen, D. L. Osborn, K. Kohse-Höinghaus, T. A. Cool, P. R. Westmoreland, *Phys. Chem. Chem. Phys.*, 2008, **10**, 20–34.
- [31] R. Barlow, G.-H. Wang, P. Anselmo-Filho, M. Sweeney, S. Hochgreb, *Proc. Combust. Inst.*, 2009, **32**, 945 – 953.
- [32] Y. Li, F. Qi, *Acc. Chem. Res.*, 2010, **43**, 68–78.
- [33] N. Hansen, S. J. Klippenstein, C. A. Taatjes, J. A. Miller, J. Wang, T. A. Cool, B. Yang, R. Yang, L. Wei, C. Huang, J. Wang, F. Qi, M. E. Law, P. R. Westmoreland, *J. Phys. Chem. A*, 2006, **110**, 3670–3678.
- [34] N. Hansen, T. Kasper, S. J. Klippenstein, P. R. Westmoreland, M. E. Law, C. A. Taatjes, K. Kohse-Höinghaus, J. Wang, T. A. Cool, *J. Phys. Chem. A*, 2007, **111**, 4081–4092.

- [35] J. Krüger, G. A. Garcia, D. Felsmann, K. Moshhammer, A. Lackner, A. Brockhinke, L. Nahon, K. Kohse-Höinghaus, *Phys. Chem. Chem. Phys.*, 2014, **16**, 22791–22804.
- [36] M. L. Heger, *Lick Obs. Bull.*, 1922, **10**, 146–147.
- [37] P. W. Merrill, *Publ. Astron. Soc. Pac.*, 1936, **48**, 179–180.
- [38] P. W. Merrill, *Astrophys. J.*, 1936, **83**, 126.
- [39] <http://dibdata.org>, DIB database, 12.05.2015.
- [40] T. P. Snow, B. J. McCall, *Annu. Rev. Astron. Astrophys.*, 2006, **44**, 367–414.
- [41] T. Oka, B. J. McCall, *Science*, 2011, **331**, 293–294.
- [42] A. G. G. M. Tielens, T. P. Snow, *The diffuse interstellar bands*, Kluwer Academic Publishers, 1995.
- [43] T. Troy, *The jet-cooled spectroscopy of resonance-stabilized radical chromophores* PhD thesis, University of Sydney, 2011.
- [44] C. Boersma, S. Hony, A. G. G. M. Tielens, *A&A*, 2006, **447**, 213–220.
- [45] A. Leger, J. L. Puget, *Astron. Astrophys.*, 1984, **137**, L5–L8.
- [46] L. J. Allamandola, A. G. G. M. Tielens, J. R. Barker, *Astrophys. J.*, 1985, **290**, L25–L28.
- [47] J. H. Waite, D. T. Young, T. E. Cravens, A. J. Coates, F. J. Crary, B. Magee, J. Westlake, *Science*, 2007, **316**, 870–875.
- [48] T. Pino, N. Boudin, P. Bréchnignac, *J. Chem. Phys.*, 1999, **111**, 7337.
- [49] P. Bréchnignac, T. Pino, *Astron. and Astroph.*, 1999, **343**, L49.
- [50] I. R. Dunkin, *Matrix isolation techniques: a practical approach*, Oxford University press, New York/Cambridge, 1998.
- [51] A. Mardyukov, W. Sander, in *Encyclopedia of Radicals in Chemistry, Biology and Materials*, John Wiley & Sons, Ltd, 2012.
- [52] M. Mudrich, F. Stienkemeier, *Int. Rev. Phys. Chem.*, 2014, **33**, 301–339.
- [53] D. H. Levy, *Spektrum Wiss.*, 1984, pp. 4529–4532.
- [54] T. Baer, W. L. Hase, *Unimolecular Reaction Dynamics - Theory and Experiments*, Oxford University press, New York/Cambridge, 1996.
- [55] J. B. Anderson, R. P. Endres, J. B. Fenn, *Molecular Beams*, 10, Wiley, 1966.
- [56] H. Dossmann, G. A. Garcia, L. Nahon, B. K. C. de Miranda, C. Alcaraz, *J. Chem. Phys.*, 2012, **136**, 204304.

- [57] B. K. Cunha de Miranda, C. Alcaraz, M. Elhanine, B. Noller, P. Hemberger, I. Fischer, G. A. Garcia, H. Soldi-Lose, B. Gans, L. A. Vieira Mendes, S. Boyele-Péronne, S. Douin, J. Zabka, P. Botschwina, *J. Phys. Chem. A*, 2010, **114**, 4818–4830.
- [58] R. G. Gilbert, S. C. Smith, *Theory of Unimolecular and Recombination Reactions*, Blackwell Scientific, Oxford, 1990.
- [59] M. Sulkes, *Chem. Phys. Lett.*, 1985, **119**, 426.
- [60] B. Sztáray, T. Baer, *Rev. Sci. Instrum.*, 2003, **74**, 3763–3768.
- [61] T. Baer, B. Sztáray, J. P. Kercher, A. F. Lago, A. Bodi, C. Skull, D. Palathinkal, *Phys. Chem. Chem. Phys.*, 2005, **7**, 1507–1513.
- [62] P. M. Mayer, T. Baer, *Int. J. Mass Spectrom.*, 1996, **156**, 133 – 139.
- [63] S. Willitsch, L. L. Imbach, F. Merkt, *J. Chem. Phys.*, 2002, **117**, 1939.
- [64] B. S. Willitsch, J. M. Dyke, F. Merkt, *Helv. Chim. Acta*, 2003, **86**, 1152–1166.
- [65] S. Willitsch, J. M. Dyke, F. Merkt, *Mol. Phys.*, 2004, **102**, 1543–1553.
- [66] M. Gasser, A. M. Schulenburg, P. M. Dietiker, A. Bach, F. Merkt, P. Chen, *J. Chem. Phys.*, 2009, **131**, 014304.
- [67] M. Gasser, J. A. Frey, J. M. Hostettler, A. Bach, P. Chen, *J. Phys. Chem. A*, 2010, **114**, 4704–4711.
- [68] M. Gasser, A. Bach, P. Chen, *Phys. Chem. Chem. Phys.*, 2008, **10**, 1133–1138.
- [69] M. Gasser, J. A. Frey, J. M. Hostettler, A. Bach, *J. Mol. Spectrosc.*, 2010, **263**, 93–100.
- [70] M. Gasser, J. A. Frey, J. M. Hostettler, A. Bach, *Chem. Commun.*, 2011, **47**, 301–303.
- [71] R. Schlachta, G. Lask, S. Tsay, V. Bondybey, *Chem. Phys.*, 1991, **155**, 267 – 274.
- [72] D. T. Anderson, S. Davis, T. S. Zwier, D. J. Nesbitt, *Chem. Phys. Lett.*, 1996, **258**, 207–212.
- [73] C. Tao, C. Mukarakate, S. A. Reid, *J. Mol. Spectrosc.*, 2007, **241**, 136–142.
- [74] E. N. Sharp, P. Rupper, T. A. Miller, *Phys. Chem. Chem. Phys.*, 2008, **10**, 3955–3981.
- [75] A. Droege, P. Engelking, *Chem. Phys. Lett.*, 1983, **96**, 316 – 318.
- [76] B. Ruscic, *Res. Adv. Phys. Chem.*, 2000, **1**, 39–75.
- [77] J. Dyke, A. Ellis, N. Jonathan, A. Morris, *J. Chem. Soc. Faraday Trans. 2*, 1985, **81**, 1573–86.
- [78] J. Baker, M. Barnes, M. C. R. Cockett, J. M. Dyke, A. M. Ellis, M. Feher, E. P. F. Lee, A. Morris, H. Zamanpour, *J. Electron Spectrosc.*, 1990, **51**, 487–511.
- [79] C. Alcaraz, C. Nicolas, R. Thissen, J. Zabka, O. Dutuit, *J. Phys. Chem. A*, 2004, **108**, 9998–10009.

- [80] D. W. Kohn, H. Clauberg, P. Chen, *Rev. Sci. Instrum.*, 1992, **63**, 4003–4005.
- [81] Q. Guan, K. N. Urness, T. K. Ormond, D. E. David, G. Barney Ellison, J. W. Daily, *Int. Rev. Phys. Chem.*, 2014, **33**, 447–487.
- [82] P. Chen, *Unimolecular and Bimolecular Reaction Dynamics*, Wiley & Sons, Inc. New York, 1994.
- [83] S. J. Blanksby, G. B. Ellison, *Acc. Chem. Res.*, 2003, **36**, 255–263.
- [84] J. C. Maxwell, *Phil. Trans.*, 1865, **155**, 459–512.
- [85] P. Willmott, *An Introduction to Synchrotron Radiation - Techniques and Applications*, John Wiley & Sons, 2011.
- [86] M. Johnson, A. Bodi, L. Schulz, T. Gerber, *Nucl. Instrum. Meth. A*, 2009, **610**, 597–603.
- [87] H. Hertz, *Ann. Phys.*, 1887, **267**, 983–1000.
- [88] J. A. Blush, H. Clauberg, D. W. Kohn, D. W. Minsek, X. Zhang, P. Chen, *Acc. Chem. Res.*, 1992, **25**, 385–392.
- [89] E. Herbst, *Angew. Chem.-Ger. Edit*, 1990, **102**, 627–641.
- [90] A. Ellis, M. Feher, T. Wright, *Electronic and Photoelectron Spectroscopy - Fundamentals and Case Studies*, Cambr, 2005.
- [91] J. Illenberger, E. Momigny, *Gaseous Molecular Ions - An introduction to Elementary Processes Induced by Ionization*, Steinkopff Verlag Darmstadt, Springer-Verlag New York, 1992.
- [92] J. Franck, E. G. Dymond, *Trans. Faraday Soc.*, 1926, **21**, 536–542.
- [93] R. L. Platzman, *Radiat. Res.*, 1962, **17**, 419.
- [94] T. Baer, *Int. J. Mass Spectrom.*, 2000, **200**, 443–457.
- [95] D. W. Turner, C. Baker, A. D. Baker, C. R. Brundle, *Photoelectron Spectroscopy*, Wiley, London, 1970.
- [96] M. J. Hollas, *Moderne Methoden in der Spektroskopie*, Vieweg, Braunschweig Wiesbaden, 2., 1995.
- [97] I. Fischer, K. Müller-Dethlefs, *Phys. Unserer Zeit*, 2000, **31**, 168–176.
- [98] K. Müller-Dethlefs, E. W. Schlag, *Angew. Chem., Int. Ed.*, 1998, **37**, 1346–1374.
- [99] S. T. Park, S. K. Kim, M. S. Kim, *J. Chem. Phys.*, 2001, **114**, 5568–5576.
- [100] A. Bodi, M. Johnson, T. Gerber, Z. Gengeliczki, B. Sztáray, T. Baer, *Rev. Sci. Instrum.*, 2009, **80**, 034101.
- [101] A. T. Eppink, D. H. Parker, *Rev. Sci. Instrum.*, 1997, **68**, 3477.

- [102] G. A. Garcia, L. Nahon, I. Powis, *Rev. Sci. Instrum.*, 2004, **75**, 4989.
- [103] G. A. Garcia, H. Soldi-Lose, L. Nahon, *Rev. Sci. Instrum.*, 2009, **80**, 023102.
- [104] D. Céolin, G. Chaplier, M. Lemonnier, G. A. Garcia, C. Miron, L. Nahon, M. Simon, N. Leclercq, P. Morin, *Rev. Sci. Instrum.*, 2005, **76**, 043302.
- [105] <http://www.roentdek.com/>, 03.01.2015.
- [106] W. C. Wiley, I. H. McLaren, *Rev. Sci. Instrum.*, 1955, **26**, 1150.
- [107] A. Bodi, P. Hemberger, T. Gerber, B. Sztáray, *Rev. Sci. Instrum.*, 2012, **83**, 083105.
- [108] A. Bodi, B. Sztáray, T. Baer, M. Johnson, T. Gerber, *Rev. Sci. Instrum.*, 2007, **78**, 084102.
- [109] P. Rupper, F. Merkt, *Rev. Sci. Instrum.*, 2004, **75**, 613–622.
- [110] T. Baer, R. C. Dunbar, *J. Am. Soc. Mass Spectrom.*, 2010, **21**, 681 – 693.
- [111] M. J. Frisch, G. W. Trucks, H. B. Schlegel, G. E. Scuseria, M. A. Robb, J. R. Cheeseman, G. Scalmani, V. Barone, B. Mennucci, G. A. Petersson, H. Nakatsuji, M. Caricato, X. Li, H. P. Hratchian, A. F. Izmaylov, J. Bloino, G. Zheng, J. L. Sonnenberg, M. Hada, M. Ehara, K. Toyota, R. Fukuda, J. Hasegawa, M. Ishida, T. Nakajima, Y. Honda, O. Kitao, H. Nakai, T. Vreven, J. A. Montgomery, J. E. Peralta, F. Ogliaro, M. Bearpark, J. J. Heyd, E. Brothers, K. N. Kudin, V. N. Staroverov, R. Kobayashi, J. Normand, K. Raghavachari, A. Rendell, J. C. Burant, S. S. Iyengar, J. Tomasi, M. Cossi, N. Rega, J. M. Millam, M. Klene, J. E. Knox, J. B. Cross, V. Bakken, C. Adamo, J. Jaramillo, R. Gomperts, R. E. Stratmann, O. Yazyev, A. J. Austin, R. Cammi, C. Pomelli, J. W. Ochterski, R. L. Martin, K. Morokuma, V. G. Zakrzewski, G. A. Voth, P. Salvador, J. J. Dannenberg, S. Dapprich, A. D. Daniels, Farkas, J. B. Foresman, J. V. Ortiz, J. Cioslowski, D. J. Fox, Gaussian 09, Revision D.01, 2009, 2009.
- [112] R. G. Parr, W. Yang, *Annu. Rev. Phys. Chem.*, 1995, **46**, 701–728.
- [113] P. Hohenberg, W. Kohn, *Phys. Rev.*, 1964, **136**, B864.
- [114] A. Becke, *Phys. Rev. A*, 1988, **38**, 3098–3100.
- [115] C. Lee, W. Yang, R. G. Parr, *Phys. Rev. B*, 1988, **37**, 785.
- [116] A. D. Becke, *J. Chem. Phys.*, 1993, **98**, 5648–5652.
- [117] K. Kim, K. D. Jordan, *J. Phys. Chem.*, 1994, **98**, 10089–10094.
- [118] A. P. Scott, L. Radom, *J. Phys. Chem.*, 1996, **100**, 16502–16513.
- [119] W. J. Hehre, R. Ditchfield, J. A. Pople, *J. Chem. Phys.*, 1972, **56**, 2257–2261.
- [120] C. Möller, M. S. Plesset, *Phys. Rev.*, 1934, **46**, 618–622.
- [121] J. A. Montgomery, M. J. Frisch, J. W. Ochterski, G. A. Petersson, *J. Chem. Phys.*, 2000, **112**, 6532–6542.

- [122] E. Runge, E. K. U. Gross, *Phys. Rev. Lett.*, 1984, **52**, 997–1000.
- [123] J. A. Montgomery, M. J. Frisch, J. W. Ochterski, G. A. Petersson, *J. Chem. Phys.*, 1999, **110**, 2822–2827.
- [124] Documentation of the program fcfit. D. Krügler, M. Schmitt; Heinrich-Heine-Universität Düsseldorf, May 19, 2010.
- [125] F. Duschinsky, *Acta Physicochim. U.R.S.*, 1937, **7**, 551.
- [126] E. V. Doktorov, I. A. Malkin, V. I. Man'ko, *J. Mol. Spec.*, 1975, **56**, 1.
- [127] E. V. Doktorov, I. A. Malkin, V. I. Man'ko, *J. Mol. Spec.*, 1977, **64**, 302.
- [128] R. A. Marcus, *J. Chem.*, 1952, **20**, 359–364.
- [129] H. M. Rosenstock, M. B. Wallenstein, A. L. Wahrhaftig, H. Eyring, *Proc. Nat. Acad. Sci.*, 1952, **38**, 667–678.
- [130] S. E. Stein, B. Rabinovitch, *Chem. Phys. Lett.*, 1977, **49**, 183 – 188.
- [131] T. Baer, P. M. Mayer, *J. Am. Soc. Mass Spectrom.*, 1997, **8**, 103 – 115.
- [132] B. Sztáray, A. Bodi, T. Baer, *J. Mass Spectrom.*, 2010, **45**, 1233–1245.
- [133] K.-M. Weitzel, J. A. Booze, T. Baer, *Chem. Phys.*, 1991, **150**, 263 – 273.
- [134] J. Troe, V. G. Ushakov, A. A. Viggiano, *J. Phys. Chem. A*, 2006, **110**, 1491–1499.
- [135] J. C. Light, *J. Chem. Phys.*, 1964, **40**, 3221–3229.
- [136] S. M. Gordon, N. W. Reid, *Int. J. Mass Spectrom. Ion Phys*, 1975, **18**, 379–391.
- [137] F. Muntean, P. B. Armentrout, *J. Phys. Chem. A*, 2003, **107**, 7413–7422.
- [138] J. Laskin, C. Lifshitz, *J. Mass Spectrom.*, 2001, **36**, 459–478.
- [139] K.-M. Weitzel, M. Malow, G. K. Jarvis, T. Baer, Y. Song, C. Y. Ng, *J. Chem. Phys.*, 1999, **111**, 8267–8270.
- [140] P. Hemberger, *Photoionisationsstudien an Radikalen und Carbenen mit VUV-Synchrotronstrahlung* PhD thesis, Universität Würzburg, 2011.
- [141] Schon, *Spektroskopie an substituierten [2.2]Paracyclophanen* PhD thesis, Universität Würzburg, 2011.
- [142] S. Lias, J. Bartmess, J. Liebman, J. Holmes, R. Levin, W. Mallard, *J. Phys. Chem. Ref. Data*, 1988, **17**.
- [143] K.-M. Weitzel, J. Mähnert, M. Penno, *Chem. Phys. Lett.*, 1994, **224**, 371 – 380.
- [144] Z. Lin, T. Wang, D. Han, X. Han, S. Li, Y. Li, Z. Tian, *Rapid Commun. Mass Spectrom.*, 2009, **23**, 85–92.

- [145] Y. Li, L. Zhang, Z. Tian, T. Yuan, J. Wang, B. Yang, F. Qi, *Energ. Fuel.*, 2009, **23**, 1473–1485.
- [146] B. Sirjean, R. Fournet, *Phys. Chem. Chem. Phys.*, 2013, **15**, 596–611.
- [147] S. E. Wheeler, W. D. Allen, H. F. Schaefer, *J. Chem. Phys.*, 2004, **121**, 8800–8813.
- [148] D. W. Kohn, P. Chen, *J. Am. Chem. Soc.*, 1993, **115**, 2844–2848.
- [149] G. Bieri, F. Burger, E. Heilbronner, J. P. Maier, *Helv. Chim. Acta*, 1977, **60**, 2213–2233.
- [150] M. Allan, E. Kloster-Jensen, J. Maier, *J. Chem. Soc. Faraday Trans. 2*, 1977, **73**, 1406–1417.
- [151] S. A. Maluendes, A. D. McLean, K. Yamashita, E. Herbst, *J. Chem. Phys.*, 1993, **99**, 2812–2820.
- [152] A. Bodi, P. Hemberger, *Phys. Chem. Chem. Phys.*, 2014, **16**, 505–515.
- [153] P. Hemberger, M. Lang, B. Noller, I. Fischer, C. Alcaraz, B. K. Cunha de Miranda, G. A. Garcia, H. Soldi-Lose, *J. Phys. Chem. A*, 2011, **115**, 2225–2230.
- [154] A. Cunje, , M. H. Lien, A. C. Hopkinson, *J. Org. Chem.*, 1996, **61**, 5212–5220.
- [155] K. S. Pitzer, W. D. Gwinn, *J. Chem. Phys.*, 1942, **10**, 428–440.
- [156] K. Kohse-Höinghaus, P. Oßwald, T. A. Cool, T. Kasper, N. Hansen, F. Qi, C. K. Westbrook, P. R. Westmoreland, *Angew. Chem. Int. Ed.*, 2010, **49**, 3572–3597.
- [157] C. K. Westbrook, *Annu. Rev. Phys. Chem.*, 2013, **64**, 201–219.
- [158] J. C. Schultz, F. A. Houle, J. L. Beauchamp, *J. Am. Chem. Soc.*, 1984, **106**, 7336–7347.
- [159] A. B. Callear, H. K. Lee, *Trans. Faraday Soc.*, 1968, **64**, 2017–2022.
- [160] J. W. Hudgens, C. S. Dulcey, *J. Phys. Chem.*, 1985, **89**, 1505–1509.
- [161] C.-C. Chen, H.-C. Wu, C.-M. Tseng, Y.-H. Yang, Y.-T. Chen, *J. Chem. Phys.*, 2003, **119**, 241–250.
- [162] J. Herterich, T. Gerbich, I. Fischer, *ChemPhysChem*, 2013, **14**, 3906–3908.
- [163] J.-V. Herterich, *Pikosekunden-zeitaufgelöste Photoionisation: 2-Methylallyl-Radikal und Pyracen* PhD thesis, Universität Würzburg, 2014.
- [164] K. Kimura, S. Katsumata, Y. Achiba, T. Yamazaki, S. Iwata, *Ionization energies, Ab initio assignments, and valence electronic structure for 200 molecules*, Handbook of Hel Photoelectron Spectra of Fundamental Organic Compounds, Scientific Soc. Press, Tokyo, Japan, 1981.
- [165] C. Baker, D. W. Turner, *J. Chem. Soc. D*, 1969, pp. 480–481.

- [166] P. Hemberger, A. J. Trevitt, T. Gerber, E. Ross, G. da Silva, *J. Phys. Chem. A*, 2014, **118**, 3593–3604.
- [167] T. Schübler, H.-J. Deyerl, S. Dümmler, I. Fischer, C. Alcaraz, M. Elhanine, *J. Chem. Phys.*, 2003, **118**, 9077–9080.
- [168] I. Fischer, T. Schübler, H.-J. Deyerl, M. Elhanine, C. Alcaraz, *Int. J. Mass Spectrom.*, 2007, **261**, 227–233.
- [169] T. Koopmans, *Physica*, 1934, **1**, 104.
- [170] A. Matsugi, A. Miyoshi, *Phys. Chem. Chem. Phys.*, 2012, **14**, 9722–9728.
- [171] M. Vala, J. Szczepanski, J. Banisaukas, S. Hirata, *NASA Laboratory Astrophysics Workshop, held May 1-3 2002 at NASA Ames Research Center, Moffett Field, CA 94035-1000*, 2002, pp. 162–164.
- [172] J. Szczepanski, J. Banisaukas, M. Vala, S. Hirata, W. R. Wiley, *J. Phys. Chem. A*, 2002, **106**, 6935–6940.
- [173] R. F. Pottie, F. P. Lossing, *J. Am. Chem. Soc.*, 1963, **85**, 269–271.
- [174] J. P. Maier, D. W. Turner, *Faraday Discuss.*, 1972, **54**, 149–167.
- [175] P. Hemberger, A. Bodi, C. Schon, M. Steinbauer, K. H. Fischer, C. Kaiser, I. Fischer, *Phys. Chem. Chem. Phys.*, 2012, **14**, 11920–11929.
- [176] K. H. Fischer, M. Schneider, I. Fischer, B. Pfaffinger, H. Braunschweig, B. Sztáray, A. Bodi, *Chem.–Eur. J.*, 2012, **18**, 4533–4540.
- [177] R. F. Pottie, F. P. Lossing, *J. Am. Chem. Soc.*, 1963, **85**, 269–271.
- [178] K. H. Fischer, J. Herterich, I. Fischer, S. Jaeqx, A. M. Rijs, *J. Phys. Chem. A*, 2012, **116**, 8515–8522.
- [179] S. Jockusch, T. Hirano, Z. Liu, N. J. Turro, *J. Phys. Chem. B*, 2000, **104**, 1212–1216.
- [180] A. Bromberg, D. Meisel, *J. Phys. Chem.*, 1985, **89**, 2507–2513.
- [181] A. Bromberg, K. H. Schmidt, D. Meisel, *J. Am. Chem. Soc.*, 1985, **107**, 83–91.
- [182] J. Bartl, S. Steenken, H. Mayr, R. A. McClelland, *J. Am. Chem. Soc.*, 1990, **112**, 6918–6928.
- [183] G. Kelly, C. J. Willsher, F. Wilkinson, J. C. Netto-Ferreira, A. Olea, D. Weir, L. J. Johnston, J. C. Scaiano, *Can. J. Chem.*, 1990, **68**, 812–819.
- [184] R. W. Brandon, G. L. Closs, C. A. Hutchison Jr., *J. Chem. Phys.*, 1962, **37**, 1878–1879.
- [185] R. W. Murray, A. M. Trozzolo, E. Wasserman, W. A. Yager, *J. Am. Chem. Soc.*, 1962, **84**, 3213–3214.

- [186] R. W. R. Humphreys, D. R. Arnold, *Can. J. Chem.*, 1977, **55**, 2286–2291.
- [187] H. Sixl, R. Mathes, A. Schaupp, K. Ulrich, R. Huber, *Chem. Phys.*, 1986, **107**, 105–121.
- [188] C. A. Hutchison Jr., B. E. Kohler, *J. Chem. Phys.*, 1969, **51**, 3327–3335.
- [189] A. M. Trozzolo, W. A. Gibbons, *J. Am. Chem. Soc.*, 1967, **89**, 239–243.
- [190] K. Akiyama, S. Tero-Kubota, J. Higuchi, *J. Am. Chem. Soc.*, 1998, **120**, 8269–8270.
- [191] K. A. Horn, B. D. Allison, *Chem. Phys. Lett.*, 1985, **116**, 114–118.
- [192] A. M. Trozzolo, W. A. Gibbons, *J. Am. Chem. Soc.*, 1966, **88**, 172.
- [193] P. Costa, M. Fernandez-Oliva, E. Sanchez-Garcia, W. Sander, *J. Am. Chem. Soc.*, 2014, **136**, 15625–15630.
- [194] P. Costa, W. Sander, *Angew. Chem., Int. Ed.*, 2014, **53**, 5122–5125.
- [195] S. Willitsch, C. Jungen, F. Merkt, *J. Chem. Phys.*, 2006, **124**.
- [196] F. Qi, L. Sheng, Y. Zhang, S. Yu, W.-K. Li, *Chem. Phys. Lett.*, 1995, **234**, 450 – 454.
- [197] A. G. Harrison, F. P. Lossing, *J. Am. Chem. Soc.*, 1960, **82**, 1052–1054.
- [198] A. Keller, R. Kovacs, K.-H. Homann, *Phys. Chem. Chem. Phys.*, 2000, **2**, 1667–1675.
- [199] W. W. Duley, S. Lazarev, A. Scott, *Astrophys. J. Lett.*, 2005, **620**, L135.
- [200] X. Huang, Z. Lintao, J. Wu, *Chem.–Eur. J.*, 2011, **17**, 14907–14915.
- [201] Johannes, *Untersuchungen zur Synthese aromatisch anellierter Pyracene und Pyracylene* PhD thesis, Universität Würzburg, 2014.
- [202] B. Noller, P. Hemberger, I. Fischer, C. Alcaraz, G. A. Garcia, H. Soldi-Lose, *Phys. Chem. Chem. Phys.*, 2009, **11**, 5384.
- [203] M. Steinbauer, M. Lang, I. Fischer, B. K. C. de Miranda, C. Romanzin, C. Alcaraz, *Phys. Chem. Chem. Phys.*, 2011, **13**, 17956–17959.
- [204] W. Kirmse, *Eur. J. Org. Chem.*, 2002, **2002**, 2193–2256.
- [205] N. P. Hacker, *Photoresists and their development*, Chapman&Hall, New York, NY, 1995.
- [206] R. A. Abramovitch, *Can. J. Chem.*, 1959, **37**, 361–365.
- [207] M. Jones, W. Ando, M. E. Hendrick, A. Kulczycki, P. M. Howley, K. F. Hummel, D. S. Malament, *J. Am. Chem. Soc.*, 1972, **94**, 7469–7479.
- [208] K. Tanigaki, T. W. Ebbesen, *J. Phys. Chem.*, 1989, **93**, 4531–4536.
- [209] A. Bogdanova, V. V. Popik, *J. Am. Chem. Soc.*, 2003, **125**, 14153–14162.
- [210] A. Bogdanova, V. V. Popik, *J. Am. Chem. Soc.*, 2003, **125**, 1456–1457.

- [211] A. Bogdanova, V. V. Popik, *J. Am. Chem. Soc.*, 2004, **126**, 11293–11302.
- [212] V. A. Nikolaev, V. V. Shevchenko, M. S. Platz, N. N. Khimich, *Russ. J. Org. Chem.*, 2006, **42**, 815–827.
- [213] V. V. Shevchenko, N. N. Khimich, M. S. Platz, V. A. Nikolaev, *Russ. J. Org. Chem.*, 2006, **42**, 1213–1219.
- [214] M. A. Winnik, F. Wang, T. Nivaggioli, Z. Hruska, H. Fukumura, H. Masuhara, *J. Am. Chem. Soc.*, 1991, **113**, 9702–9704.
- [215] H. Fujiwara, Y. Nakajima, H. Fukumura, H. Masuhara, *J. Phys. Chem.*, 1995, **99**, 11481–11488.
- [216] T. Lippert, A. Koskelo, P. O. Stoutland, *J. Am. Chem. Soc.*, 1996, **118**, 1551–1552.
- [217] T. Lippert, P. O. Stoutland, *Appl. Surf. Sci.*, 1997, **109-110**, 43–47.
- [218] G. Burdzinski, J. Réhault, J. Wang, M. S. Platz, *J. Phys. Chem. A*, 2008, **112**, 10108–10112.
- [219] G. Burdzinski, M. S. Platz, *J. Phys. Org. Chem.*, 2010, **23**, 308–314.
- [220] P. Rudolf, J. Buback, J. Aulbach, P. Nuernberger, T. Brixner, *J. Am. Chem. Soc.*, 2010, **132**, 15213–15222.
- [221] A. Steinbacher, S. Roeding, T. Brixner, P. Nuernberger, *Phys. Chem. Chem. Phys.*, 2014, **16**, 7290–7298.
- [222] V. V. Popik, *Can. J. Chem.*, 2005, **83**, 1382–1390.
- [223] S. L. Kammula, H. L. Tracer, P. B. Shevlin, M. Jones, *J. Org. Chem.*, 1977, **42**, 2931–2932.
- [224] E. A. Fogleman, H. Koizumi, J. P. Kercher, B. Sztáray, T. Baer, *J. Phys. Chem. A*, 2004, **108**, 5288–5294.
- [225] K. Furuya, S. Katsumata, K. Kimura, *J. Electron Spectrosc. Relat. Phenom.*, 1993, **62**, 237 – 243.
- [226] A.-M. Boulanger, E. E. Rennie, D. M. P. Holland, D. A. Shaw, P. M. Mayer, *J. Phys. Chem. A*, 2008, **112**, 866–879.
- [227] T. A. Cool, K. Nakajima, T. A. Mostefaoui, F. Qi, A. McIlroy, P. R. Westmoreland, M. E. Law, L. Poisson, D. S. Peterka, M. Ahmed, *J. Chem. Phys.*, 2003, **119**, 8356–8365.
- [228] T. A. Cool, J. Wang, K. Nakajima, C. A. Taatjes, A. McIlroy, *Int. J. Mass Spectrom.*, 2005, **247**, 18 – 27.
- [229] A. Parr, A. Jason, R. Stockbauer, K. McCulloh, *Int. J. Mass Spectrom. Ion Phys.*, 1979, p. 319.

- [230] C. Baker, D. W. Turner, *Chem. Commun. (Cambridge, U. K.)*, 1968, (7), 400.
- [231] H. J. Bestmann, F. M. Soliman, *Angew. Chem.-Ger. Edit*, 1979, **91**, 1012–1013.
- [232] K. D. Tucker, M. L. Kutner, P. Thaddeus, *Astrophys. J.*, 1974, **193**, L115.
- [233] V. S. Nguyen, R. M. I. Elsamra, J. Peeters, S. A. Carl, M. T. Nguyen, *Phys. Chem. Chem. Phys.*, 2012, **14**, 7456–7470.
- [234] H. M. T. Nguyen, S. A. Carl, J. Peeters, M. T. Nguyen, *Phys. Chem. Chem. Phys.*, 2004, **6**, 4111–4117.
- [235] R. J. Hoobler, S. R. Leone, *J. Geophys. Res.-Planet*, 1997, **102**, 28717–28723.
- [236] K. D. Bayes, *J. Chem. Phys.*, 1970, **52**, 1093–1097.
- [237] J. A. Miller, S. P. Walch, *Int. J. Chem. Kinet.*, 1997, **29**, 253–259.
- [238] E. P. Clifford, P. G. Wenthold, W. C. Lineberger, G. A. Petersson, K. M. Broadus, S. R. Kass, S. Kato, C. H. DePuy, V. M. Bierbaum, G. B. Ellison, *J. Phys. Chem. A*, 1998, **102**, 7100–7112.
- [239] Z. Arnold, J. Sauliova, *Collect. Czech. Chem. Commun.*, 1973, **38**, 2641–2647.
- [240] G. Maier, H. P. Reisenauer, T. Sayraß, *Chem. Ber.*, 1982, **115**, 2192–2201.
- [241] E. Wenkert, T. P. Ananthanarayan, V. F. Ferreira, M. G. Hoffmann, H. S. Kim, *J. Org. Chem.*, 1990, **55**, 4975–4976.
- [242] B. Freiermuth, C. Wentrup, *J. Org. Chem.*, 1991, pp. 2286–2289.
- [243] D. M. Birney, P. E. Wagenseller, *J. Am. Chem. Soc.*, 1994, **116**, 6262–6270.
- [244] H.-X. Wei, C. Zhou, S. Ham, J. M. White, D. M. Birney, *Org. Lett.*, 2004, **6**, 4289–4292.
- [245] D. M. Birney, *J. Org. Chem.*, 1994, **59**, 2557–2564.
- [246] M. W. Wong, C. Wentrup, *J. Org. Chem.*, 1994, **59**, 5279–5285.
- [247] H. M. Badawi, W. Förner, A. Al-Saadi, *J. Mol. Struct.*, 2000, **505**, 19–30.
- [248] S. Z. Sayyed-Alangi, M. T. Baei, *E-Journal of Chemistry*, 2012, **9**, 193–202.
- [249] R. Ohme, H. Preuschhof, H.-U. Heyne, *Org. Synth. Coll.*, 1988, **6**, 78.

Danksagung

An erster Stelle danke ich *Prof. Dr. Ingo Fischer* für das vielseitige und äußerst interessante Thema über das ich diese Arbeit anfertigen durfte. Des Weiteren gilt mein Dank für seine immerwährende Diskussionsbereitschaft und Motivation, aber auch für seine unkomplizierte Art. Ganz besonders möchte ich mich für die Möglichkeit bedanken, an zwei internationalen Tagungen teilnehmen zu können.

Großer Dank geht an *Fabian Holzmeier*, mit dem ich die meisten Experimente gemeinsam an der SLS durchgeführt habe. Dank seines großen Engagements und seines kühlen Kopfes konnten wir fast jede Messzeit erfolgreich abschließen. Weiterhin danke ihm für permanentes Mitdenken, Miträtseln und Mitlösen bei einigen Fragestellungen, die die Spektren und Breakdowndiagramme lieferten.

Ansonsten danke ich dir noch dafür, dass du der Beste bist!

Ebenso danke ich *Dr. Patrick Hemberger*, der uns bei den Messzeiten an der Swiss Light Source immer aufopfernd und uns mit vielen Ideen speisend zur Seite stand. Weiterhin danke ich ihm für die Hilfe bei den Auswertungen, den quantenchemischen Rechnungen und die stete Diskussionsbereitschaft, die besonders in der Anfangsphase der Promotion sehr hilfreich war. An dieser Stelle danke ich auch *Jana Hemberger*, die uns zusammen mit Patrick während fast jeder Messzeit ein leckeres Abendessen bescherte. Danke für die schönen und lustigen Abende in Villigen!

Ich danke auch *Dr. Andrés Bödi* für die Hilfsbereitschaft an der SLS und auch bei einigen theoretischen Herausforderungen.

Ich danke meinen ehemaligen Bürokollegen *Dr. Jörg-Viktor Herterich* und *Thiemo Gerbich* für die amüsante Zeit in Büro 205. Besonders möchte ich hierbei unsere sportlichen AK-Ausflüge mit dem Rennrad hervorheben, die immer besonders viel Spaß gemacht haben, auch wenn sie im Unwetter des Jahres endeten. Thiemo sei außerdem für die Betreuung des Kaffeeautomaten gedankt.

Danke an *Hans-Christian Schmitt*, *Phillip Constantinidis*, *Jens Giegerich*, *Kai Pachner*, *Anja Röder* für die gute Zusammenarbeit und die herzliche und freundliche Atmosphäre in der Arbeitsgruppe.

Anja Röder danke ich insbesondere für den vielen guten französischen Käse.

Zum Schluss bedanke ich mich bei meinen *lieben Eltern*, die mir mein Studium ermöglichten und mich dabei unterstützten, obwohl sie seitdem oft auf meine Anwesenheit zu Hause verzichtet haben.